Author:
Vickery, Jemma Louise

Title:
Synthesis and characterisation of novel nanocomposites using layered materials

SYNTHESIS AND CHARACTERISATION OF NOVEL NANOCOMPOSITES USING LAYERED MATERIALS

Jemma Louise Vickery

University of Bristol

Department of Chemistry

Cantock's Close

Bristol

October 2009

A dissertation submitted to the University of Bristol in accordance with the requirements of the degree of Doctor of Philosophy in the Faculty of Science, Department of Chemistry

Word Count: 38671

ABSTRACT

The central theme of this thesis explores the synthesis, characterisation and processing of layered building-blocks to produce novel nanocomposites. Sol-gel chemistry protocols were employed to synthesize aminopropyl (AMP) functionalised-magnesium phyllosilicate clay. In particular, these clays have been shown to act as attractive host matrices for the immobilisation or intercalation of guest species, due to their facile sonication-induced exfoliation in aqueous solutions and ability to co-assemble in the presence of an appropriate guest. Herein, the anionic polymer, poly(sodium 4-styrene sulfonate) (PSS) mediated immobilisation of the cationic protein cytochrome *c* in the AMP clay matrix is achieved. FT-IR and UV-vis spectroscopy studies showed that protein secondary structure and activity were retained in the bio-inorganic nanocomposite.

Aqueous dispersions of atomically-thick graphene sheets were prepared via chemical routes. Graphite was treated with strong oxidising agents and mineral acids to produce graphene oxide, which was subsequently reduced in the presence of single-stranded DNA (ssDNA) to prepare ssDNA-functionalised graphene sheets (ssDNA-G). DNA-functionalised graphene sheets are characterised using UV-Vis, FT-IR and CD spectroscopy techniques. In addition, a mechanistic discussion for the interaction of graphene sheets with ssDNA is suggested. Interestingly, ssDNA-G dispersions can be processed using vacuum or evaporation-induced self-assembly techniques to prepare self-supporting bio-nanocomposite films, with PXRD studies showing that ssDNA molecules were intercalated within the gallery regions of graphene stacks. Furthermore, addition of counter charged guest molecules (e.g. cytochrome *c*, lysozyme) to the aqueous sols of ssDNA-G produced mesolamellar films by enabling the entrapment of protein molecules within the interlayer regions of graphene layers.

Alternatively, aqueous dispersions of PSS-stabilised graphene sheets (PSS-G) were processed to produce micro-and macroporous architectures by employing two templating strategies. Self-supporting three dimensional macroporous monoliths were fabricated using uni-axial freezing protocols. In contrast, microporous graphene-based spheres were prepared based on the electrostatic-induced assembly of anionically charged PSS-G sheets.

ACKNOWLEDGEMENTS

There are many, many people that I would like to thank for both their endless support and friendship throughout my PhD.

Firstly, I would like to extend my gratitude to my supervisor, Professor Stephen Mann for giving me the opportunity to spend the last three years in such an inspiring and motivational lab group. Your knowledge and enthusiasm has been invaluable.

I would like to thank all the members of the Centre for Organized Matter (past and present) for making the group such a friendly environment to work in. In particular, I would like to say a massive thank you to Avi for numerous scientific discussion and for all his support and friendship both in and out of the lab and for being there when experiments don't always go as planned! I would like to extend a big thank you to Dr. Tom Scott at the Interface Analysis Centre for being so willing to run all my XPS samples, John and Jon in the EMU for all their assistance and advice with the microscopes and Keith and Stew for all your technical advice and support in lab.

There are many, many people outside the lab that have made my PhD experience a truly enriching one. I'd like to thank Alice and Jane for many, many hours of discussions, scientific advice and entertainment both during thesis writing and the whole duration of the PhD your support has been invaluable and I really couldn't have done it without you girls. I would also like to extend a big thank you to all my friends in and out of Bristol who have been a never-ending source of entertainment and have endured to keep me sane!

I would like to thank my whole family, Mum, Dad, Sarah, Lisa and Will for your unconditional love and support throughout my whole PhD. Finally, I would like to say a massive, massive thank you to John for his never-ending source of support and inspiration and for always believing in me.

Declaration

I declare that the work in this dissertation was carried out in accordance with the requirements of the University's Regulations and Code of Practice for Research Degree Programmes and that it has not been submitted for any other academic candidate's own work. Work done in collaboration with, or with assistance of, others, is indicated as such. Any views expressed in the dissertation are those of the author.

SIGNED: 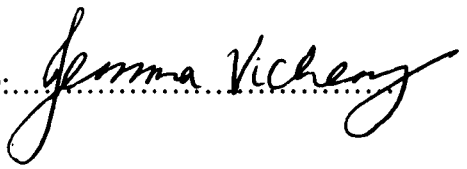 DATE:10/12/2009

TABLE OF CONTENTS

LIST OF FIGURES

LIST OF TABLES

CHAPTER 1 INTRODUCTION

1.1 Overview of thesis

Layered compounds represent a class of materials that is constantly growing and evolving in terms of composition, with a broad range of emerging applications in the fields of chemistry and nanotechnology. This thesis is concerned primarily with the synthesis and processing of two types of layered materials, namely synthetic organoclays and recently discovered and highly topical graphene nanosheets. In addition to investigating the synthesis and characterisation of these structures, the preparation of a range of hybrid nanocomposites is studied, based on the effective assembly of the delaminated lamellar sheets, using template-directed or self-assembly techniques. The combination of layered structures with biological and polymeric species is predicted to produce nanocomposite materials with advanced physio-chemical properties.

Research involving natural and synthetic silicate layered clays has been well investigated. The research presented in chapter 3, describes the synthesis and characterisation of a functional protein-inorganic construct based on the immobilisation of polymeric and biological species in the organically modified phyllosilicate clay matrix. The synthetic protocol employed, exploits the re-assembly of cationic clay particles in the presence of charged polymer and protein guest species. This chapter provides additional investigation of the structural integrity of the immobilised guest biomolecule.

In chapter 4, the synthesis and characterisation of novel DNA-functionalised graphene sols is presented. As a recently discovered material, the main goal of the research discussed in this chapter was to investigate synthetic protocols for producing graphene nanosheets in high yields. This was achieved via oxidation of graphite and subsequent reduction in the presence of a stabilising polymer which prevents the formation of irreversible, aggregated graphitic nanoparticles and effectively produces aqueous dispersions of polymer-stabilised graphene sheets. This chapter provides in-depth characterisation of the colloidal graphene nanosheets and concludes with investigation of the formation of bio-

nanocomposite graphene-based films based on vacuum filtration or self-assembly protocols.

The research presented in chapter 5 investigates the ability to effectively process aqueous dispersions of polymer-stabilised graphene sheets, previously introduced in chapter 4. Herein, well-established templating protocols were employed for the fabrication of graphene-based composites with micro- and macro-porous architectures, using ice-segregation induced self-assembly and electrostatic-induced templating techniques.

1.2 Introduction to Layered Materials

Naturally occurring and synthetic layered materials represent an extended class of compounds which has a prominent role in a range of disciplines including biology, materials chemistry, mineralogy, geology, physics and engineering, with diverse applications in, for example, catalysis,[1-3] advanced biomedical fields, including gene therapy and drug delivery systems,[4-7] batteries,[8-10] electronics[11] and environmentally-friendly "green material" as potential replacements of various existing hazardous materials.[12]

Layered materials are composed of confined two-dimensional (2D) crystalline sheets, which repeatedly stack to form extended three-dimensional (3D) arrays. These materials exhibit an array of highly attractive properties including high internal and external surface areas and adsorption capabilities. In particular, they furnish interesting chemical and intercalation abilities due to the relatively weak interlamellar forces between adjacent sheets in comparison to the strong intralamellar forces, enabling complete exfoliation or partial swelling of the 3D stacked structure in an appropriate solvent. This versatile approach enables the accommodation of a range of guest species in the gallery regions between neighbouring sheets, via ion-exchange reactions or complete exfoliation followed by assembly in the presence of a desired guest species. A variety of guests have previously been intercalated in layered hosts including organic and inorganic molecules, polymers and metal nanoparticles resulting in the formation of hybrid functional composite materials which demonstrate enhanced properties, compared to their individual components, and a broad spectrum of applications.[13]

Complete exfoliation or delamination of layered materials occurs when the interlayer spacing between adjacent layers is increased to such an extent that neighbouring layers no longer interact with each other but instead form individual, exfoliated 2D lamellae. The mechanism of exfoliation proceeds in general via two routes, either mechanical or chemical, depending on the nature and strength of the interlamellar forces and the composition of the individual layers. Mechanically-induced exfoliation can be achieved via the application of

sonication, which results in disruption of the inter-lamellar forces by mechanical shear forces, enabling effective separation of the stacked sheets. Alternatively, chemically-induced delamination can be achieved in a carefully chosen solvent with, in some cases, the additional help of mechanical stirring or sonication, if required.

In general, layered materials with low charge densities, for example smectite clays, are readily exfoliated in water[14] and the exfoliation behaviour of clay-type materials is discussed in more detail in the following section of this chapter. On the other hand, layered materials with higher charge densities require a more vigorous, exfoliation approach, as a result of stronger inter-lamellar attractive forces between, both, the individual sheets and the intercalated ions, which prevents the effective infiltration of solvent molecules in the gallery regions. In this situation, either, the surface of individual sheets can be modified or the intercalated ions residing in the gallery regions can be exchanged, resulting in the successful delamination of the stacked structure.

The successful fabrication of exfoliated 2D nanosheets creates a portfolio of opportunities for the further preparation of advanced and innovative higher-order structures based on the aggregation or re-assembly of these 2D building blocks. Addition of a range of species, including polymers, nanoparticles or biomolecules, for example, with opposing charges to the 2D nanosheets promotes the electrostatic-induced aggregation or re-assembly of the delaminated sheets to form stacked, hybrid, lamellar nanocomposites. Alternatively, the exfoliated nanosheets can be assembled into multilayer thin films, micro- and macroporous constructs or hierarchial nanomaterials by applying layer by layer (LbL), electrostatic-induced assembly or the Langmuir-Blodgett technique. **Figure 1.1**, summarises the broad range of possibilities for nanosheet assembly.

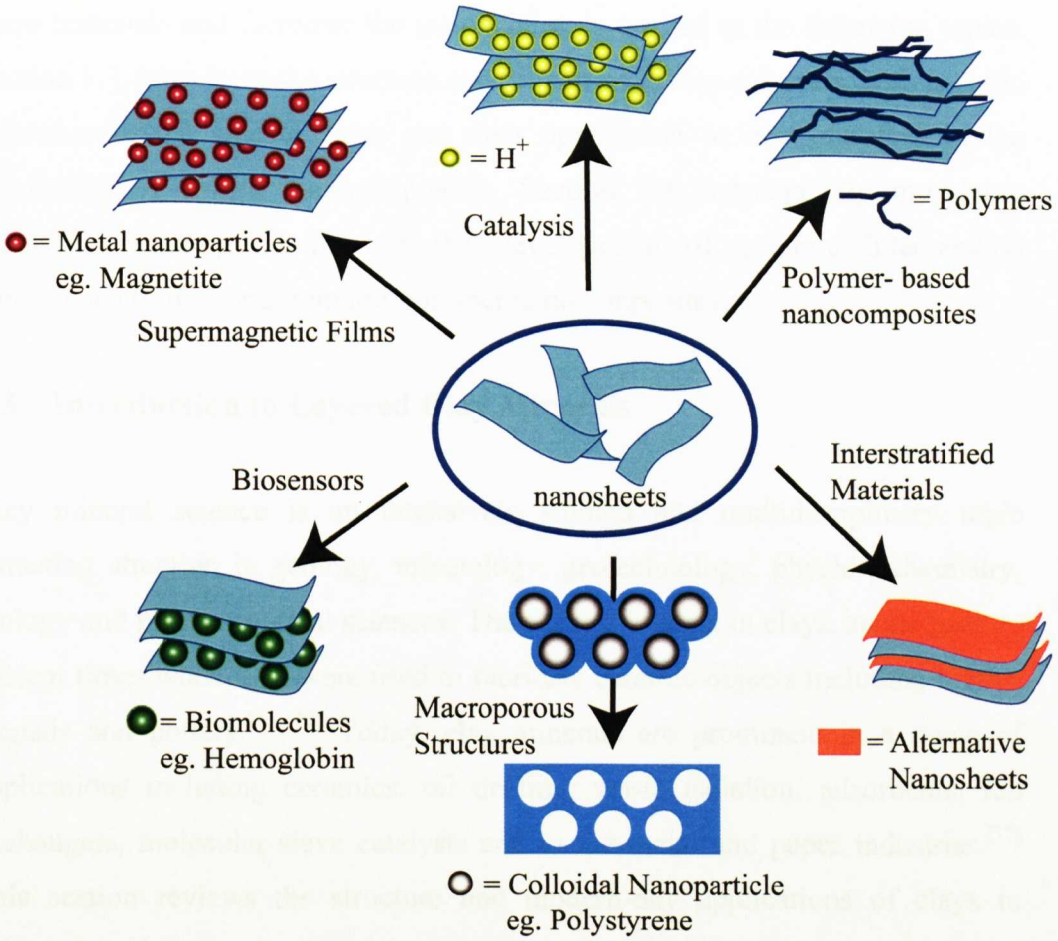

Figure 1.1 Schematic showing the application of 2D nanosheets as building blocks for hybrid nanocomposite assemblies, adapted from Bizeto et al.[15]

The range of existing layered materials is vast and their associated applications are continuously being developed. The main theme of the research reported in this thesis involves investigation of the synthesis and characterisation of two specific types of layered materials, namely magnesium organo phyllosilicate clays and graphite. These two contrasting structures form extended 3D arrays, which can be effectively exfoliated via mechanical or chemical routes to form 2D nanosheets and subsequently re-assembled in the presence of oppositely charged species, resulting in the fabrication of hybrid nanocomposites.

The remainder of this chapter discusses the history and progress that has been made with respect to the structure, properties and applications of these layered materials. Since there is a wide range of literature on both naturally occurring clays and graphite, it is beyond the scope of this thesis to cover all aspects of

these materials and therefore the introduction is limited to the following topics. Section 1.3, introduces the structure and properties of clay minerals, with specific reference to the silicate clays and their application as host matrices in the fabrication of hybrid nanocomposites. Section 1.4, subsequently introduces graphite, including scrutiny of the development of graphite intercalation compounds (GICs) and graphite-polymer nanocomposites.

1.3 Introduction to Layered Clay Minerals

Clay mineral science is an intensively studied and multidisciplinary topic attracting attention in geology, mineralogy, geotechnology, physics, chemistry, biology and pharmaceutical sciences. The earliest interest in clays, stems back to ancient times when they were used to fabricate ceramic objects including bricks, utensils and pottery.[16, 17] Today, clay minerals are prominent in a range of applications including ceramics, oil drilling, waste isolation, adsorbents, ion exchangers, molecular sieve catalysts and in the metal and paper industries.[17] This section reviews the structure and modern-day applications of clays in materials and inorganic chemistry, with specific reference to the huge scope of their application as host matrices in the fabrication of clay-based nanocomposites.

1.3.1 Silicate Clay Minerals in Nature

The silicate clay minerals represent the most abundant family of minerals found in the Earth's crust, accounting for 90 % of all known minerals.[14, 18, 19] These inexpensive and environmentally friendly minerals are composed of anionic, tetrahedral building blocks, consisting of a central silicon atom, surrounded by four oxygen atoms (SiO_4). In general, the silicate minerals can be further classified into smaller sub-groups depending on the relative, structural arrangement of the silicate tetrahedra, with charge-balancing interstitial cations present in the gallery regions, to provide structural neutrality, (**Table 1.1**).

Classification of Silicate Minerals	Arrangement of Tetrahedral Silicate Units
Nesosilicates or Orthosilicates	Isolated silicates
Sorosilicates	Isolated double tetrahedral units
Cyclosilicates	Silicates arranged in 3- or 6- membered rings
Inosilicates	Silicates arranged in interlocking single and double chains
Phyllosilicates	Silicates arranged in parallel sheets
Tectosilicates	Interconnected tetrahedrons

Table 1.1 Summary of the different types of silicate minerals.[20]

Clay minerals form an important group of the phyllosilicate mineral family (derived from the greek word phyllon, meaning leaf), which are composed of tetrahedral (T) silicate and magnesium or aluminium hydroxide octahedral (O) sheets, which co-condense to form 'sandwich-like' structures. The silicate layer is formed by the corner-sharing of three oxygen atoms per individual tetrahedra, resulting in the formation of a regular hexagonal base, with the forth remaining oxygen atom situated perpendicular to the silicate plane (**Figure 1.2a**). The octahedral magnesium or aluminium hydroxide layers, analogous to brucite, and gibbsite, respectively, are composed of Mg or Al edge-sharing octahedrons which are connected through oxygen (O) atoms or hydroxyl (OH) groups (**Figure 1.2b**). The octahedral magnesium or aluminium hydroxide sheet subsequently attaches to the fourth, apical unbound oxygen atom present in the tetrahedral silica sheet to form the phyllosilicate clay sheet (**Figure 1.2c**).

Brucite, $Mg(OH)_2$ and gibbsite, $Al(OH)_3$ are naturally occurring minerals, composed solely of octahedral sheets containing divalent Mg^{2+} or trivalent Al^{3+} ions, respectively. In the case of brucite, all the octahedral sites are occupied by divalent Mg^{2+} ions and as a result clay minerals derived from brucite are labelled trioctahedral. On the other hand, clay minerals derived from gibbsite, composed of octahedral sheets containing trivalent Al^{3+} ions, are labelled dioctahedral because only two thirds of the octahedra are filled with Al ions.[21]

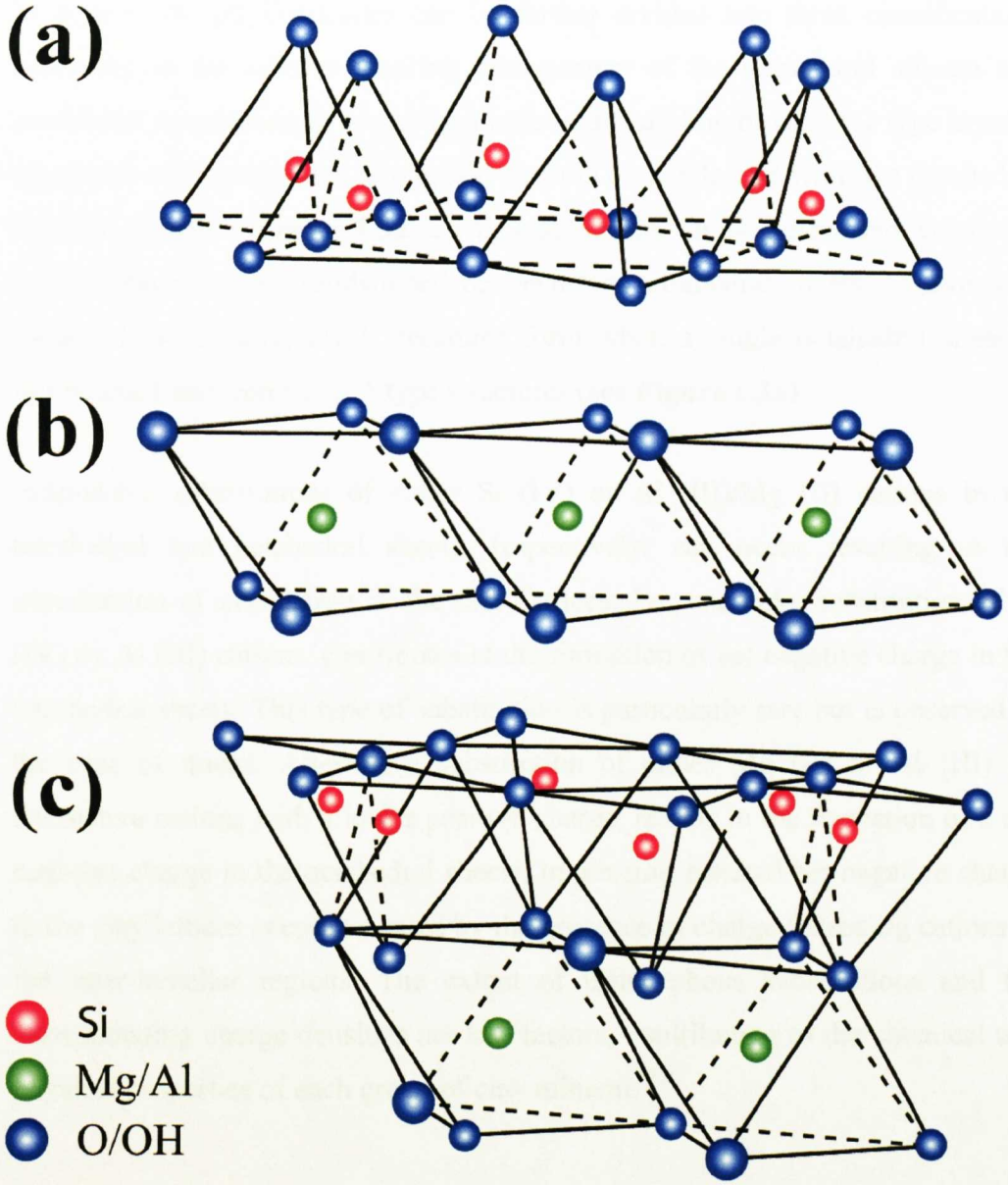

Figure 1.2 Diagram showing side views of (a) a tetrahedral silicate layer, (b) an octahedral aluminium or magnesium hydroxide layers and (c) the 1:1 phyllosilicate clay structure, which is composed of a magnesium/aluminium hydroxide layer, co-condensed with the silicate layer, adapted from Grim et al.[17]

In general the phyllosilicates can be further divided into three classifications according to the relative stacking arrangement of the tetrahedral silicate and octahedral magnesium or aluminium hydroxide building blocks. 1:1 type layered structures occur when one tetrahedral sheet is co-condensed with one octahedral sheet, as shown in **Figure 1.3a**. 2:1 type structures, on the other hand, consist of one octahedral sheet, sandwiched between two tetrahedral sheets, as shown in **Figure 1.3b**. Finally, 2:1:1 structures form when a single octahedral sheet is sandwiched between two 2:1 type structures (see **Figure 1.3a**).

Isomorphic substitutions of either Si (IV) or Al (III)/Mg (II) cations in the tetrahedral and octahedral sheets, respectively, can occur resulting in the introduction of net charge in the clay lattices. For example, substitution of Si (IV) by Al (III) cations, contributes to the formation of net negative charge in the tetrahedral sheets. This type of substitution is particularly rare but is observed in the case of micas. Alternative substitution of either Mg (II) or Al (III) by alternative cations with a lower positive charge, results in the formation of a net negative charge in the octahedral sheets. In general, residual net negative charge in the clay lattices is compensated by the presence of charge-balancing cations in the inter-lamellar regions. The extent of isomorphous substitutions and the corresponding charge densities are key factors, contributing to the chemical and physical properties of each group of clay mineral.[21]

The clay minerals are segregated into different sub-groups, according to variations in their structure and composition, this includes differences in the stacking of the tetrahedral and octahedral sheets, the extent and type of substitution of the cations in the tetrahedral or octahedral layers, the presence of intercalants and finally the impurity content, as summarised in **Table 1.2**. In particular, the interlayer spacing, also known as the 001 or basal spacing, can significantly change due to variation in the aforementioned factors. Furthermore the structure of the octahedral sheet varies depending on whether it is occupied by divalent magnesium (Mg^{2+}) ions or trivalent aluminium (Al^{3+}) ions and can be labelled trioctahedral or dioctahedral, respectively, as discussed previously.

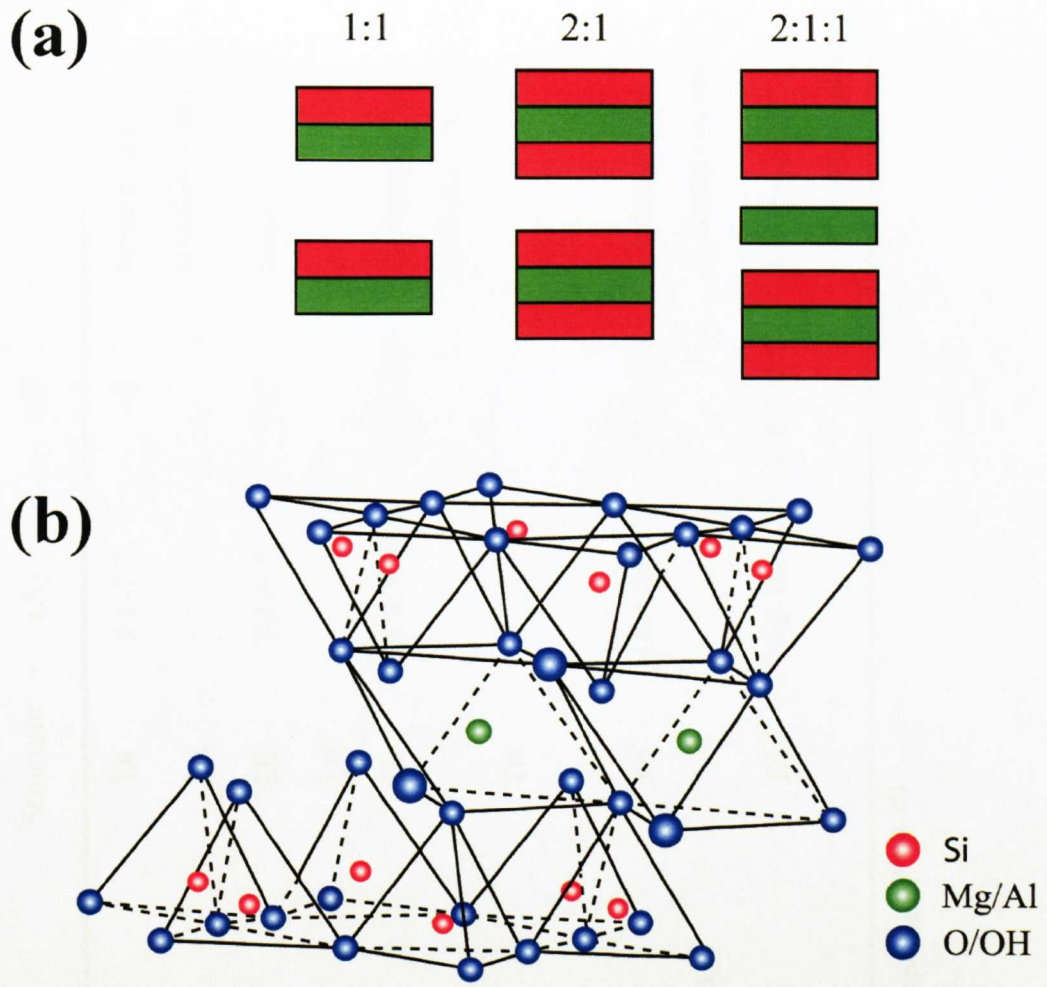

Figure 1.3 Schematic showing (a) the different types of arrangements of the tetrahedral (red) and octahedral (green) layers in the phyllosilicate clays, including 1:1, 2:1 and 2:1:1 and (b) a side view of the 2:1 phyllosilicate clay structure, which is composed of a magnesium/aluminium hydroxide layer, sandwiched between two tetrahedral silicate layers.

T:O	Clay Sub-Group	Examples and Chemical Formula	Octahedral Structure	d-spacing (Å)	Charge/unit cell	Intercalants
1:1	Kaolin-Serpentine	Kaolinite: $[Al_4Si_4O_{10}](OH)_8$	Di	7.1-7.3	~ 0	None except, possibly water
		Serpentine: $[Mg_6Si_4O_{10}](OH)_8$	Tri			
2:1	Pyrophyllite-Talc	Pyrophyllite: $[Al_4Si_8O_{20}](OH)_4$	Di	9.1-9.4	~ 0	None
		Talc: $[Mg_6Si_8O_{20}](OH)_4$	Tri			
2:1	Smectite	Montmorillonite: $[Mg_{0.67}Al_{3.33}]Si_8O_{20}](OH)_4$	Di	14.4-15.6	~ 0.2- 0.6	Exchangeable, hydrated cations
		Hectorite: $[Mg_{5.33}Li_{0.67}]Si_8O_{20}](OH)_4$	Tri			
2:1	Vermiculite	Vermiculite: $[Mg_3(Al,Si)_4O_{10}](OH)_2Mg_{0.35}4.5H_2O$	Tri	14.4-15.6	~ 0.6- 0.9	Exchangeable, hydrated cations
2:1	Mica	Muscovite: $KAl_2[AlSi_3O_{10}](OH)_2$	Di	9.6-10.1	~ 0.6- 1.0	Non-hydrated monovalent cations

Table 1.2 Different clay mineral sub-groups and their associated properties.[14, 21, 22]

Among the various silicate minerals, the smectite minerals including montmorillonite and hectorite, have been widely investigated as host matrices for guest species, due to their high cationic exchange ability, surface reactivity and adsorption properties.[23] This is related to the diffuse, negatively charged clay lattices, resulting in the presence of weakly-bound intercalated hydrated cations, which allow the stacked clay structure to be readily swelled and exfoliated in water. The relative ease of effectively delaminating these clays in aqueous solutions, whilst maintaining the crystal structure of the clay, combined with the presence of weakly bound, interchangeable cations has led to the intercalation of a broad range of species.[14] The number of intercalated hybrid nanocomposites involving smectite minerals as the layered host is vast and a selection of studies is summarised in **Table 1.3**.

Despite the diverse number of studies involving the intercalation of organic, inorganic and polymeric species in natural smectite clay minerals, there are several problems associated with the long-term use of these lamellar materials as host matrices, which has promoted the development of synthetic alternatives. The following section discusses the development of man-made alternatives and reviews their use as host matrices in the formation of intercalation composites.

Lamellar material	Intercalant	Application(s) and Properties	References
Montmorillonite/ Hectorite	Biopolymers including chitosan, cellulose, starch and sucrose	Electrochemical sensors, porous/conductive carbon-clay nanocomposites, tissue engineering and food packaging (green nanocomposites)	[4, 24-28]
Montmorillonite	Mixed biopolymers including chitosan-polyacrylic acid	Superabsorbent materials	[29]
Montmorillonite	Modified biopolymers including starch-polyacrylamide, starch-polycaprolactone and starch-polyester	Superabsorbent materials, mechanical properties,	[30-32]
Montmorillonite	Proteins and peptides including urease, gelatine and poly (L-lysine)	Sensor devices, thermal and mechanical properties	[4, 33-35]
Montmorillonite/ Hectorite	Poly(ethylene oxide) (PEO)	Electrochemical applications	[4, 36-39]

Table 1.3 Summary of range of species that can be intercalated in smectite clay minerals and their associated properties.

1.3.2 Synthetic Clay Minerals

There are two main synthetic clay minerals including smectite clay minerals and layered double hydroxides (LDHs), which will be introduced and discussed in more detail in this section.

Smectite clays are highly abundant and form one of the most important classes of phyllosilicates in nature but despite this advantage, the inability to consistently control both the structural composition and impurity content can be problematic. Furthermore smectites demonstrate extremely poor compatibility with non-polar solvents, which contributes to poor swelling behaviour in these solvents. These drawbacks have promoted the development of synthetic alternatives, with a higher level of reproducibility and a broader range of applications.[23]

The mechanism of formation of naturally-occurring clay minerals was not initially obvious due to the wide range of parameters which could potentially effect the mineral formation, including pH, temperature and concentration of reagents. Initial attempts to prepare synthetic smectite clays under ambient pressures and low temperatures (<100 °C) proved to be difficult due to the low reaction yields and the formation of a mixture of amorphous and crystalline products. The key rate determining step was proposed to be the initial hydrolysis of the octahedral cations, onto which the silicate anions can condense.[40]

Alternative investigations of the synthesis of smectite minerals via hydrothermal techniques, at higher temperatures (100-1000 °C) and pressures (several kbars) demonstrated that, in contrast to lower temperature routes, the majority of reactions reached completion, due to much faster rate of hydrolysis of the octahedral cations at elevated temperatures with an increased level of purity of the desired clay mineral.[40] However, the development of synthetic clays with finely-tuned chemical properties was further sought after, through the attachment of organic groups to the phyllosilicate sheets or by introducing organic or inorganic cations into the interlamellar gallery regions.

Synthetic hectorites proved to be of particular interest as an alternative to naturally-derived clays, due to the fact they can be readily prepared under relatively mild conditions. In general, synthetic protocols involved the combination of magnesium hydroxide, $Mg(OH)_2$, prepared from magnesium chloride hexahydrate and ammonium hydroxide, a silica sol and lithium fluoride, pre-cursors, heated under reflux at 100 °C for 4 days.[23] Ionic-exchange reactions can subsequently be applied to a range of organic and inorganic cations, resulting in displacement of the interlayer metal cations (eg. Li^+).[41]

Research by the Carrado group demonstrated an alternative intercalation route based on the direct incorporation of the guest species, during the crystallisation process.[42] A range of organically-modified synthetic hectorites can be prepared by in situ intercalation of cationic organic or organometallic species, provided they are water-soluble and thermally stable under the aforementioned reaction conditions resulting in the formation of a portfolio of clay-based nanocomposites, as summarised in **Table 1.4**.[23] The mechanism of formation of these synthetic clays is believed to proceed via the condensation of silicate pre-cursors on a pre-formed brucite sheet, with cationic species subsequently incorporated into the gallery regions as the clay layers crystallise.[43]

Intercalants	References
Alkylammonium ions including tetraethyl ammonium (TEA)	[44]
Porphyrins and metalloporphyrins including tetramethyl-*N*-pyridinium porphyrin, (TMPyP) and trimethyl-4-anilinium porphyrin, (TAP)	[45]
Dye molecules including, ethyl violet, methyl green and phalocyanines	[42, 43]
Range of polymers including polyacrylnitrile (PACN), poly(vinyl pyrrolidone) (PVP), polyaniline (PANI)	[46]

Table 1.4 Summary of the range of organic and organometallic species that can be intercalated in synthetic organo-hectorite clays to form polymer-clay composites.

In recent years the application of soft chemical, sol-gel routes has been applied to fabricated functionalised synthetic clays, containing covalently linked organic groups to the phyllosilicate framework, omitting the requirement for hydrothermal or long synthetic reaction protocols. In particular, the synthesis of organically-functionalised clays from organotrialkoxysilane and magnesium, aluminium or nickel chloride pre-cursors has been investigated.[47-49] The preparation and properties of this alternate group of synthetic clays is introduced and discussed in more detail in chapter 3, with specific focus on their application as host matrices for the development of functional bio-inorganic nanocomposites.

1.3.3 Layered Double Hydroxides

Layered double hydroxides (LDHs, general formula $Mg_2Al(OH)_6$ A, where A= an anion) are an alternative class of clays, also known as anionic clays or hydrotalcite-like materials, which are both naturally occurring and synthetically derived, with a diverse range of applications in separation chemistry, polymer additives and catalysis.[50] In brief, these layered materials are composed of positively charged brucite-like sheets, which contain $M(OH)_6$ octahedra, consisting of both divalent (M^{2+}) and trivalent (M^{3+}) metal cations, linked

together in an edge-sharing fashion, with charge-compensating hydrated, ionic species and water molecules located in the inter-lamellar regions. LDHs have a high charge density and, in contrast with the smectite minerals demonstrate anionic exchange ability, which allows a range of anionic guest species to be intercalated in the gallery regions, contributing to the preparation of a portfolio of LDH-based hybrid nanocomposites, a selection of which are summaried in **Table 1.5**.

Intercalant	**Applications/Properties**	**References**
Nucleoside monophosphates (CMP, AMP, ATP and GMP) and DNA	Gene therapy and controlled drug delivery systems	[5, 6, 51, 52]
Polyphenol and urease	Biosensors	[33, 53, 54]
Polysaccharides including: alginate, pectin, κ-carrageenan, ι-carrageenan and xantan gum	Electrochemical sensors	[55, 56]
Polymers including poly(acrylic acid) (PAA), poly(vinylsulfonate) (PVS), poly(styrene sulfonate) (PSS) and poly(vinyl alcohol) (PVA)	Preparation of layered polymer nanocomposites	[57, 58]
Amino acids including asparatic and glutamic acids and a polyamino acid derivative, poly(α, β-aspartate)	Biodegradable or biocompatible properties	[59]

Table 1.5 Summary of the range of anionic species that can be intercalated in the layered double hydroxides (LDHs) and their associated properties.

1.4 Carbon-based layered materials

Section 1.3 provided a general review of the properties and applications of naturally-derived and synthetic forms of smectite clay minerals. The final section of this chapter introduces a group of lamellar materials, based solely on the arrangement of carbon atoms, more commonly known as graphite. Research on graphite and carbon nanomaterials is introduced with specific focus on the generation of graphite-based composites and graphite intercalation compounds (GICs).

1.4.1 Carbon

Carbon, derived from the Latin word "carbo" which referred to charcoal in Roman times is an ancient element present in relatively low abundances in the earth's crust, compared with silicon and oxygen but highly abundant in stars and comets, representing the forth most abundant element in the universe, after hydrogen, helium and oxygen.[60, 61] It is an essential element to all living systems and well known for its ability to form long chains of C-C single bonds. When chemically bonded with other elements including, oxygen, hydrogen, nitrogen, sulphur or phosphorus, carbon forms extensive groups of biologically important organic molecules. In addition to its unparalleled presence in all known lifeforms, carbon is additionally well known for its diverse range of industrial applications notably as fossil fuels, refrigerants and chemical feedstocks for the manufacture of plastic and petrochemicals.

From a materials science perspective, carbon is a versatile element forming a diverse array of structures or allotropes, based on the different arrangements and bonding interactions of the individual carbon atom building blocks as shown in **Figure 1.4**. These allotropes include diamond and graphite, in addition to recently discovered buckminsterfullerene and carbon nanotubes and interestingly exhibit very different properties despite their similar chemical composition, as is clearly displayed in the case of diamond and graphite, as shown in **Table 1.6**. Despite the array of carbon allotropes that exist, diamond and graphite are the only structures which are naturally occurring on earth.

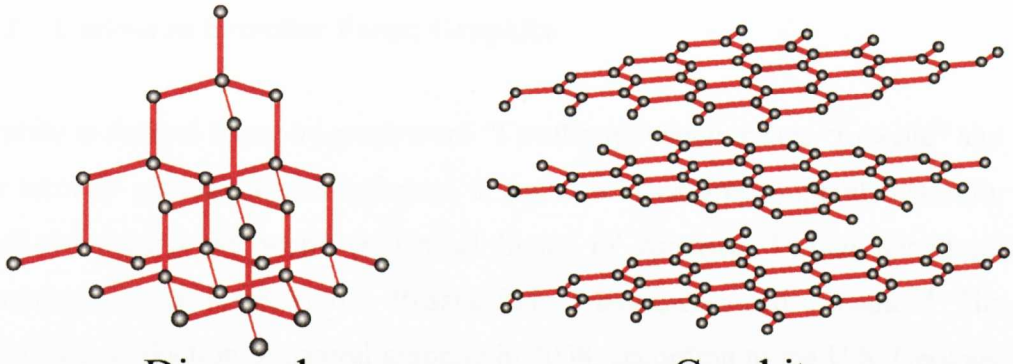

Diamond Graphite

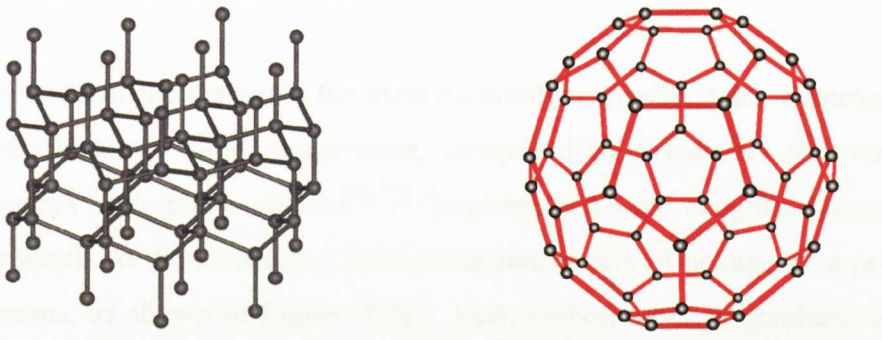

Lonsdaleite Buckminsterfullerene

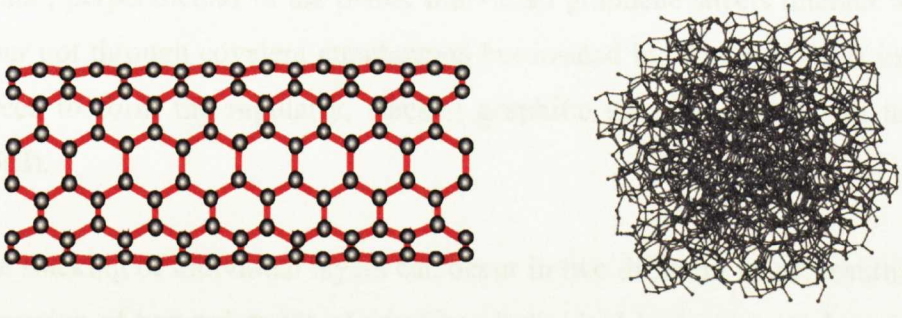

Carbon Nanotubes Amorphous Carbon

Figure 1.4 Diagrams showing the different allotropes of carbon.

Property	**Diamond**	**Graphite**
Electical conductivity	Insulator	Conductor
Hardness	Hard	Soft
Transmission of visible light	Transparent	Opaque

Table 1.6 Comparison of the physical properties of diamond and graphite.

1.4.2 Carbon in Lamellar Form: Graphite

Graphite is derived from the greek word "ΓραΦειη" which means "to write" and is a term in geology which refers to a lustrous black-grey mineral, naturally found throughout the world in United States of America, United Kingdom, Germany, Siberia, Korea, India, Russia, Italy, Madagascar and Canada.[62] The worldwide production of natural graphite in 2008, according to the U.S. Geology survey (USGS), was quoted as 800 million tonnes.[63]

Graphite is one of the main and the most thermodynamically stable allotropes of elemental carbon at room temperature, composed of a lamellar structure of stacked arrays of graphene sheets.[41, 62] Graphene is a well recognized term that refers explicitly to the extended, two-dimensional sheets of hexagonal arrays of carbon atoms, as shown in **Figure 1.5(i)**. Each carbon atom in graphene is sp^2 hybridised and bonded to three neighbouring carbon atoms, leaving a vacant π-orbital, perpendicular to the plane. Individual graphene sheets interact with each other not through covalent attachments but instead by Van der Waals interactive forces to form the regularly, stacked graphitic structure, as shown in **Figure 1.5(ii)**.

The stacking of individual layers can occur in two different ways, resulting in the formation of two polytypes of graphite. Individual layers can stack in an ABAB sequence resulting in the formation of a hexagonal (α) geometry, with unit cell dimensions of a = b = 2.456 Å and c = 6.694 Å. Alternatively, in defective graphite, layers can stack in an ABCABC sequence, corresponding to the formation of a rhombohedral (β) geometry, which can be transferred into hexagonal graphite by heating at high temperature.[64, 65] This contributes to an inter-lamellar separation of 3.354 Å, with a carbon atom separation (C-C) of 1.42 Å, compared with C-C bond lengths of 1.35 Å observed in benzene, due to the sp^2 hybridised nature of the carbon atoms.[41]

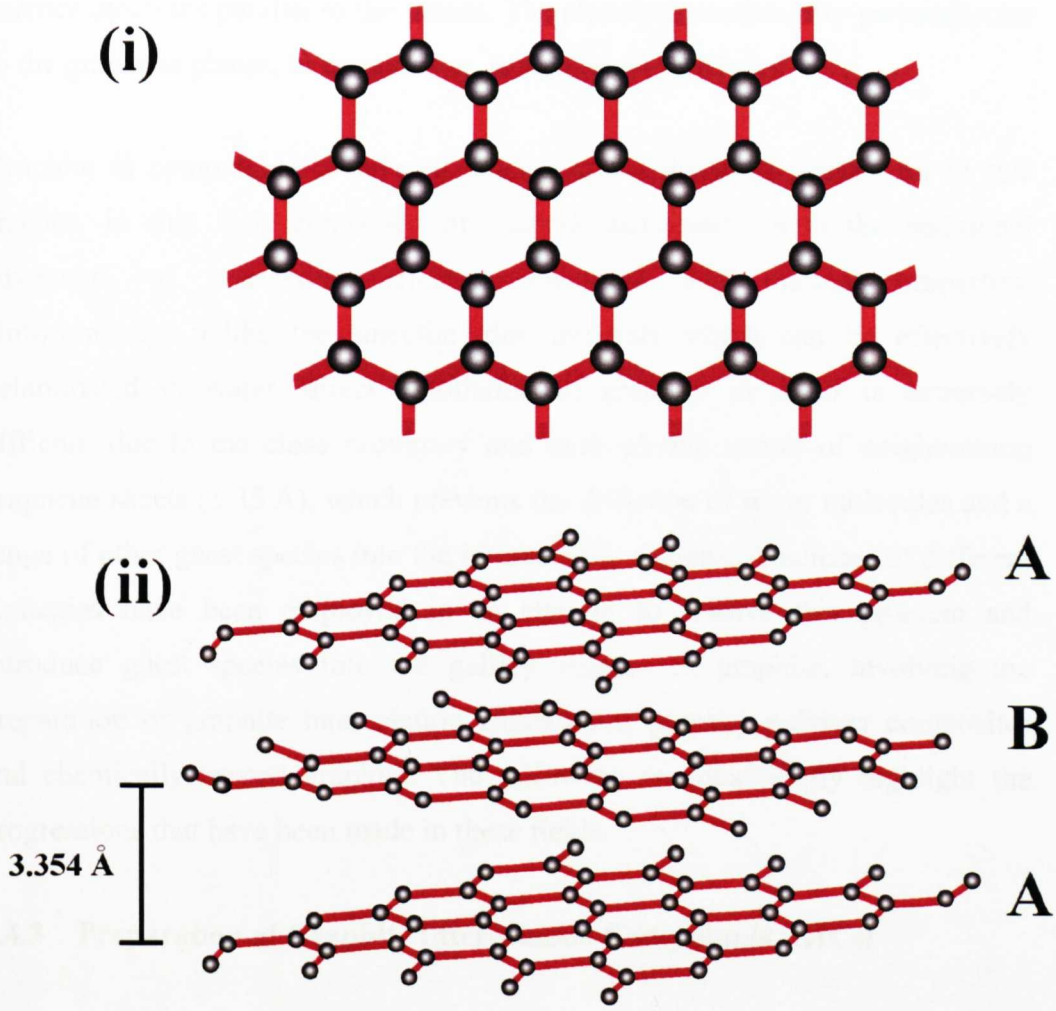

Figure 1.5 Schematic showing (i) the structure of a graphene sheet and (ii) the stacked crystal structure of graphene sheets to form hexagonal graphite.

Historically, graphite was commonly used as a writing material in well-known pencil "lead," however it also plays a significant role in the electrical, chemical and mechanical industries due to its exceeding physical and chemical properties and in 2008, according to the USGS, graphite was employed in a range of applications spanning from steelmaking to brake lining, batteries and lubricants.[63] The strong intraplanar forces and weak interlamellar Van der Waals forces between adjacent graphene sheets contribute to anisotropic physical properties. Unlike diamond, which is an insulator, graphite is an efficient conductor, due to the presence of π-orbitals, situated perpendicular to the planes of hexagonal graphene sheets, which facilitates the movement of delocalized

valence electrons parallel to the planes. The electrical conductivity perpendicular to the graphene planes, in comparison, is significantly reduced.

Graphite is comparable to layered silicate clays, discussed earlier on in this chapter, in that it is composed of stacked nanosheets, with the additional advantage of possessing effective electrical and thermal properties. Unfortunately, unlike the smectite clay minerals which can be effectively delaminated in water, direct exfoliation of graphite in water is extremely difficult, due to the close proximity and hydrophobic nature of neighbouring graphene sheets (3.35 Å), which prevents the diffusion of water molecules and a range of other guest species into the interlamellar regions. A number of different strategies have been employed in an attempt to resolve this problem and introduce guest species into the gallery regions of graphite, involving the preparation of graphite intercalation compounds, graphite-polymer composites and chemically treated graphite. The following sections briefly highlight the progressions that have been made in these fields.

1.4.3 Preparation of Graphite Intercalation Compounds (GICs)

This section focuses, in particular on the progress that has been made in the preparation of graphite intercalation compounds (GICs) or expandable graphite and explains why these compounds have received considerable attention.

GICs are formed when atomic or molecular guest species are inserted between adjacent layers in the bulk graphitic matrix, resulting in effective expansion in the c-axis direction. The degree of expansion is tightly controlled by the size and geometry of the intercalant. Crystallographic investigation of GICs have reported a high degree of structural ordering, with periodic ordering of the intercalant and individual graphite layers, a phenomenon which is commonly known as staging. Staging is classified by an index n, which describes the number of graphite layers between adjacent intercalant layers,[66] as shown schematically in **Figure 1.6.**

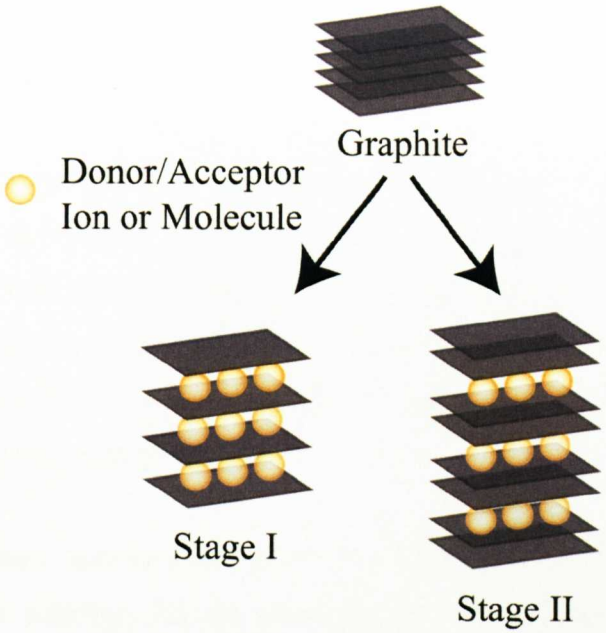

Figure 1.6 Schematic illustrating examples of the staging phenomenon which are prevalent in GICs.

Advances in graphite intercalation chemistry were made nearly 170 years ago when experiments investigating the efficacy of sulphuric acid as an effective solvent for graphite, unexpectantly discovered, that the sulphuric acid was in fact intercalated in the gallery regions between adjacent graphene sheets, providing the first known example of a graphite intercalation compound (GIC).[41] This was quickly followed, 1 year later, with reports of the successful intercalation of potassium ions in the inter-layer regions of graphite.[67]

Since this point research involving GICs, has demonstrated the intercalation of a vast number of atomic and molecular species, including ionic species, diatomic molecules and large organic molecules, which can generally be classified into two distinct categories either electron donor or electron acceptor intercalants. Electron donor compounds include the group 1 alkali metals (Li, Na, K, Rb and Cs), the group 2 alkaline earth metals, lanthanides and metal alloys composed of the lanthanides and/or the alkali metals. Ternary donor graphite intercalation compounds have additionally been prepared, based on the intercalation of alkali metals and polar molecules, including ammonia and tetrahydrofuran. Among the donor intercalants, the alkali metal compounds are the most easily prepared and

well understood from a structural perspective with the highest degree of order, including for example C_8K.[66]

Electron acceptor compounds can additionally be formed when lewis acid-type molecules, including halogens or halogen mixtures and strong Brönsted acids, are intercalated into the inter-lamellar regions of the graphitic matrix. Among the acceptor compounds, bromine-graphite compounds are one of the simplest compounds that form but do not form stage I compounds, which is commonly seen for other acceptor compounds.

Intercalation has been achieved for more than 100 different solid, liquid or gaseous intercalant reagents via the application of one of four main routes including a two-zone vapour transport technique, liquid intercalation and co-intercalation methods and an electrochemical method, which are briefly outlined below. In general, the extremely high chemical instability of the majority of GICs means that they have to be prepared and stored in ampoules, under pressure or in the presence of the intercalant vapour. Cooling samples with liquid nitrogen can additionally help to improve the stability of the sample.[66] Furthemore, the nature of the graphite host matrix is important in the preparation of GICs with different types of natural and synthetic graphitic host matrices available, including natural graphite flakes, or synthetically produced highly order pyrolytic graphite (HOPG), kish graphite or carbon fibres.[66]

In general, the two-zone vapour technique is the most widely used technique to prepare GICs with distinctive staging properties. This method involves heating the graphite host (g) and intercalation species (i), which are contained in a two zone ampoule and separated by a small distance, at two different temperatures, T_g and T_i, to create a vapour of the intercalant which is subsequently incorporated into the interlayer regions of the graphite matrix. GICs with different stages can be produced by variation of the temperature difference, with smaller temperature differences contributing to GICs with lower stages. Examples of the range of temperatures applied for the preparation of donor, alkali metal GICs, with different stages is shown in **Table 1.7**.[66]

Alkali Metal Intercalant	**K** $T_i = 250°C$	**Rb** $T_i = 208\ °C$	**Cs** $T_i = 194\ °C$
Stage	T_g (°C)	T_g (°C)	T_g (°C)
1	225-320	215-330	200-425
2	350-400	375-430	475-530
3	450-480	450-480	550

Table 1.7 Example of the conditions applied for the preparation of alkali metals GICs with different staging.[66]

GICs can alternatively be prepared using liquid intercalation methods by immersing graphite in liquid or molten-based reagents. Examples of molten and liquid/solvent-based intercalants include molten lithium, bromine in tetrachloromethane, ferric chloride in acetone and metal donor ions (Li, Na, Rb, Cs, Co, Sr, Ba) in ammonia. This route is relatively facile but can prove to be difficult when preparing well-staged compounds.[66]

Alternatively co-intercalation can be used to prepare low-staging GICs, containing alloys and mixtures of atoms and molecules, which are otherwise difficult to intercalate directly. An example includes the improved intercalation of sodium by employing a sodium containing alloy containing caesium and potassium. Alternatively, sequential intercalation routes can be applied to intercalate species, which cannot be directly intercalated. Examples include the intercalation of hydrogen, which can be successfully intercalated in alkali metal GICs. Finally, GICs can alternatively be prepared through the application of electrochemical techniques and this route is used particularly for the preparation of GICs containing strong acid intercalants, including sulphuric and nitric acids.[66]

GICs have received considerable interest, in particular, in the development of primary and secondary battery devices. Graphite fluoride or $(CF)_x$, which consists of a graphite host matrix with covalently attached fluorine atoms has been used in the development of cathode electrodes in primary lithium batteries,

with applications in a broad range of electronic devices. Stage 1 $(CF)_n$ can be prepared by reacting graphite with fluorine gas at temperatures as high as 500 °C and the alternative stage 2, compounds can be produced by heating at reduced temperatures between 300 and 400 °C. The development of primary battery devices can, however, pose several safety issues and operational problems due to the use of lithium metal and alternative lithium intercalated graphite compounds were used as anodes in the development of secondary lithium-ion devices. Secondary battery devices in contrast to the previously mentioned primary devices are composed of a lithium ion rather than a lithium metal anode. In particular lithium-intercalated graphite compounds, (Li_xC_6), first synthesised in 1955 by Hérold have been applied as the anode electrode in secondary devices.[67]

One of the main advantages of GICs is that they permit the study of intercalated species, which would otherwise be very difficult to investigate due to severe chemical instabilities. This is observed in the case of thallium bromide ($TlBr_3$) which does not exist on its own but instead forms stable graphite intercalation compounds.[68] Despite this advantage, the main drawbacks of GICs are associated with their long-term chemical stability when exposed to air, which requires that they have to be carefully stored in pressurised ampoules. For example, GICs prepared with electron donor intercalants are easily oxidised when exposed to air and in some cases are pyrophoric, in addition, GICs prepared with electron acceptor intercalants are easily decomposed at ambient temperature and can be very hygroscopic.[66] Furthermore there are no known examples, reported to date, involving the generation of GIC containing biologically-derived intercalants, which require more ambient synthetic protocols.

1.4.4 The Preparation of Graphite-Polymer Composites

The integration of polymers with layered host matrices, including for example silicate clays, has received considerable attention as a means of producing nanocomposites, in the form of intercalated or exfoliated structures with enhanced mechanical and thermal properties.[69-71] In particular, the possibility of

introducing electrical conductivity to the composites, has provoked the investigation of graphite as an electrically conductive host matrix. Initial attempts to intercalate polymers in graphite proved to be challenging and the following section reviews the progress that has been made in the development of polymer nanocomposites based on graphite.

Several advances have been made involving the intercalation of polymers in graphite, based on the application of a chemically modified graphite-based intermediate compound, as detailed below. In particular, progress has been made through the application of GICs or expandable graphite (EG) as a host matrix. EG can be obtained, in general, by treating graphite with acid or mixtures of acids, for example sulphuric acid, with subsequent thermal treatment, by heating up to temperatures of 900-1000°C or by microwave irradiation.[72, 73] Research reported by Chen and co-workers demonstrated the ability to intercalate polystyrene and maleic anhydride grafted polypropylene (gPP) in graphite via in situ polymerisation of styrene or direct intercalation of gPP, in EG, respectively, as shown in **Figure 1.6a-b**. [72, 74] Further studies investigated the in situ polymerisation of polyaniline (PANI) in the interlayer regions of microwave treated graphite nanosheets.[73] The application of the stage I potassium-tetrahydrofuran GIC, as an intermediate host matrix in the preparation of a polystyrene-graphite nanocomposite was additionally investigated, using similar in situ polymerisation protocols, ensuring the GIC was freshly prepared and maintained under vacuum.[75]

Intercalation in graphite can additionally be achieved by the application of chemically modified graphite, commonly known as graphene oxide (GO), as an intermediate host. Graphite oxide is simply an oxidised form of graphite which can be readily exfoliated in water, due to its increased hydrophilicity. A variety of polymers have been intercalated in GO, including PANI, polypyrrole (PPy), poly(ethylene glycol) (PEG) and poly(vinyl alcohol) (PVA) via in situ polymerisation in the presence of exfoliated GO or by direct intercalation of the polymer, as shown in **Figure 1.6c-e**.[76-80] Furthermore, Kotov and co-workers, investigated the intercalation of poly(diallyldimethyl ammonium chloride) (PDADMAC) into the GO gallery regions, followed by chemical or

electrochemical reduction as a means of removing the GO surface modifications and restoring the composite to an electrically conductive graphitic state (**Figure 1.6f**).[81]

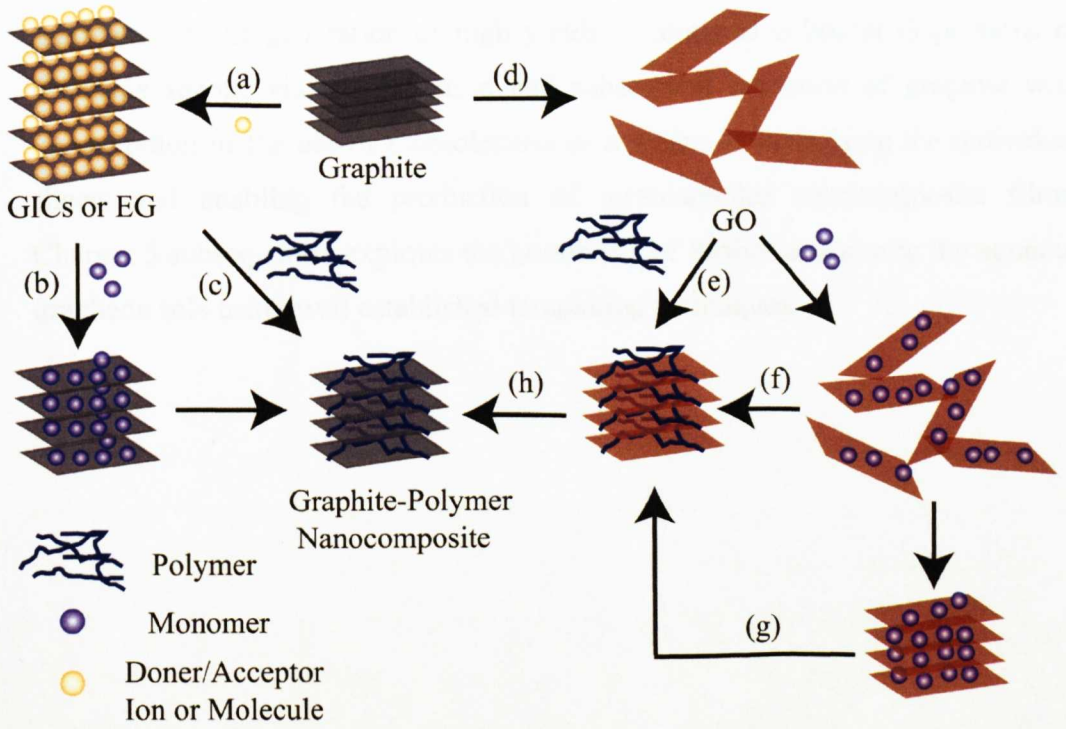

Figure 1.6 Schematic showing the different routes that can be undertaken to effectively intercalate polymer guest species into the interlamellar regions of graphite, via the formation of graphite intercalation compounds (GICs) or exfoliated graphene oxide (GO). Step (a) displays the formation of GICs via two-zone, intercalation or electrochemical routes, or EG via treatment with acid, which can subsequently be intercalated with monomers, followed by polmerisation, (b), or directly intercalated with a polymer, (c). Graphite-polymer nanocomposites can additionally be prepared via the synthesis of GO, by reacting graphite with strong mineral acids and oxidising agents, (d) followed by the direct intercalation of the polymer (e), in situ polymerisation of the monomer in the presence of exfoliated GO sheets (f) or by the assembly of monomer intercalated GO sheets, followed by polymerisation of the guest monomer species (g). Step (h), highlights the possibility of applying electrochemical or chemical reduction techniques to reform electrically conducting graphitic-based sheets from polymer intercalated GO.

The recent discovery of single sheets of free-standing graphene, as discussed in chapter 4, demonstrates for the first time the ability to completely delaminate stacked graphitic materials into its native, individual component sheets, creating a huge scope of potential applications and opportunities. Chapter 4 focuses in particular on the generation of high yields of aqueous colloidal dispersions of graphene sheets, via the oxidation and subsequent reduction of graphite with investigation of the use of biomolecules as a means of stabilising the individual sheets and enabling the production of mesolamellar nanocomposite films. Chapter 5 subsequently explores the possibility of further processing the aqueous graphene sols using well established templating techniques.

CHAPTER 2 EXPERIMENTAL TECHNIQUES

The aim of this chapter is to provide a thorough review of the experimental techniques applied throughout the thesis.

2.1 Transmission Electron Microscopy (TEM)

TEM microscopy was conducted using a JEOL 1200 EX electron microscope, fitted with a tungsten filament, operating at an accelerating voltage of 120 kV. Digital images were recorded using a Soft Imaging MegaView II digital camera.

Sample Preparation

Dilute samples were viewed on carbon coated 300 or 400 mesh copper grids, which were prepared in the following procedure. Carbon grids were placed on the base of a Buchner funnel, containing water. Carbon film was subsequently prepared on freshly cleaved mica, using an Agar Turbo Carbon Coater and transferred onto the surface of the water. The water was slowly drained whilst guiding the carbon film onto the grids. Alternatively, holey grids were purchased from Agar Scientific. In general, 5 μL of an aqueous dilute sample was placed on the carbon-coated grids, which were left to air dry. In some cases, the grids were additionally washed with water, before being left to air dry.

2.2 Scanning Electron Microscopy (SEM)

SEM microscopy was conducted using a JEOL JSM SEM 5600 instrument with EDX analysis (Oxford Instruments ISIS300), operating at an accelerating voltage of 10 kV. Higher resolution SEM images were obtained using a JEOL JSM 6330 field emission gun (FEG) microscope. Digital images were recorded.

Sample Preparation

SEM images of aqueous solutions were obtained by drying samples directly onto 10 mm aluminium stubs, which were coated with 15 mm Pt/Pd. Alternatively, solid samples were imaged by directly mounting the samples onto adhesive carbon pads attached to aluminium stubs, before coating with Pt/Pd.

2.3 Energy Dispersive X-ray Analysis (EDXA)

EDX analysis was conducted on both the SEM and TEM using Oxford Instruments X-ray Analysis ISIS 300 system. EDX on the TEM was equipped with a silicon detector and a beryllium window, enabling identification of elements with atomic mass greater than sodium. The same system was used on the SEM with the addition of a 'windowless' detector, enabling detection of elements with atomic mass lower than sodium.

2.4 Atomic Force Microscopy (AFM)

AFM microscopy was conducted using a multimode AFM equipped with Nanoscope V controller (Veeco Instruments Ltd, USA) and tapping probes Tap300Al or SS-NCL. Images were analysed using Gwyddion, an open source software program for SPM analysis.

Sample Preparation

Samples were prepared by depositing dilute aqueous samples (5-10 μL) onto freshly cleaved mica and subsequently air-drying at room temperature before imaging using tapping mode.

2.5 Powder X-Ray Diffraction (PXRD)

PXRD measurements were obtained using a Bruker D8 Advanced X-ray powder diffractometer with a CuKα X-ray source (λ = 1.5405 Å). Measurements were typically recorded for 2θ values from 2.00 ° to 80.00°, with step sizes varying from 0.00262° to 0.05° at a scan rate of 1 second/step. The sample rotation mode was not applied during the measurement.

Sample Preparation and Data Analysis

Solutions requiring analysis were dried directly onto a silicon wafer holder as thin films. In the case of solid samples, plastic holders were occasionally used or finely ground samples were pressed onto the surface of the silicon wafer holders.

The data obtained was analysed and interpreted using Bragg's Law (Equation 2.1), allowing calculation of the inter- and intra-planar distances:

Equation 2.1: $n\lambda = 2d\sin\theta$

where n = order of diffraction, λ = the wavelength of CuKα X-Rays (Å), d = the inter-planar distance of the atomic lattice and θ = the angle between the incident X-ray beam and the scattering planes (angle of diffraction).

2.6 Fourier Transform Infra-red Spectroscopy (FT-IR)

FT-IR spectra were obtained using a Perkin Elmer Spectrum One spectrometer fitted with Spectrum Analysis software. In each case ten scans were run from 4000 to 450 cm^{-1} at a resolution of 4 cm^{-1} and a scan speed of 0.2 cms^{-1}.

Sample Preparation

A few mg of sample were typically ground with approximately 100 mg of infrared-grade potassium bromide (KBr), using a pestle and mortar. A KBr pellet was then made by pressing the sample in a hydraulic press (Perkin-Elemer, 5 tons) for FT-IR analysis.

2.7 Ultraviolet Visible Spectroscopy (UV-Vis)

UV-Vis spectroscopy measurements were obtained using a Perkin-Elmer Lambda 25 UV-Vis spectrophotometer containing Perkin Elmer UV Winlab computer software (version 1.1). Enzyme activity studies were conducted and analysed using Kinlab computer software.

Sample Preparation and Data Analysis

Aqueous samples were placed in quartz cuvettes (1 cm path length) for analysis. Absorbance measurements were used in a quantitative manner to determine the concentration of samples, using the Beer-Lambert law (Equation 2.2).

Equation 2.2: $A = -\log_{10}(I/I_o) = \varepsilon.c.\ell$

Where A = the absorbance of a sample, I_o = the intensity of the incident light, I = the intensity of transmitted light, ℓ = the pathway along the sample, which is equivalent to the width of the cuvette, c = the concentration of the sample and ε = the extinction coefficient.

2.8 Circular dichroism spectroscopy (CD)*

CD spectra were obtained using a JASCO J-810 spectropolarimeter. Aqueous samples were typically analyzed from 190-260 nm; data pitch and band width = 1 nm; response time = 2s, scan rate = 50 nm min^{-1} and 3 accumulations.

Sample Preparation and Data Analysis

Samples were analysed in a quartz cuvette with a 0.1 cm path length.

(CD spectroscopy was conducted by Dr. Avinash Patil in the Centre for Organized Matter, University of Bristol)*

2.9 X-ray Photoelectron Spectroscopy (XPS)*

XPS was conducted using a Thermo VG Scientific Spectrometer under high vacuum using Al-K_α 1486.6 eV radiation at 400 W (15 kV). High resolution scans were acquired with a 30 eV pass energy, 300 ms dwell times and 0.1 eV step. Wide-scan surveys were acquired with 100 eV pass energy, 300 ms dwell times and 1 eV step size.

Sample Preparation

Aqueous samples (less than 50 μL) were dried onto ozone plasma cleaned silicon wafer substrates.

(X-ray photoelectron spectroscopy was conducted by Dr. Tom Scott at the Interface Analysis Centre, University of Bristol)*

2.10 pH Measurement

pH measurements were determined using a Mettler Toledo MP220 pH meter, calibrated using standard buffer solutions at pH 4, 7 and 10.

2.11 Zeta Potential Analysis

Zeta potential measurements of aqueous dispersions were obtained at room temperature using a Brookhaven Instruments Zeta Potential Analyser. Results were interpreted using a PALS Zeta Potential Analyser (Ver. 3. 25), fitted with a gold electrode.

2.12 Compression Testing

Compression testing was carried out using a TA-XT plus texture analyser (load cell 50 N) at room temperature. Stress versus strain measurements were plotted at a compression rate of 0.06 mms^{-1}. Specimens used for testing were approximately 4 mm in radius and length and were cut from different sections of the main scaffold with a sharp razor blade.

2.13 ^{13}C Nuclear Magnetic Resonance (NMR)*

Solid state NMR experiments were performed on Bruker Avance 300 NMR spectrometer, operating at 75.51 MHz, using a standard 4 mm cross-polarization magic angle-spinning (CP/MAS) probe. The ^{13}C chemical shifts were referenced with respect to tetramethysilane (0 ppm), using solid adamantane as a secondary standard.

(Solid state NMR was conducted by Jessica Martin in the Solid State NMR suite in the Department of Chemistry, University of Bristol)*

CHAPTER 3 IMMOBILISATION OF CYTOCHROME *C* IN AMINOPROPYL FUNCTIONALISED MAGNESIUM PHYLLOSILICATE CLAY

(Published in *Molecular Biosystems*, 2009, **5**, 744-749)

3.1 Introduction

3.1.1 Chapter Outline and Aims

It has been well reported that the integration of biomolecules with inorganic materials results in the formation of bio-inorganic hybrid materials which have unique physical, chemical and mechanical properties, compared with their individual counterparts. The preparation of bio-inorganic composites, using a range of techniques, is an established field with significant work involved in investigating the use of lamellar magnesium phyllosilicate clays as inorganic supports. In particular, the development and application of aminopropyl functionalised 2:1 magnesium phyllosilicate clays (AMP clay) has been well explored. Simple sonication-assisted exfoliation of AMP clay in water results in the formation of positively charged lamellae, which can subsequently be successfully restacked in the presence of a range of anionically charged biomolecules or polymers. This chapter demonstrates the polymer assisted immobilization of cytochrome *c* in the organoclay matrix with full characterisation of this novel bio-inorganic composite and additional evidence showing the sustained stability and catalytic properties of the immobilised enzyme under adverse conditions of pH.

3.1.2 Protein Structure and Applications

Protein macromolecules are extremely diverse biomolecules with a broad range of applications, some of which are detailed in **Table 3.1**.

Type of Protein	Application
Enzyme	Catalysts
Transport	Transportation/Storage of oxygen (O_2)
Structural	Provide structural support/Build connective tissue
Antibody	Provide immune protection by targeting foreign bodies for destruction
Motor	Generate/control movement

Table 3.1 Table listing some example applications of proteins.

Proteins are composed of linear chains of amino acid residues, which are linked together by polypeptide bonds to form flexible polypeptide chains. There are a total of twenty distinct amino acids, which share the same fundamental structure consisting of a central, tetrahedral carbon atom bonded to a carboxylic acid group, an amino group, a hydrogen atom and a variable side chain (R), (**Figure 3.1a**). In solution, at neutral pH, the carboxylic and amino groups are predominantly ionised, contributing to the zwitterionic (dipolar) form of the amino acid (**Figure 3.1b**), with variations in the pH, altering the ionisation of these groups. Under acidic conditions the carboxyl groups are predominantly neutral with the amino groups protonated. In contrast, basic conditions promote the reverse situation in which the carboxyl groups are predominantly dissociated and the amino groups are neutral. The nature of the side chain varies considerably in size, charge and hydrophobicity and is composed of a broad range of functional groups including, for example, alcohol, thiol and carboxylic acid groups. All of the amino acid residues are stereochemically chiral, existing primarily in the L-isomeric form, apart from one exception, glycine, which is not chiral.[82]

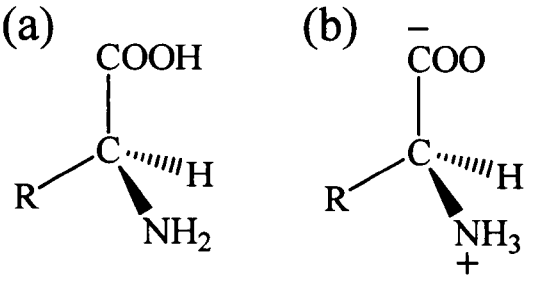

Figure 3.1 General molecular structure of the (a) unionized form and (b) zwitterionic form of an amino acid.

The flexible polypeptide backbone allows the protein to fold or coil to form a three-dimensional structure. The localised three dimensional structure can be described by one of two secondary structures; the α-helix or β–sheet. An α-helix forms a rod-like shape in comparison to the sheet like structures of β–sheets. α-helices form tightly packed arrangements of amino acids due to hydrogen bonding interactions between the amino, hydrogen atom at position n and the carbonyl group at position (n + 4). On the other hand, β–sheets form when two or more sequences of amino acids are arranged adjacently and in parallel, resulting in hydrogen bonding interactions between the amino, hydrogen atom on one strand with the carbonyl group on an adjacent strand. When secondary structural units interact with each other through hydrogen bonds, disulphide bonds and hydrophobic interactions, a three-dimensional tertiary structure is formed. The three-dimensional structure is extremely important as it controls the function and properties of the protein.[82]

3.1.3 Immobilisation, Intercalation and Encapsulation of Biomolecules

In recent years there has been extensive work involving interdisciplinary projects at the interface of biology and materials chemistry to produce bio-mimetic or bio-inspired hybrid materials, which have highly desirable, versatile applications in catalysis, sensing, regenerative medicine and nanotechnology, with several examples highlighted in chapter 1.[83, 84] Enzymes, in particular, have been reported to act as highly attractive biocatalysts in the industrial synthesis of a range of bulk chemicals, pharmaceutical and food ingredients, due to their high level of enantio- and regio- selectivity and efficiency, however, despite these

advantages, as with other biomolecules, they lack long term structure and function under industrially viable conditions, which has hampered their extended application.[85-87] The integration of biomolecules with biologically inert, inorganic or polymeric matrices is a well reported strategy which has been applied to prevent functional loss of biomolecules under detrimental conditions, by maintaining and, in many cases, enhancing structural and chemical stability.[88, 89] This section briefly reviews the key synthetic approaches currently available to support biomolecules and fabricate bio-inorganic hybrid materials.

Physio-chemical adsorption or covalent attachment onto solid substrates provides a facile approach for the immobilisation of biomolecules, including proteins, enzymes and lipases. A range of supports have been reported including high surface area, porous titanium dioxide films,[90, 91] mesoporous silica,[92-96] latex or polystyrene colloidal particles,[97-99] potassium sulphate microcrystals,[100] and magnetic γ-Fe_2O_3 nanoparticles.[101] In all cases the immobilised biomolecules were proven to demonstrate efficient and in many cases enhanced activities.

Further to the use of solid supports as substrates for biomolecules, sol-gel processing is one of the most extensively studied methods for the entrapment of a range of biomolecules including proteins (enzymes and antibodies), DNA/RNA, phospholipids, polysaccharides and plant/animal cells inside a silica, metal-oxide or hybrid sol-gel polymer cage or shell. Bio-inorganic hybrid composites produced in this manner have well reported applications in, for example, catalysis, optical/electrochemical biosensors and cell therapy.[88, 102-104] The first example of the use of sol-gel processing to immobilise biomolecules stems back to 1955 when proteins and enzymes including urease, catalase, muscle adenylic acid and cytochrome *c*, in addition to a range of dyes were entrapped inside silica matrices.[105] Subsequent biomolecule encapsulation studies followed in 1984 and 1985 by Venton[106] and Glad,[107] respectively, but it was not until the early 1990s that the full potential of this strategy was realised and a plethora of research was conducted to optimise the synthetic approach.

This route is highly attractive due to both the myriad of starting reagents and the biocompatible, aqueous, room temperature synthetic conditions that are followed

leading to the formation of porous matrices with controllable surface chemistries, areas and pore diameters and high surface areas. The key advantage of sol-gel processing, that has promoted its extensive investigation in bioimmobilisation, is the maintained and in many cases enhanced biomolecule activity, as a result of the protective polymer cage encasing the biomolecule, which restricts irreversible conformational changes or structural deformation, as demonstrated in **Figure 3.2**.[108]

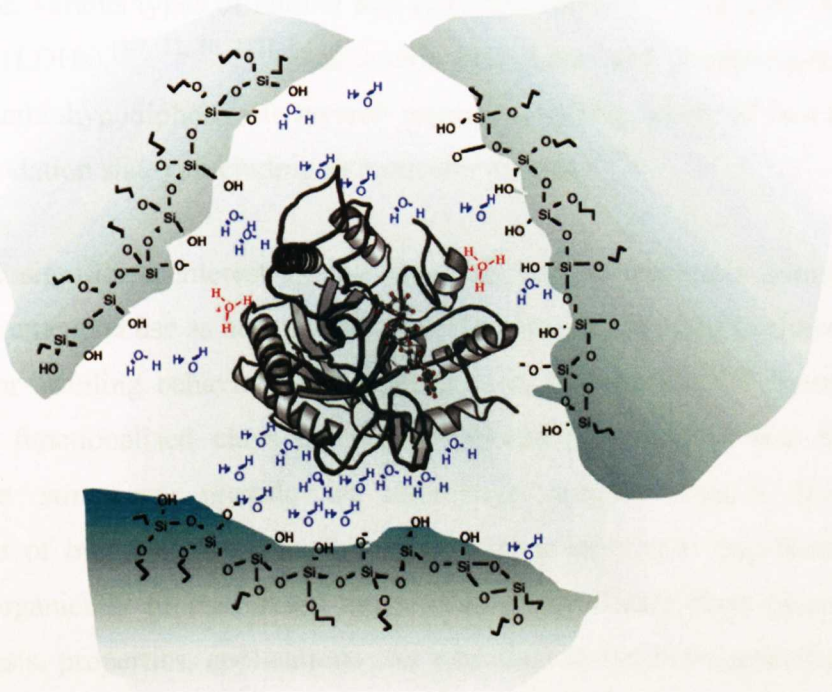

Figure 3.2 Schematic showing an entrapped or caged enzyme, in this case alkaline phosphatise, in a sol-gel matrix.[108]

Biomolecules can additionally be encapsulated or wrapped to fabricate bio-inorganic hybrid nanoparicles containing functionally intact cores encased in a porous, inert, inorganic matrix through the application of reverse microemulsions. This facile approach involves exploiting the use of nanoscale water droplets of a reverse microemulsion to isolate and subsequently envelop single protein molecules in an ultrathin inorganic shell, resulting in effective stabilisation of the native biostructure.[109, 110]

A popular, alternative, bioimmobilisaton strategy is manifested through the application of inorganic layered materials as host matrices. Layered materials are highly attractive inorganic supports for a range of biomolecules due to their high external surface area and confined interlayer gallery regions, enabling biomolecules to be intercalated between adjacent layers. As discussed in chapter 1, there is a plethora of available synthetic and naturally-derived layered materials that have proven to act as viable host matrices for a broad range of biomolecules. Layered materials which have shown particular success in this field include, various types of natural and synthetic clays,[59, 111] layered double hydroxides (LDHs),[5-7, 12, 50, 112] α-zirconium phosphates and phosphonates,[113-115] and hexathiohypodiphosphate layered materials, (MPS_3, where M is a metal in the +2 oxidation state) , including in particular $MnPS_3$.[116]

Despite the significant interest in the range of layered materials mentioned above, their extended use as host matrices for biomolecules is often hindered due to their poor swelling behaviour and heterogenous composition.[117] Synthetic, organically functionalised clays containing tailored functionality and highly reproducible structures, provide an alternative lameller matrix for the intercalation of biomolecules. The following section introduces this family of synthetic, organically functionalised magnesium phyllosilicate clays discussing their synthesis, properties, applications and relevance in the bio-immobilisation field.

3.1.4 Synthetic, Organically-Functionalised 2:1 Magnesium Phyllosilicate Clay as a Host Matrix for Biomolecules

Synthetic clays, as introduced in chapter 1, have gained significant interest as host matrices for biomolecules as a result of their high surface areas and controllable exfoliation and swelling behaviour. During the past decade, the preparation of synthetic, organically modified 2:1 trioctahedral magnesium phyllosilicate clays via sol-gel routes has been investigated, consisting of a central magnesium hydroxide layer co-condensed between two 'sandwich' silicate layers. A naturally-derived example of these clays is talc, $Si_8Mg_6O_{20}(OH)_4$.

The preparation of the first example of an organo-clay derivative of talc, 3-[(methacryloxy)propyl] functionalised magnesium organosilicate, was reported by Fukushima and co-workers, in 1995.[48] The synthetic route involved a simple, one-step sol-gel reaction containing 3-[(methacryloxy)propyl] methoxysilane, magnesium chloride hexahydrate and sodium hydroxide. The framework of the organo-clay was reported to be very similar to talc, (approximate composition given as $Si_8R_8Mg_6O_{16}(OH)_4$) with the additional feature of methacrylate functional groups anchored to the central magnesium phyllosilicate clay architecture, via a covalent Si-C bond (**Figure 3.3**).

The ability to anchor organo moieties to the clay framework, using a one-pot, soft chemical approach has led to a profusion of investigations, resulting in the preparation of an extensive range of organically functionalised magnesium phyllosilicate clays. Layered magnesium organosilicates containing a wide range of functional groups anchored to the framework, including methyl, propyl, phenyl, allyl, 3-aminopropyl, epoxy, ethylenediamino, imidazole, 3-mercaptopropyl (thiol), hexadecyl and mixtures of these organic groups, to name just a selection, were prepared through the simple incorporation of the appropriate organotrialkoxysilane.[47, 49, 59] Each clay provides a unique specific functionality and application. For example, the epoxy functionalised clays were cross-linked, in situ, with m-phenylenediamine, to form a polymer-inorganic lamellar hybrid composite.[59] Whereas, the thiol functionality was exploited for the synthesis of gold nanoparticles in the gallery spacing between the organoclay layers, via in situ reduction of tetrachloroauric (III) acid.[47]

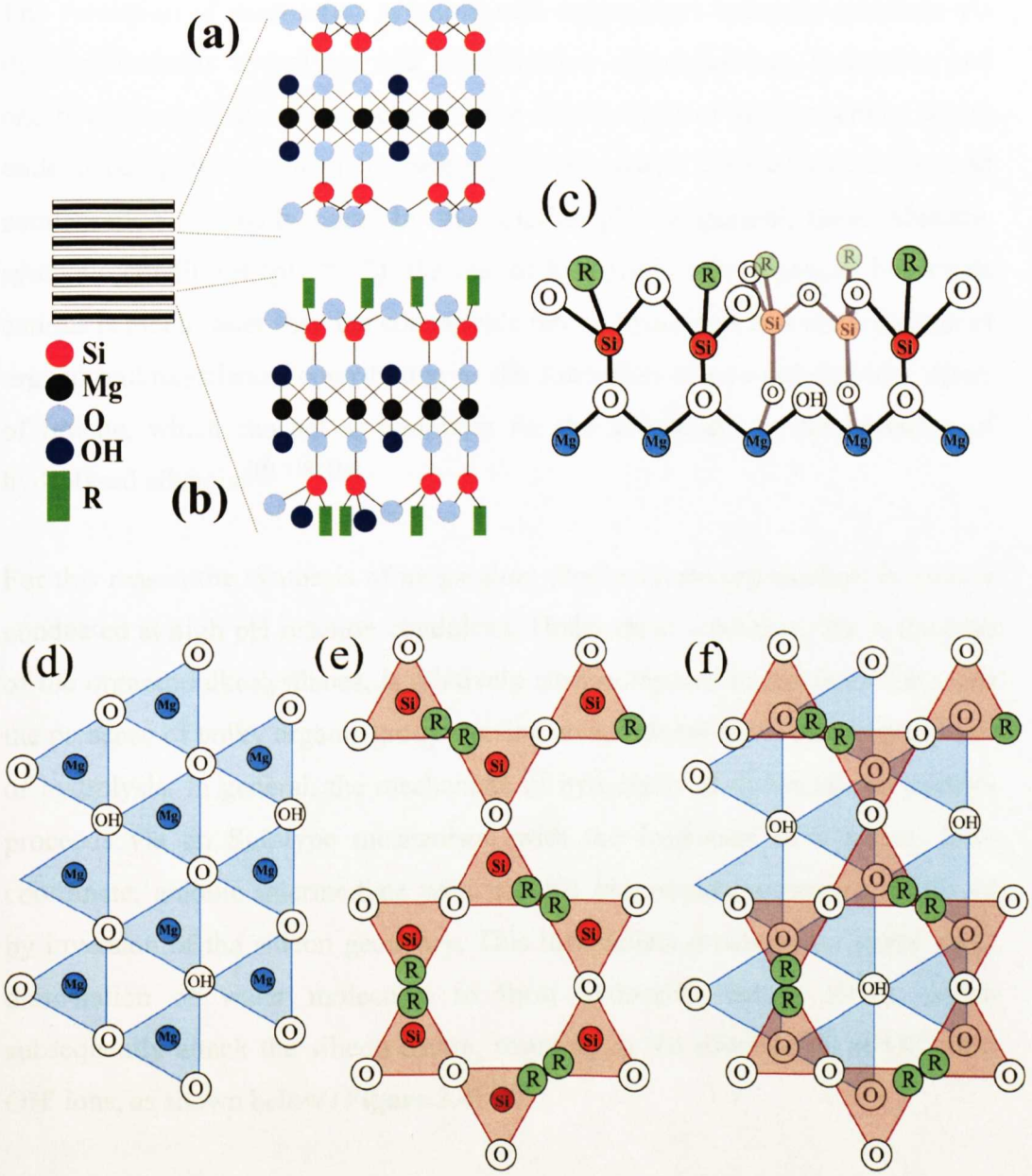

Figure 3.3 Diagram showing the two-dimensional structure of (a) 2:1 trioctahedral magnesium phyllosilicate, talc, (b) organically functionalised 2:1 magnesium phyllosilicate with a range of organic groups (R) attached to the main framework, re-drawn from Burkett et al.[47] (c) side view of organically functionalised 2:1 magnesium phyllosilicate and planar views of (d) the octahedral magnesium hydroxide layer, (e) the tetrahedral organosilicate layer and (f) both layers combined, with Si/Mg atoms and the second tetrahedral layer omitted for clarity.

The formation of magnesium phyllosilicate organoclays normally proceeds via the simultaneous hydrolysis and condensation of magnesium hydroxide and organotrialkoxysilanes precursors with the relative rates of these reactions key to understanding the mechanistic pathway. The relative rates of hydrolysis and condensation are finely tuned by the solution pH. In general, under alkaline, synthetic conditions (pH ≈ 12), the rate of hydrolysis of magnesium hydroxide cations is much faster than the comparable rate of hydrolysis and condensation of organotrialkoxysilanes, contributing to the formation of two-dimensional sheets of brucite, which can act as templates for the subsequent co-condensation of hydrolysed silanols.[59, 118, 119]

For this reason the synthesis of magnesium phyllosilicate organoclays is usually conducted at high pH reaction conditions. Under these conditions the hydrolysis of the organotrialkoxysilanes, is relatively slow compared to condensation, with the presence of bulky organic groups having an additional steric effect on the rate of hydrolysis. In general, the mechanism of hydrolysis of the silane pre-cursors proceeds via an S_N2-type mechanism, with the formation of a stable, five-coordinate, anionic intermediate with trigonal bipyramidal geometry, followed by inversion of the silicon geometry. This mechanism proceeds via initial rapid dissociation of water molecules to form hydroxide anions (OH^-), which subsequently attack the silicon centre, resulting in the substitution of OR^- with OH^- ions, as shown below (**Figure 3.4**).[120]

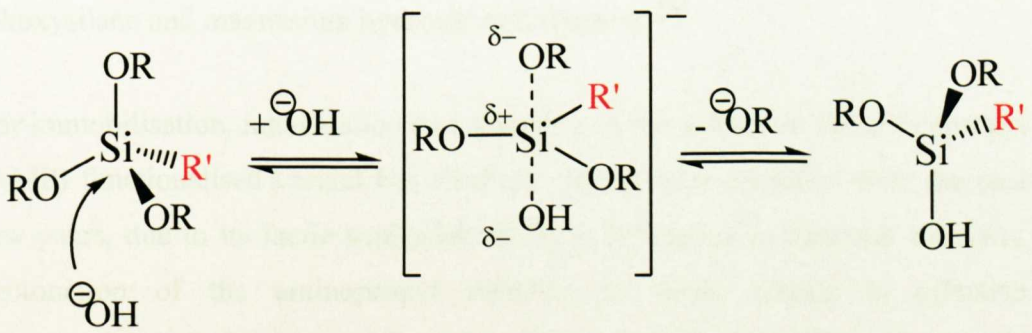

Figure 3.4 Mechanism of hydrolysis of organotrialkoxysilane pre-cursors.

Subsequent, condensation reactions between hydrolysed organosilanol derivatives can be hindered due to the presence of bulky organo groups which

therefore promotes condensation reactions between organosilicate precursors and hydrolysed, magnesium hydroxide species to proceed. These reactions are additionally favoured due to the favoured formation of Si-O-Mg and Mg-O-Mg bonds, under basic conditions.[118] This results in the co-operative assembly of hydrolysed metal hydroxide and silanol pre-cursors, contributing to the formation of lamellar hybrids consisting of a central brucite layer, co-condensed between two tetrahedral sheets of silicate, with the formation of the central octahedral magnesium hydroxide layer acting as the primary structure determinant.[59, 83]

In contrast, under acidic reaction conditions the converse mechanistic pathway is suggested for the formation of magnesium/aluminium organophyllosilicates. Under these conditions the rate of hydrolysis of organoalkoxysilanes is significantly faster than the rate of condensation, resulting in the rapid formation of partially condensed, lamellar, silanol derivatives, analogous to surfactant molecules. These negatively charged surfactant-like templates provided highly suitable templates for the subsequent co-condensation of metal(III) ions.[49]

Further work by Mann and co-workers, demonstrated that the synthesis of selective organoclays can be conducted at neutral pH. These studies reported that both 3-aminopropyl and ethylenediamine-functionalised magnesium phyllosilicate clays could be prepared at neutral pH, as a result of the basic nature of the organo pendent group, which shifts the local pH to higher values and successfully simultaneously catalyses both the hydrolysis reactions of the alkoxysilane and magnesium hydroxide pre-cursors.[59]

For immobilisation, intercalation and wrapping of biomolecules, the aminopropyl (AMP) functionalised variant has received considerable attention, over the past few years, due to its facile sonication assisted exfoliation in aqueous solutions. Protonation of the aminopropyl moieties in water results in effective delamination of the clay structure to form individual, exfoliated cationic organoclay sheets or oligomers, which can subsequently be spontaneously re-assembled in the presence of oppositely charged, anionic guest species. Previous research has demonstrated that a range of anionic proteins/enzymes including myoglobin (Mb), haemoglobin (Hb) and glucose oxidase (GOx) could

successfully be intercalated into the synthetic AMP clay to produce functional protein-lamellar nanocomposites, which demonstrated sustained enzyme activity under extreme conditions, such as pH or temperature.[121] Subsequent studies showed that a similar electrostatically induced mechanism could be used to co-intercalate anionic guest polymers and drug molecules into the gallery regions of AMP clay, such as ibuprofen, epigallocatechin gallate (EGCG), poly(styrene sulfonate) (PSS), poly (acrylic acid), (PAA) and polymethyl-acrylamidopropanesulfonic acid (PMAPSA) to produce a range of novel intercalated layered nanocomposites with applications in drug release and consumer care products.[122] Other studies demonstrated that smaller fractionated organoclay oligomers could be used to effectively incarcerate individual biomolecules including myoglobin, haemoglobin, glucose oxidase and DNA molecules.[123, 124]

Significantly, the application of AMP clay in bioimmobilisation has been limited to the intercalation of anionic species. This chapter investigates the use of electrostatic interactions and co-assembly processes to immobilise cationic guest molecules. In particular, the work in this chapter involves the use of an anionic water soluble polymer (poly(sodium 4-styrene sulfonate, (PSS)) to mediate the immobilisation of a cationic, redox protein, ferri-cyt *c* into the organoclay matrix during spontaneous restacking of delaminated AMP clay sheets. The next section introduces the structure and properties of cytochrome *c*.

3.1.5 Cytochrome *c*: An Electron Shuttle Protein

Cytochrome *c* (Cyt *c*, M_w = 12400 Daltons) is a heme-containing, redox protein, which is roughly spherical in shape (25 × 25 × 37 Å)[125] and composed of 104 amino acid residues which are arranged in a single polypeptide chain.[82, 104, 125, 126] (**Figure 3.5**) The protein has an isoelectric point of 10.5, which means it is positively charged at neutral pH.[127, 128] Cyt *c* is primarily responsible for electron transfer in the mitochondria, the "cell's power plant" and more specifically in the respiratory chain, where electrons are shuttled from cytochrome *c* reductase to cytochrome *c* oxidase resulting in the oxidation of dioxygen to water, which provides the driving force for ATP synthesis.[82, 126]

The heme group in cyt *c* is surrounded by a number of tightly packed hydrophobic chains, leaving only the edge of the heme group accessible to the surface (**Figure 3.5a**). It is centred by a redox-active iron centre, which is surrounded by four equatorial ligands, composed of nitrogen atoms from the porphyrin ring and two strong field axial ligands, consisting of sulphur and nitrogen atoms from methionine (Met-80) and histidine (His-18) amino acid residues, respectively (**Figure 3.5b**). The iron core in the central heme group can be effectively reduced from Fe^{3+} to Fe^{2+}, with a generic reducing agent, for example sodium dithionite. This redox behaviour contributes to the observed facile electron transfer, demonstrated by this protein.[126, 129]

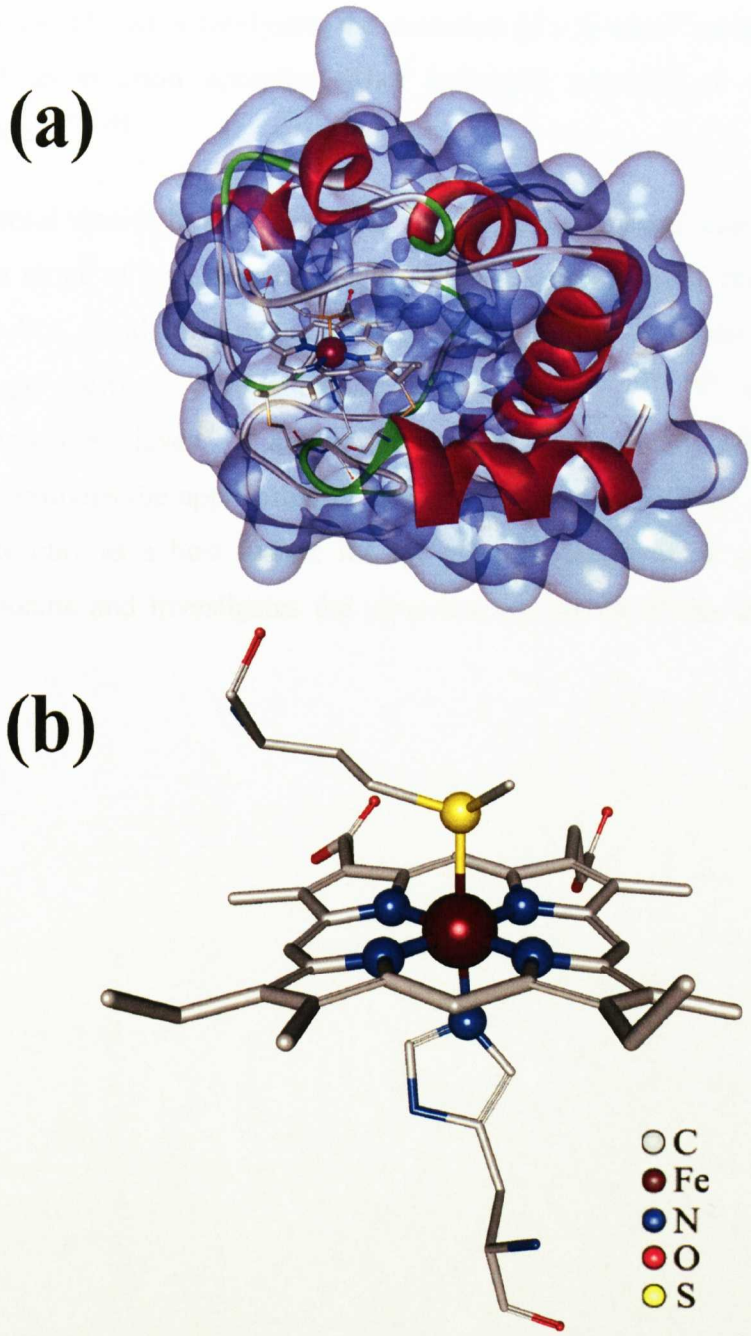

Figure 3.5 Image showing (a) the structure of native cytochrome *c* (from horse's heart) with (b) a higher magnification image showing coordination around the heme centre.

In addition to playing a central role in the transport of electrons in biological systems, it has been reported that heme-containing enzymes demonstrate effective peroxidise activity, in addition to traditional peroxidises.[130] Cytochrome *c*, is not a exception to this rule, demonstrating effective peroxidise-

type activity by efficiently catalysing the oxidation of a range of substrates in the presence of an electron acceptor either hydrogen peroxide or an organic hydroperoxide.[130-134]

To date, several studies have investigated the encapsulation and immobilisation of cyt *c* in a range of host matrices, as a means of enhancing the chemical and thermal stability, in addition to the activity of the protein. Supports of interest include sol-gel derived, porous silicate glasses,[104, 129, 135, 136] mesoporous silicas,[92] molecular sieves[137] and nanoporous titanium dioxide films.[90] This chapter demonstrates the application of amino-propyl functionalised magnesium phyllosilicate clay as a host matrix for cyt *c* in the presense of poly(sodium styrene) sulfonate and investigates the structural properties of the immobilised protein.

3.2 Materials

All reagents were purchased from Aldrich or Fischer Scientific, UK unless otherwise stated.

3.2.1 Preparation of Aminopropyl Functionalised Magnesium Phyllosilicate Clay

Chemical	Molecular Formula	Molecular Weight (g/mol)	Supplier
3-aminopropyltriethoxysilane, 99 %	$C_9H_{23}NO_3Si$	221.37	Aldrich
Magnesium Chloride, Hexahydrate	$MgCl_2 \cdot 6H_2O$	203.31	Aldrich
Ethanol	C_2H_6O	46.07	Aldrich

3.2.2 Preparation of Cytochrome *c*-PSS-AMP Clay Nanocomposites

Chemical	Molecular Formula	Molecular Weight (g/mol)	Supplier
Poly(sodium 4-styrene-sulfonate) (PSS)	$(C_8H_7NaO_3S)_n$	70,000	Aldrich
Ferri-Cytochrome *c*, from Horse (Equine) Heart Muscle	-	12384	Aldrich

3.2.3 Redox Activities of Native and Immobilised Cytochrome *c*

Chemical	Molecular Formula	Molecular Weight (g/mol)	Supplier
Sodium Hydrosulfide or Sodium Dithionite, tech 85 %	NaS_2O_4	174.1	Aldrich

3.2.4 Determination of the Enzyme Activity of Native and Immobilised Cytochrome *c*

Chemical	Molecular Formula	Molecular Weight (g/mol)	Supplier
Hydrogen Peroxide	H_2O_2	34.01	Fischer Scientific
2, 2'-Azino-bis(3-ethyl benzothiazoline-6-sulfonic acid) diammonium salt (ABTS)	$C_{18}H_{24}N_6O_6S_4$	548.7	Sigma
Sodium Dihydrogen Phosphate, Monohydrate, 98 %	NaH_2PO_4	142.0	Aldrich
Sodium Phosphate Dibasic, 99 %	Na_2HPO_4	138.0	Aldrich

3.3 Experimental Details

3.3.1 Preparation of Aminopropyl Functionalised Magnesium Phyllosilicate Clay

Aminopropyl functionalised magnesium phyllosilicate (AMP) clay was prepared as described previously.[121] Magnesium chloride hexahydrate (1.68 g, 8.26 mmoles) was dissolved in ethanol (40 g) and 3-aminopropyltriethoxysilane (2.6 mL, 11.1 mmoles) was added dropwise. The mixture became cloudy after five minutes, and was left to stir for 18 hours. The resulting white precipitate was isolated by centrifuging the solution for 30 minutes, and excess starting reagents were removed by washing with ethanol, followed by centrifugation for a further twenty minutes. The AMP clay was then dried in the oven at 40°C for 18 hours.

3.3.2 Preparation of Cytochrome *c*-PSS-AMP Clay Nanocomposite

Exfoliation of the AMP clay was achieved by addition of deionised water (4 mL) to the dried organoclay (20 mg), followed by sonication in an ultrasonic bath for 15 minutes at 25°C. Addition of water resulted in protonation of the aminopropyl groups of the as-synthesized organoclay and caused delamination by inter-layer charge repulsion. Immobilisation of ferri cyt *c* molecules was achieved in two steps, firstly by slow, dropwise addition of poly(sodium 4-styrene-sulfonate) (PSS, 100 μL, 10 mg/mL) to the exfoliated AMP clay to obtain a stable colloidal dispersion, followed by immediate dropwise addition of 1 mL of a stock solution of ferri-cyt *c* (1 mg/mL, 80.8 μM, 0.0808 μmoles) to produce a red precipitate. The precipitate was left for 24 hours and then isolated by centrifugation. The nanocomposite was left to dry in an open Eppendorf tube in the oven at 30°C before being ground into a fine powder.

3.3.3 Determination of the Concentration of Cytochrome *c* in the AMP Clay Matrix

The concentration of immobilised cyt *c* was determined by measuring the absorbance at 410 nm (ε_{410} = 1.06 × 10^5 M^{-1} cm^{-1})[138] of the supernatant

solutions collected during a washing cycle, and using **Equation 3.1**, where C_f, C_i and C_s are the concentrations of immobilised cyt *c*, initital concentration of cyt *c* and concentration of cyt *c* in the supernatant, respectively.

Equation 3.1 $C_f = C_i - C_s$,

3.3.4 Redox Activities of Native and Immobilised Cytochrome *c*

Reduction of ferri-cyt *c* was carried out by addition of sodium dithionite (0.1 mL, 1 mg/mL) to native or immobilised cyt *c*. Oxidation of the native and powdered cyt *c* nanocomposite was additionally achieved by bubbling dioxygen through a native protein solution or a powdered dispersion of the composite (0.1 mL).

3.3.5 Determination of the Enzyme Activity of Native and Immobilised Cytochrome *c*

The peroxidase activity of cyt *c* molecules intercalated within the lamellae of an AMP nanocomposite was assessed by using the electron donor dye, 2,2'-azino-bis(3-ethylbenzthiazoline-6-sulfonic acid) (ABTS), as described previously.[132] The concentration of immobilised cyt *c* was determined as described in section 3.3.3 by measuring the absorbance at 410 nm of the supernatant solutions collected. The rates of ABTS oxidation by cyt *c*-catalysed hydrogen peroxide were determined by absorption changes at 414 nm. Typically, the reactions were carried out at 25°C and pH 7 in quartz cuvettes. The assay mixtures typically consisted of cyt *c*-PSS-AMP (100 μL, [cyt *c*] = 2.67μM), sodium phosphate buffer (pH 7, 1.6 mL, 10 mM) and ABTS (100 μL, 50 mM) in a total volume of 2 mL. Peroxidise activity was initiated by addition of H_2O_2 (200 μL, 40-100 mM). Similar experiments to determine the peroxidise activity of native cyt *c* were also carried out. Changes in absorbance at 414 nm were converted to units of enzyme specific activity (μmol/mg/min), using an extinction coefficient of 3.6 $\times 10^4$ $M^{-1}cm^{-1}$. Double reciprocal plots of 1/V (V = initial rate) against 1/S (S = $[H_2O_2]$) showed linear behaviour, consistent with Michaelis-Menten kinetics, and the Michaelis constant (K_m) and the maximal rate (V_{max}) was determined directly from the plots.

3.3.6 Determination of the pH Dependence of the Peroxidase Activity of Cytochrome *c*

The peroxidase activities of native cyt *c* and intercalated cyt *c* were also investigated using procedure described in the previous section (section 3.3.5) under a range of pH conditions (3 to 10) at a H_2O_2 concentration of 50 mM. The specific activity in $\mu molmg^{-1}min^{-1}$ was calculated for each assay.

3.4 Results and Discussion

3.4.1 Characterisation of Aminopropyl Functionalised Magnesium Phyllosilicate Clay

This section discusses the preparation and characterisation of aminopropyl functionalised magnesium phyllosilicate clay, based on a previously reported procedure.[121]

Aminopropyl functionalised magnesium phyllosilicate clay was readily prepared by slow, dropwise addition of 3-aminopropyltriethoxysilane to an ethanolic solution of magnesium chloride, resulting in immediate precipitation of a white solid, which after stirring for 24 h to ensure complete reaction was isolated using centrifugation (30 mins, 13.2 rpm) and subsequently washed with ethanol, to remove excess starting reagents. After air-drying, the organo-clay formed a white powder, which was subsequently analysed by powder X-ray diffraction (PXRD) and fourier-transform infra-red spectroscopy (FT-IR) to assess both the structural and compositional features of the organically-functionalised clay.

PXRD provided conclusive evidence for the lamellar nature of the clay. The diffraction pattern of a dried, film of AMP clay gave rise to characteristic features at 2θ = 5.3, 9.9, 21.2, 35.9 and 59.2, corresponding to d_{001}, d_{002}, $d_{020,110}$, $d_{130,200}$ and $d_{060,330}$ inter- and intra-plane reflections, respectively, (**Figure 3.6, Table 3.2**) which were consistent with the diffraction patterns of previously reported organo phyllosilicate clays,[47, 48] composed of a central brucite layer, co-condensed or sandwiched between two layers of tetrahedral silicate.

One of the key differences observed in the diffraction pattern of AMP clay was the expanded inter-layer or basal spacing (d_{001}), at 1.61 nm compared with 0.934 nm in the parent magnesium phyllosilicate clay, talc, due to the presence of aminopropyl functional groups covalently attached to the clay framework and residing in the gallery regions, thereby increasing the distance between adjacent sheets of clay. Furthermore, the diffraction peaks of AMP clay were, in general,

slightly broader as a result of the incorporation of organic functionalities in the gallery regions.

FT-IR spectroscopy, provided complimentary evidence for the formation of a 2:1 magnesium phyllosilicate, inorganic framework, analogous to talc, with the additionally feature of covalently attached organic functionalities to the main framework (**Figure 3.7**, **Table 3.3**). Stretching bands displayed at 568 cm^{-1} corresponding to Mg-O and Mg-O-Si stretching vibrations, were inherent of a central brucite layer, co-condensed between two silicate layers. Additional vibrational features displayed at 1139 cm^{-1} and 1501/1619 cm^{-1}, corresponding to C-Si and N-H stretching vibrations, respectively, provided evidence for the covalent attachment of aminopropyl organic functionalities to the outer silicate layer of the main framework.

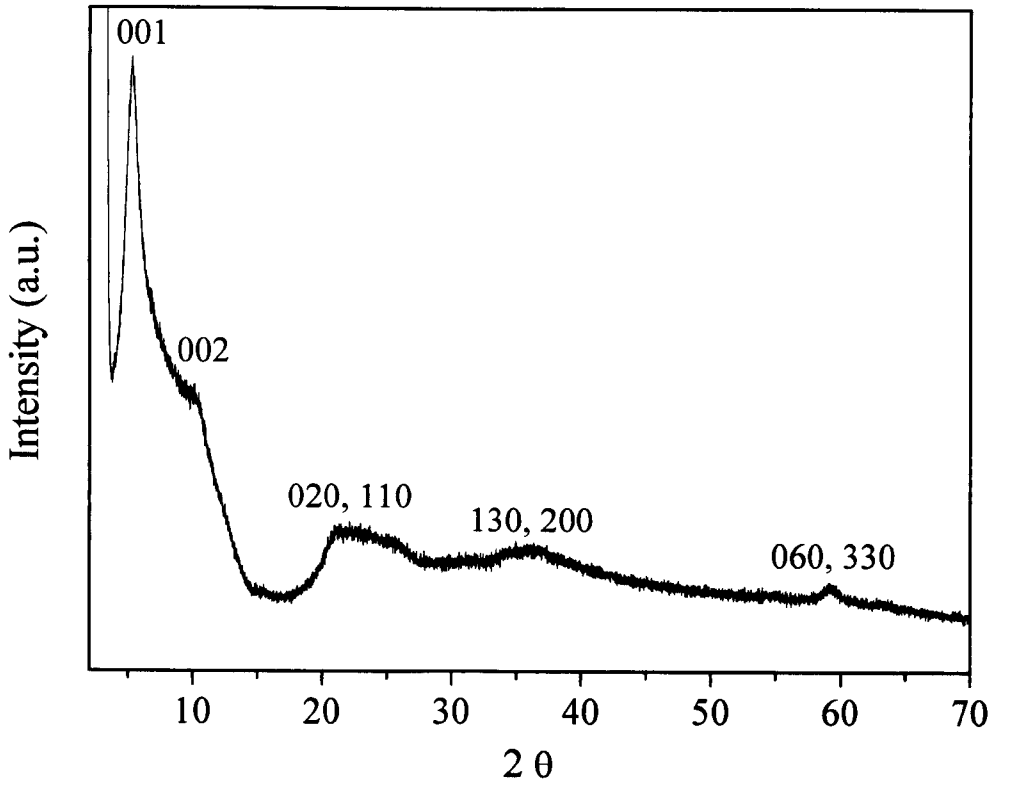

Figure 3.6 PXRD patterns of aminopropyl functionalised magnesium phyllosilicate clay (AMP clay).

Sample	2 Theta	d-spacing (nm)	hkl indices
AMP Clay	5.32	1.66	001
	9.86	0.897	002
	21.22/25.18	0.418/0.353	020,110
	35.85	0.250	130, 200
	59.20	0.156	060, 330

Table 3.2 Summary of 2 theta values, d-spacing and corresponding hkl indices for the peaks observed in the PXRD pattern of AMP clay.

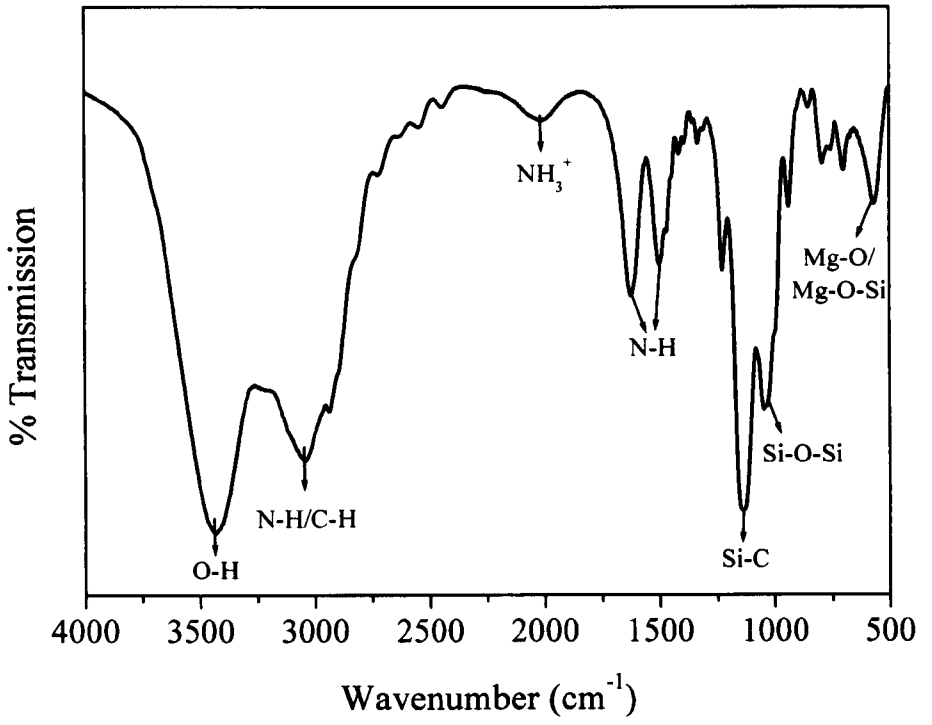

Figure 3.7 FT-IR spectrum of aminopropyl-functionalised magnesium phyllosilicate clay (AMP Clay).

Sample	Peak Shift (cm^{-1})	Assignments
AMP Clay	3435	O-H Stretch
	3043	N-H Stretch (NH_2)
	2937	C-H Stretch (CH_2 groups)
	2010	NH_3^+ Stretch
	1619/1501	N-H Deformation (NH_3^+)
	1139	Si-C Stretch
	1045	Si-O-Si Stretch
	568	Mg-O Stretch
	480	Mg-O-Si Stretch

Table 3.3 Table showing the FT-IR peak assignments for the main inorganic and organic group vibrations in AMP clay.

3.4.2 Preparation and Characterisation of Cytochrome *c*-PSS-AMP Clay Nanocomposite

This section discusses the preparation and characterisation of a novel cyt *c*-PSS-AMP clay nanocomposite based on the use of the anionic polymer, poly(sodium styrene sulfonate) (PSS), as a mediating reagent for the stepwise immobilisation of the cationic protein ferri-cyt *c*.

AMP-functionalised organoclay was initially delaminated by sonication assisted exfoliation in distilled water, prior to addition of PSS. PSS was slowly added to the exfoliated clay dispersion followed by immediate dropwise addition of ferri-cyt *c*, resulting in the formation of a red precipitate, which was left for 24 h to allow complete precipitation to occur. After centrifugation/washing and drying steps a red protein/clay composite was observed, compared with the white solid organoclay, signifying the association of ferri-cyt *c* with the clay matrix (**Figure 3.8**).

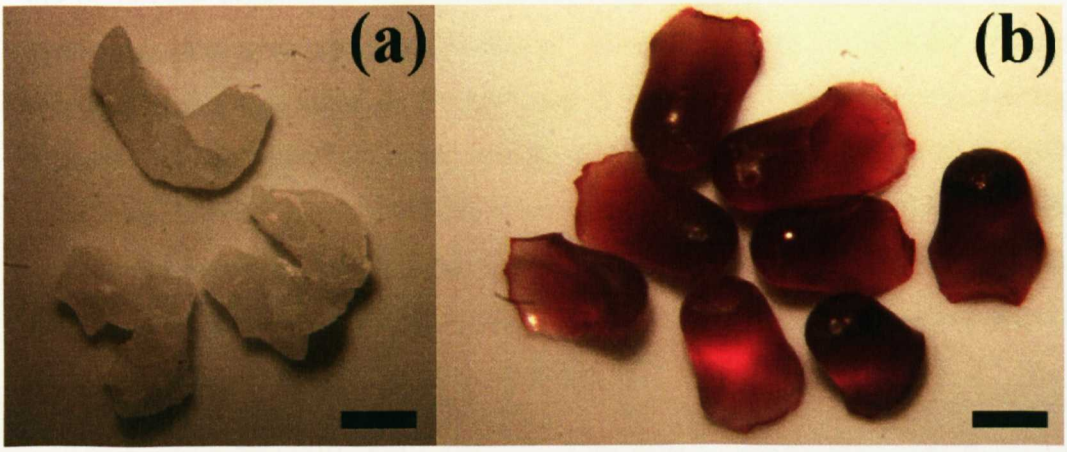

Figure 3.8 Photograph of (a) AMP clay and (b) cyt *c*-PSS-AMP nanocomposite, scale bar is approximately 5 mm.

Favourable electrostatic interactions between the anionic sulfonate groups of PSS with the cationic amino groups covalently linked to the organo-functionalised magnesium phyllosilicate clay framework resulted in the formation of a stable colloidal dispersion. In this procedure, PSS behaves as a mediator for the immobilisation of ferri-cyt *c*, as the cationic protein successfully interacts with

the anionic polymer adsorbed on the delaminated organoclay sheets and is effectively incorporated into the clays on re-stacking of the AMP clay layers.

Powder X-ray diffraction was applied to assess the structural features of the cyt *c*-PSS-AMP clay nanocomposite. PXRD diffraction patterns (**Figure 3.9b, table 3.5**) showed characteristic in-plane broad reflections at 0.437 nm ($d_{020, 110}$), 0.255 nm ($d_{130,200}$) and 0.156 nm ($d_{060, 330}$), consistent with the inorganic magnesium phyllosilicate framework, indicating that the clay structure was retained during the immobilisation of the polymer and protein molecules.[121, 139] In comparison with the diffraction pattern for AMP clay, which displayed a sharp, low angle peak at 1.6 nm, corresponding to the d_{001} interlayer spacing, the cyt *c*-PSS-AMP composite, displayed a low-angle peak at a 2θ value of 3.70, corresponding to an interlayer spacing of 2.38 nm. Similar control PSS-AMP composites (**Figure 3.9a, table 3.4**), prepared in the absence of ferri-cyt *c*, displayed a peak at a lower 2θ value of 4.21, corresponding to an interlayer spacing of 2.10 nm. This data indicated that the PSS was readily intercalated within the gallery regions of the re-stacked organoclay matrix to produce an ordered nanocomposite with an expanded interlayer spacing. However, absence of any significant further increase in the d_{001} value in the presence of cyt *c* suggested that this ordering process did not involve co-intercalation of both the polymer and protein molecules. Instead, immobilization of the protein was most likely associated with entrapment between grain boundaries of the clay matrix to produce a condensed hybrid nanocomposite comprising both intercalated and exfoliated AMP sheets, as demonstrated in the schematic in **figure 3.10**.

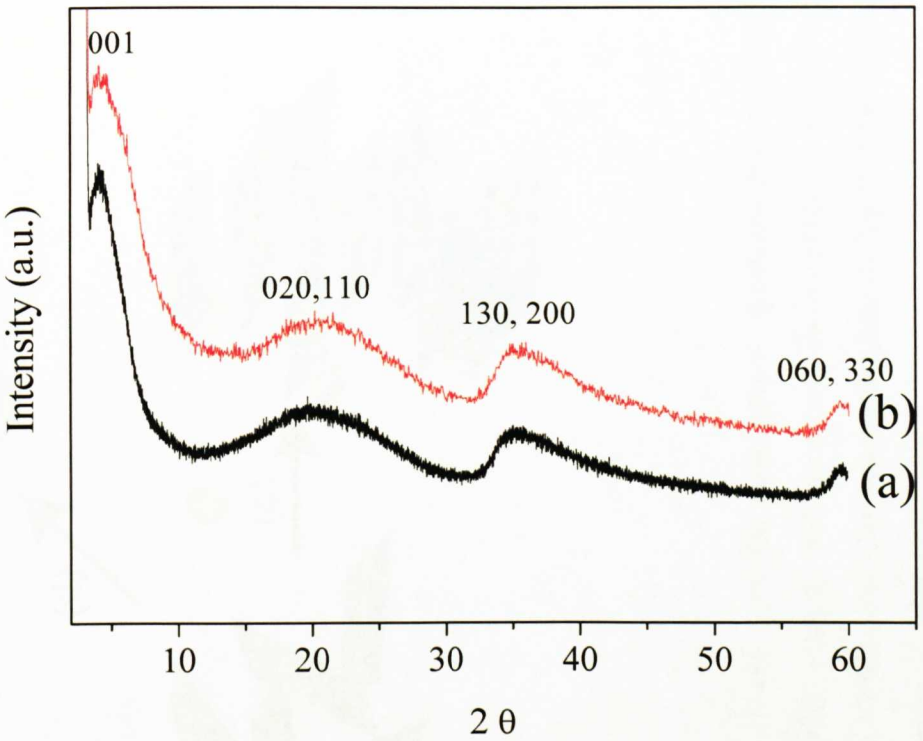

Figure 3.9 PXRD patterns of (a) PSS-AMP and (b) cyt *c*-PSS-AMP clay composite.

Sample	2 Theta	d-spacing (nm)	hkl indices
(a) PSS-AMP Clay Composite	4.21	2.10	001
	19.9	0.446	020, 110
	35.0	0.256	130,200
	59.3	0.156	060, 330
(b) cyt *c*-PSS-AMP Clay Composite	3.70	2.38	001
	20.3	0.437	020, 110
	35.2	0.255	130,200
	59.4	0.156	060, 330

Table 3.4 Summary of 2 theta values, d-spacing and corresponding hkl indices for the peaks observed in the PXRD pattern of cyt *c*-PSS-AMP clay composite.

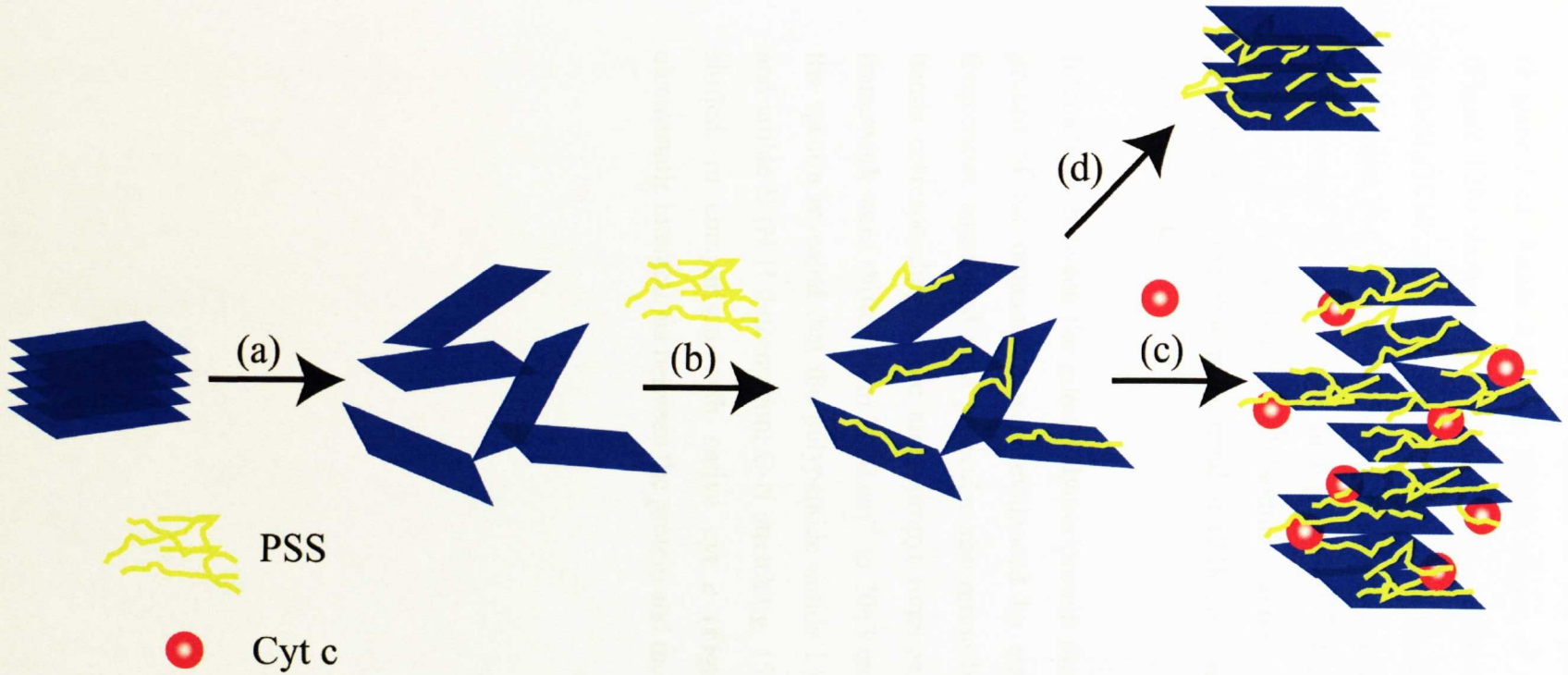

Figure 3.10 Schematic showing a generalised strategy for the immobilization of cyt *c* in the aminopropyl functionalised magnesium phyllosilicate clay matrix. Stepwise addition of poly(sodium 4-styrene sulfonate) (PSS) (step b) and cyt *c* (step c) to exfoliated aminopropyl magnesium phyllosilicate (AMP) clay (step a) results in spontaneous assembly of cyt *c*-PSS-AMP clay nanocomposite. Aging of AMP clay and PSS, in the absence of cyt c results in intercalation of PSS to form a PSS-AMP nanocomposite (step d).

Fourier-Transform Infra-Red Spectroscopy (FT-IR) was applied to analyze the structural and compositional aspects of the protein/polymer nanocomposite (**Figure 3.11**, **Table 3.5**). The FT-IR spectra of AMP clay-immobilised cyt *c* (Figure 12b) showed peaks corresponding to Si-O/Mg-O/Mg-O-Si (555 cm^{-1}), Si-O-Si (1034 cm^{-1}), Si-C (1126 cm^{-1}) and CH_2 (2924 cm^{-1}) vibrational bands, confirming that the organo-functionalised clay was intact after re-assembly, in the presence of the protein and polymer.[47] Furthermore, evidence for the presence of the polymer, poly(sodium styrene sulfonate) was additionally provided from the absorption band at 1218 cm^{-1}, inherent of the sulfonate, S-O stretching mode.

Interactions between the guest polymer/protein molecules and the aminopropyl groups of the organoclay were evidenced by small shifts in the vibrational frequencies associated with particular absorption bands. Firstly, the vibrational bands corresponding to the aminopropyl functionalities anchored to the clay framework were shifted from 2010 cm^{-1} to 2063 cm^{-1} (NH_3^+ stretch). Moreover, the spectra revealed that the polypeptide amide I (C=O stretching, 1635 cm^{-1}) and amide II (N-H deformation; C-N stretching, 1522 cm^{-1}) bands were slightly shifted, in comparison with native cyt *c* (**Figure 3.11a**), as a result of electrostatic interactions between the protein and the polymer.[140]

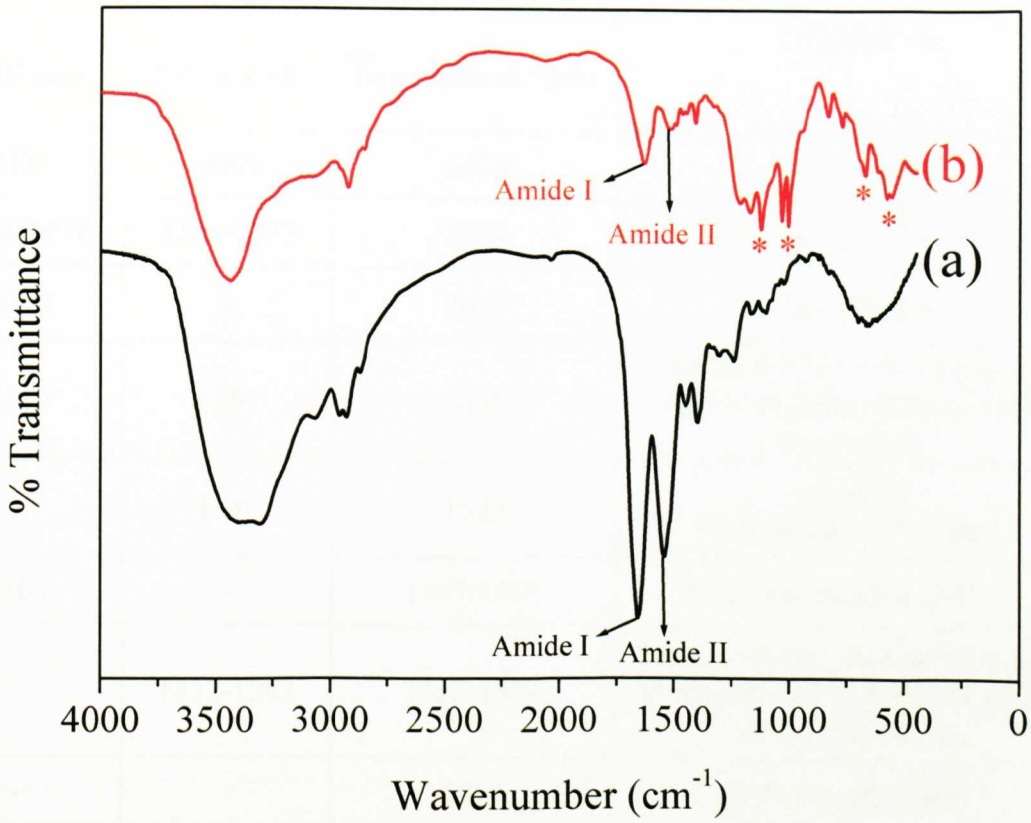

Figure 3.11 FT-IR spectrum of (a) native cytochrome *c* and (b) cyt *c*-PSS-AMP clay nanocomposite, with the asterick (*), corresponding to additional features from AMP clay.

Sample Peak Shift (cm^{-1})			Assignment
AMP clay	**Native Cyt *c***	**Immobilised Cyt *c***	
3435	3401	3436	O-H Stretch
3043/2937	3306-2873	2924	N-H/C-H Stretch (NH_2/CH_2)
2010	-	2065	NH_3^+ Stretch
1619	1657	1635	Amide I, C=O Stretch (cyt c) And N-H Deformation (AMP clay-NH_3^+)
-	1540	1522	Amide II, N-H Bend; C-N Stretch
1501	-	1497/1465	N-H Deformation (NH_3^+)
-	1452-1243	1453-1334	1500-1100 cm^{-1} Amide III bands, (absorption from chemical groups in the side chain)
-	-	1218	S=O Stretch (PSS)
1139	1170/1105	1174/1126	Si-C Stretch
1045	1026	1034/1007	Si-O-Si Stretch
-	933		O-H deformation (out of plane)
568/480	-	555	Mg-O/Mg-O-Si Stretch

Table 3.5 Table showing the FT-IR peak assignments for native and AMP-clay immobilised cytochrome *c*.

3.4.3 Redox Activities of Native and Immobilised Cytochrome *c*

The functional integrity and accessibility of the AMP-immobilised cyt *c* molecules was investigated using UV-Visible (UV-Vis) spectroscopy. The UV-Vis of native ferri-cyt *c* displayed characteristic soret and visible bands at 407 nm and 529 nm, respectively, due to absorptions of the porphyrin chromophore, (**Figure 3.12a (i)**). Reduction of ferri-cyt *c* (Fe III) to ferrous-cyt *c* (Fe II), using sodium dithionite as the reducing agent, resulted in an observable characteristic colour change from red to orange and a corresponding shift in the soret band

from 407 to 415 nm, with the additional formation of α and β bands at 520 and 550 nm (**Figure 3.12a (ii)**).[125]

In contrast, the UV-Vis spectra for the cyt *c*-PSS-AMP clay composite showed that even in the absence of an external reducing agent there was a small red-shift in the soret band from 408 to 414 nm, as well as the presence of α and β bands at 520 and 550 nm (**Figure 3.12b (i)**). This was consistent with the presence of almost fully reduced protein molecules and *in situ* formation of ferro-cyt *c*, possibly due to reaction of the immobilised biomolecules with the aminopropyl groups of the organoclay framework. However, subsequent, bubbling of oxygen through a dispersion of the nanocomposite hybrid resulted in a shift in the soret band from 414 to 408 nm (**Figure 3.12b (ii)**) corresponding to re-oxidation of the heme centre back to ferri-cyt *c*, and indicating that the immobilised protein remained accessible to small molecule oxidants. These spectroscopy results confirmed that the protein molecules were associated with the organoclay matrices, and indicated that structural and functional aspects of the immobilised protein molecules was retained in the hybrid materials.

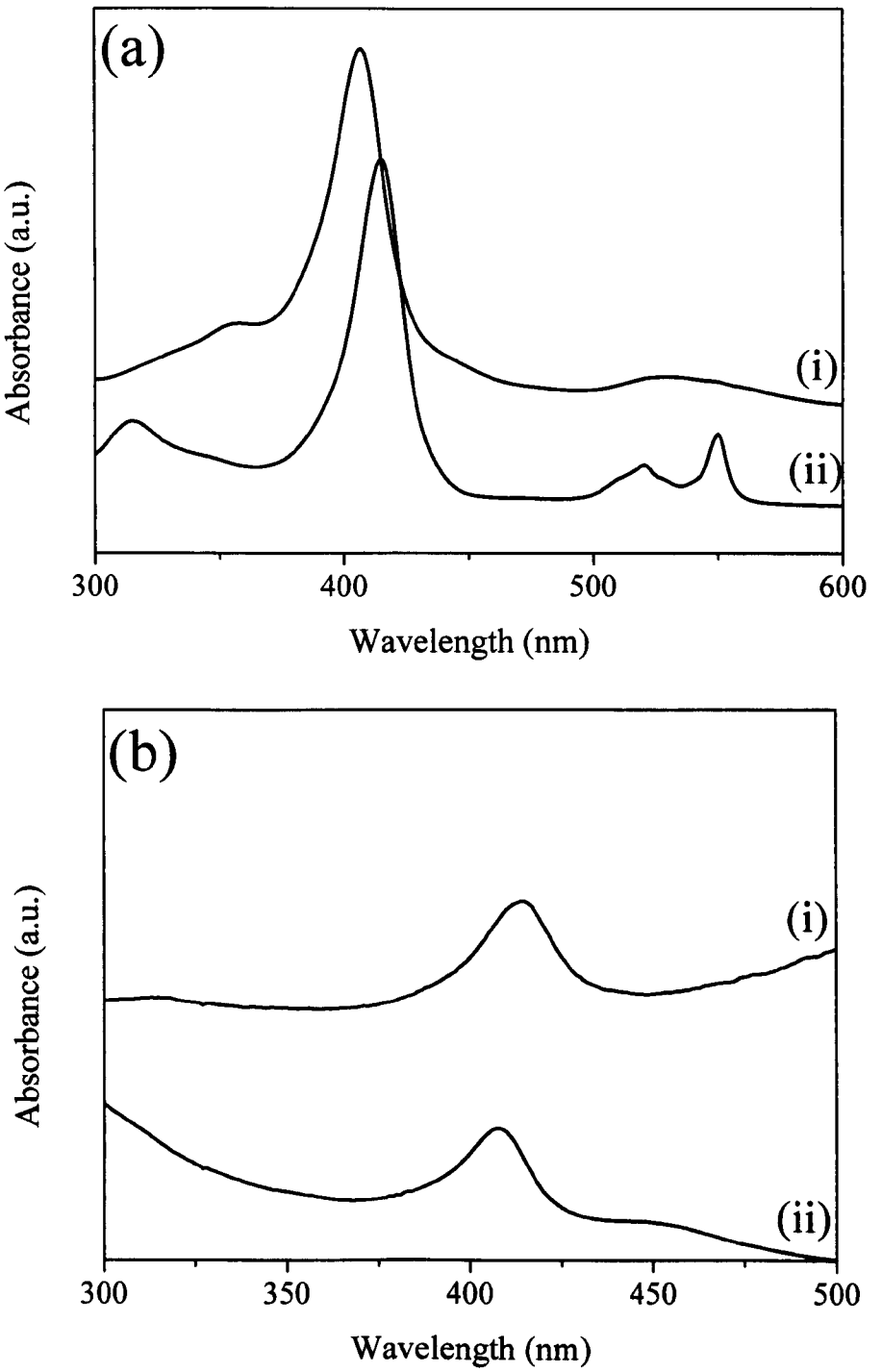

Figure 3.12 UV-Vis spectra of (a) native ferri-cyt *c*, (i) before reduction and (ii) after reduction to form ferrous-cyt *c* and (b) as-prepared cyt *c*-PSS-AMP clay composite (i) showing the presence of ferro-cyt *c* and (ii) after addition of dioxygen, showing in situ oxidation of ferri-cyt *c*.

3.4.4 Determination of the Enzyme Activity of Native and Immobilised Cytochrome *c*

The biochemical activity of heme-containing proteins is highly dependent on a range of factors including the coordination geometry and accessibility of the heme group, the redox properties of the heme ion and the polarity of the heme environment.[141]

The peroxidase activity of native cyt *c* and AMP-immobilised cyt *c* was investigated using a previously reported assay involving the oxidation of a water-soluble dye molecule, 2, 2'-azino-bis (3-ethylbenzethiazoline-6-sulfonic acid) (ABTS), at a range of hydrogen peroxide substrate concentrations.[132] More specifically, cyt *c* catalyses the oxidation of ABTS with hydrogen peroxide to form the cationic radical $ABTS^{\cdot+}$, as shown in the reaction schematic below (**Figure 3.13**) resulting in the formation of blue-green solutions which can be conveniently monitored spectrophotometrically at 414 nm (extinction coefficient = $3.6 \times 10^4\ M^{-1}\ cm^{-1}$).

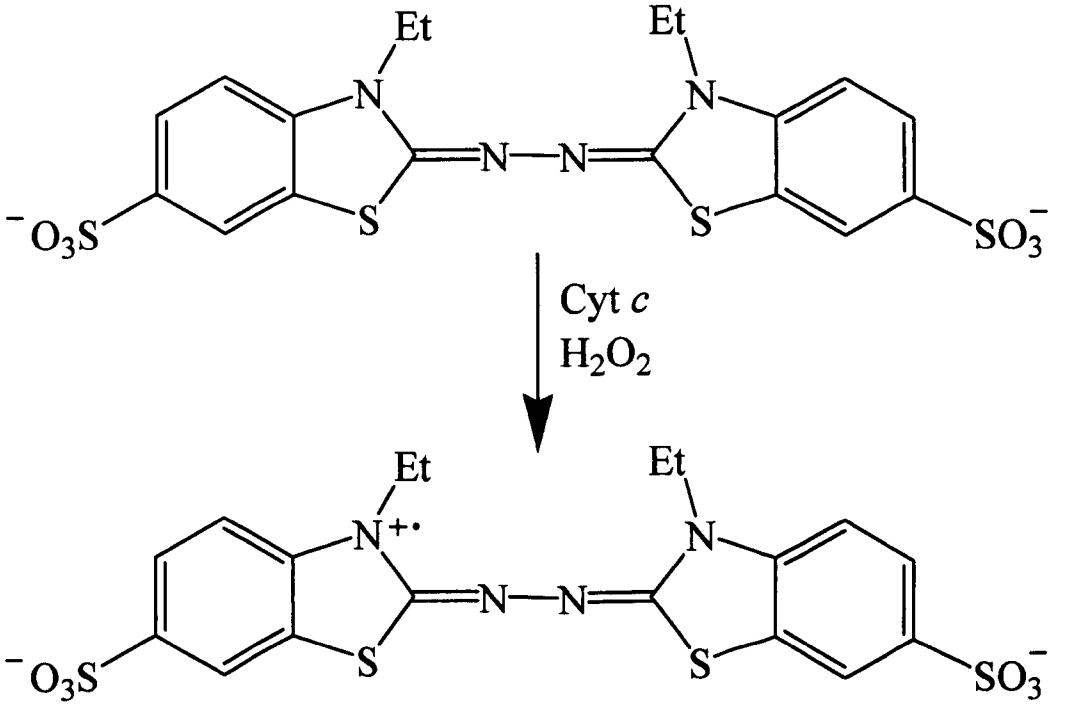

Figure 3.13 Reaction of the cyt *c*-catalysed oxidation of ABTS with hydrogen peroxide to form the cationic, radical $ABTS^{\cdot+}$.

Previous studies investigating the oxidation of ABTS by hydrogen peroxide, catalysed by an alternative peroxidase-type enzyme, horseradish peroxidase (HRP), suggested that the oxidation mechanism generally proceeds via the formation of 2-oxo ferryl intermediates, compound I and II, as shown in the schematic in **Figure 3.14**.[142] Cytochrome *c* is reported to follow a similar peroxidase catalytic cycle to classical peroxidises, as follows.[132, 143]

The mechanism involves initial activation of the hydrogen peroxide by binding to the heme iron centre in the protein. The O-O single bond in hydrogen peroxide subsequently undergoes bond cleavage, resulting in the formation of compound I, which is composed of a ferryl radical cation, with corresponding loss of a water molecule. ABTS is subsequently oxidised by compound I, the actual oxidising species, in two separate electron steps, resulting in the oxidation of two ABTS molecules. These oxidising steps lead to the regeneration of cytochrome *c* in its Fe(III) oxidation state.[134, 142]

In classical peroxidase enzymes, the distal histidine and arginine residues assist with cleavage of the O-O bond. These residues contribute to the binding of the hydrogen peroxide substrate to the heme centre and the subsequent displacement of a water molecule. In particular, the polar nature of the arginine residue creates an electrostatic attraction between the heme centre and the hydrogen peroxide substrate molecules, thereby faciliatating the access and binding of the substrate molecule to the heme centre. In addition, the histidine residue behave as an acid-base type catalyst in the binding of hydrogen peroxide to the heme centre, by promoting ionization and binding of the H_2O_2 substrate, in addition to assisting with the formation of a water molecule. The absence of these catalytic residues in the vicinity of the heme binding centre in native cyt *c* may contribute to reduced rate of reactions in comparison to their classical peroxidase counterparts.[133, 143]

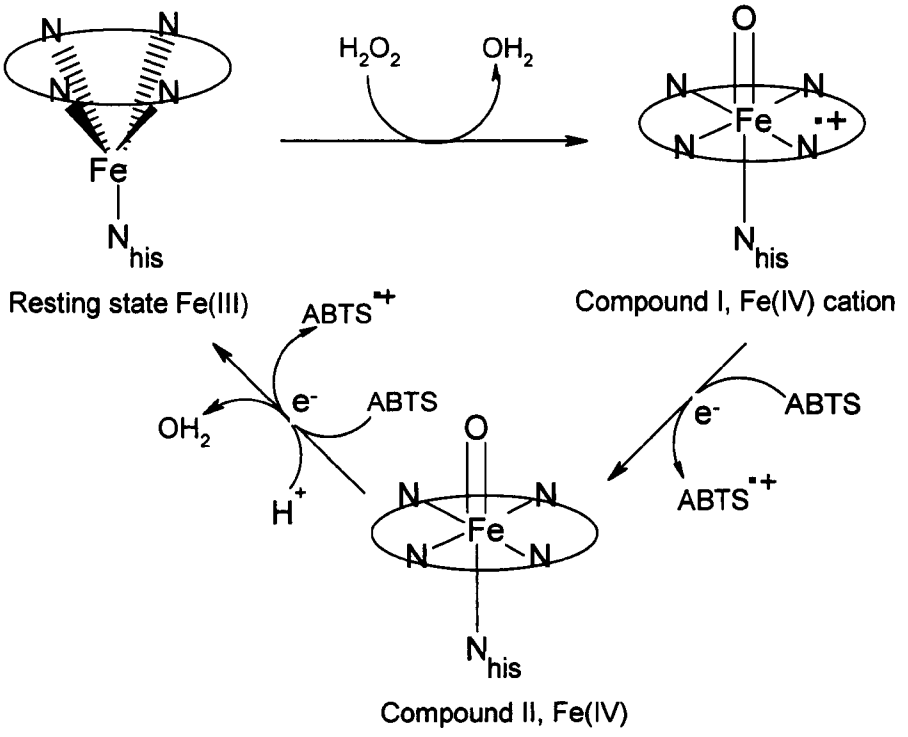

Figure 3.14 Schematic of the peroxidase catalytic involving horseradish peroxidase.[142]

The enzymatic activity of both the immobilised cyt *c*-PSS-AMP organoclay composite and control solutions containing a mixture of cyt *c* and PSS, was determined and compared with similar control experiments involving native cyt *c* in aqueous solution. In each case, plots monitoring the formation of oxidised ABTS (A_{414}) against time were obtained (**Figure 3.15**). Analysis of the gradient of these plots enabled calculation of the rate or reaction and subsequent linear Lineweaver-Burk plots of 1/V versus 1/S were obtained, which were consistent with Michaelis-Menten behaviour (**Figure 3.16**). Michaelis-Menten kinetic parameters (**Table 3.6**) obtained from the gradient and intercept of the Lineweaver-Burk plots allowed comparisons to be made between the peroxidise activities of native and AMP-immobilised cyt *c*, (see the appendix for full explanation and description of the Michaelis-Menten kinetic analysis).

The V_{max} values of native cyt *c* (2.67 μM), aqueous cyt *c*-PSS, and cyt *c*-PSS-AMP nanocomposite were 23.9, 12.6 and 10.6 μM min^{-1}, respectively. The lower V_{max} value for immobilised cyt *c* and aqueous sols containing PSS and cyt *c*,

corresponded to a slight decrease in turnover rate, possibly attributed to diffusional limitation of the substrate through the PSS-AMP organoclay matrix. In addition, the dissociation constants (K_m) determined for aqueous cyt *c*-PSS (9.55 mM) and cyt *c*-PSS-AMP nanocomposite (6.46 mM) were significantly reduced compared with the native enzyme (204.4 mM), suggesting that there is a stronger affinity between immobilised cytochrome *c* and the hydrogen peroxide substrate and therefore more effective binding, possibly due to the active site of the enzyme being arranged in a more favouarable orientation for interaction with the substrate molecules.

Michaelis-Menten Kinetic Parameter	**Native cyt *c***	**Aqueous Cyt *c*-PSS**	**Cyt *c*-PSS-AMP clay nanocomposite**
V_{max} ($\mu M\ min^{-1}$)	23.9 (4.11- 24.9)	12.6 (10.7-34.0)	10.6 (9.86-11.4)
K_m (mM)	204.4 (30.8-225.5)	9.55 (3.26-68.1)	6.46 (5.79- 7.32)

Table 3.6 Comparison of the average Michaelis-Menten kinetic parameters, V_{max} and K_m for native cyt *c*, aqueous cyt *c*-PSS and AMP-immobilised cyt *c*, with the ranges of values shown in brackets.

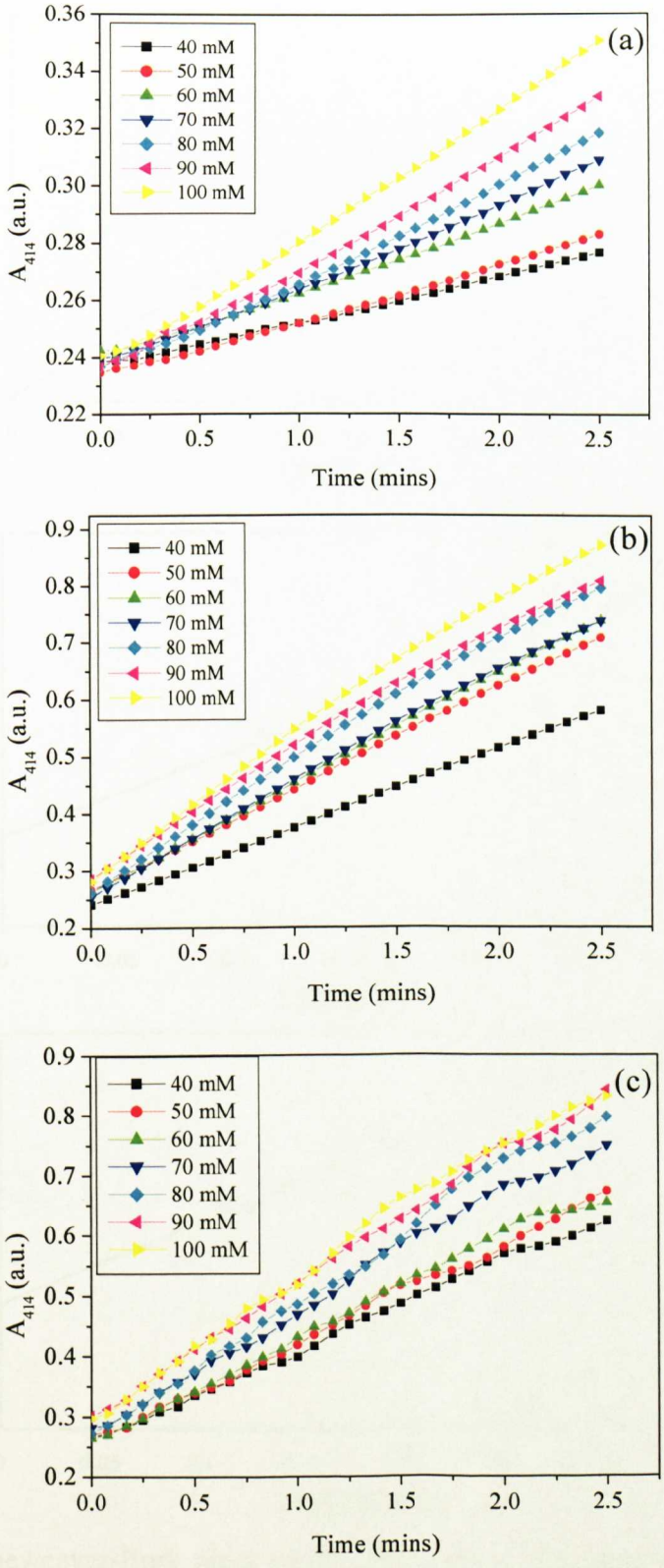

Figure 3.15 Examples of plots showing the formation of oxidised ABTS, at 414 nm, against time for (a) native cyt *c*, (b) aqueous cyt *c*-PSS and (c) cyt *c*-PSS-AMP clay nanocomposite.

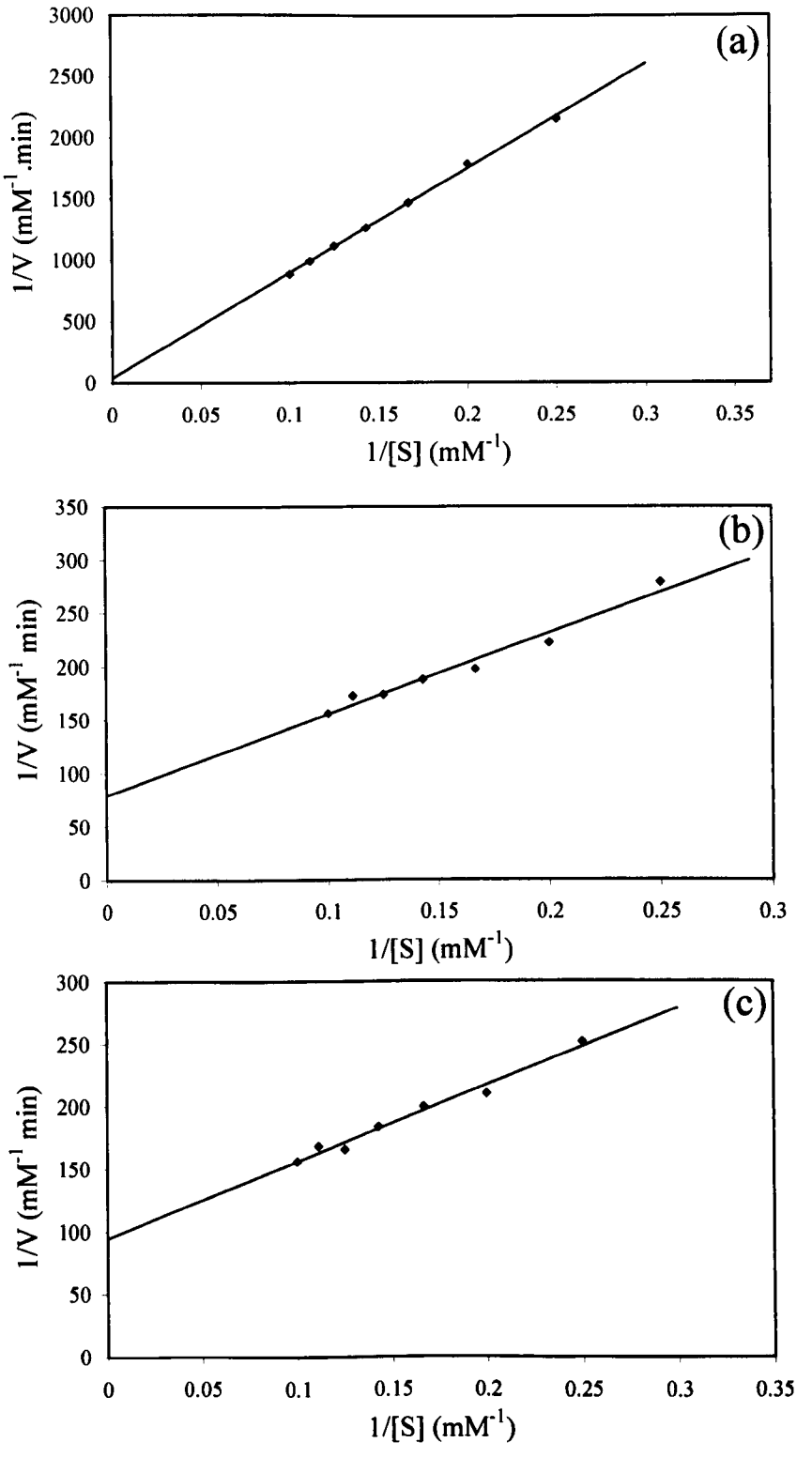

Figure 3.16 Lineweaver-Burk plots of (a) native cyt *c*, (b) aqueous cyt *c*-PSS and (c) cyt *c*-PSS-AMP clay nanocomposite.

3.4.5 Determination of the pH Dependence of the Peroxidase Activity of Cytochrome *c*

The catalytic activity of an enzyme is highly dependent on the pH of the enzyme environment and the majority of enzymes are most stable at physiological pH.[144] The peroxidise activity of immobilised cyt *c* was investigated under different pH conditions. Interestingly, AMP-clay immobilised cyt *c* demonstrated sustained specific activities over an extended range of pH values, compared to the native protein in aqueous solution (**Figure 3.17**). At pH values of 3 to 5, native and immobilised cyt *c* showed comparable specific enzyme activities. In contrast, the enzyme activity in the pH range 6 to 10 was sustained by immobilising the cyt *c* molecules in the AMP clay matrix, compared with the native protein in solution.

In general, the significant increase in biomolecule stability associated with the hybrid material could be attributed to two separate factors. Firstly, the sustained stability of the immobilised enzyme may be due to physical confined in the AMP clay matrix preventing the protein from unfolding and, as a result of this, denaturing. Secondly, the effect of large changes in pH in bulk solution may equate to a much smaller change in the pH of the local microenvironment surrounding the protein molecule due to the buffering ability of the organoclay matrix and the presence of fewer water molecules, in the local microenvironment. This similar result was observed in the case of sol-gel encapsulated alkaline and acid phosphatase, where high and low pH conditions, corresponded to much smaller changes in local pH, contributing to the maintained stability of the enzyme under extremely alkaline and acidic environments.[108]

Furthermore, the increased specific enzyme stability of the PSS-cyt *c* control solution, in the pH range 4-10 (**Figure 3.17c**) suggested that electrostatic interactions between the counter charged protein and polymer may also contribute to the additional stabilisation of the immobilised cyt *c* molecules. Indeed, it has been previously suggested that immobilised enzymes can be stabilised by electrostatic interactions with negatively charged supports, which

concentrate H^+ ions around the biomolecule, and as a consequence lowers the effective pH of the local environment in comparison to the native enzyme in solution.[145]

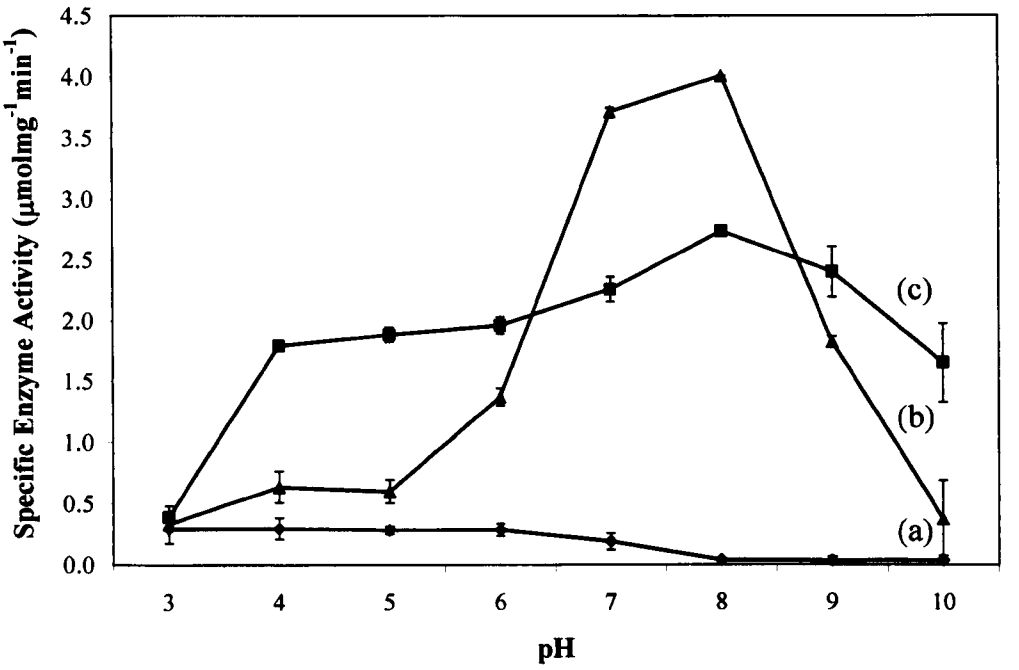

Figure 3.17 Plot of specific enzyme activity against pH for (a) native cyt *c*, (b) cyt *c*-PSS-AMP clay composite and (c) aqueous cyt *c*-PSS sol.

In general the extent of binding of the hydrogen peroxide substrate to the heme centre in cytochrome *c* is dependent on a range of factors including the shape of the heme pocket, the coordination geometry of the heme iron centre and the non bonding interactions surrounding the heme group, which make the enzyme kinetics extremely difficult to monitor.[121] Native cytochrome *c* is hexacoordinated, however, unfolding of the protein can result in rupturing of the Fe-S bond, contributing to dissociation of the methionine residue from the iron centre and significant opening of the heme pocket, as observed previously.[143] This opening may significantly improve the accessibility of the iron centre to the substrate molecules. The differences observed in the Michaelis-Menten kinetic parameters and the enzyme activities of native cytochrome *c*, compared with PSS-Cyt c and AMP-clay immoblised cyt *c*, may be attributed to differences in the geometry and conformation of the protein and subsequently the accessibility of the heme pocket.

3.5 Conclusions and Further Work

The studies reported in this chapter provide strong evidence for the formation of a protein-inorganic conjugate consisting of cyt *c* molecules immobilised in an aminopropyl-functionalised magnesium phyllosilicate matrix, resulting in the fabrication of a bulk nanocomposite. For the first time, this chapter extends the previously reported method of electrostatically induced self-assembly of anionic biomolecules or polymers and cationic clay sheets, to entrap cationic biomolecules with the same charge as the exfoliated organoclay layers by using an anionic polymer chaperone. This study was limited solely to investigation of the immobilisation of one cationic protein, ferri-cytochrome *c*, but further work could be applied to further extend this strategy to the immobilisation of alternative cationic biomolecules, for example lysozyme.

Photographic images of the AMP-immobilised cyt *c* composite displayed effective incorporation of the red, redox protein within the organoclay matrix. Additionally, PXRD data revealed that the majority of the protein molecules are immobilised between the organoclay grain boundaries. Significantly as the protein-containing nanocomposites are fabricated by a "soft chemisty" method, both FT-IR and UV-Vis spectroscopy provided evidence that the immobilised protein retained both its structure and function. Furthermore, as the inorganic clay matrix is nanoporous, UV-Vis spectroscopy demonstrated that the immobilised protein molecules were accessible to external small molecules, including sodium dithinonite and dioxygen. Further investigation of the peroxidise-type activity of the protein, demonstrated that the enzymatic activity was additonally retained and indeed sustained under adverse chemical conditions such as high pH. These studies provided further evidence that immobilised protein molecules were not only easily accessed by external molecules but in addition were significantly protected from denaturisation.

Further work, could investigate the application of resonance raman spectroscopy (RR) as an alternative technique to further investigate the structure of the immobilised protein. This technique has been extensively applied to examine the structure of heme proteins with the position of the raman bands providing

information on the structural parameters of the heme group, including the oxidation and spin state, in addition to the coordination number of the heme centre.[132, 146] In addition, the peroxidase activity of native and immobilised cyt *c* could be further investigated using an different assay, for example guaiacol, an alternative electron donor in peroxidase-type reactions, which is oxidised to tetraguaiacol and can be conveniently followed spectrophotometrically at 470 nm.[147]

In summary, the work discussed in this chapter highlights the potential importance of combining inorganic materials chemistry procedures with biomolecular science, and suggest that this interdisciplinary approach will be of significant value for the general fabrication of novel bioinorganic constructs with extended stability and function. The studies reported in this chapter represent an effective route to immobilise cationic proteins in a readily available aminopropyl-functionalised clay matrix, resulting in sustained enzyme activity over a broadened range of pH, in comparison to the native protein. Such protein-inorganic conjugates are expected to be potentially useful in a range of bio-related applications operating under non-standard conditions.

CHAPTER 4 PREPARATION, CHARACTERISATION AND SELF-ASSEMBLY OF DNA STABILISED GRAPHENE DISPERSIONS

(Published in *Advanced Materials*, 2009, **21**, 3159-3164)

4.1 Introduction

4.1.1 Chapter Outline and Aims

Research involving atomically thick graphene sheets has gained significant attention since it was first isolated in 2004.[148] The low yields of graphene produced provoked further investigation of alternative higher yield synthetic protocols. Chemical routes involving oxidative treatment and subsequent reduction of graphite, reported in 2006, demonstrated the feasibility of fabricating stable, aqueous dispersions of atomically thick reduced graphene sheets, in much higher yield.[149] One of the requirements associated with the production of graphene dispersions via this route is the inclusion of a polymer stabilising agent during the reduction stage, to prevent aggregation of the graphene sheets.

This chapter investigates an alternative route to the synthesis of graphene sheets via the application of chemical treatment. The main challenge is to prevent aggregation of the graphene sheets during the reduction step, which was achieved through the integration of biologically-derived single-stranded deoxyribonucleic acid (ssDNA) with atomically thick graphene sheets, to effectively produce aqueous dispersions of ssDNA coated graphene sheets. One of the primary goals of the research presented in this chapter is firstly, to demonstrate full characterisation of ssDNA-stabilised graphene dispersions, using a range of physio-chemical techniques and secondly to demonstrate the ability to further process these dispersions to form self-supporting bio-nanocomposite films using vacuum filtration or evaporation-induced self-assembly techniques. This chapter concludes with a "proof of concept" approach for the fabrication of bio-nanocomposite films by examining the application of ssDNA-coated graphene

sheets as anionic host matrices for the post synthetic co-intercalation of cationic proteins, including in particular ferri-cytochrome *c* (ferri-cyt *c*) and lysozyme.

4.1.2 The Principal Routes to Graphene Formation

Graphite is a highly abundant, cheap material, composed of stacked sheets of graphene, which until recently could not be readily exfoliated to isolate individual graphene sheets. The discovery and isolation of single, atomically thick sheets of graphene has initiated a plethora of research on this material. Pinnacle to the investigation of both the physical and chemical properties of this relatively "young" material is the ability to produce high yields of superior quality graphene sheets. Graphene sheets were first isolated in 2004, by Novoselov and Geim, at the University of Manchester using a mechanical cleavage technique, also known as the 'scotch-tape approach.' This extremely simple but yet effective approach involved repetitively peeling apart highly ordered pyrolytic graphite, using scotch tape or cellotape, to produce both high-quality single and multi-layers of graphene, up to 10 μm in length.[148] The main limitation of this route is the isolation of extremely low yields of material.

More recent studies in the quest to fabricate and isolate graphene have investigated the preparation of single and multi-layers on single crystal silicon carbide (SiC) substrates, using an ultra high vacuum (UHV) annealing process.[150, 151] This technique is based on studies, conducted in 1962, which demonstrated that at high temperatures and vacuum, silicon sublimes leaving well ordered graphene lattices.[152] Unfortunately, the application of high vacuum and temperatures can lead to unfavourable decomposition of the SiC substrate. Subsequent modifications of this route have demonstrated that graphene layers can be produced in an argon atmosphere under ambient conditions, omitting the requirement for high vacuums and temperatures.[153] Alternative substrates to SiC have also been investigated including a high temperature route, reported by Sutter, for the controlled growth of graphene layers on ruthenium substrates.[154] Furthermore, Reina and co-workers demonstrated the formation of single and few-layer graphene on polycrystalline nickel substrates, using chemical vapour

deposition (CVD) at ambient pressures, with the potential to remove the substrate by wet-etching techniques.[155]

Alternative techniques involving the thermal fusion of polyaromatic hydrocarbons (PAHs) provides a bottom-up strategy for physically fusing together low molecular weight species, to form graphene-based films. In this study, sols composed of superphenalene derivatives, containing flexible alkyl side-chains, were spin coated onto substrates and subsequently heated to temperatures as high as 1100 °C under an Ar atmosphere, resulting in effective fusion of graphene basic units to form larger graphene films, with conductivities as high as 3000 Scm^{-1}.[156]

The portfolio of routes presented thus far, catalogues just a few of the primary routes currently being investigated for the synthesis of high quality single and multi-layer graphene and, despite being successful approaches, also have their associated disadvantages. The production of graphene sheets via mechanical cleavage produces high-quality graphene but in low yields, as mentioned previously and can prove to be tedious when attempting to isolate single layers. Epitaxial growth of graphene sheets, on the other hand, is a higher yield route, affording large areas of graphene films (approx 1 cm^2), however, the interaction of the individual graphene sheets with external substrates may hinder both, the mobility of the electrons through the graphene sheets and the ability to further process the sheets. In addition, the use of single crystal substrates and ultra high vacuum conditions can prove to be expensive. Thermal fusion of PAHs, involving the effective 'patching together' of individual monomeric aromatic species again requires the use of an external substrate, which could potentially hinder both the electronic properties and the ability to furthermore process the graphene sheets, as mentioned previously. An alternative higher yield route to the formation of graphene is possible using chemical modification techniques, involving oxidation and subsequent reduction of graphite and advances in this area are discussed further in the next section.

4.1.3 Chemical Oxidation of Graphite to form Graphene Oxide

Chemical oxidation of graphite was first investigated 150 years ago but it is only in the past five years that the potential of these reactions to form high yields of graphene sheets was realized. Early studies, performed by Brodie[157, 158] in 1859, demonstrated that treating graphite with a combination of fuming nitric acid and potassium chlorate resulted in the effective modification and expansion of graphitic layers. Alternative routes were subsequently reported by Staudenmaier[159] in 1898 and Hummers and Offeman[160] in 1958 involving treating graphite with a mixture of concentrated mineral acids and strong oxidising agents. Further investigation of these expanded graphitic materials showed that they formed high yields of oxygen-functionalised graphene monolayers, commonly known as graphene oxide or GO.

Graphene oxide has demanded a significant amount of attention since 2004 as a viable route to the high yield formation of graphene monolayers and extensive research has been employed to investigate its chemical structure. Despite several models being presented, detailed ^{13}C NMR and FT-IR analysis of individual GO layers, demonstrated that they are, in general, composed of a mixture of unoxidised aromatic rings and aliphatic 6-membered rings containing both sp^2 and sp^3 hybridised carbon atoms, including phenolic hydroxyl and epoxide surface functionalities on the basal planes of the sheets with minor carbonyl and carboxylic acid groups present at the edges of the sheets (as shown in **Figure 4.1**). The presence of phenolic hydroxyl groups, containing tetrahedral carbon atoms contributes to a slight in-plane distorted configuration, resulting in the formation of wrinkles on the surface of individual sheets.[161, 162] These oxygen functionalities render the individual sheets to be highly hydrophilic and therefore readily dispersed in aqueous solutions to form stable colloidal dispersions of GO. The degree of oxidation is highly dependent on the synthetic protocol and the pre-cursor graphite used. Electrical measurements of the individual sheets displayed low electrical conductivity ($\sigma = 10^{-3}$ S cm^{-1}) as a result of disruption of the conjugated network of sp^2 hybridised carbon atoms.[163]

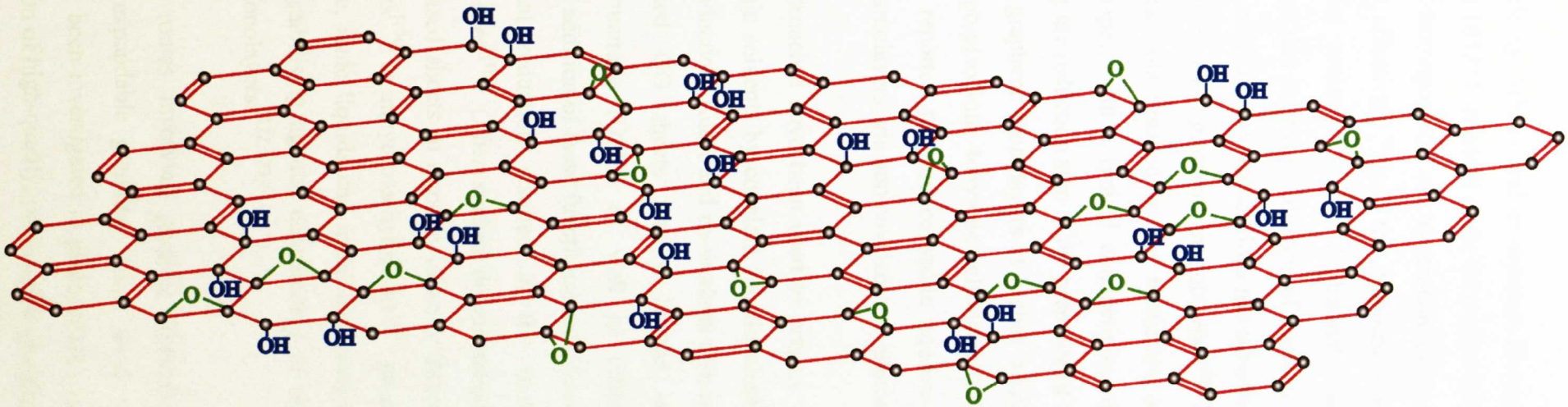

Figure 4.1 Schematic showing the chemical structure of graphene oxide after treatment of graphite with a mixture of H_2SO_4 and $KMnO_4$. The minor functional groups present at the edges of the sheets are omitted for clarity, adapted from He et al.[161]

Recent work by Arksay and co-workers discovered that thermal treatment of solid GO at 1050 °C resulted in the formation of individual graphene monolayers due to the decomposition of oxygen-containing surface functionalities to form CO_2 which effectively 'blast' the graphene sheets apart due to the increased inter-lamellar pressure.[164, 165] Additional studies, by the Wallace group, demonstrated that chemical reduction of aqueous dispersions of exfoliated GO in an alkaline medium at concentrations not exceeding 0.025 wt. %, can be used to produce stable sols of graphene monolayers.[166] Subsequent vacuum filtration of the graphene sols resulted in the formation of self-assembled free-standing graphene paper, with a typical conductivity of 72 S cm^{-1}. Furthermore, by undertaking the reduction step in the presence of a stabilising polymer or organic molecules, graphene monolayers at higher concentrations can be produced. In particular, poly(sodium 4-styrene sulfonate) (PSS)[149] and pyrene butyrate[167] have been reported to produce stable aqueous dispersions of functionalised graphene monolayers, via non covalent π-π interactions.

Similar approaches have been used to prepare stable graphene dispersions in polar organic solvents by covalent functionalisation of GO sheets followed by chemical reduction. Ruoff and co-workers demonstrated that phenyl iso-cyanate functionalised GO sheets readily formed stable dispersions in N, N-dimethylformamide (DMF) as well as other polar, aprotic solvents.[168] Subsequent addition of these functionalised sheets to organic polymers, followed by chemical reduction resulted in the fabrication of graphene-polymer nanocomposites.[169] Other studies demonstrated the possibility of stabilising graphene-based sheets in organic solvents through the covalent attachment of alkyl amines[170] or anhydrous hydrazine[171] groups to the surface of the sheets. Furthermore, ionic liquids and metal nanoparticles have also proven to act as successful stabilising agents, contributing to the fabrication and isolation of graphene monolayers.[172, 173]

Alternative routes involving graphite intercalation compounds (GICs) also known as expandable graphite, which were introduced in chapter 1, have additionally been investigated in place of GO, as an intermediate compound to the formation of high-quality, processable graphene sheets. Thermal treatment of

commercially available sulfuric acid (H_2SO_4) and nitric acid (HNO_3) intercalated graphitic compounds (Graftech Incorporation) produces exfoliated graphene sheets, which can be sonicated in both conjugated monomeric and polymer solutions to produce non-covalently functionalised graphene sheets.[174, 175] Furthermore, organic solvent-induced exfoliation of graphite intercalation compounds has also proved to be an important route to the formation of processable graphene sheets. Valles and co-workers demonstrated that the simple addition of N-methyl-pyrrolidone (NMP) to a potassium-intercalated graphite compound, resulted in spontaneous exfoliation to produce negatively charged, reduced graphene sheets.[176] Furthermore, Li and co-workers investigated the sonication of oleum-intercalated graphite compounds in phospholipid solutions, to form graphene sheets containing a trace of oxygen functionalities, which could subsequently be removed by annealing at 800 °C in H_2 to form high-quality graphene.[177]

This chapter demonstrates, for the first time, the application of ssDNA, as a stabilising agent, for the fabrication of aqueous dispersions of graphene monolayers. The proceeding section introduces the structure and properties of DNA and explains why it is a suitable biopolymer for the stabilisation of graphene sheets.

4.1.4 Deoxyribonucleic Acid: An Effective Biological Stabilising Agent

DNA is nature's most fundamental biopolymer, first discovered by James Watson and Francis Crick in 1953.[178] It is composed of two polynucleotide chains, which coil around each other in an anti-parallel fashion to form the well-known double helical structure. Each individual polymer strand is composed of a main backbone containing a sugar and phosphoric acid moiety, attached to one of four heterocyclic nucleobases including adenine (A), cytosine (C), guanine (G) or thymine (T). Adenine and guanine are fused 5- and 6-membered heterocyclic compounds known as purines and cytosine and thymine are 6-membered rings called pyrimidines. The sugar residue found in the nucleotide unit is a 5-carbon sugar called 2-deoxyribose which is bridged via a phosphodiester bond at the 3' and 5' positions of neighbouring sugar molecules, as shown in **Figure 4.2b**.

Hydrogen bonding interactions between A-T or C-G bases, contribute towards the formation of the double helical structure, with the bases occupying the core of the helix and the sugar-phosphate chain present on the periphery, minimising repulsive interactions between charged phosphate group, (**Figure 4.2**).[179]

The exceeding physical and chemical properties of DNA have contributed to its broader application in materials science to develop a range of bio-inorganic hybrid nanocomposites. As discussed in chapter 1, several studies have demonstrated the successful intercalation of negatively charged DNA strands into layered double hydroxides (LDHs) to produce functional bio-inorganic nanocomposites, which have potential application in gene therapy, by facilitating the delivery and uptake of DNA into mammalian cells (endocytosis) as shown in **Figure 4.3a**.[5, 6] Furthermore, DNA nanocomposites have been developed in conjunction with organically-modified magnesium phyllosilicate clays, using electrostatic interactions to effectively intercalate or wrap DNA for DNA storage applications, as illustrated schematically in **Figure 4.3b**.[124]

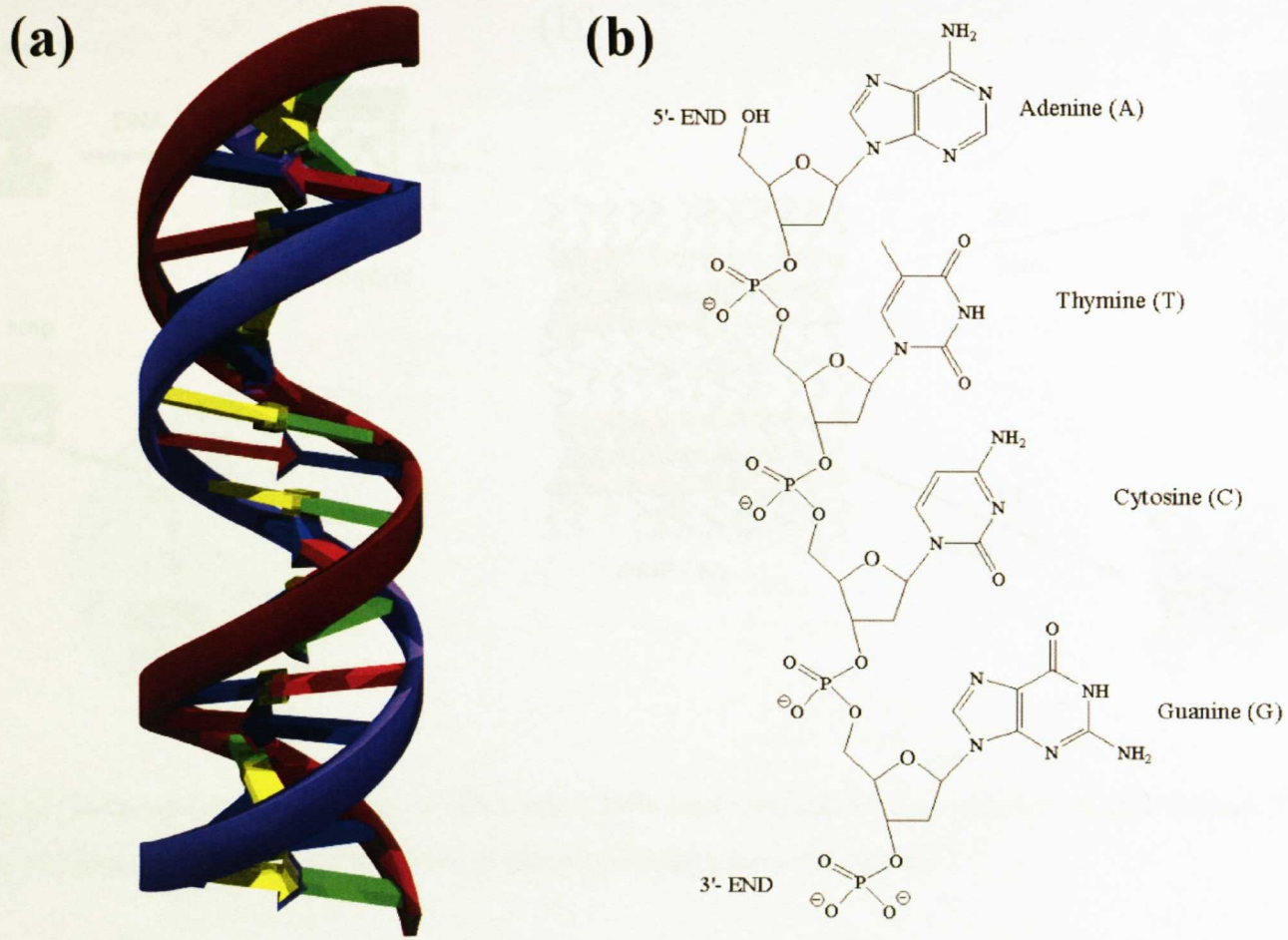

Figure 4.2 Schematic showing (a) the double helical structure of DNA and (b) the molecular structure of a single DNA strand.[179]

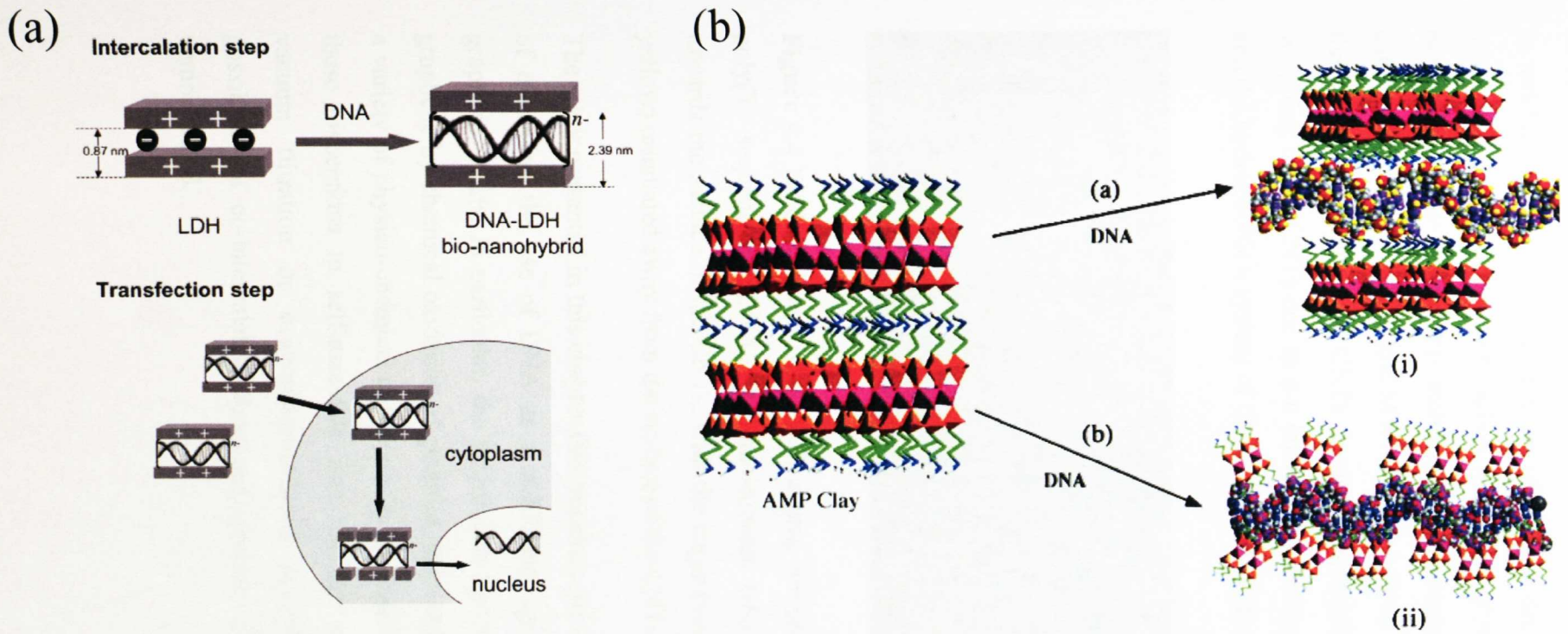

Figure 4.3 Schematics showing (a) the intercalation of DNA into LDHs host matrices with application in gene therapy,[6] and (b) the wrapping and intercalation of DNA using organically functionalised phyllosilicate clays for DNA storage.[124]

In addition to forming lamellar nanocomposites, DNA has played a central role in tackling one of the key challenges of the past decade involving the effective separation and dispersion of carbon nanotubes (CNTs). Several studies have demonstrated the successful stabilisation of single-walled and multi-walled carbon nanotubes (SWNTs and MWNTs) using DNA.[180-182] These studies show that simple sonication of CNTs in single-stranded DNA result in effective wrapping of the CNTs due to π-π interactions between the nucleobases in DNA and the hydrophobic π system of CNTs, as shown schematically in **Figure 4.4**.

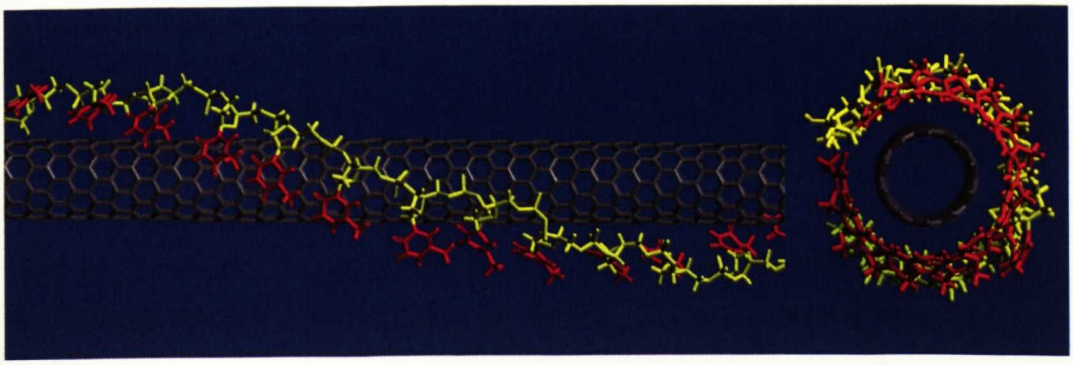

Figure 4.4 Binding model of a (10,0) zigzag carbon nanotube, wrapped with a poly(T) sequence of DNA. The nucleobases (shown in red) are orientated towards the surface of the CNTs, with the sugar-phosphate backbone (shown in yellow) orientated away from the surface of the CNTs.[180]

The work presented in this chapter demonstrates for the first time, the possibility of extending the use of DNA as a stabilising agent for CNTs to individual graphene sheets. In particular, the preparation and characterisation of ssDNA-graphene by chemical oxidation of graphite, followed by in situ reduction, using a variety of physico-chemical techniques is discussed. Furthermore the ability of these dispersions to self-assemble into lamellar nanocomposite films using vacuum filtration or evaporation-induced assembly techniques, with the possibility of co-intercalating functional proteins into the gallery regions, is demonstrated.

4.2 Materials

All reagents were purchased from Aldrich or Fischer Scientific, UK and used without purification, unless otherwise stated.

4.2.1 Preparation of Graphene Oxide

Chemical	Molecular Formula	Supplier
Graphite powder, 20 μm	C	Aldrich
Sulfuric acid, 98 %	H_2SO_4	Fischer Scientific
Potassium permangante	$KMnO_4$	Aldrich
Hydrogen peroxide, 30 %	H_2O_2	Fischer Scientific
Barium chloride	$BaCl_2$	Aldrich
Acetone	CH_3COCH_3	Aldrich
Sodium hydoxide	NaOH	Fischer Scientific
Nitric acid, 70 %	HNO_3	Fischer Scientific
Potassium Chlorate	$KClO_3$	Aldrich
Hydrochloric Acid, 37 %	HCl	Fischer Scientific

4.2.2 Preparation of Single-Stranded Deoxyribonucleic Acid Stabilised Graphene

Chemical	Specification/ Molecular Formula	Molecular Weight (g/mol)	Supplier
Deoxyribonucleic acid sodium salt, from salmon testes	2000 base pairs, 42 % G-C	-	Aldrich
Hydrazine (35 wt. % in H_2O)	NH_2NH_2	32.05	Aldrich
Sodium sulphide	Na_2S	78.04	Aldrich

4.2.3 Preparation of Co-Intercalation Bio-Nanocomposites

Chemical	Specification	Molecular Weight (g/mol)	Supplier
Cytochrome *c*, from equine heart	Dark-red powder, 98 % purity	12384	Sigma
Lysozyme, from chicken egg white	White powder, 90 % purity	14700	Sigma

4.3 Experimental Details

The experimental protocols undertaken in sections 4.3.1 and 4.3.2 were extremely hazardous and additional safety precautions were undertaken. These include wearing full personal protective equipment, including lab coat, plastic apron and face shield and using a reinforced safety shield in the fume hood for the duration of the experiment.

4.3.1 Preparation of Graphene Oxide Based on the Hummers-Offeman Route

Graphene oxide (GO) was prepared from graphite using a modified Hummers-Offeman method, as follows.[160, 183] Graphite powder (1 g) was dispersed in cold concentrated sulphuric acid (18.0 M, 23 mL, dry ice bath) and potassium permanganate ($KMnO_4$, 3 g) was gradually added with continuous vigorous stirring and cooling to maintain the temperature below 20°C. The dry ice bath was removed and replaced by an oil bath and the temperature of the mixture was maintained at 35°C for 30 minutes, with continuous stirring, using additional heating, if required, followed by slow addition of distilled water, which produced a rapid increase in the solution temperature up to a maximum temperature of 100°C. The reaction was maintained at 98°C for a further 15 minutes and was then terminated by further addition of more distilled water (140 mL) followed by hydrogen peroxide solution (H_2O_2, 30 %, 10 mL). The solid product was separated by centrifugation at 5000 rpm and washed initially with 5 % HCl until sulphate ions were no longer detectable with barium chloride ($BaCl_2$) followed by three acetone washes, before being air-dried overnight at 65°C.

4.3.2 Preparation of Graphene Oxide Based on the Staudenmaier Route

Graphene oxide was prepared from graphite using the Staudenmaier method, as follows.[159] Graphite powder (5 g) was carefully added to a mixture of cooled concentrated sulphuric acid (18.4 M, 87.5 mL) and concentrated nitric acid (15.6 M, 45 mL), immersed in an ice bath, with vigorous stirring. Potassium chlorate ($KClO_3$, 55 g) was gradually added over 15 minutes, with vigorous

stirring and cooling. The reaction vessel was loosely capped and stirred at room temperature for 120 hours, with samples removed after 24, 48 and 96 hrs for analysis. The solid product, after 120 hrs, was added to deionised water (4 L) and separated using a 'Sartolon' membrane (pore size = 0.22 μm) before being repeatedly washed with 5 % HCl until sulphate ions were no longer detectable with barium chloride ($BaCl_2$) before being air-dried overnight at 40°C.

4.3.3 Preparation of ssDNA Stabilised Graphene Dispersions

A stable dispersion of GO sheets (10 $mgmL^{-1}$), prepared as described previously (section 4.3.1), was sonicated for 2 hours to ensure complete exfoliation and subsequently dialysed (12-14 kD cut off) for 2 hours to remove any excess salts and acids. The dispersion was centrifuged for 20 mins (3000 rpm), to remove the non-exfoliated material and the supernatant, containing the exfoliated GO sheets was removed. The GO supernatant (ranging from 6-9 $mgmL^{-1}$) was diluted further to obtain dispersions with concentrations ranging from 1-5 $mgmL^{-1}$. DNA derived from salmon testes (2000 base pairs, 42 % G-C) was heated at 95 °C for 1-2 hours to obtain single-stranded DNA (ssDNA). DNA stabilised graphene dispersions were typically prepared by mixing the GO dispersion (10 mL) with ssDNA (10 mL, 2$mgmL^{-1}$) and hydrazine (20 μL, 35 wt. %; hydrazine: GO ratio = 7:10) and the mixture was refluxed at 100 °C for 1 hour. A range of ssDNA-stabilised graphene dispersions were prepared by varying the GO:ssDNA weight ratios from 1:2, 1:5, 1:10, 1:20 and 1:33. Excess DNA and hydrazine were removed by dialysis against water overnight.

4.3.4 Control Experiment: Preparation of Reduced Graphene Oxide

Reduced GO dispersions were obtained by mixing GO (10 mL, 1-5 $mgmL^{-1}$) with distilled water (10 mL) and hydrazine (20 μL, 35 wt. %; hydrazine: GO ratio = 7:10) and the mixture was refluxed at 100 °C for 1 hour. Excess hydrazine was removed by dialysis against water overnight.

4.3.5 Preparation of ssDNA-Graphene Lamellar Nanocomposite Films

Self-standing films and papers of ssDNA-graphene were fabricated by both vacuum filtration and evaporation-induced self-assembly techniques. As-prepared dispersions of ssDNA-G were vacuum filtered using Anodisc membrane filters (Whatman, 25 mm in diameter, pore size 0.2 μm) to produce films up to 4 cm in diameter. Films were also prepared on silicon wafers by slow evaporation overnight at room temperature using 100-200 μL dispersions of ssDNA-G (0.5-2.5 $mgmL^{-1}$).

4.3.6 Preparation of Co-Intercalation Nanocomposites

(a) Co-intercalation of ferri-cytochrome *c* (ferri-cyt *c*)

Stable dispersions of ssDNA-G (wt. ratio = 2:1, 100 μL, 0.5-1.0 $mgmL^{-1}$) were added dropwise to solutions of ferri-cytochrome *c* (1 mL, 1 $mgmL^{-1}$, horse heart muscle). The mixture was equilibrated overnight, and the resulting precipitate was centrifuged (13.2 rpm, 10 mins) and air-dried at room temperature.

(b) Co-intercalation of lysozyme

Stable dispersions of ssDNA-G (wt. ratio = 5:1, 100 μL, 0.5-1.0 $mgmL^{-1}$) was added dropwise to lysozyme (1 mL, 0.5 $mgmL^{-1}$, chicken egg white). The mixture was equilibrated overnight, and the resulting precipitate was centrifuged (13.2 rpm, 10 mins) and air-dried at room temperature.

4.4 Results and Discussion

4.4.1 Characterisation of Graphene Oxide Prepared via the Hummers-Offeman Route

The results discussed in the next two sections compare the preparation and characterisation of graphene oxide (GO) via two different routes as an intermediate compound to the formation of reduced graphene dispersions.

Graphene oxide (GO) was readily prepared in high yield by chemical oxidation of graphite using a modified Hummers-Offeman method, as discussed in section 4.3.1. After isolation by centrifugation and subsequent drying at 65°C overnight, the as-prepared GO consisted of a brown powder (**Figure 4.5a**), which on sonication in water formed aqueous, brown suspensions (1-10 $mgmL^{-1}$) of highly negatively charged (zeta potential = -67.3 mV, pH = 3.55) exfoliated GO sheets (**Figure 4.5b**). Importantly, these dispersions were observed to be stable to sedimentation (1 $mgmL^{-1}$) for several months. Addition of water to graphite powder, in contrast, demonstrated extremely poor dispersibility, with the formation of two distinct separate layers, as a result of the hydrophobic nature of the individual sheets and the inter-lamellar attractive Van der Waals forces (**Figure 4.5c**).

The morphology of the GO sheets was initially examined by transmission electron microscopy (TEM). TEM images of exfoliated GO dispersions revealed highly transparent, ultra-thin flat sheets ranging from 500 nm to several microns in size (**Figure 4.6a-b**). The sheets appeared to be particularly flexible containing crinkles, folds and in some case rolled edges due to their atomically thin nature and the presence of in-plane defects, which occur as a result of the oxidative treatment. In particular, the presence of sp^3 hybridised carbon atoms in the graphene planes introduces tetrahedral carbon centres, contributing to the in-plane distortions and wrinkles.[161]

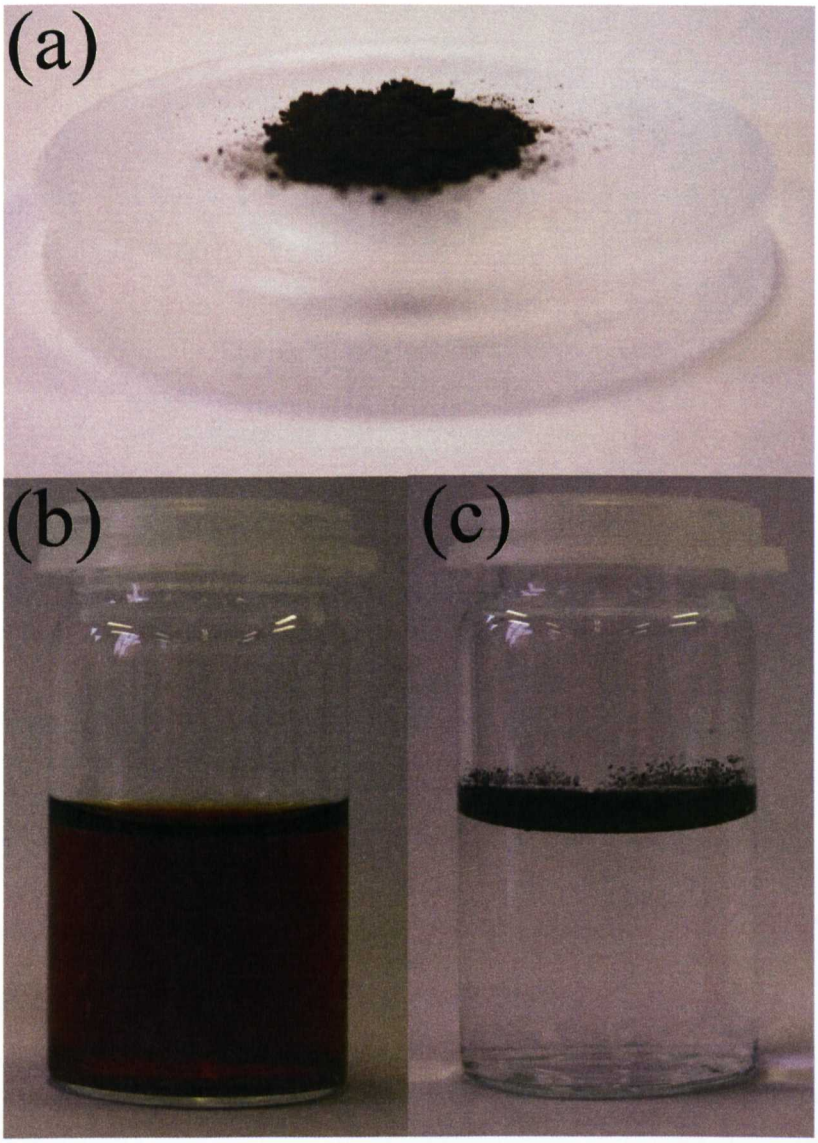

Figure 4.5 Photographic images showing (a) dried, powdered GO, (b) aqueous dispersion of GO (1 $mgmL^{-1}$) and (c) graphite powder mixed with water, showing the formation of a separate film of hydrophobic graphite powder on top of the water layer.

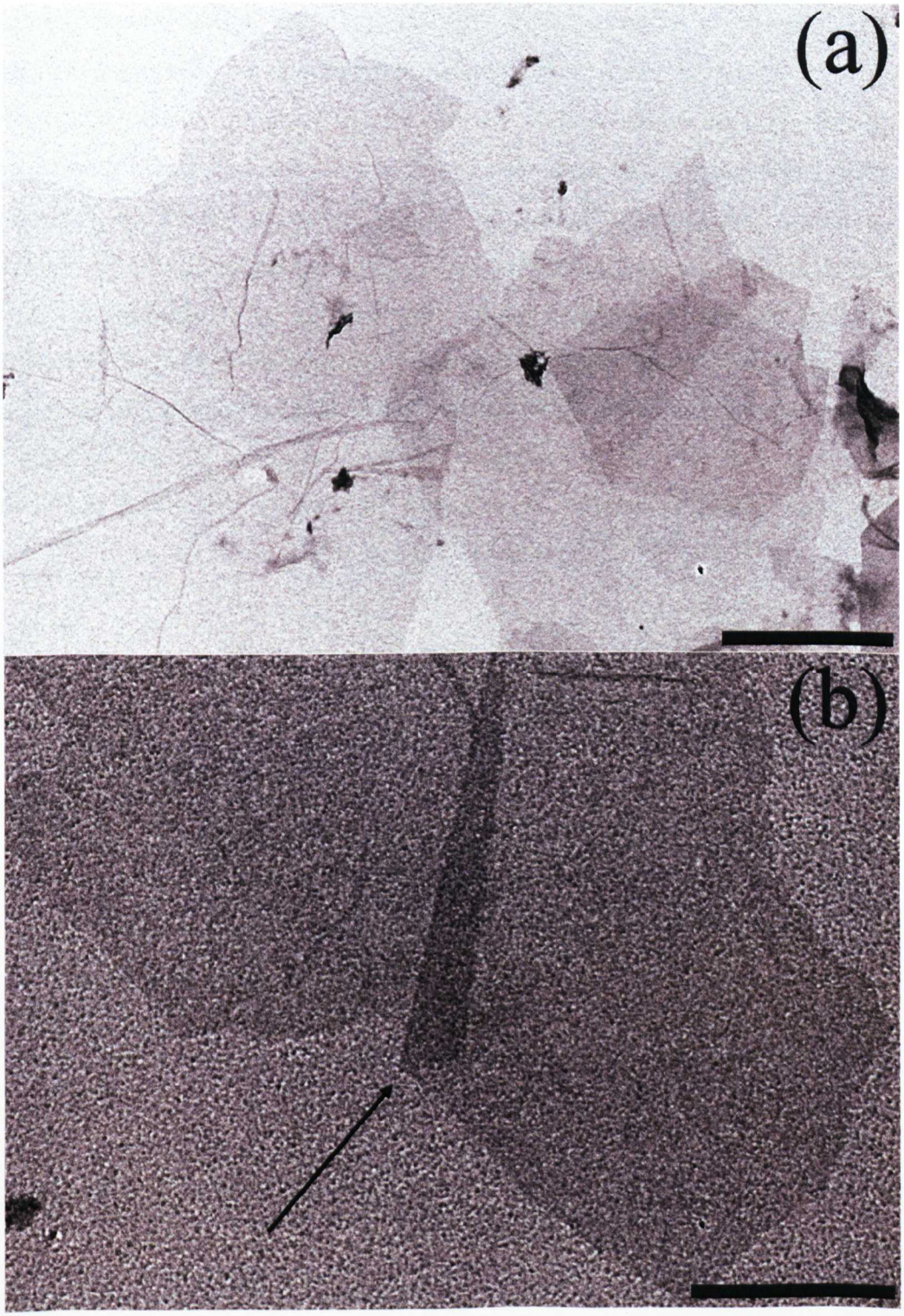

Figure 4.6 TEM images of exfoliated graphene oxide dispersions, prepared via a modified-Hummers route, showing ultra-thin sheets containing occasional folds at the edges (as shown by the arrow) and in-plane crinkles, due to the presence of distorted tetrahedral carbon centres. Scale bar (a) 500 nm and (b) 200 nm.

Tapping mode atomic force microscopy (AFM) studies provided further conclusive evidence for the ultra-thin nature of the sheets. Analysis of a 5 μm area of GO sheets dried on freshly cleaved mica revealed irregular shaped, overlapping sheets with average heights of individual sheets measuring 1.8 nm (**Figure 4.7a**). More detailed investigation of a smaller area (1 μm) containing overlapping GO sheets revealed that, significantly, the thickness of overlapping sheets was between 1-1.5 nm (ii) with a larger initial step onto the sheet (i) (**Figure 4.7b-c**). These measurements are slightly larger than predicted literature values for GO, possibly related to the presence of adsorbed water on the surface of the mica and the hydrophilic nature of the GO sheets. With these factors in mind, this data points towards the formation of fully delaminated atomically thick GO layers, as previously observed in literature.[163, 164, 167, 169, 184]

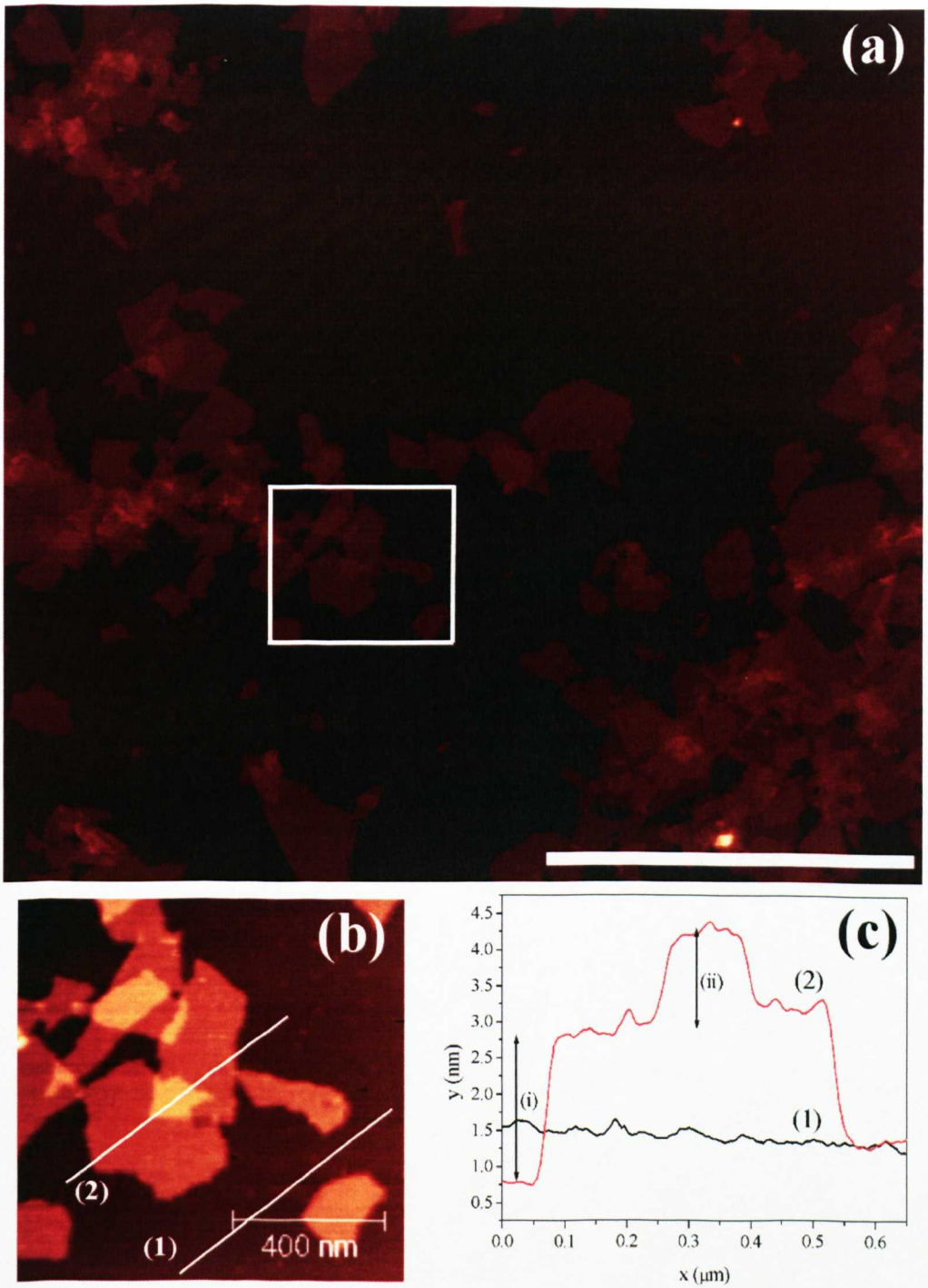

Figure 4.7 Tapping mode AFM data of an (a) exfoliated GO dispersion on freshly cleaved mica, scale bar = 2μm, with (b) the enclosed section shown in higher magnification and (c) corresponding height profile showing an initial step onto the GO sheet of 1.9 nm (i) and the thickness of the overlapping sheet of 1-1.5 nm (ii). Profile 1 and 2 correspond to the traces across the mica substrate and graphene oxide sheets, respectively.

Successful functionalisation of the graphite surface during oxidation, to produce GO was further confirmed using powder X-ray diffraction (PXRD). The PXRD pattern of graphite powder (**Figure 4.8a, Table 4.1**) showed a strong (002) reflection at $2\theta = 26.6^{o}$, corresponding to the graphite interlayer spacing of 0.335 nm, consistent with JCPDS data files.[185] In comparison, the PXRD pattern of GO films, prepared via evaporation-induced assembly of GO dispersions on silicon wafer (**Figure 4.8b, Table 4.1**), showed that after oxidation, the d_{002} peak diffraction peak disappears and is replaced instead by a sharp, low angle (001) reflection at $2\theta = 11.6^{o}$, corresponding to an increased interlayer d_{001} spacing of 0.759 nm. This spacing was in agreement with previously reported values for GO which range from 0.56-0.85 nm, depending on the nature of the oxidative treatment and the amount of water present in the gallery region of the re-assembled, stacked assembly.[79, 81, 186-190] In addition, a much weaker, broader second order reflection (002) at $2\theta = 22.0^{o}$ is observed, signifying that there is a certain degree of stacking of the GO sheets with increased in-plane disorder, due to the presence of defect oxygen containing surface functional groups.

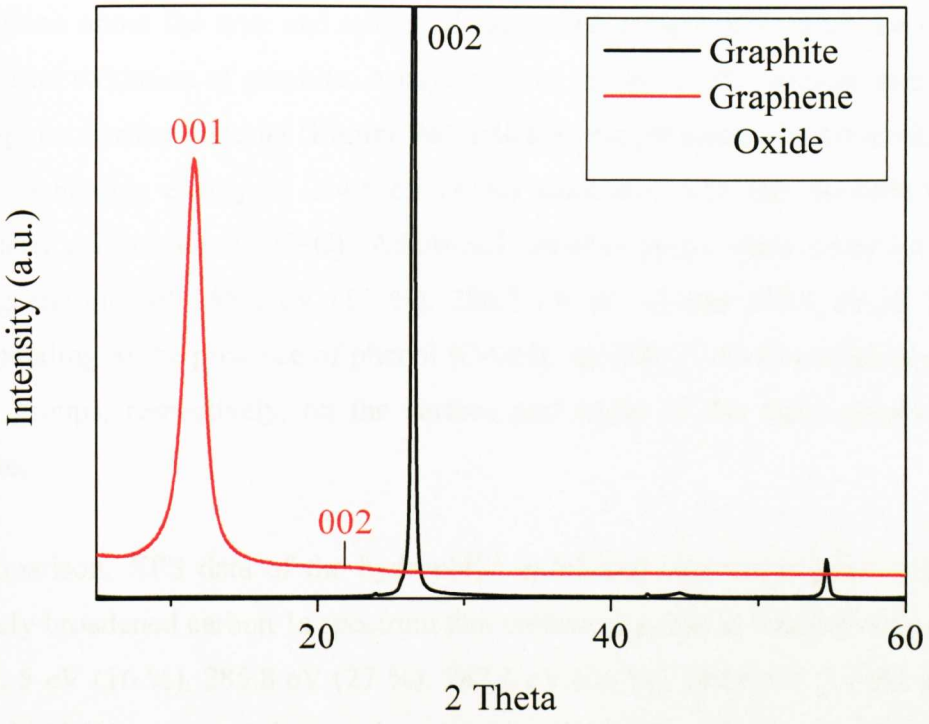

Figure 4.8 PXRD pattern of graphite and graphene oxide (GO)

Sample	2 Theta	d-spacing (nm)		hkl indices
		Experimental	Theoretical[185]	
Graphite	26.6	0.335	0.338	002
	42.5	0.213	0.212	100
	44.6	0.203	0.202	101
	54.6	0.168	0.169	004
Graphene Oxide (GO)	11.6	0.759	-	001
	22.0	0.403	-	002

Table 4.1 Summary of 2θ values, d-spacing and corresponding hkl indices for the peaks observed in the PXRD pattern of graphite and graphene oxide (GO).

X-ray photoelectron spectroscopy (XPS) provided extensive quantitative information about the type and extent of functional groups present on the GO sheets after oxidation of graphite. Analysis of the carbon 1s (C 1s) peak area of the graphite starting material (**Figure 9a**) indicated the presence of a dominating peak at a binding energy of 284.5 eV (81%) associated with the aromatic sp^2 hybridised carbon atoms (C=C). Additional, smaller peaks were observed at binding energies of 285.6 eV (11 %), 286.7 eV (6 %) and 288.1 eV (2 %) corresponding to the presence of phenol (C-OH), epoxide (C-O-C) and carbonyl (C=O) groups, respectively, on the surface and edges of the basal planes of graphite.

In comparison, XPS data of the hydrophilic exfoliated GO sheets presented a relatively broadened carbon 1s spectrum that contained peaks at binding energies of 284. 5 eV (16 %), 285.8 eV (27 %), 287.2 eV (36 %), 288.6 eV (17 %) and 290.4 eV (4 %), corresponding to the presence of aromatic (C=C), phenolic (C-OH), epoxide (C-O-C), carbonyl (C=O) and carboxylic (O-C=O) functional groups, respectively (**Figure 4.9b**). The significant reduction in the percentage composition of aromatic carbon atoms and the corresponding increase in the % abundance of sp^3 hybridised C atoms and oxygen containing carbonyl and carboxylic acid functional groups, accompanying the oxidative treatment, was additionally observable in oxygen 1s XPS spectra. The O 1s spectra of graphite (**Figure 4.9c**), presented a negligible presence of oxygen-containing functionalities on the surface of the sheets. In contrast, the O 1s spectra of GO (**Figure 4.9d**) exhibited a broad band composed of carbonyl, phenol, epoxide and adsorbed water molecules (90 %) and carboxyl oxygen atoms (10 %) at binding energies of 532.8 and 534.5 eV, respectively.[191, 192]

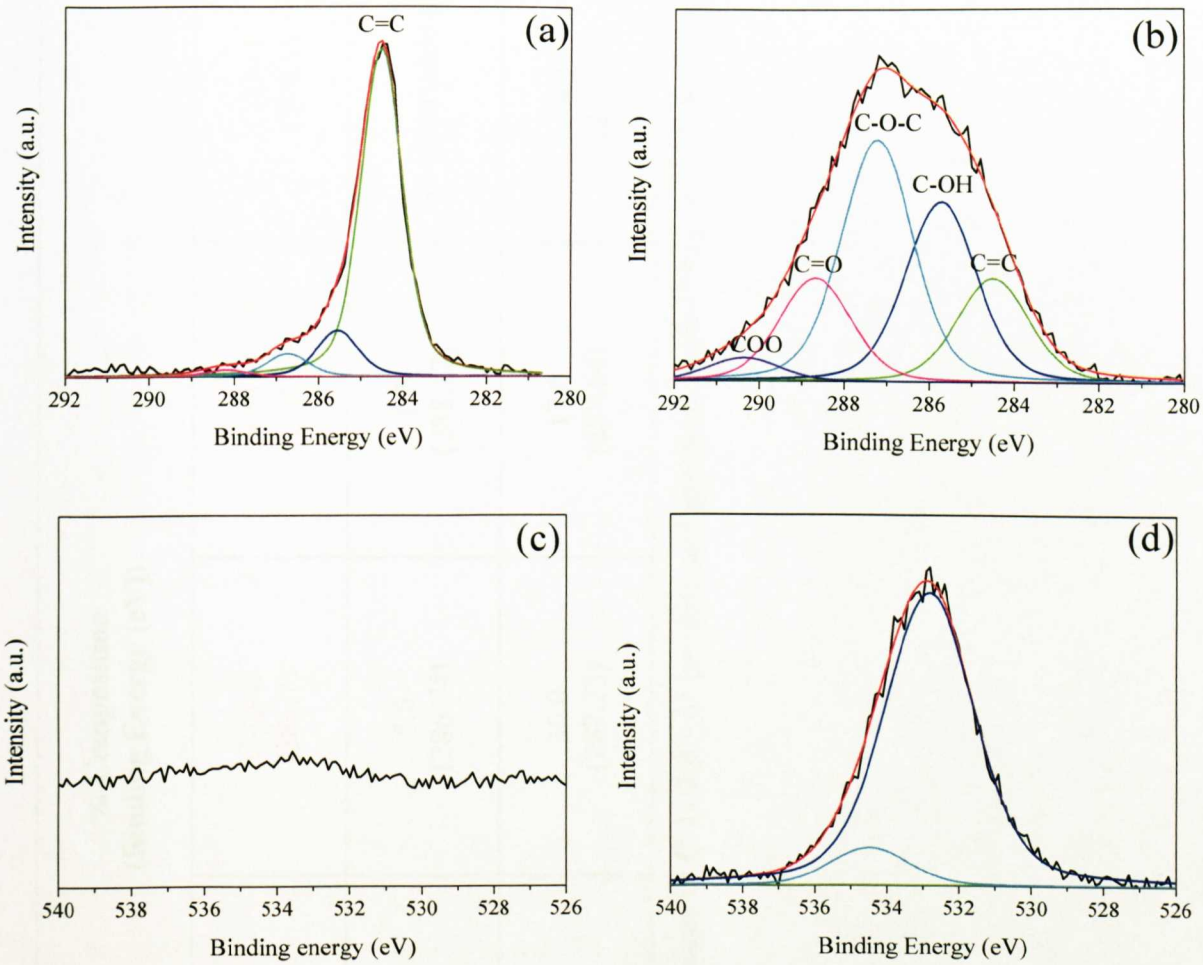

Figure 4.9 C 1s XPS data of (a) graphite and (b) exfoliated graphene oxide (GO); O 1s XPS data of (c) graphite and (d) exfoliated graphene oxide (GO).

SAMPLE	% Composition (Binding Energy (eV))				
Graphene Literature Values[149, 193, 194]	C=C (284.6)	C-OH (285.7)	C-O-C (286.7)	C=O (288.0)	C(O)O (289.1)
Graphite	81.3 (284.5)	11.4 (285.55)	5.6 (286.74)	1.7 (288.17)	No observable peak
Graphene Oxide	15.6 (284.53)	27.1 (285.75)	36.0 (287.23)	17.0 (288.64)	4.3 (290.39)

Table 4.2 Summary of percentage composition of functional groups in C 1s XPS of graphite and graphene oxide (GO), with their associated peak positions in brackets.

Fourier-Transform Infra-red spectroscopy (FT-IR) provided further qualitative evidence for the modification of the graphite surface during oxidative treatment. The FT-IR spectrum of graphite (**Figure 4.10a**) did not show many prominent features apart from stretching bands at 3446 cm^{-1}, 2925/2852 cm^{-1} and 1627 cm^{-1}, corresponding to O-H, C-H and C=C stretching vibrations from adsorbed water molecules, alkyl groups (at the edges) and graphitic sp^2 hybridised networks, respectively. In contrast the FT-IR spectrum of GO (**Figure 4.10b**) displayed additional stretching bands at 3378 cm^{-1}, 1718 cm^{-1} and 1225 cm^{-1}, characteristic of hydroxyl, carbonyl/carboxylic acid and epoxide groups, respectively on the surface of the basal planes of graphite. The band at 3378 cm^{-1} was particularly broadened, due to the extremely hygroscopic nature of the GO sheets, as previously reported.[167, 168, 195-198]

Additional qualitative evidence for modification of the graphene sheets was obtained using ^{13}C magic angle spinning (MAS) NMR analysis (carried out by Jessica Martin), which was in good agreement with the XPS data. The ^{13}C MAS NMR spectrum (**Figure 4.11**) displayed three strong peaks at 60.8, 70.7 and 132.9 ppm, corresponding to epoxide (C-O-C), hydroxyl (C-OH) and sp^2-hybridised conjugated double bonds (C=C), respectively.[161, 162, 199] In addition a small peak at 31.1 ppm was observed, which is possibly a spinning sideband of the peak at 132.9 ppm, characteristic of aromatic carbon.[200] Unfortunately, ^{13}C MAS NMR could not be conducted on graphite powder, possibly due to the presence of trace ferromagnetic material in the synthetically-derived graphite starting material.

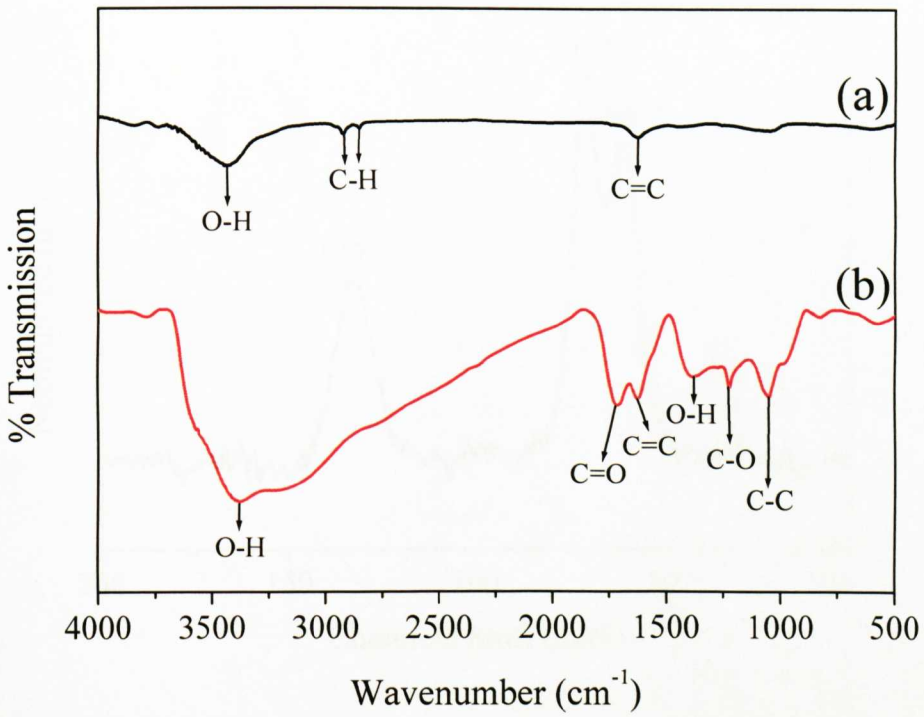

Figure 4.10 FT-IR spectrum of (a) graphite and (b) graphene oxide (GO)

Sample Peak Shift (cm^{-1})		Assignment
Graphite	**GO**	
3446	3378	O-H Stretch
2923/2852	2775 (broad)	C-H Stretch (alkyl)
-	1718	C=O Stretch (carbonyl)
1627	1624	C=C Stretch
1443	-	C-H Deformation (alkyl)
	1385	O-H Deformation
-	1225	C-O Stretch (epoxide/hydroxyl)
-	1052	C-C skeletal vibration
	831	Epoxide ring vibration

Table 4.3 Table showing the FT-IR peak assignments for graphite oxide.

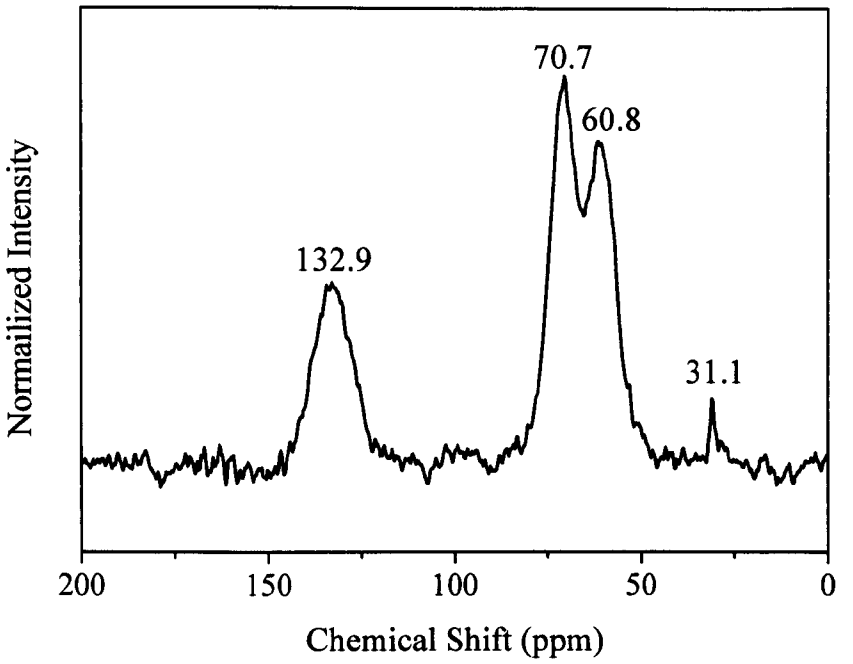

Figure 4.11 ^{13}C NMR spectrum of graphene oxide (GO), prepared via the Hummers route (carried out by Jessica Martin).

Chemical Shift (ppm)	Functional Group Assignment
132.9	Aromatic C=C
70.7	C-OH
60.8	C-O-C
31.1	Aromatic C=C sideband

Table 4.4 Table showing the C13 NMR peak assignments for graphite oxide.

4.4.2 Alternative Preparation of Graphene Oxide via the Staudenmaier Route

An alternative route to the formation of GO was followed, based on the Staudenmaier route.[159] This synthetic route involved treating graphite for a longer period of time (3-4 days) with a mixture of nitric acid, sulphuric acid and potassium chlorate. Unfortunately, this route proved to be extremely hazardous, with the combination of reagents exploding, during a repeat reaction, after 12-16 hours treatment. Furthermore as discussed herein, XPS data (**Figure 4.13**) suggests that oxidative treatment via this route was not as effective as following the modified-Hummers route. For these reasons, only limited characterisation data is included in this section, with the modified Hummers route followed instead, as a safer route to the high yield production of GO.

The morphological features of the GO sheets were not investigated in detail by TEM or AFM analysis. However, successful modification of the individual sheets of graphite was confirmed using PXRD analysis. The PXRD patterns of GO after 120 h treatment (**Figure 4.12**) showed a low angle (001) reflection at $2\theta = 13.6^{o}$, corresponding to an increased interlayer spacing of 0.650 nm. Furthermore, it is possible that higher order (002) and (003) reflections are present providing significant evidence for the formation of an ordered lamellar structure, comprising a stacked arrangement of oxidised graphene sheets. However this needs to be addressed with caution as the reflections at 26.4^{o} and 42.3^{o} are also consistent with the peak positions for the 002 and 100 reflections for graphite (**Table 4.5** in blue font).

Analysis of X-ray photoelectron spectroscopy (XPS) data of the hydrophilic exfoliated GO sheets, prepared via the Staudenmaier route, presented a relatively broadened carbon 1s spectrum that was deconvoluted into two peaks at binding energies of 284. 5 eV (45 %) and 286.4 eV (55 %) corresponding to the presence of aromatic sp^2 hybridised carbon atoms and carbon atoms attached to oxygen atoms in phenol (C-OH) and epoxide (C-O-C) functional groups (**Figure 4.13a**). The reduction in the percentage composition of aromatic carbon atoms, accompanying the oxidative treatment, was not as high as observed for GO

prepared via the Hummers route (**Figure 4.9b**), 45 %, in comparison with 16 %. This suggested that this oxidative route was not as effective as the modified Hummers-Offeman route, as suggested previously. Complimentary O 1s spectra of GO exhibited a broad band composed of a single peak at a binding energy of 532.3 nm, corresponding to the presence of phenol, epoxide and carbonyl oxygen atoms.[191, 192]

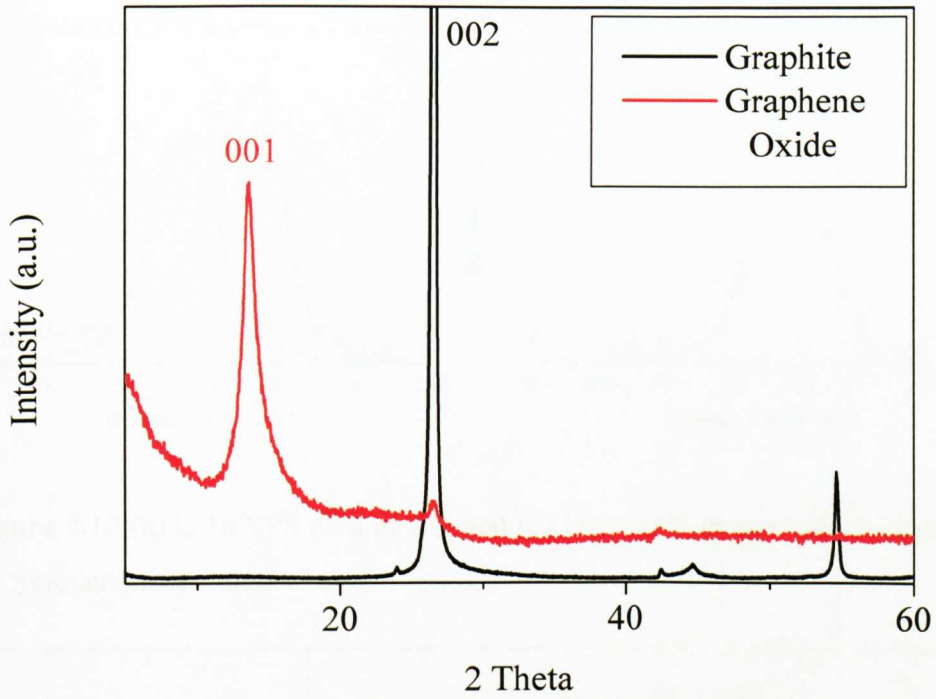

Figure 4.12 PXRD patterns of graphite and GO after 120 hours treatment, using the Staudenmaier Approach

Sample	2 Theta	d-spacing (nm)	hkl indices
Graphite	26.6	0.335	002
	42.5	0.213	100
	44.6	0.203	101
	54.6	0.168	004
Graphene Oxide (GO)	13.6	0.650	001
	26.4	0.337	002
	42.3	0.214	003

Table 4.5 Summary of 2 theta values, d-spacing and corresponding hkl indices for the peaks observed in the PXRD pattern of graphite and (GO) prepared via the Staudenmaier route.

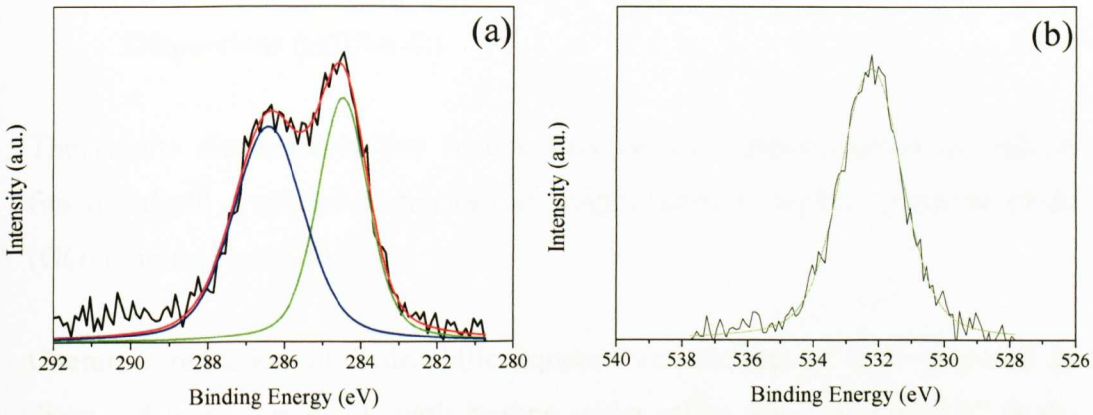

Figure 4.13 (a) C 1s XPS data of GO and (b) O 1s XPS data of GO prepared via the Staudenmaier route.

SAMPLE	**% Composition (Binding Energy (eV))**			
Graphene Literature Values[149, 193, 194]	C=C (284.6)	C-OH/ C-O-C (285.7/286.7)		C=O (288.0)
Graphite	81.3 (284.5)	11.4 (285.55)	5.6 (286.74)	1.7 (288.17)
Graphene Oxide (Staudenmaier)	44.8 (284.5)	55.2 (286.4)		No observable peak

Table 4.6 Summary of percentage composition of functional groups in C 1s XPS of graphite and GO prepared via the Staudenmaier route with their associated peak positions in brackets.

4.4.3 Single-Stranded Deoxyribonucleic Acid Stabilised Graphene Dispersions (ssDNA-G)

The results discussed in this section involve the characterisation of ssDNA functionalised graphene dispersions at weight ratios of ssDNA:graphene oxide (GO) ranging from 1 to 33.

Chemical reduction of hydrophilic aqueous suspensions of GO, prepared as discussed in section 4.4.1, with heating under reflux for 1 h at 100 °C in the presence of hydrazine and freshly prepared single-stranded DNA (ssDNA, from salmon testes, concentration varied from 1-33 $mgmL^{-1}$), resulted in the formation of stable black sols. Samples were subsequently dialysed for 24-48 h to remove excess hydrazine and ssDNA (**Figure 4.14a**). An optimum hydrazine:graphene oxide weight ratio of 0.7 was chosen, based on previous work by the Wallace group which showed that increasing concentrations of hydrazine resulted in a decrease in the stability of the graphene-based dispersions.[166] The hydrophilic nature of the ssDNA-stabilised graphene dispersions was confirmed by zeta potential analysis which demonstrated that the surface charge of the functionalised graphene sheets measured -3, -13 and -41 mV for GO: ssDNA weight ratios of 1:2, 1:4 and 1:33, respectively. Significantly, the black sols were observed to be stable to sedimentation for several months.

Reduction in the presence of double-stranded DNA (dsDNA) demonstrated the formation of partially stable aqueous sols possibly due to base-pair disruption during heating at 100°C. In comparison, control experiments involving the chemical reduction of GO, under the same conditions in the absence of ssDNA or dsDNA, resulted in the formation of black sols containing aggregated particles, which could not be further stabilised post-synthetically by the addition of either double-or single-stranded DNA (**Figure 4.14b**).

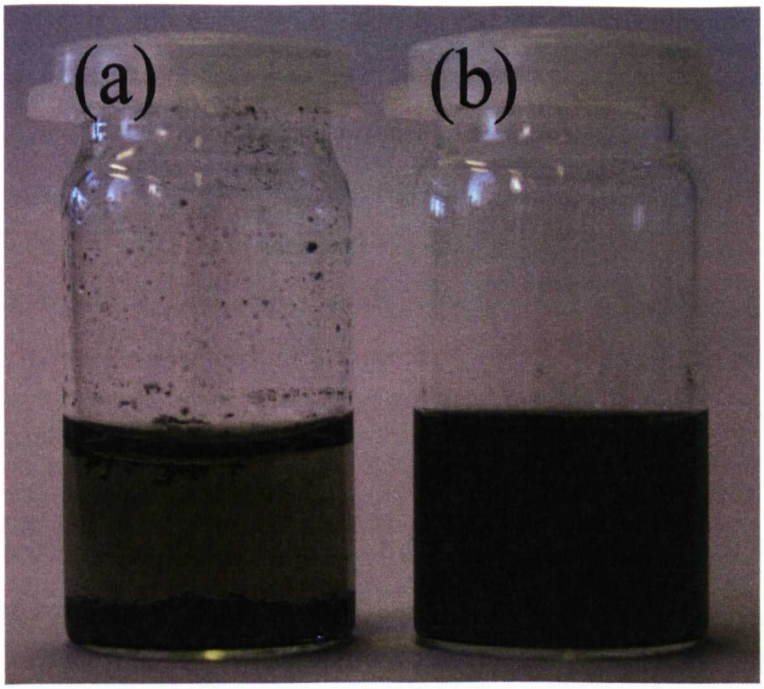

Figure 4.14 Photographic images showing (a) an aggregated sol of reduced GO, in the absence of ssDNA and (b) a ssDNA stabilised graphene sol, after reduction of GO with hydrazine (ssDNA: graphene wt. ratio = 2), left for 2 months on the bench.

Transmission electron microscopy (TEM) images of ssDNA stabilised graphene dispersions (wt. ratio ssDNA:graphene = 2) revealed similarly ultra-thin sheets, with a high level of transparency as observed for GO, ranging from 100 nm to up to 5-10 μm in lateral dimensions. Importantly EDX analysis, conducted on individual sheets of ssDNA-G showed the presence of phosphorus which is solely associated with DNA (shown inset, **Figure 4.15c**), therefore confirming the presence of single-stranded DNA on the surface of the graphene sheets (**Figure 4.15**). TEM images of ssDNA: graphene dispersions, prepared at a higher ssDNA:graphene ratio of 20, presented similarly highly transparent overlapping sheets containing curled and folded edges (**Figure 4.16**).

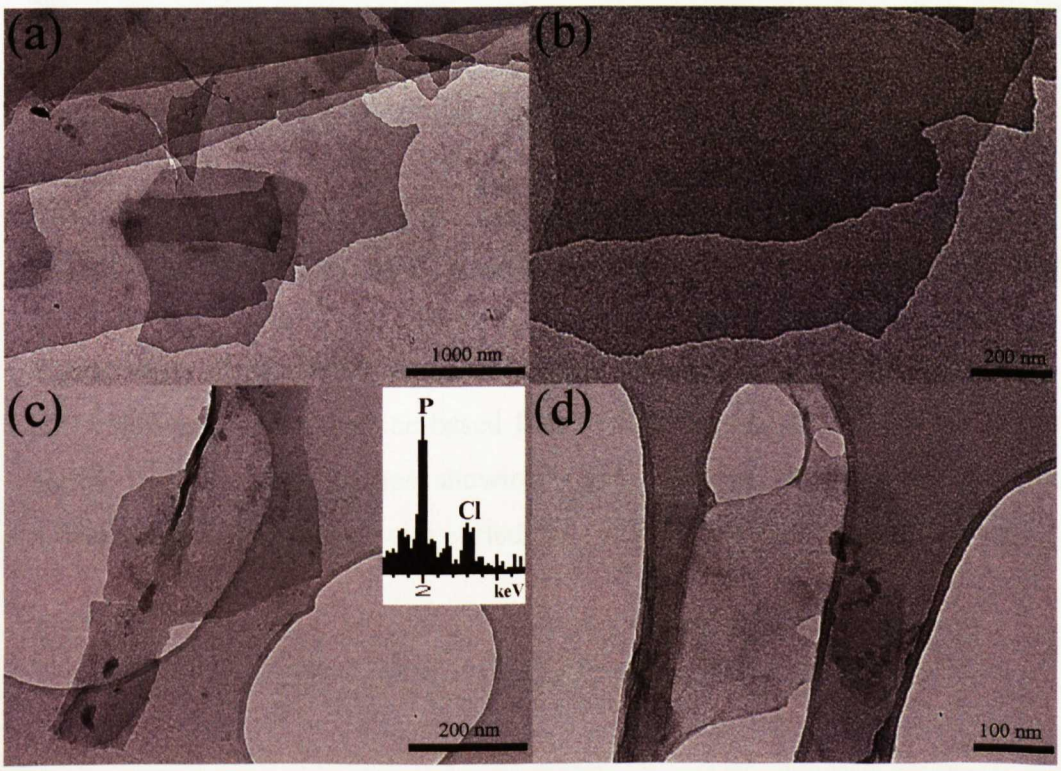

Figure 4.15 TEM images of exfoliated ssDNA-graphene dispersions (Ratio = 2:1) showing (a) overlapping multi-layers of different geometric shapes, (b) 2 sheets overlapping each other, (c) a single sheet on a holey grid, showing a curled edge, with EDX analysis shown inset and (d) a single sheet on a holey grid, demonstrating a high-transparency.

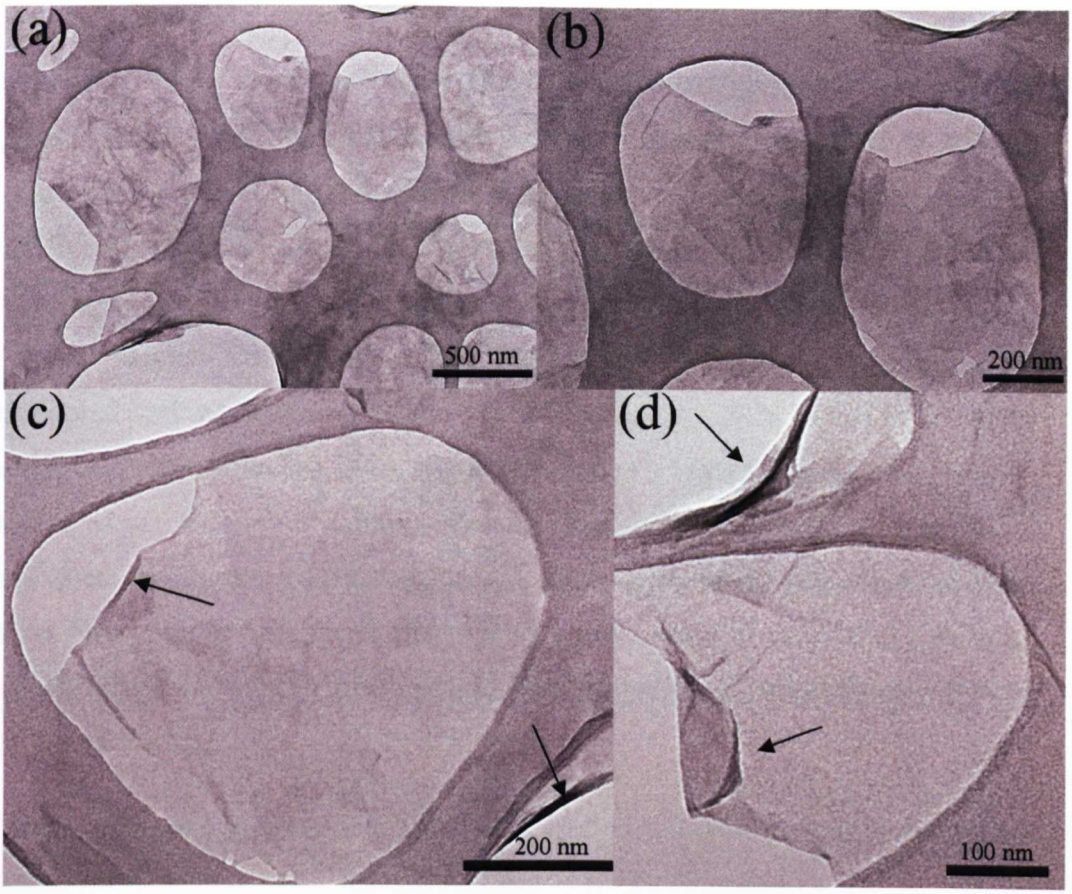

Figure 4.16 TEM images of exfoliated ssDNA-graphene dispersions (Ratio = 20:1) showing (a) a graphene-based film of overlapping sheets, (b), (c) and (d) higher magnification images showing highly transparent ultra-thin sheets of different geometric shapes with curled and folded edges (shown with arrows).

Tapping mode AFM studies on ssDNA-graphene dispersions, (ratio of ssDNA: graphene = 33:1), dried on freshly cleaved mica substrates, indicated that the apparent height of the sheets measured between 2.1 and 2.7 nm, with an average height of 2.4 nm (**Figure 4.17a-b**). The height of the graphene sheets was significantly greater than the theoretical thickness of individual graphene sheets/layers (0.35 nm) and slightly greater than the thickness of GO layers (Average height= 1.8 nm, **Figure 4.7**). Furthermore, the sheets appeared to show substantial surface roughness but no strand-like features, as observed in the AFM image of double-stranded DNA (figure not shown), suggesting that the ssDNA molecules are forming secondary globular structures (molecular thickness = 1 nm) when adsorbing on the atomically thick graphene sheets. Additional analysis of ssDNA-stabilised graphene sheets with a lower content of ssDNA, (ratio of ssDNA: graphene = 2:1) showed a similar height profile of approximately 2.7 nm (**Figure 4.17c-d**).

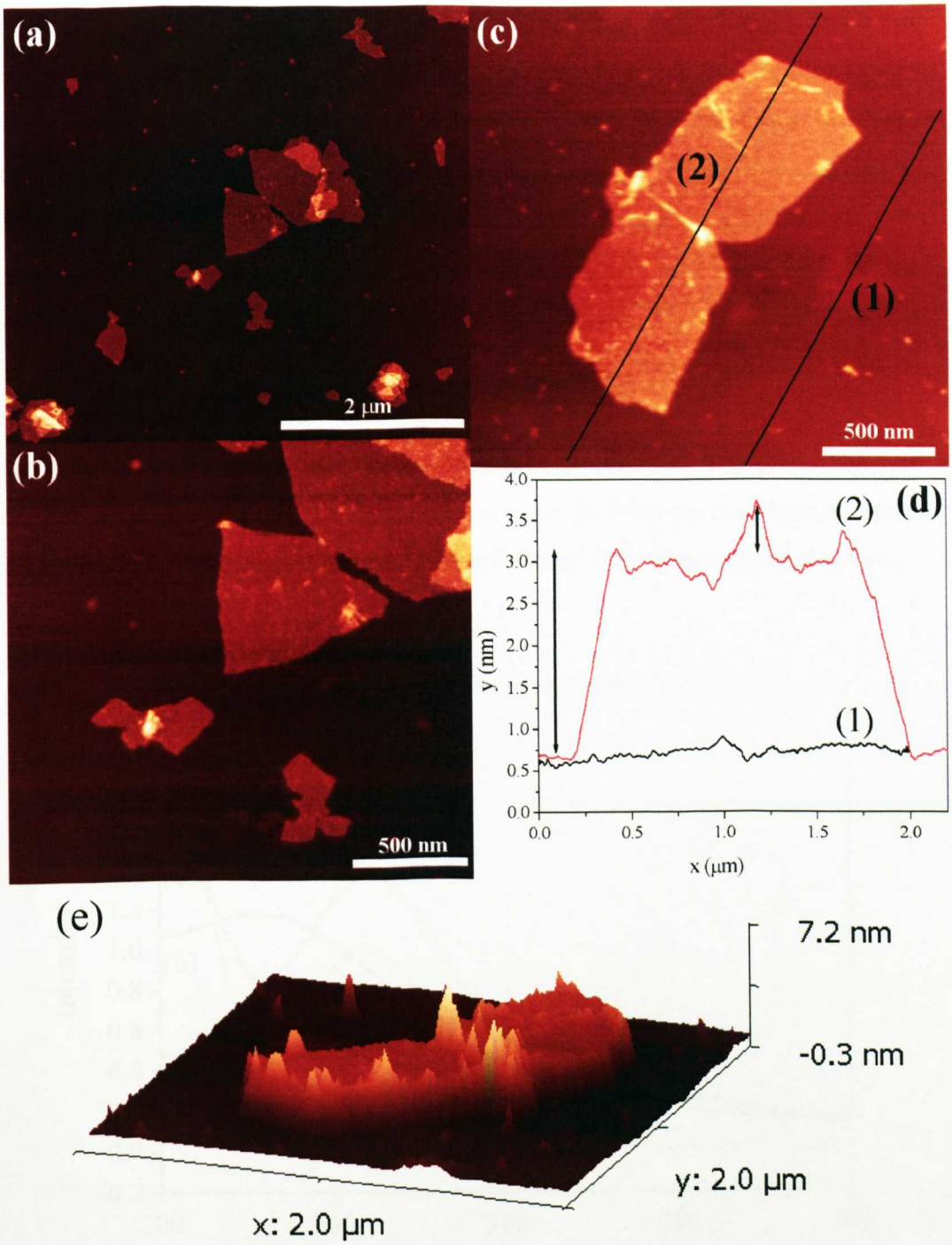

Figure 4.17 Tapping mode AFM data of ssDNA-stabilised graphene dispersions, dried on freshly cleaved mica at a ssDNA: graphene wt. ratio of (a-b) 33:1 and (c) 2:1, with (d) associated height profile showing an initial step onto the ssDNA-graphene sheet of 2-2.5 nm and a smaller step corresponding to a curled edge, measuring 0.5-1 nm and (e) corresponding three-dimensional profile.

Restoration of electronic conjugation in the chemically reduced ssDNA-graphene dispersions was consistent with UV-Vis spectroscopy measurements (**Figure 4.18**). In the case of GO, a typical absorption band at 231 nm was observed, corresponding to the π-π^* transitions of aromatic C-C bonds which bathochromically shifts (redshifts) to a band at 266 nm, after treatment with hydrazine due to the re-formation of conjugated C-C sp^2 hybridised bonds, present in graphene.[166] The UV-Vis spectrum for ssDNA-stabilised graphene dispersions did not present a feature at 231 nm but instead displayed a broad band at 258 nm suggesting that significant reduction of the GO sheets had occurred. This feature is considerable masked by the ssDNA absorption centre at 258 nm making it difficult to ascertain the exact position of the graphitic band and subsequently the degree of restoration of the sp^2 hybridised carbon network.

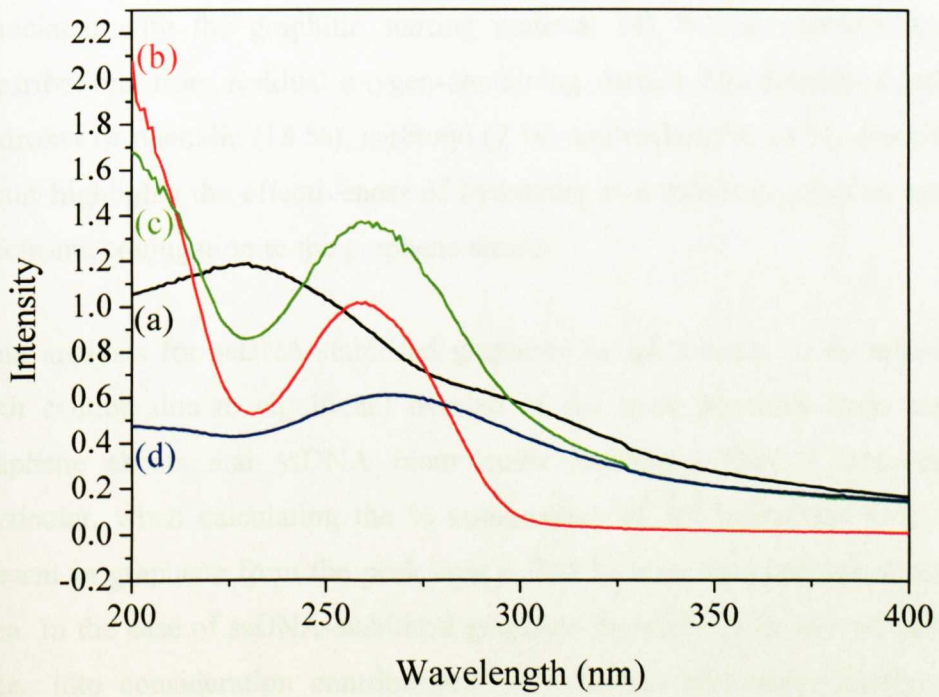

Figure 4.18 UV-Vis spectroscopy showing (a) GO, (b) single-stranded DNA (ssDNA), (c) ssDNA-graphene and (d) reduced graphene oxide, in the absence of DNA (control).

X-ray photoelectron spectroscopy (XPS) enabled detailed structural and compositional analysis of ssDNA stabilised graphene dispersions, providing information about the type and extent of surface functionalisation present in addition to the degree of restoration of sp^2 hybridised C=C bonds after reduction with hydrazine. All C 1s XPS data is summarised in **Table 4.7**.

As discussed previously, in section 4.4.1, C 1s XPS of graphene oxide (**Figure 4.9**) demonstrated a reduction in the abundance of aromatic carbon groups (C=C, 284. 6, 16 %) and a corresponding increase in the abundance of a range of surface functionalities, including phenol, epoxide, carbonyl and carboxylic groups, as a result of oxidative treatment. In comparison, C 1s XPS data for the chemically reduced GO control sample, prepared in the absence of ssDNA (**Figure 4.19b**), showed considerable restoration of the aromatic sp^2 hybridised carbon atoms (C=C, 284.6 eV, 70 %), 10 % lower that than the aromaticity associated with the graphitic starting material (81 %), in addition to small contributions from residual oxygen-containing surface functionalities including hydroxyl or phenolic (18 %), carbonyl (7 %) and carboxylic (4 %) groups. This result highlights the effectiveness of hydrazine as a reducing agent in restoring electronic conjugation to the graphene sheets.

Data analysis for ssDNA-stabilised graphene samples needs to be approached with caution due to significant overlap of the peak positions from both the graphene sheets and ssDNA biomolecule stabiliser. This is important, in particular, when calculating the % composition of sp^2 hybridised C=C bonds present in graphene from the peak area at 284.5 eV as a percentage of the total area. In the case of ssDNA-stabilised graphene dispersions the overall peak area takes into consideration contributions from carbon containing functionalities present in both graphene and ssDNA, which means direct comparisons with data obtained for reduced graphene oxide control sample cannot be made.

C 1s XPS of ssDNA (**Figure 4.19a**) presented peaks at 284.78 eV (47.1 %), 286.21 eV (30.7 %), 287.38 eV (16.6 %) and 288.53 eV (5.6 %) attributed to carbon functionalities present in the backbone sugar residues and the nucleic bases (see **Table 4.8** for data analysis). Comparable studies conducted on

ssDNA-graphene dispersions (weight ratio G: ssDNA = 1:2) showed a similarly broaden peak (**Figure 4.19c-d**). Deconvolution of the peak area presented peaks at 284.78 (60 %), 286.28 (23.4 %), 287.59 (11.5 %) and 289.08 (5.1 %), corresponding to significant restoration of the C=C aromatic network with additional contributions from functional groups present in DNA (amide/urea functionalities) and residual oxygen-containing groups on the basal planes of the graphene sheets.

Furthermore, oxygen 1s, nitrogen 1s and phosphorus 2p XPS data, provided additional evidence for the presence of ssDNA biomolecules on the surface of the graphene sheets. The O 1s spectra presented a broadened peak, with contributions from oxygen containing functionalities present in the sugar residues and bases from ssDNA as well as residual groups on the graphene sheets (**Figure 4.20**, **Table 4.8**). Additional N 1s and P 2p XPS data (**Figure 4.19e-f**) presented peaks at 400 eV and 133.8 eV, respectively, corresponding to amide, amine and aromatic nitrogen functionalities originating from the DNA base pairs and phosphate groups (P-O) on the DNA backbone.[201]

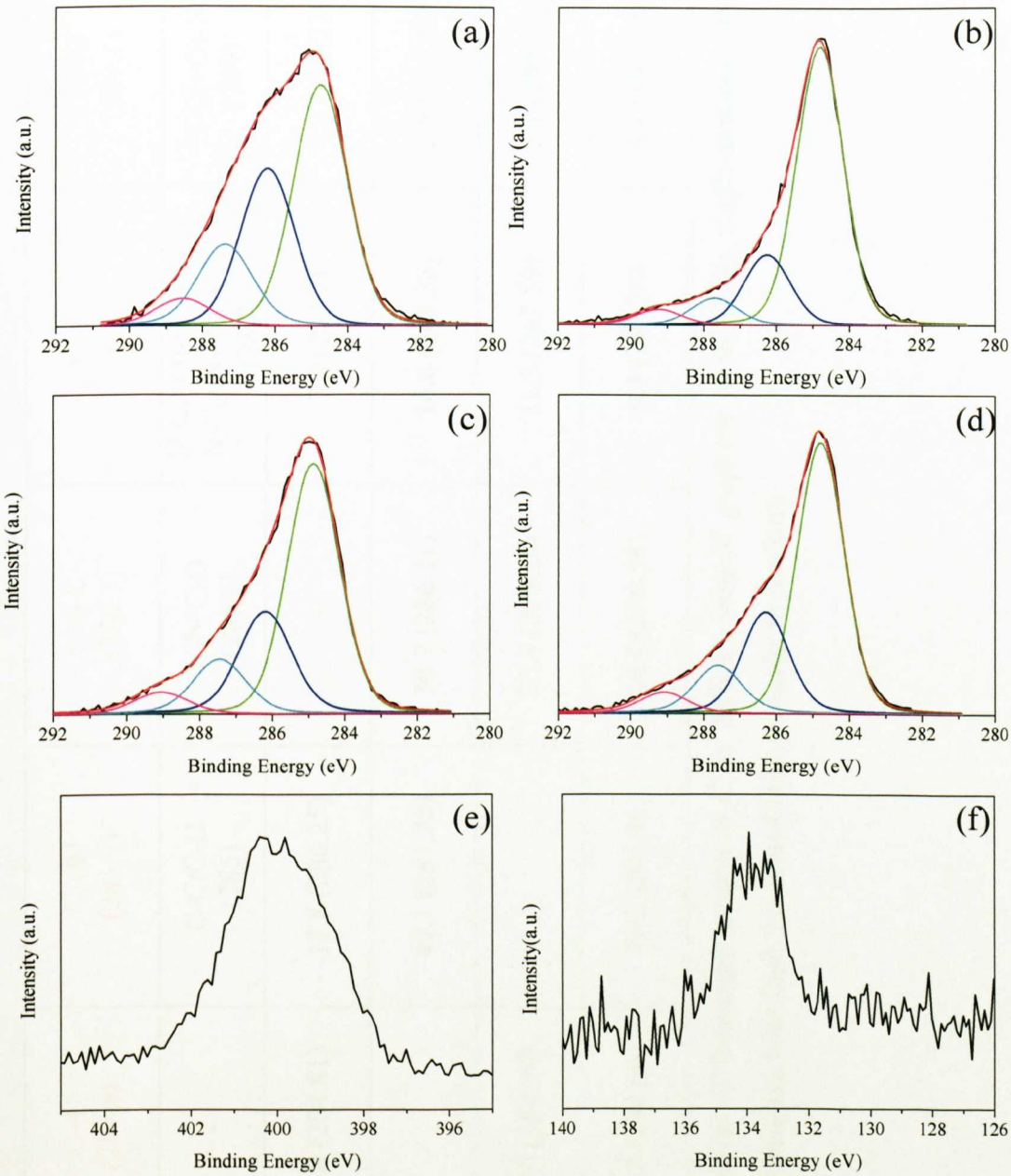

Figure 4.19 C 1s XPS profiles of (a) single-stranded DNA, (b) chemically reduced GO prepared in the absence of ssDNA, (c) ssDNA-stabilised graphene dispersions (wt. ratio ssDNA:G = 4) and (d-f) XPS profiles for ssDNA graphene dispersions (wt. ratio ssDNA:G = 2) ; (d) C 1s (e) N 1s and (f) P 2p.

SAMPLE	Binding Energy (eV)	% Composition				
	Graphene[149, 191, 193]	C=C (284.6)	C-OH (285.7)	C-O-C (286.7)	C=O (288.0)	C(O)O (289.1)
	DNA[201]	-	C-C/C-H (285)	C-N/C-O (286.5)	N-C(=O)-C/ N-C-O/ N-C(=N)-N/ N=C-N (288)	N-C(=O)-N (289)
Reduced Graphene Oxide (no DNA)		70.8 (284.81)	17.8 (286.25)	-	7.2 (287.7)	4.2 (289.22)
Single-stranded DNA			47.1 (284.75)	30.7 (286.21)	16.6 (287.38)	5.6 (288.53)
G-DNA (1:2)		60.0 (284.78)	-	23.4 (286.28)	11.5 (287.59)	5.1 (289.08)
G-DNA (1:4)		37.5 (284.64)	30.2 (285.46)	18.4 (286.58)	9.4 (287.74)	4.4 (289.16)

Table 4.7 Summary of percentage composition of functional groups in C 1s XPS of reduced graphene oxide (GO), single-stranded DNA (ssDNA) and ssDNA-stabilised graphene dispersions, with their associated peak positions in brackets.

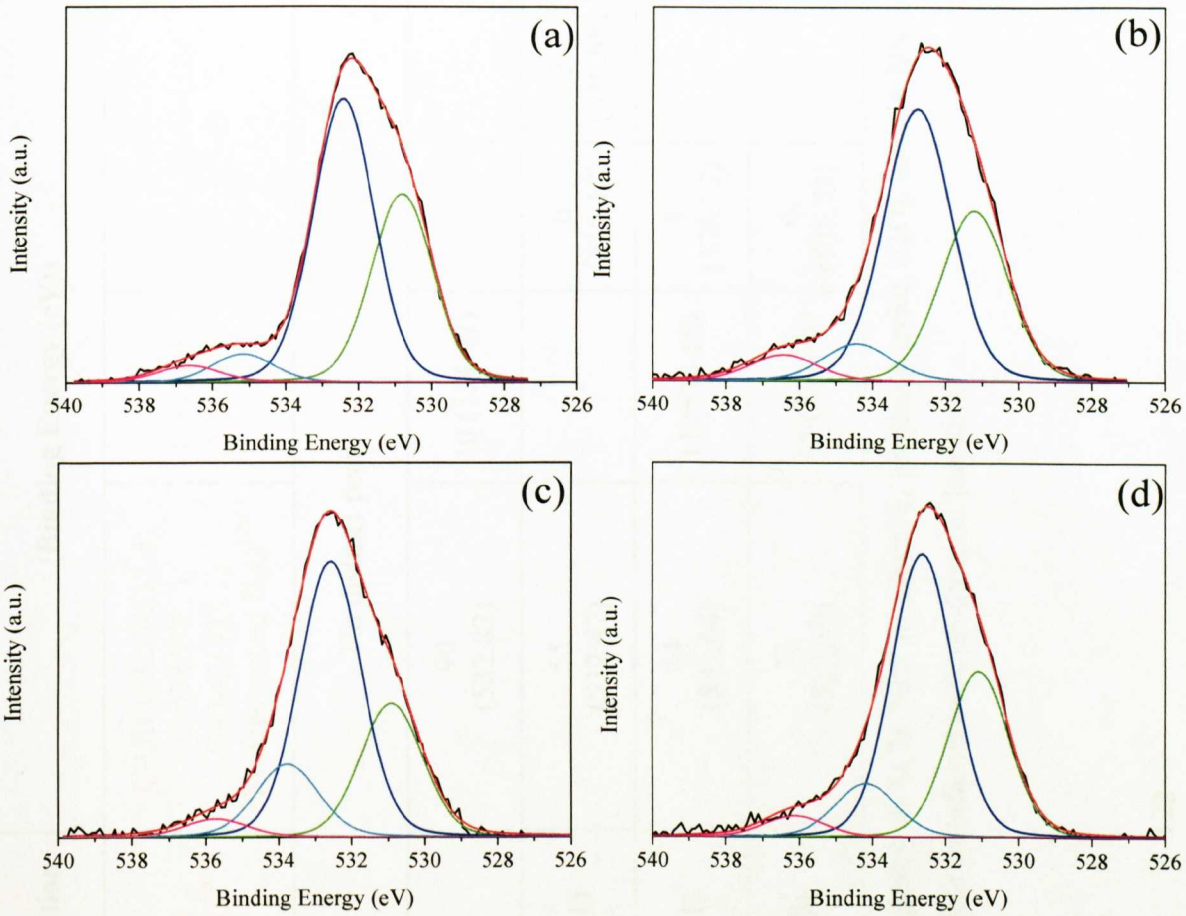

Figure 4.20 O 1s XPS profiles of (a) single-stranded DNA, (b) chemically reduced GO prepared in the absence of ssDNA and ssDNA-stabilised graphene dispersions at ssDNA:graphene wt. ratios of (c) 4 and (d) 2.

SAMPLE	% Composition	(Binding Energy (eV))			
Graphene Literature Values	C(O)NH (531.4-532.0)[202]	C-OH (532.9-533.6), C=O (532.3), C-O-C (533.1), Physioadsorbed H_2O[192]	C(O)-OH (534.2)[191]	Charged O-H or C=O	
Graphite	No distinct peak				
Graphene Oxide	-	90 (532.82)	10 (534.47)	-	-
Control DNA	36 (530.81)	55 (532.42)	-	6 (535.18)	3 (536.65)
ssDNA-G (2:1)	31 (531.11)	54 (532.64)	11 (534.16)	4 (536.17)	-
ssDNA-G (4:1)	27 (530.92)	55 (532.59)	15 (533.78)	4 (535.73)	-

Table 4.8 Summary of percentage composition of functional groups in O 1s XPS of graphite, graphene oxide (GO), control DNA, ssDNA-graphene films at a ssDNA: graphene wt. ratio of 2 and 4, with their associated peak positions in brackets.

Fourier-Transform Infra-red spectroscopy (FT-IR) provided further qualitative evidence for the functionalisation of graphene sheets with ssDNA. The FT-IR spectrum of GO, as discussed previously (**Figure 4.21b**) presented stretching bands at 3378 cm^{-1}, 1718 cm^{-1} and 1225 cm^{-1}, characteristic of hydroxyl, carbonyl, carboxylic acid and epoxide groups. In comparison, the FT-IR spectrum of dried, graphene oxide reduced in the presence of no stabilising agent (**Figure 4.21a**), showed features from aromatic and residual, saturated cyclic carbon atoms (1630 cm^{-1}, C=C str.; 1054 cm^{-1}, C-C skeletal ring vibration) in addition to residual oxygen-containing defects and adsorbed water molecules on the graphene sheets, at lower intensities (3440 cm^{-1}, O-H str.; 1451 cm^{-1}, O-H def.). The FT-IR spectrum of ssDNA-stabilised graphene films displayed, in addition to these peaks, vibrational structures originating from DNA molecules, providing significant evidence for the association of ssDNA with graphene sheets (**Figure 4.21b-c, Table 4.9**).

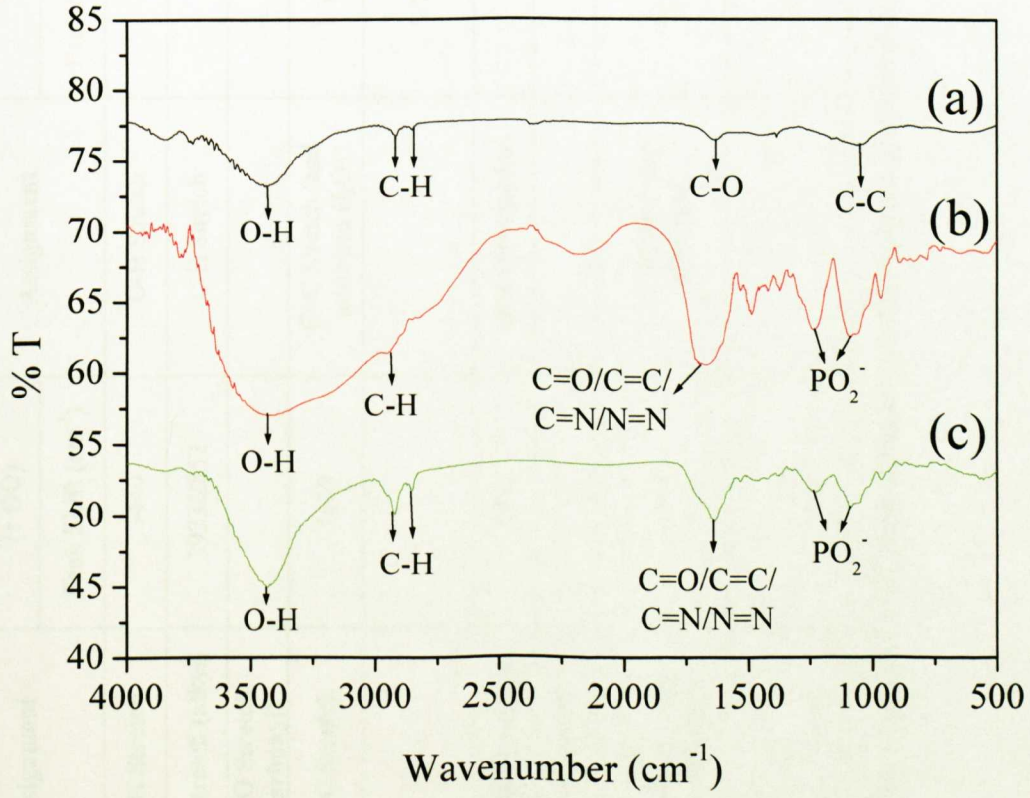

Figure 4.21 FT-IR spectrum of (a) reduced graphene oxide in the absence of DNA (rGO, control) (b) salmon testes DNA (control) and (c) ssDNA-graphene films.

GO	Assignment	Reduced GO (r GO)	Assignment	DNA	Assignment	ssDNA-Graphene (5:1)	Assignment
Peak Shift (cm^{-1})		Peak Shift (cm^{-1})		Peak Shift (cm^{-1})		Peak Shift (cm^{-1})	
3378	O-H Stretch	3440	O-H Stretch	3429	O-H Stretch	3429	O-H Stretch
2775 (broad)	C-H Stretch (alkyl)	2923/2852	C-H Stretch	-	-	2918/2852	C-H Stretch
1718	C=O Stretch (carbonyl)	-	-	2187	NH^+ Stretch	2060	NH^+ Stretch
1624	C=C Stretch	1630	C=C Stretch (and adsorbed H_2O)	1668/1528	C=O/C=C/C=N/N=N Stretch	1635/1531	C=O/C=C/C=N/N=N Stretch
-	-	-	-	1484/1418	Base deformations coupled with the sugar vibrations	1465/1421	Base deformations coupled with the sugar vibrations
1385	O-H Deformation	1451	O-H Deformation	1372	O-H Deformation	1377	O-H Deformation
1225	C-O Stretch	-	-	-	-	-	-
1052/831	C-C Skeletal/epoxide ring vibrations	1054	C-C skeletal ring vibrations	1232/1089	PO_2^- bands including: ν_{as} (PO_2^-)/ν_s (PO_2^-)	1232/1086	PO_2^- bands including: ν_{as} (PO_2^-)/ν_s (PO_2^-)
-	-	-	-	1062/963	Vibrations of the sugar-phosphate backbone	1054/1015/963	Vibrations of the sugar-phosphate backbone

Table 4.9 Table showing the FT-IR peak assignments for reduced graphite oxide (r GO), DNA from salmon testes and ssDNA-graphene films.

4.4.4 Mechanistic Discussion of the Interaction of ssDNA with Individual Graphene Sheets

The data discussed in the previous results section provided considerable evidence for the association of single-stranded DNA with graphene sheets, resulting in their stabilisation in aqueous solutions. This section includes mechanistic discussion about how and why this interaction occurs.

The well known double-helical structure of double-stranded DNA occurs as a result of the hydrogen bonding base-pair interactions between complimentary nucleobase pairs on individual polymer strands of DNA. It is well reported that thermal treatment of a solution of double-stranded DNA, above the characteristic melting or denaturisation temperature, results in disruption of the base-pair interactions and causes the DNA double strand to unwind into separated, single strands of DNA, which are arranged in random conformations, (**Figure 4.22**).[179]

In the case of the research discussed in this chapter, denaturisation of dsDNA resulted in exposure of the aromatic nucleotide bases to the graphene oxide sheets. Reduction of GO in the presence of ssDNA, enabled restoration of the carbon sp^2 hybridised network, in addition to interaction of the ssDNA polymer strands with the reduced graphene sheets, enabling their separation and resultant stabilisation. The ssDNA-stabilised graphene sheets were shown to be highly hydrophilic as confirmed by zeta potential surface charge measurements, with an increase in anionic behaviour occurring as the concentration of DNA is increased. TEM and AFM analysis provided evidence for the ultra-thin, transparent nature of the sheets, with EDX analysis confirming the presence of ssDNA on the surface on the sheets due to the presence of a phosphorus K_α peak at 2.0134 KeV.

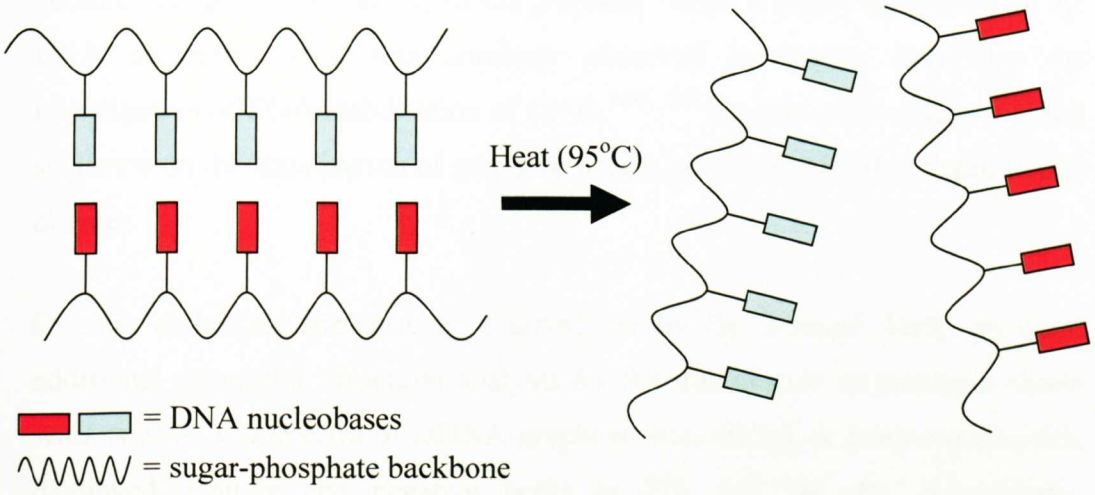

Figure 4.22 Schematic demonstrating DNA denaturisation, as a result of the thermal disruption of the base-pairing in dsDNA (left hand side) to form randomly arranged individual strands of ssDNA.

These observations suggest that ssDNA strands interact predominantly through hydrophobic (π stacking) in addition to weak electrostatic/hydrogen bonding interactions between the primary amines associated with the base pairs and the residual carboxylic and phenolic groups associated with the planes of the graphene surfaces, allowing the anionically charged/polar moities on the sugar-phosphate backbone to be orientated at the periphery towards the solvent. This model is reinforced by similar experiments involving the reduction of GO in the presence of dsDNA, which resulted in the formation of less stable graphene sols, due to the unavailability of the base pairs for π-π stacking interactions with the graphene sheets.

This mechanism is similarly observed in the case of ssDNA stabilization of CNTs, where the DNA strands wrap the surface of the CNTs in a helical fashion, due to the flexibility of the sugar-phosphate DNA backbone.[181] In the case of graphene, the flattened morphology of the sheets means the ssDNA strands cannot wrap helically but instead forms secondary structures in the form of globules of DNA which coat the surface of the graphene sheets. Similar experiments using, DNA derived from herring testes, composed of a different DNA sequence, did not appear to stabilise graphene sheets in the same manner,

demonstrating that the stability of the graphene sheets is highly dependent on the DNA sequence. This was similarly observed in studies involving the investigation of DNA stabilisation of CNTs.[180, 181] Studies of the effect of DNA sequence on the stabilisation of graphene sheets were not studied in detail in this chapter.

Circular dichroism spectroscopy (carried out by Dr. Avinash Patil) provided additional supporting structural analysis for the stabilisation of graphene sheets with ssDNA. CD spectra of ssDNA-graphene dispersions, at room temperature, displayed positive and negative peaks at 276 and 249 nm, respectively, characteristic of ssDNA **(Figure 4.23).** Importantly no evidence was provided for the presence of dsDNA, which should display CD bands at 275 and 247 nm (cross-over point 258 nm).[203] These observations provided strong evidence, firstly, for the stabilisation of graphene sheets with helical ssDNA strands during the reduction process of GO at high temperature and secondly, for the inhibition of re-hybridisation of ssDNA as a result of the disruption of base-pairing interactions.

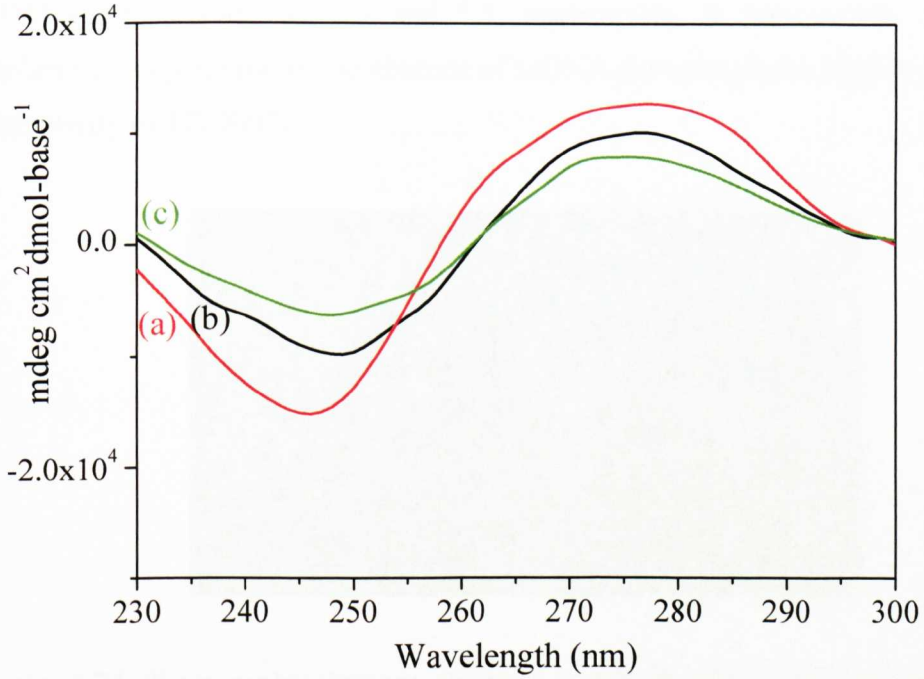

Figure 4.23 Circular dichroism (C-D) spectra of (a) double-stranded DNA (dsDNA), (b) single-stranded DNA (ssDNA) and (c) ssDNA-stabilised graphene sheets (carried out by Dr. Avinash Patil).

4.4.5 Self-Assembly of ssDNA-Graphene Dispersions to form Lamellar Nanocomposite Films

The generation of graphene-based films is predicted to be highly applicable in solar cells and electronic devices fabrication owing to their exceptional electrical, mechanical and thermal properties. In particular, solution processing of reduced graphene sheets, using spin coating techniques, has been shown to be highly attractive for the development of large-area films.[204] This section investigates the ability to effectively process aqueous graphene dispersions into electrical conductive films using relatively simple techniques, as follows.

Aqueous dispersions of ssDNA-stabilised graphene sheets were processed using either vacuum filtration or evaporation-induced assembly techniques resulting in the formation of free-standing, self-supported graphene-based nanocomposite films (**Figure 4.24a**). Preliminary testing of their electrical conductivity, using the Van der Pauw, four probe technique demonstrated that the conductivity of ssDNA-graphene films, prepared via drop-casting ranged from 4.76-104 Sm^{-1} for

ssDNA:graphene ratios of 2:1 and 5:1, respectively. In comparison, control graphene films prepared in the absence of ssDNA demonstrated a slightly higher conductivity of 172 Sm^{-1}.

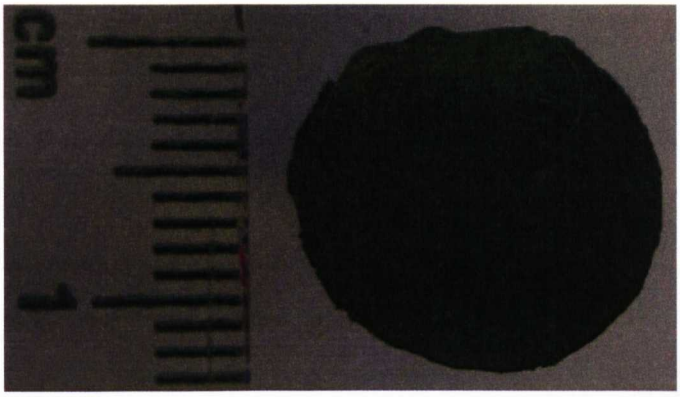

Figure 4.24 Photographic images showing a self-supported ssDNA-graphene lamellar nanocomposite film obtained via evaporation-induced assembly of the dispersed sheets on a silicon wafer substrate (ssDNA: graphene ratio of 5:1).

Powder X-ray diffraction (PXRD) provided conclusive evidence for structural changes associated with the effective stacking of ssDNA-graphene dispersions, prepared via evaporation-induced assembly on silicon wafer substrates. The diffraction pattern of GO films, as discussed previously in section 4.4.1, gave rise to a strong, single reflection at $2\theta = 11.65$, that corresponded to an interlayer d_{001} spacing of 0.759 nm (**Figure 4.8, Table 1.1**). In comparison, thin nanocomposite films of ssDNA-graphene dispersions, at various ssDNA: graphene weight ratios, presented lower angle reflections, ranging from 5.86° (ssDNA: graphene wt. ratio = 1:1) to 6.62° (ssDNA: graphene wt. ratio = 20:1) corresponding to expanded interlayer d_{001} spacings ranging from 1.51 to 1.33 nm (**Figure 4.25**). Despite the significant broadening of the d_{001} reflection, in comparison to that observed for the GO film, the presence of higher order d_{002}, d_{003} and d_{004} peaks, (see **Table 4.10** for peak positions) provided significant evidence for the formation of an ordered lamellar nanostructure, comprising a stacked arrangement of graphene sheets, intercalated with a monolayer of surface adsorbed ssDNA molecules.

Increases in ssDNA concentration did not appear to significantly affect the interlayer spacing, suggesting that ssDNA is not re-hybridising to form dsDNA.

Furthermore, analysis of aggregated black particles produced by the reduction of GO in the absence of ssDNA biomolecules, gave rise to a single, sharp reflection at $2\theta = 28.35^{\circ}$, corresponding to an interlayer spacing of 0.315 nm, consistent with the reformation of graphitic-based nanoparticulate material. These observations indicate that the formation of graphene-based nanocomposite films is facilitated by biomolecule-induced stabilisation of the individual graphene sheets. Aggregation of the graphene sheets is prevented by the intercalation of single-stranded DNA.

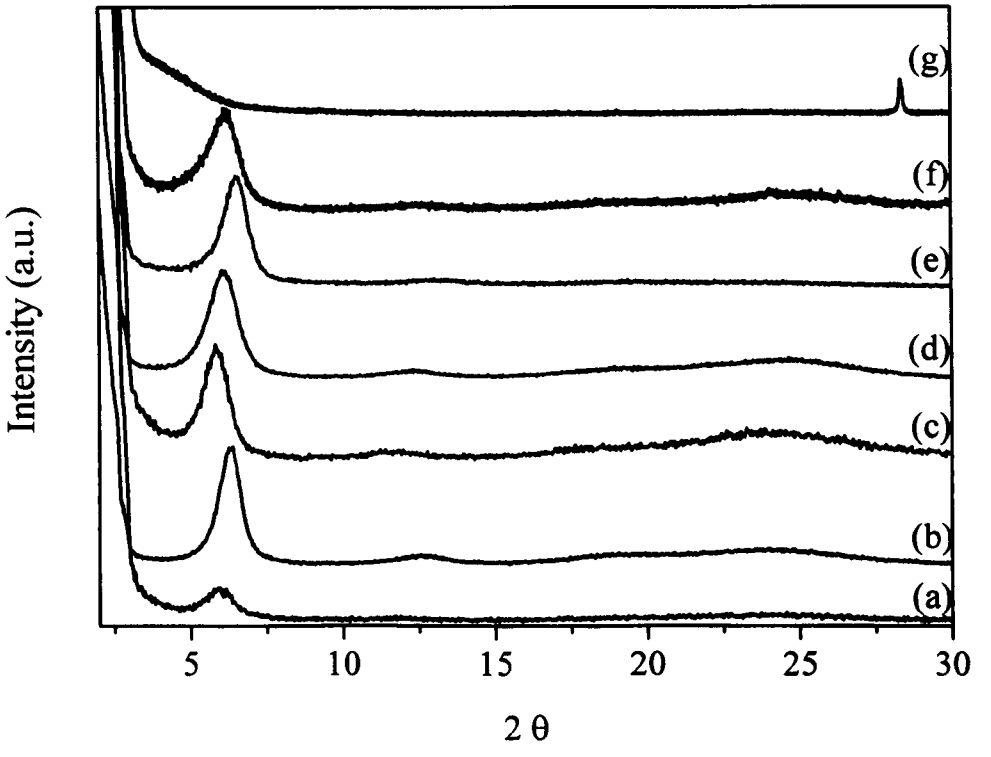

Figure 4.25 PXRD pattern of evaporation-induced assembled films of ssDNA stabilised graphene dispersions at various ssDNA: graphene weight ratios as follows: (a) 1:1, (b) 2:1, (c) 5:1, (d) 10:1, (e) 20:1, (f) 33:1 and (g) reduced GO.

Ratio ssDNA:G	2 θ	d-spacing (nm)	hkl indices	Ratio ssDNA:G	2 θ	d-spacing (nm)	hkl indices
1:1	5.86	1.51	001	10:1	6.08	1.45	001
	11.36	0.78	002		12.35	0.72	002
	19.73	0.45	003		19.00	0.47	003
	23.95	0.37	004		24.50	0.36	004
2:1	6.32	1.40	001	20:1	6.62	1.33	001
	12.59	0.70	002		13.35	0.66	002
	18.95	0.47	003		20.00	0.44	003
	23.93	0.37	004		23.92	0.37	004
5:1	5.84	1.51	001	33:1	6.15	1.44	001
	11.58	0.76	002		12.44	0.71	002
	17.75	0.50	003		18.51	0.48	003
	23.88	0.37	004		24.11	0.37	004

Table 4.10 Table showing the PXRD peak assignments for ssDNA-stabilised graphene films and reduced graphene oxide in the absence of ssDNA.

4.4.6 Co-Intercalation of Proteins to Form Graphene Bio-Nanocomposites

The preparation of bio-inorganic nanocomposites has become an emerging area of interest due to the generation of hybrid materials with advanced and versatile applications.[13] In particular, as discussed in chapter 1, the intercalation of biomolecules in layered materials has generated hybrid nanocomposites with a wide range of applications in biosensor devices and non-viral vectors in gene therapy.[4] The work discussed in this section investigates the possibility of effectively co-intercalating cationic biomolecules in the gallery regions of ssDNA-stabilised graphene sheets.

As discussed previously, the as-synthesised ssDNA-graphene dispersions consisted of anionically charged graphene sheets, functionalised with single-stranded DNA biomolecules. The high negativity of the functionalised graphene sheets enabled them to be further assembled in the presence of oppositely charged species. Slow addition of graphene sols containing negatively charged ssDNA-stabilised graphene sheets to positively charged protein solutions, resulted in sedimentation, not observed in the absence of the cationic protein. Two different cationic proteins were investigated including the metallo redox protein ferri-cytochrome *c* (ferri-cyt *c*, zeta potential = + 24.49 mV) and lysozyme (zeta potential = + 46.24 mV). Self-assembly of both the anionically charged ssDNA-coated graphene sheets and the cationic metallo protein ferri-cytochrome *c* (ferri-cyt *c*), occurred slowly (24-48 h) due to charge neutralisation. Addition of lysozyme, on the other hand, resulted in slightly quicker sedimentation (within 24 h) due to the higher surface charge density of the protein.

Powder X-ray diffraction (PXRD) provided conclusive evidence for the spontaneous assembly of cationic proteins and ssDNA molecules to effectively produce a stacked array of graphene sheets and biomolecules. The diffraction pattern of graphene oxide and ssDNA-graphene (wt. ratio = 2:1) films, as discussed previously in sections 4.4.1 and 4.4.5 gave rise to single reflections corresponding to interlayer d_{001} basal spacings of 0.759 and 1.40 nm, respectively (**Figure 4.8 and 4.25**). Addition of ssDNA-graphene sols (ssDNA:

graphene wt. ratio = 2:1) to ferri-cyt *c* sols (1 $mgmL^{-1}$), resulted in overnight sedimentation of a red/black solid. Isolation of the sedimentation using centrifugation/washing cycles and subsequent PXRD analysis presented a broad, low angle reflection at 1.75°, corresponding to an expanded interlayer d_{001} spacing of 5.06 nm, which was 3.66 nm larger than the basal spacing observed in ssDNA-graphene films (**Figure 4.26a**).

No additional reflections were observed suggesting that ferri-cyt *c* (molecular dimensions: 2.5 × 2.5 × 3.7 nm)[125] and ssDNA molecules were effectively fully co-intercalated within the gallery regions of the stacked array of graphene sheets, to form a stacked mesolamellar structure. PXRD analysis of repeat preparations of ferri-cyt *c*-ssDNA-graphene composites, displayed similarly broadened, low angle reflections at 1.88° and 1.86° corresponding to interlayer d_{001} basal spacings of 4.69 and 4.74 nm. This slight variation in d-spacing could be attributed to the different orientation of the cyt *c* biomolecules within the interlayer spaces of the ssDNA-graphene sheets.

Addition of ssDNA-graphene sols (ssDNA: graphene wt. ratio = 5:1) to lysozyme sols (0.5 $mgmL^{-1}$), resulted in the overnight sedimentation of a black solid and subsequent isolation as discussed previously using centrifugation/washing cycles. PXRD analysis, of this solid, presented a low angle reflection at 2.50°, corresponding to an expanded interlayer d_{001} spacings of 3.53 nm, 2.0 nm larger than the basal spacing observed in the comparable ssDNA-graphene films (**Figure 4.26b**). These results implied that lysozyme (molecular dimensions: 3.0 × 3.0 × 4.5 nm)[205] was partially co-intercalated within the gallery regions of the functionalised graphene sheets.

Protein	**Dimensions (nm)**
Cytochrome *c*	2.5 × 2.5 × 3.7
Lysozyme	3.0 × 3.0 × 4.5

Table 4.11 Summary of the dimensions of the co-intercalated proteins.

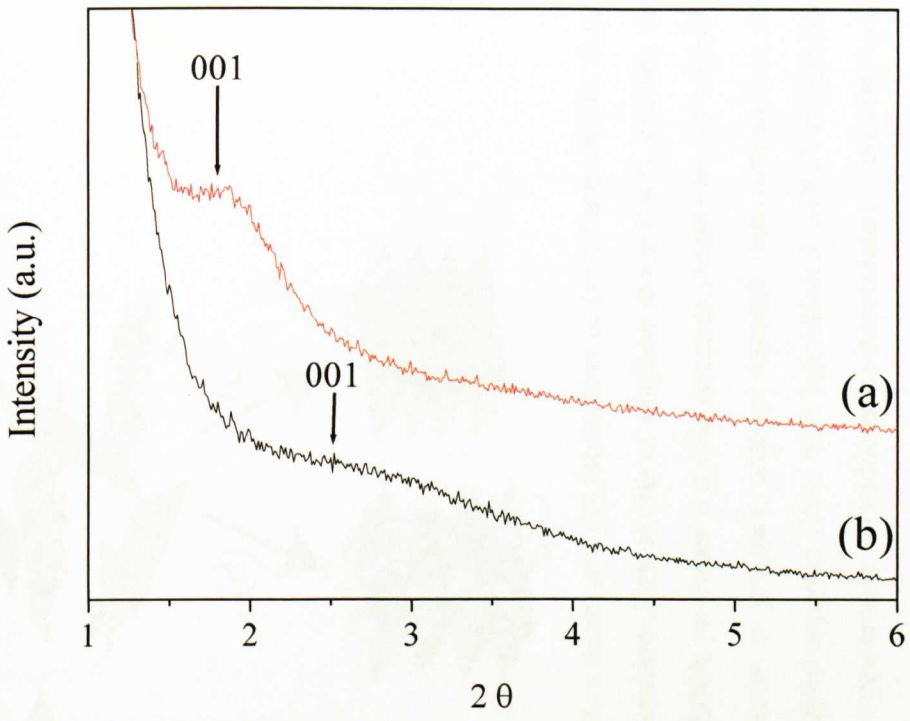

Figure 4.26 PXRD pattern of protein-ssDNA-graphene meso-lamellar composites showing the co-intercalation of ssDNA with (a) ferri cytochrome *c* and (b) lysozyme.

Sample	d(001) Interlayer Spacing (nm)	Increase in d(001) Spacing (nm)
ssDNA-graphene (wt. ratio 2:1)	1.40	-
ssDNA-graphene (2:1)-ferri-cytochrome *c*	5.06	3.66
ssDNA-graphene (wt. ratio 5:1)	1.51	-
ssDNA-graphene (5:1)-lysozyme	3.53	1.99

Table 4.12 Summary of the inter-lamellar basal spacing of graphene-based nanocomposites.

A generalised schematic for the development of DNA stabilised graphene dispersions and their subsequent assembly in the presence of cationic proteins is shown in **Figure 4.27**, with the potential of extending this strategy to the co-intercalation of alternative cationic species, including biomolecules and nanoparticles.

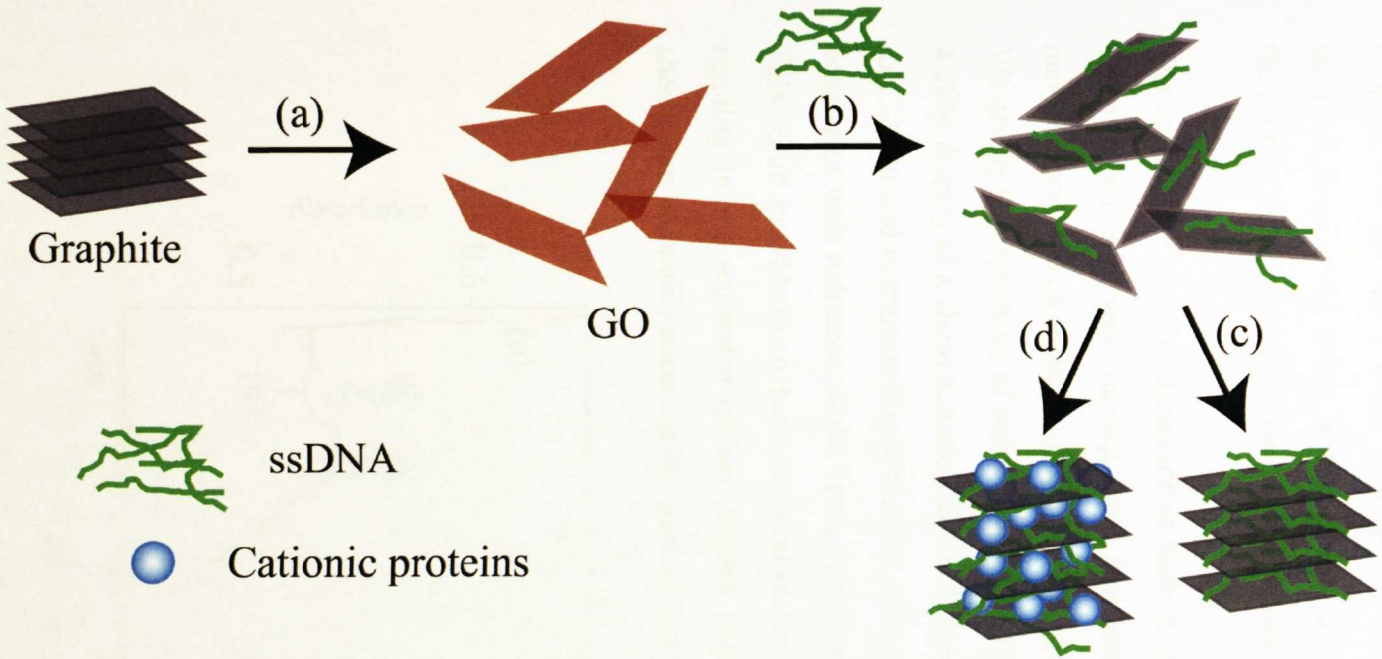

Figure 4.27 Schematic showing the synthesis of ssDNA-stabilised graphene aqueous suspensions and the fabrication of lamellar multifunctional nanocomposites. Step (a) oxidative treatment of graphite (grey) yields delaminated nanometre-thick sheets of graphite oxide (GO) (brown). (b) Chemical reduction of GO sols with hydrazine in the presence of freshly prepared ssDNA produces a stable aqueous suspension of ssDNA-functionalised graphene sheets (ssDNA-G). (c, d) Processing of ssDNA-G dispersions to produce ordered layered nanocomposites; (c) evaporation-induced deposition or self-assembly on flat substrates results in lamellar nanocomposite films with intercalated ssDNA molecules, and (d) co-assembly of negatively charged ssDNA-G sheets and positively charged cytochrome *c* produces co-intercalated multifunctional layered nanocomposites.

UV-Vis spectroscopy was conducted on ferri-cyt *c*-ssDNA-graphene nanocomposite to assess the protein structure and function on entrapment within ssDNA-functionalised graphene layers. The UV-Vis absorption spectrum of the co-intercalated ferri-cyt *c* nanocomposite (**Figure 4.28a**) displayed a strong Soret band at 408 nm and a broad band at 530 nm, as observed previously for the oxidised form of the redox protein (ferri-cyt *c*), consistent with the retention of the protein terniary structure on entrapment within the ssDNA-G lamellar sheets.

The accessibility of the incarcerated protein to small molecules present in the external solution was subsequently examined by treating the cyt *c*-based nanocomposite with a reducing agent, in this case, sodium dithionite. The UV-Vis absorption spectrum of reduced co-intercalated cyt *c* nanocomposite (**Figure 4.28b**) displayed a characteristic shift in the position of the Soret band from 408 to 432 nm and corresponding formation of Q band features at 520 and 550 nm, consistent with reduction of the heme, iron centre from ferri-cyt *c* to ferro-cyt *c*. This result provided conclusive evidence that the entrapped protein molecules, residing in the expanded gallery regions between ssDNA-stabilised graphene sheets, can be readily accessed by small molecules.

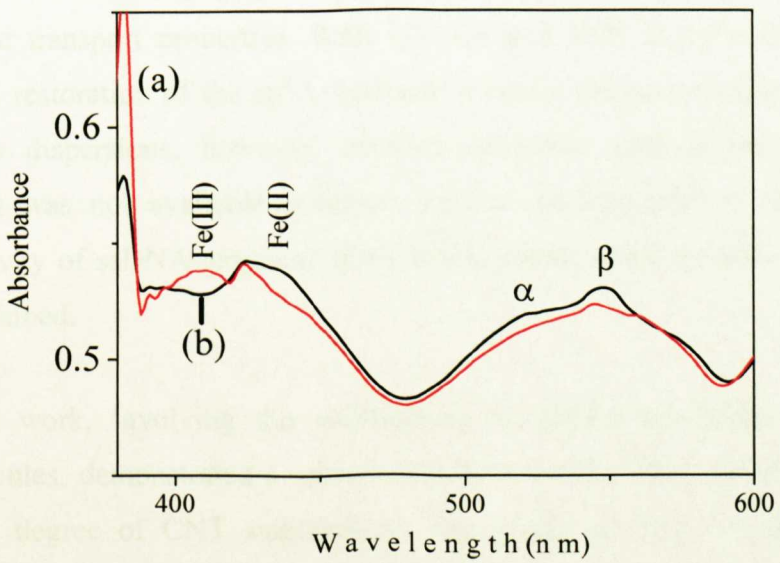

Figure 4.28 UV-Vis absorption spectra of (a) as-prepared oxidised ferri-cytochrome *c* nanocomposite and (b) reduced cytochrome *c* nanocomposite, showing characteristic changes in the position of the Soret band and the Q band features, consistent with the formation of reduced ferro-cytochrome *c*.

4.5 Conclusions and Further Work

The first part of this chapter demonstrated the stabilisation of graphene sheets with single-stranded DNA biomolecules, by chemical oxidation of graphite followed by subsequent in situ reduction of GO in the presence of ssDNA. This is the first known example of the use of a biopolymer to stabilize graphene sheets. Both graphene oxide and ssDNA coated graphene sheets were fully characterised using a range of physico-chemical techniques including TEM, AFM, EDXA, PXRD, UV-Vis, FT-IR, XPS and MAS solid state NMR. TEM images revealed highly transparent ssDNA functionalised graphene sheets with a high degree of flexibility shown from the presence of folded or curled edges. Additional AFM analysis of the sheets displayed individual sheets with roughened surfaces and an average apparent height of 2.4 nm due to the formation of secondary globular DNA structures on the surface of the graphene sheets.

GO is well reported to be a poor electrical conductor due to the loss of in-plane electronic conjugation, during oxidative treatment. However, reduction of GO is shown to restore conjugation to the sheets and subsequently improve the electronic transport properties. Both UV-Vis and XPS analysis demonstrated chemical restoration of the sp^2 hybridised aromatic carbon network of ssDNA-graphene dispersions, however, detailed electronic measurements of these materials was not available in-house. Further investigation of the electrical conductivity of ssDNA-graphene films would enable more detailed information to be obtained.

Previous work, involving the stabilisation of carbon nanotubes with DNA biomolecules, demonstrated a relationship between the DNA sequence and the resultant degree of CNT stabilisation. The effect of DNA sequence on the stability of the graphene sheets was not investigated in detail in this study. It would therefore be interesting to assess if this relationship is applicable to the stabilisation of graphene sheets, making these dispersions potentially applicable in DNA sensing and other biotechnological applications.

The final stages of this chapter showed that simple vacuum filtration or evaporation-induced self-assembly of ssDNA-graphene dispersions enabled effective fabrication of mesolamellar, nanocomposite films composed of stacked graphene sheets, intercalated with globularised ssDNA, as shown from the expanded inter-lamellar spacing in the PXRD data. Increases in the ssDNA concentration did not correspond to an increase in the inter-lamellar spacing, suggesting that rehybridisation of ssDNA did not occur after in situ reduction of GO. Furthermore, post synthetic addition of cationic proteins to ssDNA-graphene dispersions demonstrated a general strategy for the spontaneous, co-intercalation and assembly of ssDNA-graphene sheets to produce ordered graphene-based lamellar hybrid bionanocomposites.

PXRD analysis showed that addition of positively charged proteins, ferri cytochrome *c* and lysozyme, resulted in further expansion of the inter-lamellar spacing due to charge neutralisation driven co-intercalation. UV-Vis spectroscopy of ferri-cyt c-ssDNA-graphene nanocomposites demonstrated that the co-intercalated protein was fully accessible to external molecules. The encapsulation and intercalation of protein molecules is well reported to contribute towards an enhancement in the protein activity. It would, therefore, be applicable to investigate the effect of co-intercalation on the enzyme activity in future studies. Furthermore, as cytochrome *c* is a redox protein, further work on the electrochemical properties of the cyt *c*-ssDNA-graphene nanocomposites would be extremely applicable to this work.

In summary, the work discussed in this chapter represents a potential high-yield route to the production of aqueous, processable graphene sheets via oxidative treatment of graphite, enabling subsequent formation of lamellar, multifunctional nanocomposites.

CHAPTER 5 FABRICATION OF GRAPHENE-POLYMER NANOCOMPOSITES WITH HIGHER-ORDER ARCHITECTURES USING TEMPLATING TECHNIQUES

(Published in *Advanced Materials*, 2009, **21**, 3159-3164)

5.1 Introduction

5.1.1 Chapter Outline and Aims

The ability to prepare stable, aqueous dispersions of graphene on a large scale opens up the possibility of using graphene sheets as a viable and inexpensive alternative material in carbon-based fillers and nanocomposites. The main goal of this chapter was to demonstrate, for the first time, the conceptual application of well established self-assembly principles to the organisation of polymer-stabilised graphene sheets for the fabrication of graphene-polymer nanocomposites. Two main templating strategies are discussed, demonstrating the effective assembly of polymer-stabilised graphene sheets into highly-ordered architectures.

The first approach, examined the application of cryogenic processing to homogenous mixtures of PSS-stabilised graphene sheets and poly(vinyl alcohol) (PVA) to form self-supported sponge-like monoliths with internally aligned macroporosity. In particular, uni-axial freezing protocols were applied, more commonly known as ice-segregation induced self-assembly (ISISA). The second approach involved the electrostatic-induced assembly of negatively charged PSS-G dispersions and positively charged poly(allylamine hydrochloride) (PAH)-functionalised polystyrene (PS) beads to form PSS-G coated polymer microparticles, with the possibility of forming hollow graphene-based micrometer-sized spheres by dissolution of the sacrificial latex core. The complex morphologies produced in both templating strategies are fully investigated using scanning and transmission electron microscopy (SEM/TEM) with additional mechanical compressional testing conducted on the ice-templated

monoliths demonstrating the enhanced mechanical properties of the graphene-based scaffolds.

5.1.2 Templating and Self-Assembly based on Cryogenic Processing

In recent years, the formation of ice crystals during cryogenic processing, has attracted significant attention as a simple, versatile, cheap and environmentally benign structural template for the fabrication of organised materials with a high level of macro-, meso- and micro-porosity. In particular, structurally organised materials with high internal surface areas and extended, hierachial porous channels are of current technological interest in a range of fields including catalysis, drug storage and release, bioremediation and tissue engineering.[206-209] Typically, cryogenic processing refers to a two step protocol, involving initial freezing of a desired material in liquid nitrogen followed by thawing of the frozen construct using freeze-drying techniques. Interestingly, structural organisation based on ice templating is naturally observed at the surface of frozen ocean water, where impurities, including salt and biological organisms, are observed to be segregated in channels between neighbouring ice crystals.[210]

Traditionally, cryogenic processing was well exploited in the field of regenerative medicine to produce biocompatible, porous scaffolds with applications in drug delivery systems and tissue and bone engineering. In particular, scaffolds containing a range of biopolymers, proteins and inorganic materials including poly(L-lactic acid) (PLLA),[211] poly(DL-lactic-co-glycolic acid) (PGLA),[211] chitosan,[212, 213] alginate,[213] chitosan-alginate hybrid,[214] gelatine-based,[215-217] poly(glutamic acid)-chitosan hybrid,[218] collagen-based,[219-221] silk sericin,[222] agarose[223] and hydroxyapatite,[224] were successfully fabricated following freezing and thawing protocols. In addition, various ceramic materials were successfully processed using cryogenic methods including silica,[225] titania[226] and alumina.[227, 228]

Cryogenic processing is highly effective in producing porous architectures as a result of stepwise freezing and defrosting. The initial step of freezing results in the formation of ice crystals, which forces all solute to assemble in the external

or outer regions surrounding the ice crystals. Subsequent removal of these ice crystals by sublimation and thawing results in the formation of voids or vacant pores, in the positions where the ice crystals originally resided. The size and shape of the ice crystals formed during the freezing step is therefore crucial to controlling the final morphology of the scaffolds and this is affected by a range of factors including the freezing rate, freezing temperature, size and concentration of the solute and the freezing direction, as demonstrated previously.[229, 230]

Recent developments in ice-templating processes have sought to optimise this technique to develop a reproducible method for the production of highly ordered, micro-, meso- and macroporous hybrid scaffolds. One way to do this is to control the freezing direction, which effectively orientates the growth of arrays of polygonal ice crystals, as demonstrated in the schematic in **Figure 5.1**. This technique has recently become defined by the Del Monte group as ice-segregation induced self-assembly (ISISA).[231] Uni-axially freezing processes enable the formation of highly ordered micro-, meso- or macro-channelled structures, which are well-aligned in the direction of freezing. To date, a range of inorganic, ceramic and polymeric materials have been uni-directionally frozen, demonstrating the high versatile nature of this method, including silica[232-235] and titania hydrogels,[226] platinum nanoparticle decorated multi-walled carbon nanotubes,[236] water-soluble polymers[209, 229] and inorganic/metal nanoparticle composite sols[209] to produce orientated fibrous, honeycomb or lamellar structures, with some examples shown in **Figure 5.2**. Furthermore, biological hybrid materials have been uni-axially frozen to produce biohybrid composite materials comprising immobilised proteins,[237] liposomes,[238] bacteria cells[231] and antibiotics[229] with applications in drug delivery systems, biocatalysis and bioremediation.[230]

Recent work in the Mann group has sought to further extend the ISISA technique to a broader range of materials, including TiO_2 chitosan-based composite scaffolds containing TiO_2 nanoparticles, with potential applications in the photocatalytic degradation of organic pollutants.[239] This chapter demonstrates, for the first time, the application of ISISA to homogeneous dispersions of

polystyrene sulfonate-stabilised graphene sheets and poly (vinyl alcohol) (PVA), to produce porous architectures with internally aligned macroporosity.

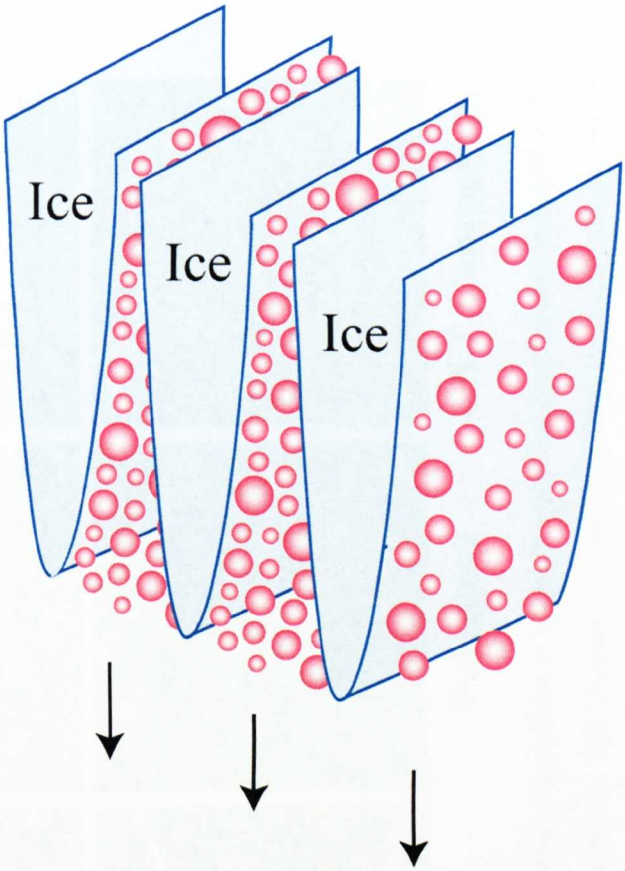

Figure 5.1 Schematic showing the segregation of inorganic, polymer or biological particles (red particles) in the channels between adjacent ice crystals during directional freezing in the direction of the arrows, adapted from Deville and co-workers.[240]

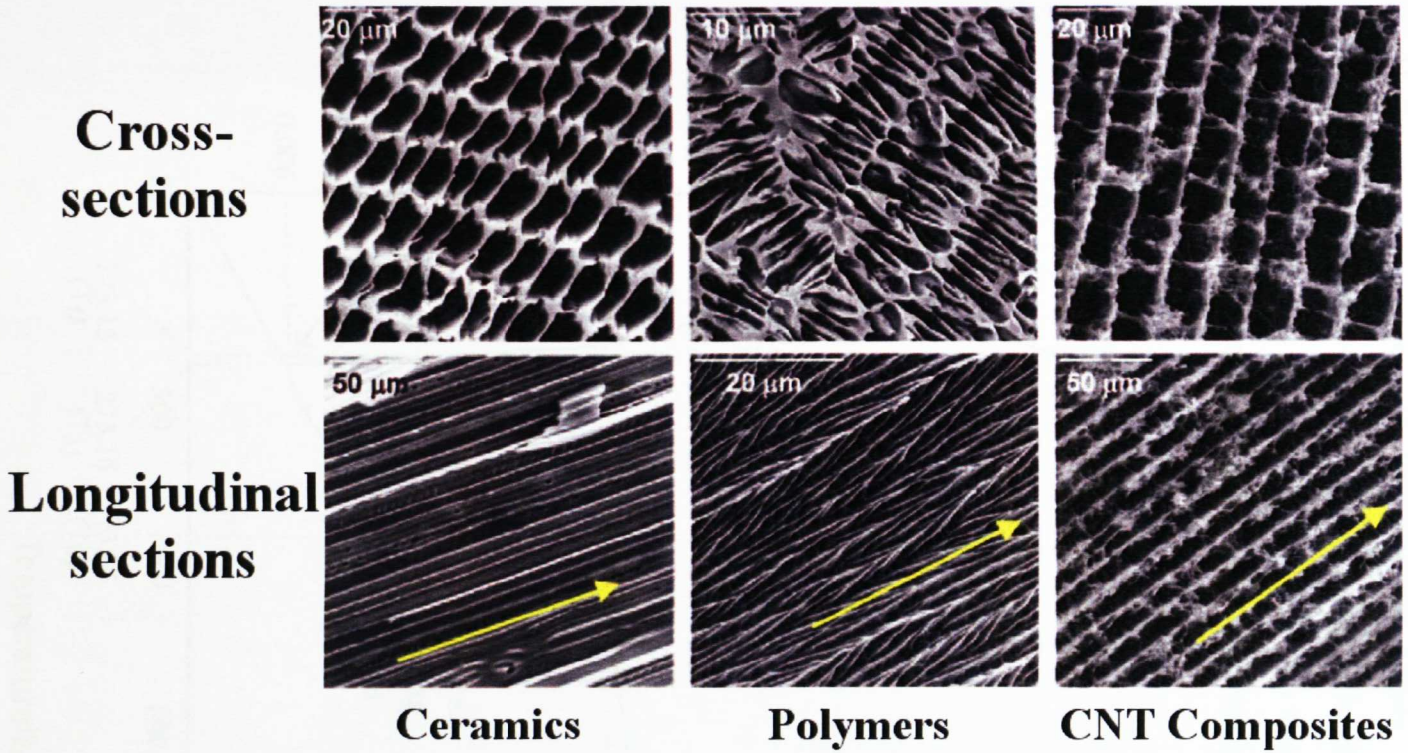

Figure 5.2 SEM images of cross and longitudinal sections of different materials processed using ice-segregation induced self-assembly, with the yellow arrows showing the direction of freezing including, from left to right, ceramics, polymers and CNT composite, showing a well-formed channel structure and effective pore alignment, adapted from Gutierrez et al.[229, 230, 236, 241]

5.1.3 Ice Crystallisation

The formation of ice is a naturally observed crystallisation phenomenon, with approximately 5% of the earth's surface covered by ice throughout the year.[242] At the molecular level, ice crystallisation occurs through the formation of hydrogen bonds between neighbouring water molecules, when water is frozen. The phase diagram in **Figure 5.3** illustrates the equilibrium between the ice, liquid and vapour phases at different temperatures and pressures.

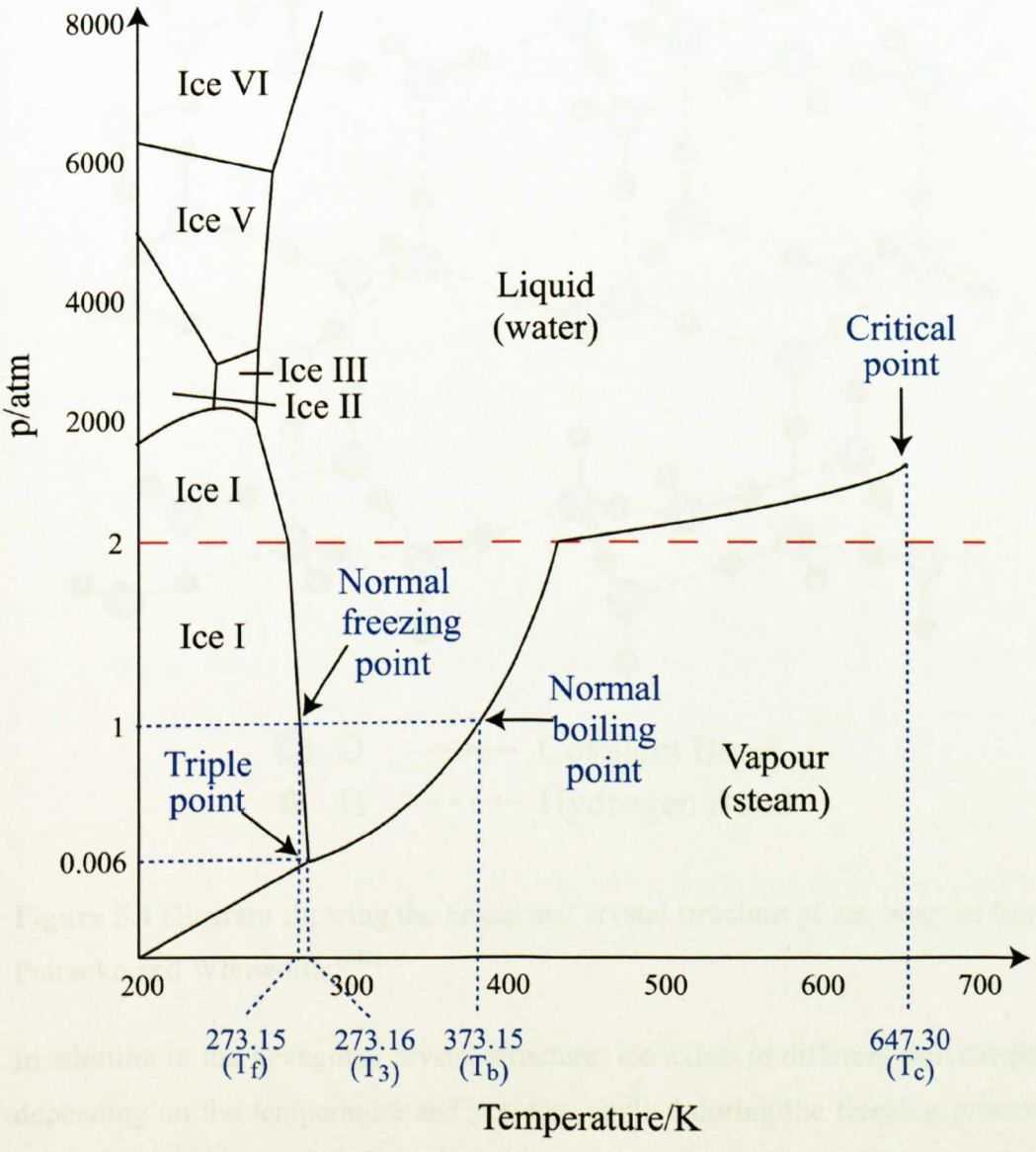

Figure 5.3 Schematic illustrating the equilibrium between the ice, liquid and vapour phases, with a change in the vertical scale at a pressure of 2 atmospheres, adapted from Atkins' Physical Chemistry.[243]

The most commonly observed crystal structure of ice is the hexagonal form (I_h), present in ice and snow, which forms when water is cooled below 0 °C at ambient pressures. The molecular structure of hexagonal ice was well established by Linus Pauling (1935) and is composed of oxygen atoms arranged in a hexagonal lattice, with each O atom surrounded by four neighbouring O atoms at the edge of a tetrahedron, as shown schematically in **Figure 5.4**.[242]

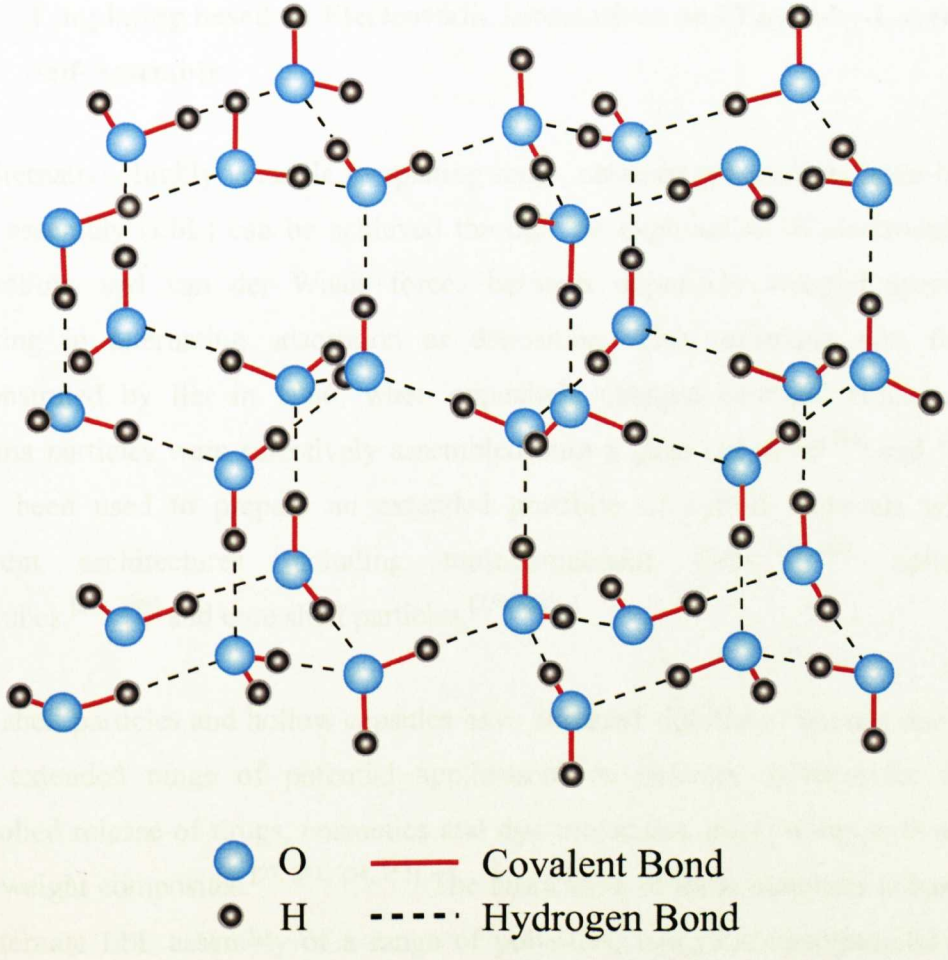

Figure 5.4 Diagram showing the hexagonal crystal structure of ice, adapted from Petrenko and Whitworth.[242]

In addition to the hexagonal crystal structure, ice exists in different polymorphs depending on the temperature and pressure applied during the freezing process, due to the structural versatility of the water molecule and the modification of the hydrogen bonding at high pressures. These phases include ice II, III, V, VI, VII, as shown in the phase diagram in **Figure 5.3**. Furthermore, if pure water is cooled rapidly (supercooled), at rates exceeding 10^6 °C/s, below its glass

transition temperature (T_g = -137 °C), ice crystal nucleation is prevented and instead amorphous ice is formed.[230]

The cryogenic processing demonstrated in this chapter is conducted by freezing monoliths in liquid nitrogen at -196 °C at relatively low freezing rates and ambient pressure, suggesting that hexagonal ice crystals will form.

5.1.4 Templating based on Electrostatic Interactions and Layer-by-Layer Self-Assembly

An alternative, highly versatile templating route, commonly known as layer-by-layer assembly (LbL) can be achieved through the exploitation of electrostatic interactions and van der Waals forces between oppositely charged species resulting in alternating adsorption or deposition. This technique was first demonstrated by Iler in 1966, when oppositely charged colloidal silica and alumina particles were selectively assembled onto a glass substrate[244] and has since been used to prepare an extended portfolio of hybrid materials with different architectures including multicomponent films,[245-247] hollow nanotubes,[248, 249] and core shell particles.[250-253]

Core shell particles and hollow capsules have attracted significant interest due to their extended range of potential applications as delivery systems for the controlled release of drugs, cosmetics and dye molecules, catalyst supports and light-weight composites.[97, 251, 254, 255] The fabrication of these materials is based on alternate LbL assembly of a range of polymers, inorganic nanoparticles or biomolecules on a core template, for example latex, polystyrene particles or other inorganic and metal particles, followed by removal of the template using thermal (calcination) or chemical dissolution techniques.[255] For example the Caruso group fabricated core-shell particles composed of titania by alternating templated layers of an anionic titanium precursor and a cationic polyelectrolyte, poly(diallyl dimethyl ammonium chloride), (PDADMAC) on polystyrene (PS) particles, followed by removal of the PS core using calcination (**Figure 5.5**).[252] Uniform, hollow spheres have additionally been fabricated from a range of inorganic materials including, for example, silica,[250, 256] zeolite (silicalite),[206]

titanium dioxide[257] and magnetite (Fe_3O_4).[258] The main advantage of LbL assembly is control of both the structural composition and morphology of the assembled hybrid composite materials by careful selection of the type, diameter and shape of the colloidal template in addition to the number of layers deposited.[245, 251, 255]

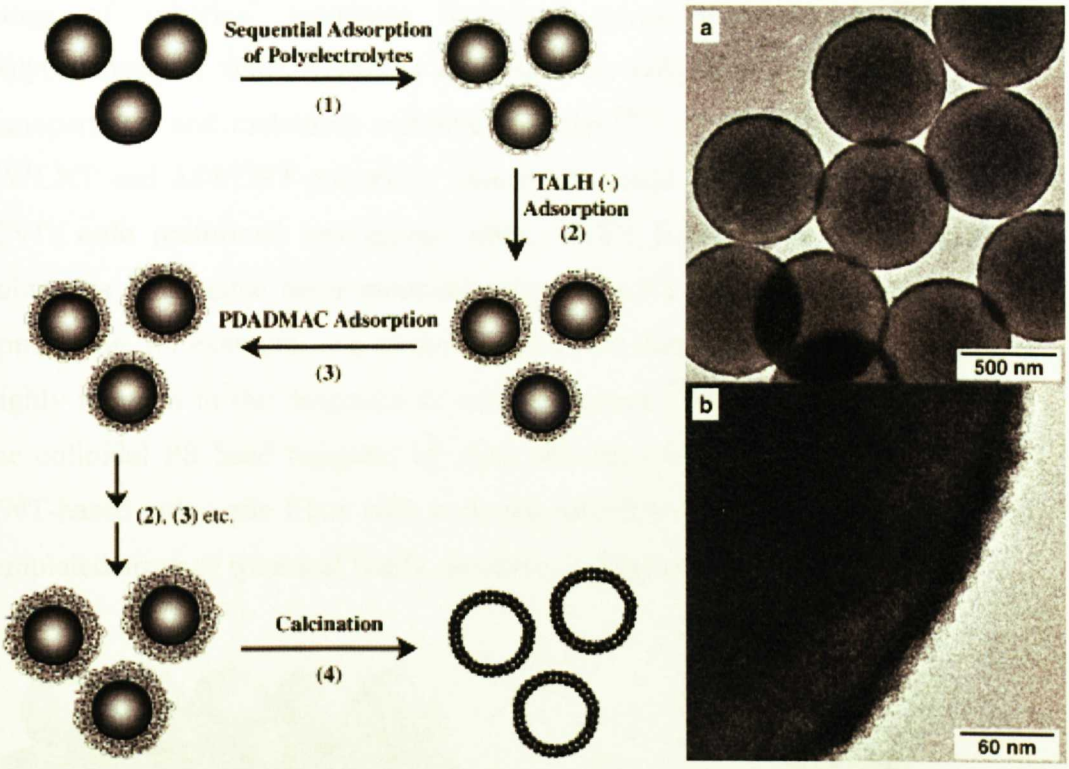

Figure 5.5 Schematic showing the procedure followed by the Caruso group to construct hollow titania spheres, using titanium (IV) bis(ammonium lactate) dihydroxide (TALH) as a water-soluble and stable inorganic precursor and PS beads which were initially coated with three alternating PDADMAC/PSS layers with associated TEM images of (a) Uniformly coated PS spheres with five TALH/PDADMAC layer pairs and (b) the corresponding high magnification image showing the surface of the beads.[252]

The assembly of CNTs using LbL assembly has, additionally, been of interest as an alternative route to fabricate hybrid CNT materials. The formation of self-supporting and mechanically strong CNT-polymeric multilayer hybrid films was reported to be extremely successfully using the LbL approach, enabling the film

thickness and CNT content to be tightly controlled, by varying the concentration and number of layers of CNT deposited.[259, 260]

This strategy was further extended to produce composite core-shell particles and hollow capsules or cage-like structures based on the assembly of single-walled (SWNTs) and multi-walled (MWNTs) carbon nanotubes onto the surface of a range of spherical templates including amine-functionalised silica gel, poly(methacrylic acid), (PMAA) microspheres, polystyrene (PS) beads, silica nanoparticles and melamine colloidal particles.[261] Alternatively, sophisticated SWCNT and MWCNT-polymeric assemblies could be prepared by adsorbing CNTs onto preformed heaxagonal arrays of PS beads deposited on external substrates to produce hemi-spherical arrays of CNT coated microspheres with application, for example, as a sensor device in the detection of uric acid, which is highly relevant in the diagnosis of certain diseases.[262] Subsequent removal of the colloidal PS bead template by slow sintering resulted in the formation of CNT-based polymeric films with a curved morphology based on the hexagonal templated array of spherical beads, as shown in **Figure 5.6**.[263]

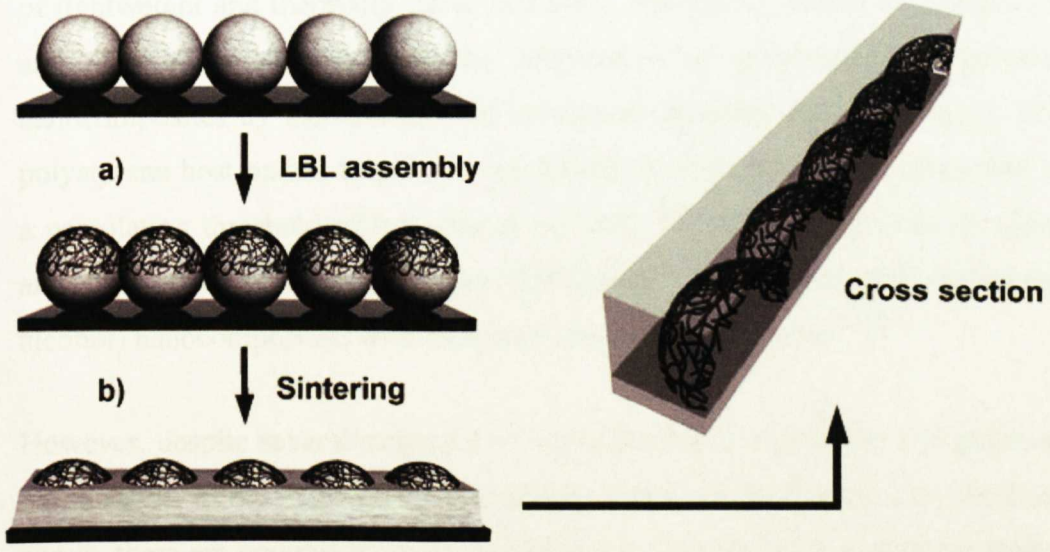

Figure 5.6 Schematic showing the preparation of CNT-polymeric films comprising (a) the LBL assembly of CNTs onto a hexagonally ordered array of PS spheres, followed by (b) sintering of the array, to remove the PS bead template and form a CNT-polymer film as shown in the cross-sectional image on the right hand side.[263]

Despite the successful application of the LbL strategy to the assembly of CNTs, this approach has not been extended, to date, to the assembly of graphene sheets to form highly-ordered graphene-based nanocomposites. This chapter demonstrates for the first time, the application of electrostatic induced assembly to the organisation of graphene sheets to produce graphene-polymer nanocomposites with higher order three dimensional architectures.

5.1.5 The Applications of Graphene Sheets in Nanocomposites

As a relatively 'young' material few reports, to date, have investigated the fabrication of more complex graphene-based architectures, exploiting self-assembly and templating techniques, some of which have already been introduced in this section. Recent reports have shown that graphene sheets can be used as fillers in polymeric matrices. Studies of interest include work conducted by Verdejo and co-workers, which demonstrated the fabrication of graphene-based silicone foam nanocomposites, prepared from thermally-derived functionalised graphene sheets.[264] These nanocomposite foams exhibit efficient heat dissipation properties, making them potentially applicable in the production of lightweight and thermally stable materials. Alternative studies by Stankovich and co-workers demonstrated the preparation of graphene-based polymer nanocomposites by incorporation of chemically modified graphene sheets, in a polystyrene host matrix to produce an electrically conductive nanocomposite, at a percolation threshold of 0.1 volume per cent.[169] More recent work by Liang and co-workers demonstrated the fabrication of graphene oxide-poly(vinyl alcohol) nanocomposites, with enhanced mechanical properties.[265]

However, despite several examples of the application of graphene and graphene oxide sheets in the preparation of graphene-based nanocomposites, as discussed above, there are no known reports to date reporting the use of templating routes, as a means of fabricating highly-ordered, three-dimensional graphene-based composites with complex architectures. The work discussed in this chapter investigates the application of ice-templating and electrostatically-induced assembly for the formation of graphene-based structures with sophisticated architectures.

5.2 Materials

All materials were purchased from Aldrich, UK and used without purification, unless otherwise stated.

5.2.1 Preparation of Graphene Oxide

As described in section 4.3.1.

5.2.2 Preparation of Polystyrene Sulfonate-Stabilised Graphene Dispersions (PSS-G)

Chemical	Molecular Formula		Supplier
Poly (sodium 4-styrene sulfonate) (PSS), sodium salt	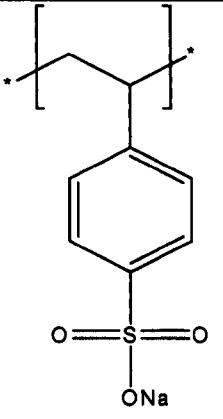	70,000	Aldrich
Hydrazine hydrate	$NH_2NH_2.\ H_2O$, 32.05		Aldrich
Graphene oxide (GO)	Synthesised as described in chapter 4		

5.2.3 Polymer-Based Ice Templating of PSS-G Dispersions

Chemical	Molecular Formula	Supplier
Poly(vinyl alcohol) (PVA)	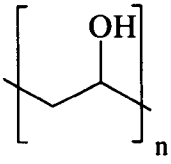 70,000	Aldrich
PSS-G	As described in section 5.2.2	

5.2.4 Polystyrene Bead Templating of PSS-G Microspheres

Chemical	Molecular Formula	Supplier
Poly (allylamine hydrochloride), PAH	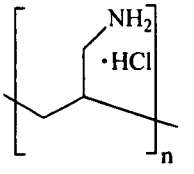 8500-11000	Aldrich
Poly (4-styrene sulfonate), PSS	As described above	Aldrich

5.3 Experimental Details

5.3.1 Preparation of Graphene Oxide based on the Hummers-Offeman Route

Graphene oxide was prepared as discussed in section 4.3.1.

5.3.2 Preparation of Polystyrene Sulfonate-Stabilised Graphene Dispersions

A stable dispersion of GO sheets (10 $mgmL^{-1}$), prepared as described previously (section 4.3.1), was sonicated for 2 hours to ensure complete exfoliation and subsequently dialysed (12-14 kD cut off) for 2 hours to remove any excess salts and acids. The dispersion was centrifuged for 20 mins (3000 rpm), to remove the non-exfoliated material and the supernatant, containing the exfoliated GO sheets was removed. The GO supernatant (ranging, in general, from 7-9 $mgmL^{-1}$) was diluted further to obtain solutions with a concentration of 1 $mgmL^{-1}$. Polystyrene sulfonate-stabilised graphene sheets (PSS-G) were prepared referring to a method developed by Ruoff and co-workers, as follows.[149] A stable dispersion of the exfoliated GO sheets (10-20 mL, 1 gL^{-1}) was mixed with hydrazine hydrate (0.5-1 mL, 17.7 mM) and PSS (10-20 mL, 10 gL^{-1}, M_w = 70000, 0.143 mM) and heated at 100°C for 24 h. Excess polymer and hydrazine hydrate were removed by repeated centrifugation and washing cycles (13200-20,000 rpm, 20 mins-1 h), followed by redispersion of the PSS-stabilised graphene nanoplatelets in deionised water.

5.3.3 Ice Nucleation-Induced Templating of Macroporous PVA Monoliths

Poly(vinyl alcohol) (PVA) monoliths were prepared similar to previously reported protocols.[209, 229] PVA (0.5 mL, 1-10 wt. %, M_w= 70,000) was added to water (0.5 mL) and homogenised using a pipette. The resulting mixture was then transferred to a 1 ml insulin syringe and immersed in liquid nitrogen at constant dipping rates (2.0, 5.9 or 10.0 mm min^{-1}). The unidirectionally frozen cryogels were subsequently freeze-dried for 24-48 h and removed from the syringes as

intact white monoliths. Cross-sections and longitudinal (vertical) sections were prepared by cutting with a sharp razor blade, for SEM and mechanical analysis.

5.3.4 Ice Nucleation-Induced Templating of Macroporous PSS-G/PVA Monoliths

PVA (0.5 mL, 5 wt. %, M_w= 70,000) was added to a PSS-G dispersion (0.5-1.5 mL, approx concentration ranged from 0.1-0.5 wt.%) and homogenised using a pipette. PSS-G:PVA weight ratios between 1:5 and 1:10 were typically used. The resulting mixture was then transferred to a 1 ml insulin syringe and immersed in liquid nitrogen at a constant dipping rate (5.9 mm min^{-1}). The unidirectionallly frozen cryogels were subsequently freeze-dried for 24-48 h and removed from the syringes as intact black monoliths. Cross-sections and longitudinal (vertical) sections were prepared by cutting with a sharp razor blade, for SEM and mechanical analysis.

5.3.5 Mechanical Testing of the Monoliths

Compression testing of the PVA control and PSS-G/PVA monoliths was conducted using a TA-XT plus texture analyzer (load cell = 50 N), at room temperature. Specimens for testing were approximately 4 mm in radius and length and were cut from the different sections of the main scaffold with a sharp razor blade. Stress versus strain measurements were plotted at a compression rate of 0.06 mm s^{-1}.

5.3.6 Polystyrene Bead Templating of PSS-G Microspheres

Positively charged polystyrene (PS) beads (diameter = 990 nm, Bangs Laboratories, Inc.) were prepared by addition of 0.5 mL of poly (allylamine hydrochloride) (PAH, 1 $mgmL^{-1}$ in 0.5 M NaCl, M_w= 8,500-11,000) to 0.5 mL of a 2.5 wt. % dispersion of polystyrene beads. The mixture was left for 30 min and then repeatedly centrifuged (3000 rpm, 20 mins, 3 times) and washed to remove excess polymer, redispersing the beads in deionised water after each step. Zeta potential measurements were obtained to confirm adsorption of PAH onto the

surface of the beads. Prior to use the PAH-coated PS beads were sonicated for 10-30 mins in an ultrasonicator bath to disassemble any large aggregates.

Graphene-wrapped polystyrene beads were prepared by adding 100–200 μL of PAH-coated polystyrene beads (typical 2.5 wt% aqueous solution) to 250 μL of a PSS-G dispersion (0.02–0.1 wt%). The solution was vortexed at high speed for 20-30 s. A black precipitate was immediately observed and isolated using centrifugation (3000 rpm, 10 min), followed by washing, redispersion in deionised water three times to remove residual and unattached PSS-G sheets followed by drying overnight.

5.3.7 Chemical Removal of Sacrifical Core Template

Dissolution of the polystyrene-bead template was achieved by immersion of dried PSS-G/PS bead composite in toluene for 15-20 mins, at room temperature.

5.4 Results and Discussion

5.4.1 Characterisation of Poly(sodium styrene sulfonate) Stabilised Graphene Dispersions

Black, aqueous dispersions of polystyrene sulfonate-stabilised graphene sheets (PSS-G, zeta potential = -30.51 mV) were readily prepared as described in section 5.3.2 using a previously reported method,[149] involving the chemical reduction of hydrophilic aqueous suspensions of GO, in the presence of polystyrene sulfonate and hydrazine hydrate, with heating under reflux for 24 h at 100 °C. The PSS-G dispersions were highly stable, compared with control samples prepared in the absence of PSS, which contained aggregated black material (**Figure 5.7a-b**).

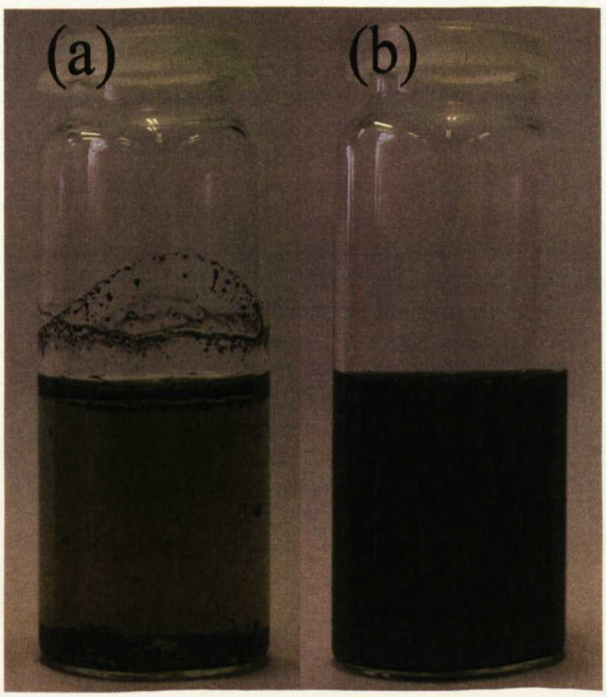

Figure 5.7 Photographic images showing (a) an aggregated sol of reduced GO, prepared in the absence of PSS and (b) a PSS-stabilised graphene sol, which was stable for several months.

As demonstrated in the case of GO, the morphological features of the PSS-stabilised graphene sheets were successfully observed using transmission electron microscopy (TEM). TEM images of PSS-G dispersions revealed highly translucent sheets ranging from 166 nm to 1.516 μm in lateral dimensions, with an average size of 549 nm (**Figure 5.8a-d**). The atomically thin nature of the sheets can be observed from the folds and curled edges (**Figure 5.8**, arrows). Energy dispersive X-ray analysis (EDXA) on individual sheets showed a high intensity sulfur K_{alpha} peak at 2.308 KeV, confirming the presence of polystyrene sulfonate (**Figure 5.8c**).

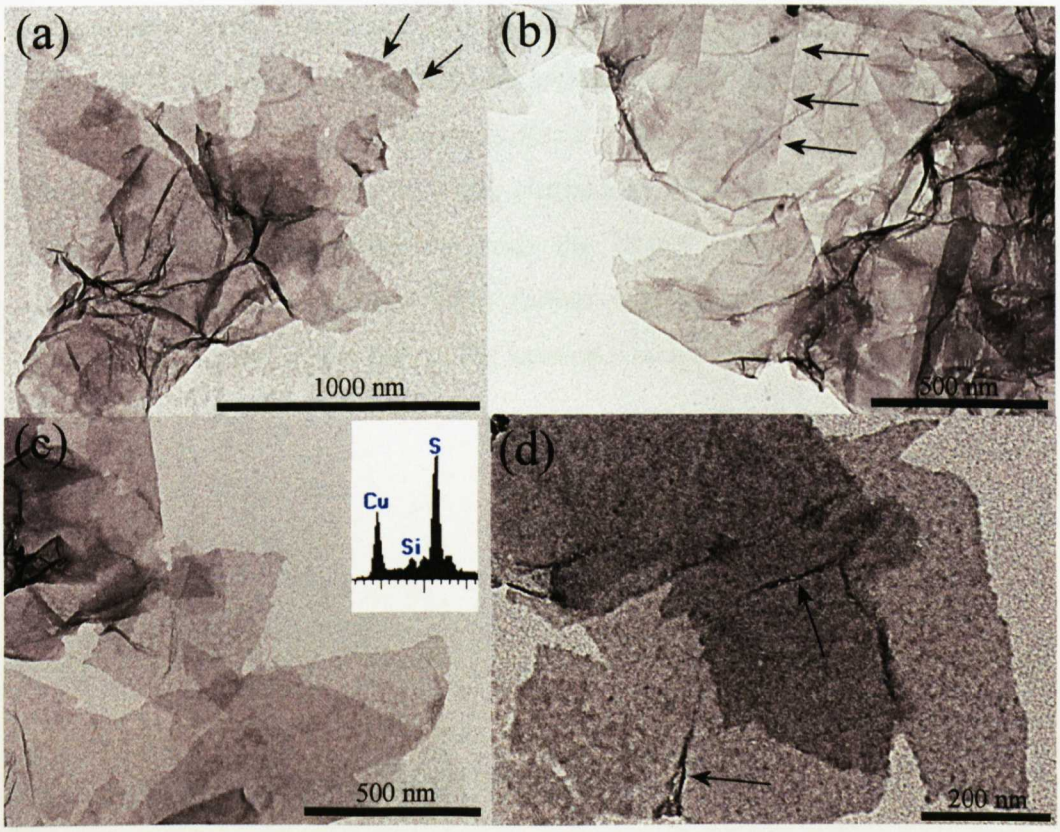

Figure 5.8 TEM images of exfoliated PSS-graphene sheets (Ratio = 10:1) showing examples of (a) folded edges, demonstrating the sheet flexibility, (b) edge features from highly transparent overlapping sheets, (c) overlapping sheets and (d) apparent crinkled features corresponding to in-plane defects or rolled edges. EDX analysis is shown inset in Figure (c) demonstrating the presence of sulphur from the PSS stabilising polymer, which effectively functionalises the surface of the graphene sheets.

Additional evidence for the ultra-thin nature of PSS-stabilised graphene sheets was obtained from atomic force microscopy (AFM) images. Height images (**Figure 5.9a, c**) and associated height profiles (**Figure 5.9b, d**) of dilute PSS-G dispersions, dried on freshly cleaved mica, enabled calculation of the thickness of graphene sheets with respect to the mica substrate. Analysis of the height profiles, revealed individual sheets with a roughened surface morphology and initial height steps of 2-2.2 nm, approximately 2 nm smaller than previously reported by Stankovich and co-workers (**Figure 5.9b, d; step i**).[149] Additional steps of 1.2 and 1.6 nm were observed due to the presence of adsorbed polymer and in-plane buckling or crinkling, respectively (**Figure 5.9b, d; step iii**). In comparison with previously reported AFM data of graphene oxide sheets (Chapter 4, section 4.4.1) which demonstrated the thickness of GO sheets to range from 1-1.5 nm, PSS-coated sheets were up to a nanometre larger in thickness corresponding to a single atomically thick sheet of graphene with a layer of polymer adsorbed on both the upper and lower surface. Three-dimensional images (**Figure 5.10**) further highlighted the roughened surface morphology of the sheets due to the uneven adsorption of PSS on the surface of the sheets.

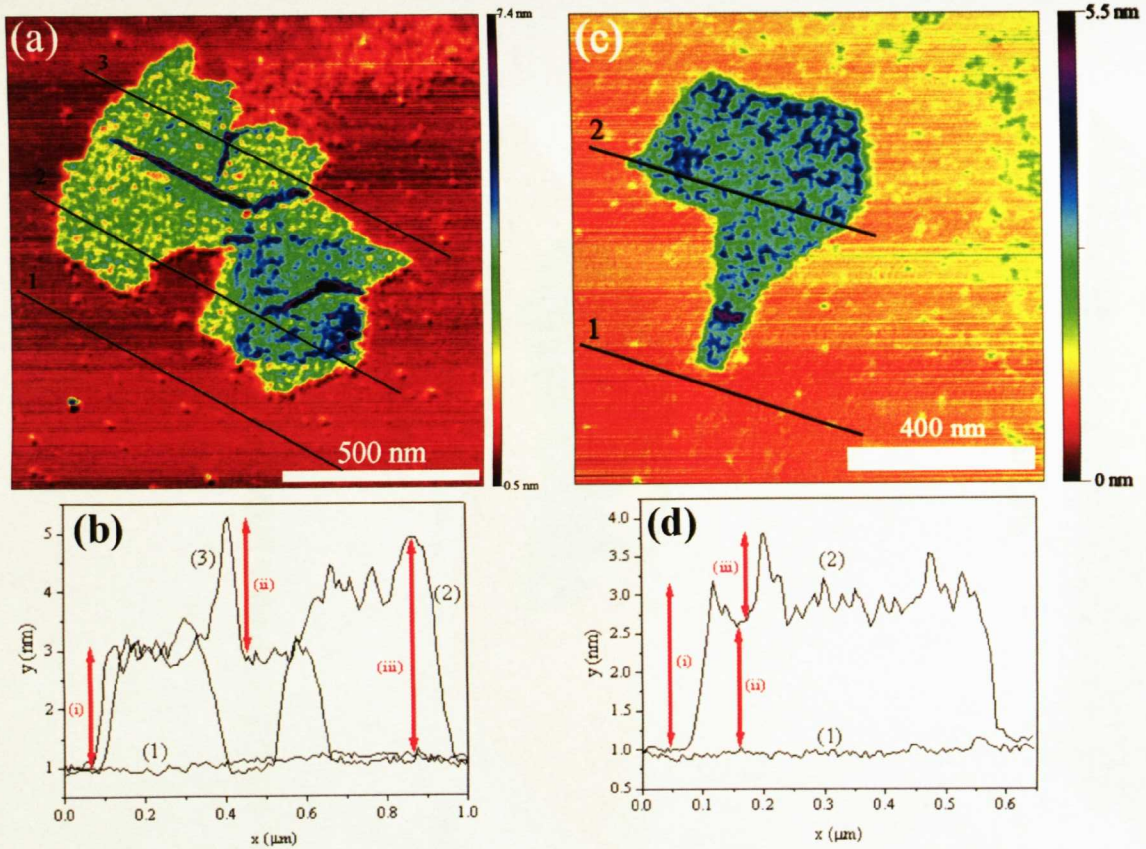

Figure 5.9 Tapping mode AFM data of (a, c) PSS-stabilised graphene dispersions, dried on freshly cleaved mica at a weight ratio of 10:1 and (b, d) the associated height profiles.

(a)

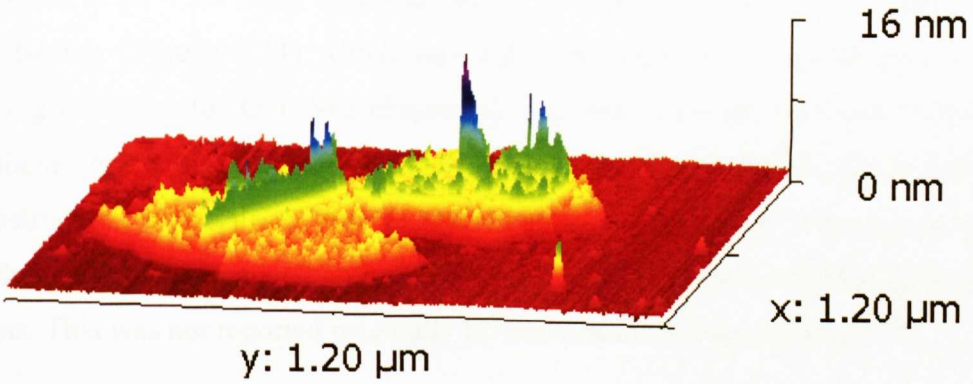

(b)

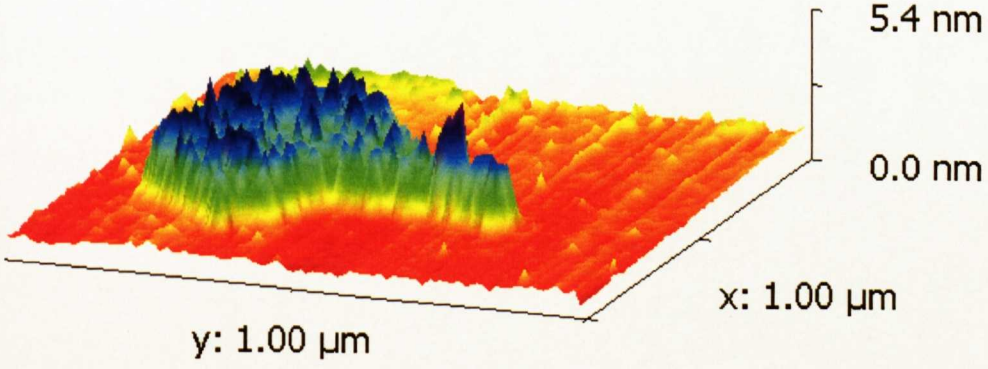

Figure 5.10 Three-dimensional AFM images of (a) figure 9a and (b) figure 9c.

PXRD analysis of PSS-G films, dried onto Si wafer substrates at room temperature, using evaporation-induced assembly, presented a low angle reflection at $2\theta = 5.4^{\circ}$, that corresponded to an expanded interlayer d_{001} spacing of 1.64 nm (**Figure 5.11**) which was 0.88 nm larger that the interlayer d_{001} spacing observed for GO (See chapter 4). As observed with ssDNA-stabilised graphene sheets, discussed in chapter 4, PSS-G forms an ordered mesolamellar nanostructure, when dried into a film, comprising a stacked arrangement of graphene sheets intercalated with a monolayer of surface-adsorbed PSS polymer chains. This was not reported originally by Stankovich and co-workers.[149]

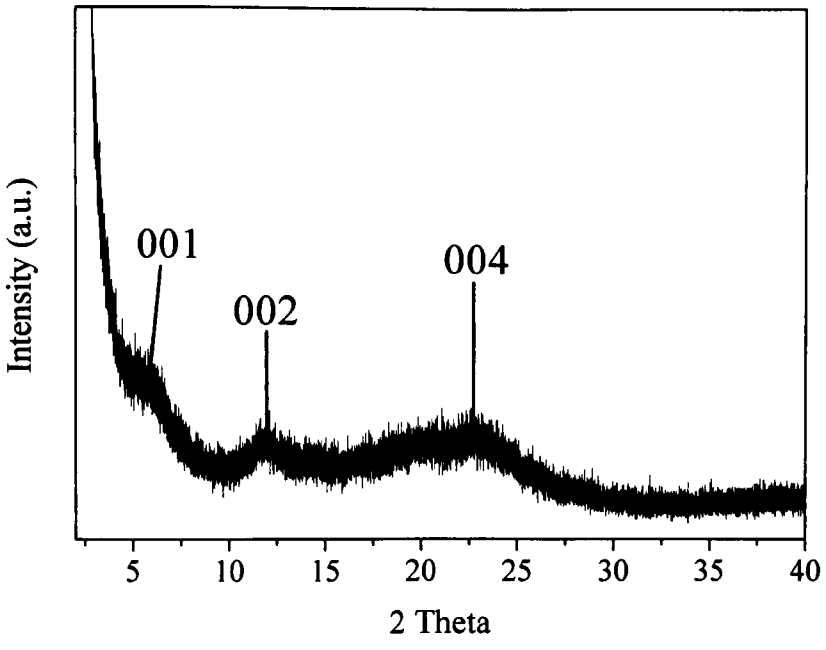

Figure 5.11 Powder X-ray diffraction (PXRD) data showing dried PSS-G film with low angle d_{001}, d_{002}, d_{003} and d_{004} reflections (see **table 5.1** for positions), indicating the formation of an expanded mesolamellar graphene-based structure due to the intercalation of PSS between a stacked array of graphene sheets.

Sample	2 Theta	d-spacing (nm)		hkl indices
		Experimental	Theoretical	
PSS-Graphene	5.37	1.64	-	001
	11.83	0.747	0.82	002
	22.84	0.388	0.41	004
Graphene Oxide (GO)	11.6	0.759	-	001
	22.0	0.403	-	002

Table 5.1 Summary of 2θ values, d-spacing and corresponding hkl indices for the peaks observed in the PXRD pattern of graphene oxide (GO) and PSS-stabilised graphene sheets.

X-ray photoelectron spectroscopy (XPS) was consistent with previously reported data[149, 193, 194] Analysis of the carbon 1s (C 1s) peak area of PSS-G (**Figure 5.12a, Table 5.1**) indicated the presence of a dominating peak at a binding energy of 284.5 eV (72 %, compared with 81 % in graphite) associated with effective restoration of the aromatic carbon atoms (C=C). Additional peaks were observed at binding energies of 285.3 eV (21 %), 286.6 eV (6 %) and 288.6 eV (1 %) corresponding to a small percentage of residual phenol (C-O), epoxide (C-O-C) and carbonyl or carboxylate (C=O/C(O)O) groups, respectively, on the basal planes and edges, which unfortunately could not be completely removed using chemical reduction with hydrazine hydrate. The peak at 285.3 eV, which contributes towards 20 % of the total carbon atoms present, is consistent with the presence of sulfur atoms bonded to carbon atoms in PSS (C-S), as seen in the C 1s spectrum of PSS (**Figure 5.12c**, Table 5.1), providing further complimentary evidence for the presence of PSS on the surface of the graphene sheets.[149]

Additional O 1s XPS of PSS-G (**Figure 5.12b, Table 5.2**) provided evidence for the presence of some residual oxygen containing groups, in addition to oxygen atoms originating from PSS. Analysis of the oxygen 1s (O 1s) peak area presented a broad band composed of contributions from S=O groups in PSS (71%, 531.1 eV), as seen in the O 1s spectrum of PSS (**Figure 5.12d, Table 5.2**) and residual oxygen-containing functional groups originating from the graphene sheets including phenol, carbonyl, epoxide and carboxyl group (23 %, 533.4 eV).

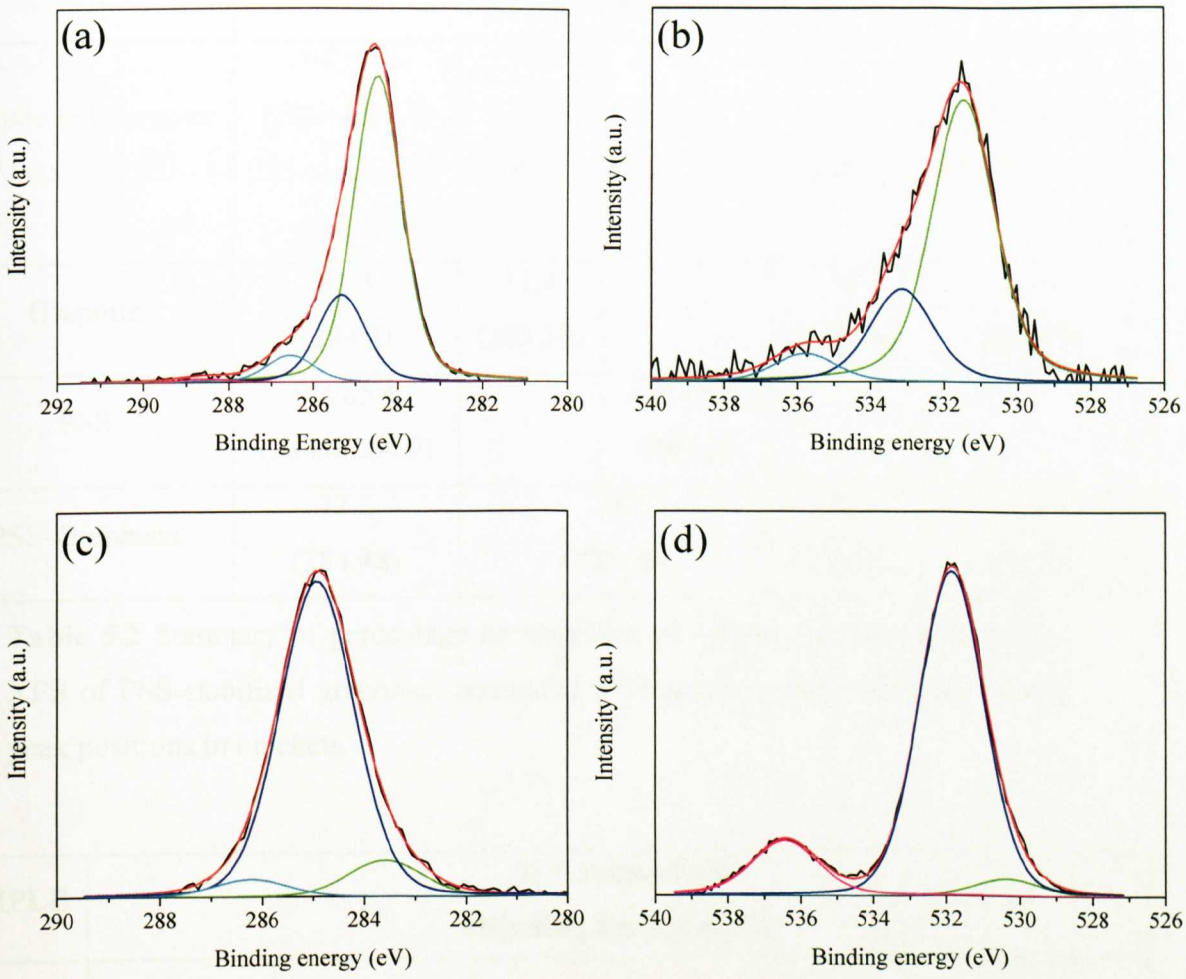

Figure 5.12 (a) C 1s and (b) O 1s XPS data of PSS-G, respectively; (c) C 1s and (d) O 1s XPS data of a control film of PSS.

SAMPLE	% Composition (Binding Energy (eV))				
Graphene Literature Values[193, 194]	C=C/C-C (283.6/284.6, 283.6-charging effects)	C-OH (285.7)	C-S (285.2)[149]	C-O-C (286.7)	C=O/ C(O)O (288.0/289.1)
Graphite	81.3 (284.5)	11.4 (285.55)	-	5.6 (286.74)	1.7 (288.17)
PSS	9.8/85.4 (283.6/284.9)	-	4.8 (C-S) (286.2)	-	-
PSS-Graphene	72.2 (284.48)	20.7 (285.33)		6.3 (286.55)	0.8 (288.57)

Table 5.2 Summary of percentage composition of carbon functional groups in XPS of PSS-stabilised graphene, compared with graphite, with their associated peak positions in brackets.

SAMPLE	% Composition (Binding Energy (eV))				
Literature Values	PSS^-Na^+ (530.7)[266]	S=O (531.72)[192]	C-OH (532.9-533.6) C=O (532.3) C-O-C (Epoxide, 533.1) Physioadsorbed H_2O [192]	C(O)-OH (534.2)[191]	Charged O-H or C=O
Graphene Oxide	-	-	90 (532.82)	10 (534.47)	-
PSS	4.3 (530.3)	80.7 (531.9)	-		15 (536.4)
PSS-G	-	71.2 (531.71)	22.6 (533.42)		6.3 (536.01)

Table 5.3 Summary of percentage composition of oxygen functional groups in XPS of PSS-stabilised graphene, compared with graphite, with their associated peak positions in brackets.

Fourier-Transform Infra-red (FT-IR) and UV-visible (UV-Vis) spectroscopy provided supporting evidence for the restoration of electronic conjugation to the graphene sheets, in addition to, the association of PSS with the graphene sheets, contributing to their stabilisation. The FT-IR of PSS-G (**Figure 5.11, Table 5.4**) showed that reduction of GO, in the presence of PSS, resulted in the loss of the carbonyl/carboxyl and epoxide bands at 1718 and 1225 cm^{-1}, respectively which were instead replaced by a sulfonate band at 1075 cm^{-1}, inherit of PSS polymer chains on the surface of the graphene sheets.

UV-Vis spectroscopy displayed, in the case of GO, a typical absorption band at 231 nm, as discussed in chapter 4, which was shifted to a band at 270 nm, after treatment with hydrazine hydrate, exhibiting significant restoration of in-plane electronic conjugation (C=C) (**Figure 5.12**). Furthermore, an additional band at 227 nm, inherent of PSS provided significant evidence for the association of polymer with the surfaces of the graphene sheets.[267]

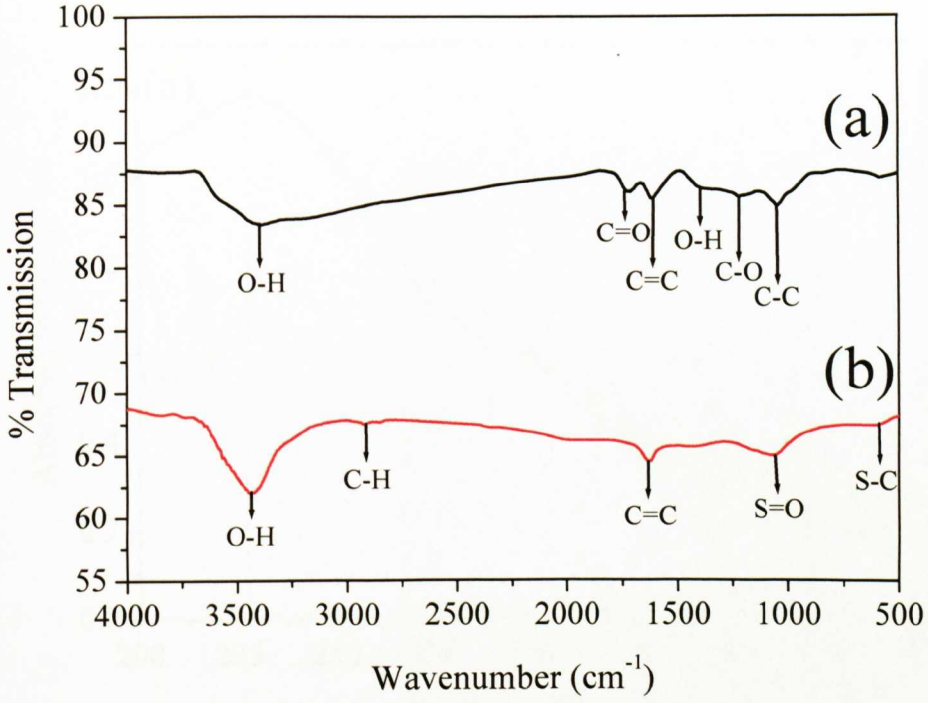

Figure 5.13 FT-IR spectrum of (a) graphene oxide (GO), from chapter 4, (b) PSS-stabilised graphene dispersions.

Sample Peak Shift (cm^{-1})		Assignment
GO	**PSS-G**	
3378	3437	O-H Stretch
2775 (broad)	2919/2850	C-H Stretch (alkyl)
1718	-	C=O Stretch (carbonyl)
1624	1627	C=C Stretch
-	1449	C-H Deformation (alkyl)
1385	-	O-H Deformation
1225	-	C-O Stretch (epoxide/hydroxyl)
-	1075	S=O /C-C skeletal vibration
1052	-	C-C skeletal vibration
831		Epoxide ring vibration

Table 5.4 Table showing the FT-IR peak assignments for dried, PSS-stabilised graphene dispersions.

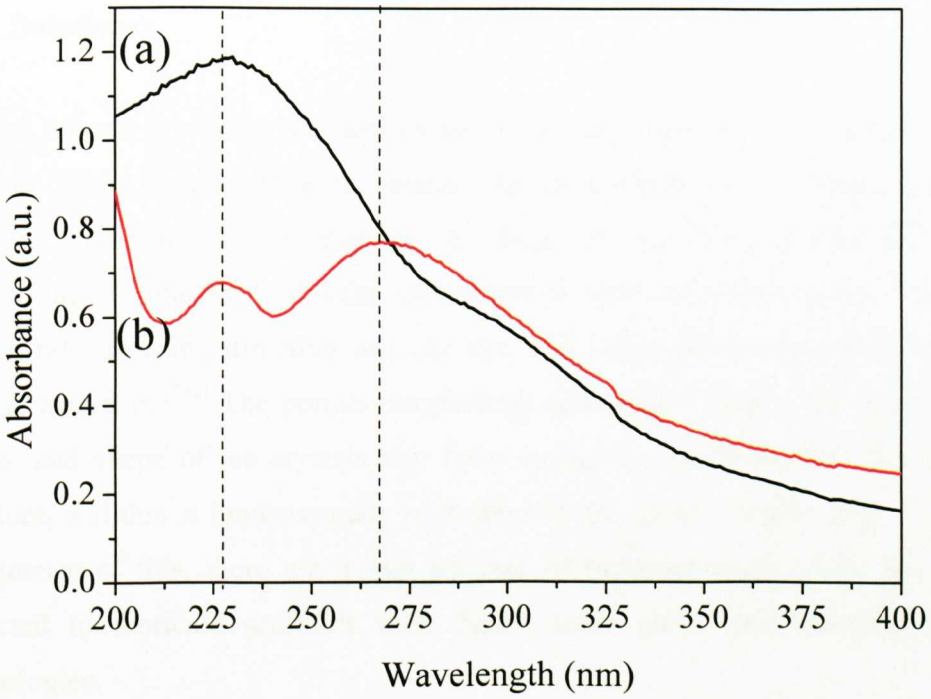

Figure 5.14 UV-Vis spectra of (a) graphene oxide, showing absorption band at 231 nm associated with oxidised conjugated carbon centres, and (b) PSS-G sheets showing bands at 227 and 270 nm corresponding to PSS and reduced graphene sheets, respectively.

5.4.2 Ice-Crystal Templating (ISISA) of Poly(vinyl alcohol) Control Solutions

Previous reports involving the application of the ice-segregation induced self-assembly (ISISA) technique demonstrated that the morphology of cryogenically processed monoliths is effected by a range of variables, including the composition of solute(s), solute(s) concentration and molecular weight (M_w), freezing rate, freezing direction and the size and shape of the mould that the solute is frozen in.[230] The porous morphology produced is ultimately based on the size and shape of ice crystals that form during the unidirectional freezing procedure, and this is fundamentally controlled by the factors listed above. As a consequence of this, there are a vast number of potential studies that can be conducted to fabricate scaffolds with finely tuned meso- and macroporous morphologies.

The primary aim of this chapter was to demonstrate the application of ISISA processing to aqueous dispersions of graphene sheets to fabricate macroporous monoliths. In general, the samples were transferred to 1 mL plastic, insulin syringes and unidirectionally frozen at freezing rates of 2, 5.9 and 10 mm min^{-1} in liquid nitrogen, as shown in the experimental set-up in **Figure 5.15**. Initial attempts to freeze aqueous dispersions containing PSS-stabilised graphene dispersions were unsuccessful, possibly due to the low solution viscosity and concentration, which contributed to the formation of scaffolds with poor mechanical properties. In order to provide structural stability to the graphene-based monoliths, an additional polymer was initially mixed with the graphene dispersion, prior to freezing, to provide precursor homogeneous sols with a higher viscosity than graphene dispersions alone.

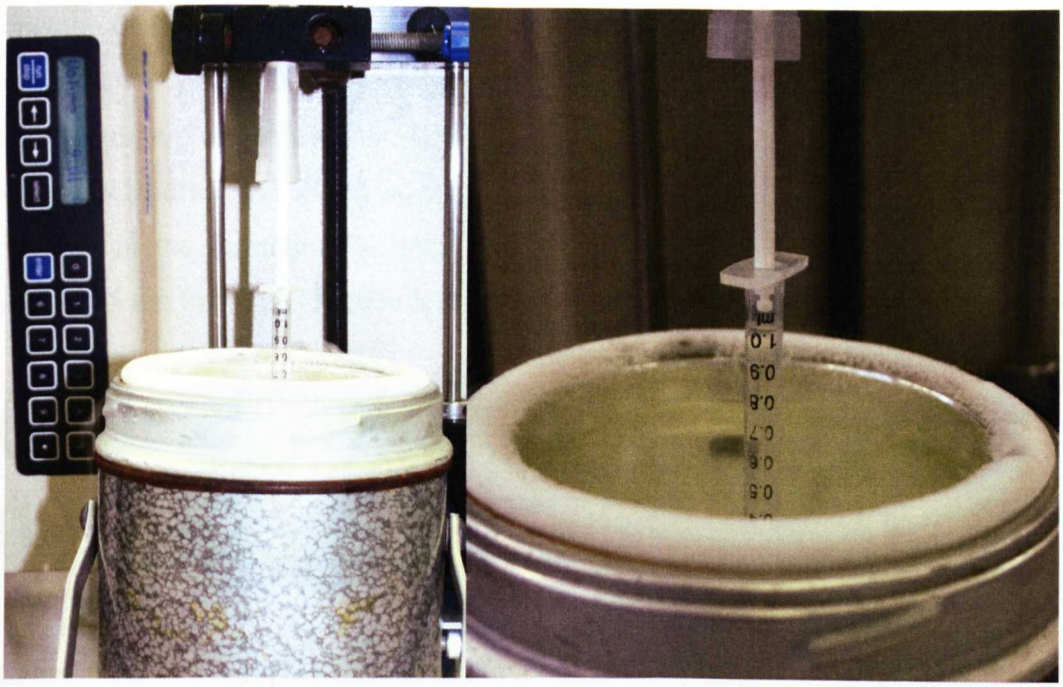

Figure 5.15 Photograph showing the experimental set-up for uni-directional freezing.

Previous investigations demonstrated that there are a range of polymeric materials that can be cryogenically processed using the ISISA technique to produce scaffolds with meso- and macroporous morphologies, including poly(vinyl alcohol) (PVA), chitosan, agar and a range of alternative biopolymers, as discussed in section 5.1.2. PVA proved to be an ideal candidate, for this study, due to its water-solubility and compatibility with PSS-G to form aqueous, homogenous sols. Furthermore, previous reports showed that PVA sols can be successfully cryogenically processed individually and in combination with various additives including silica (Ludox particles), cerium oxide colloidal suspensions and biomolecules to produce self-supporting, functional microporous monoliths.[209, 229] In order to choose an appropriate concentration of PVA to combine with PSS-G sols, a range of control PVA scaffolds were prepared with variation of the polymer molecular weight and the freezing rate.

Poly (vinyl alcohol) (PVA) control monoliths were initially prepared by placing aqueous polymer solutions (0.5 mL, 1, 5 and 10 wt.%, diluted with 0.5 mL H_2O) into 1 mL insulin syringes, which were subsequently uni-directionally frozen at

constant dipping rates of 2, 5.9 and 10 mm min^{-1} by lowering the syringe perpendicularly into liquid nitrogen (-196 °C). Once completely immersed in liquid nitrogen, the samples were kept in a liquid nitrogen bath (1-2 h), before being freeze-dried for 24-48 hours to remove the ice crystals by sublimation, resulting in the formation of intact, white, handleable monoliths, which were typically 5 cm in length (**Figure 5.16**).

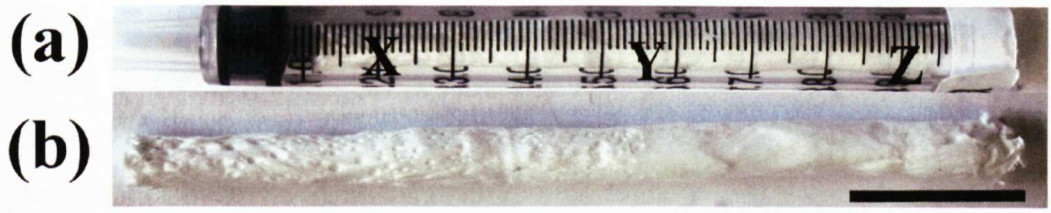

Figure 5.16 Photographic images of PVA control monoliths (2.5 wt.%) prepared by the ISISA technique at dipping rates of 5.9 mm min^{-1}, (a) before removal from the syringe showing the different sections X (immersion end), Y and Z and (b) after removal from the syringe showing white, handleable monoliths, scale bar is approximately 1 cm.

The effect of variation of the concentration of PVA on the monolith formation was initially investigated. PVA monoliths prepared at the lowest concentration (0.5 wt.%) exhibited poor mechanical properties and as a result could not be removed from the syringes and cut into sections for further analysis. This is a consequence of the small amount of polymeric matter in the solution which cannot support the macroporous channel formation. Scaffolds prepared at higher concentrations (2.5 and 5 wt.%) were much stronger but care was still required when cutting the scaffolds into sections for morphological assessment, to ensure their structure was not greatly distorted. Unfortunately, sections from the Z region could not be analysed as this region was particularly soft and as a result, difficult to cut efficiently without damaging and distorting the shape of the monolith. For this reason, the morphology of sections from the regions proximal to the immersion end (X) and in the middle of the scaffold (Y) were investigated.

The effect of the freezing rate on the monolith formation, in addition to PVA concentration, was subsequently investigated. Closer inspection, using scanning

electron microscopy (SEM) analysis, of cross and longitudinal sections obtained from regions proximal to the immersion end of the syringe (X) and in the middle (Y) of the monolith showed that the monoliths were highly porous (**Figures 5.15-5.18**). Furthermore it was apparent that the pore diameters and shapes were highly dependent on the initial concentration of PVA, the freezing rate and the area of the scaffold being examined (section X or Y).

SEM images of cross-sections from the X regions of control PVA scaffolds (2.5 wt.%) displayed pores with a distorted, spherical shape (**Figure 5.17a-c**). In general scaffolds prepared at the lowest dipping rate of 2 mm min^{-1} displayed smaller pores observed at the centre, with average diameters of 6.93 μm and larger pores at the edges, with larger, average pore sizes of 19.5 μm (**Figure 5.17a**). Increasing the freezing rate, displayed comparable, irregularly shaped pores with average diameters which decreased in size with increasing freezing rate, measuring 12.1 and 7.2 μm for dipping rates of 5.9 and 10 mm min^{-1}, respectively (**Figure 5.17b-c**).

In comparison, SEM images of sections taken from the central region (Y) of the scaffold prepared at the slowest freezing rate of 2 mm min^{-1}, revealed, in general, well-defined, cross-linked pores, with increased average diameters of 23.6 μm (**Figure 5.17d**). In contrast, SEM images from the comparable regions (Y) of scaffolds prepared at faster freezing rates of 5.9 and 10 mm min^{-1} revealed the formation of layered architectures, consisting of poorly connected parallel layers of PVA sheets (**Figure 5.17e-f**). (Average pore diameters and ranges are summarised in **Table 5.5**).

Furthermore SEM images of longitudinal sections of control PVA scaffolds (2.5 wt.%), cut parallel to the direction of freezing, revealed well-aligned macroporous channels. In general, the channels observed in the region proximal to the immersion end (X) were not as well defined as in the central region (Y). The average separation of the channels in the central region of the scaffold (Y) was 30.2, 33.0 and 32.5 μm at freezing rates of 2, 5.9 and 10 mm min^{-1}, respectively, showing a high degree of consistency (**Figure 5.18**).

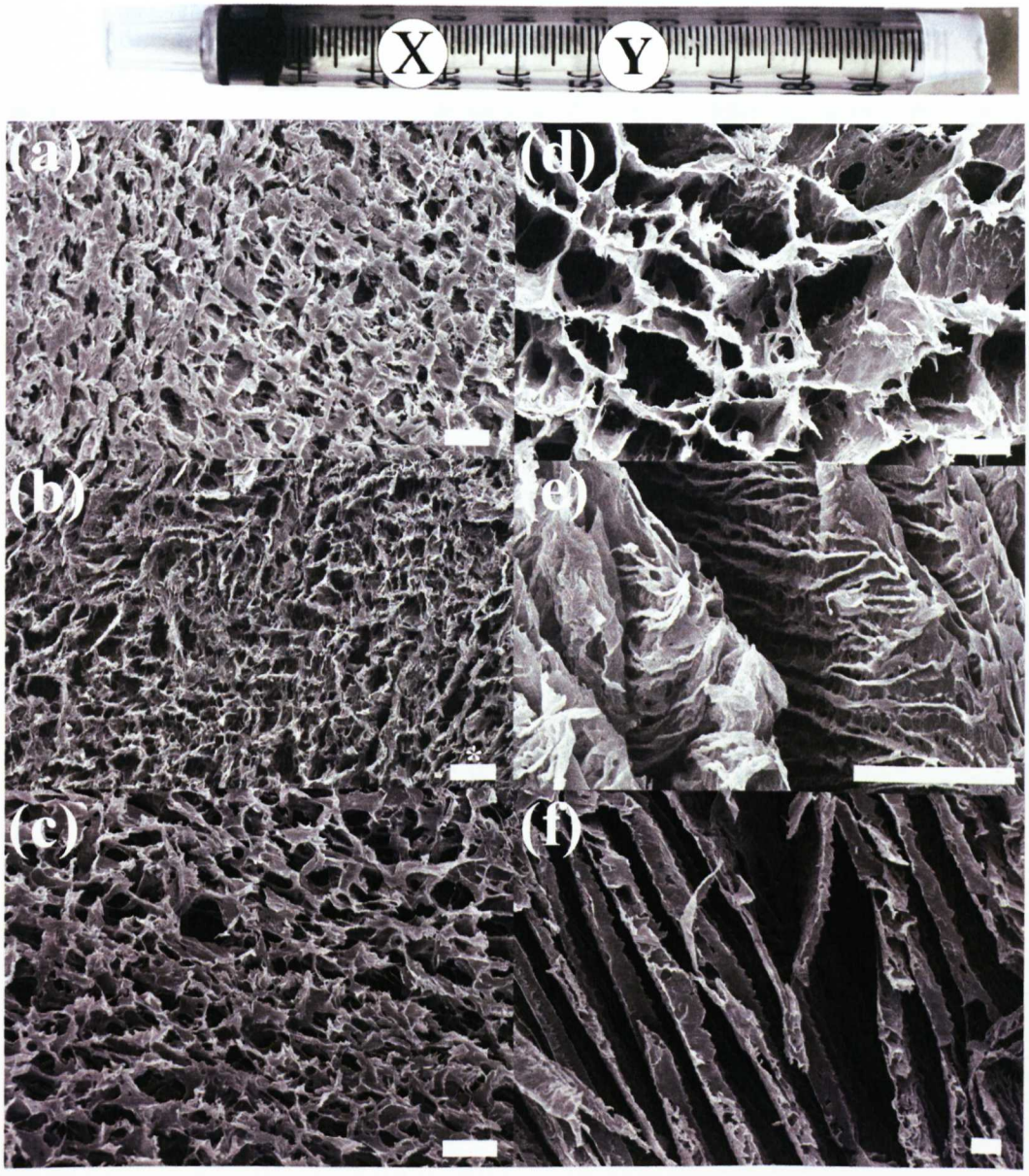

Figure 5.17 Cross-sectional SEM images of PVA monoliths (2.5 wt.%) originating from (a-c) the X and (d-f) Y regions, respectively, prepared at dipping rates of (a, d) 2 mm min^{-1}, (b, e) 5.9 mm min^{-1} and (c, f) 10 mm min^{-1}. Scale bars: (a), (c- f) = 20 μm and (b) = 50 μm (*).

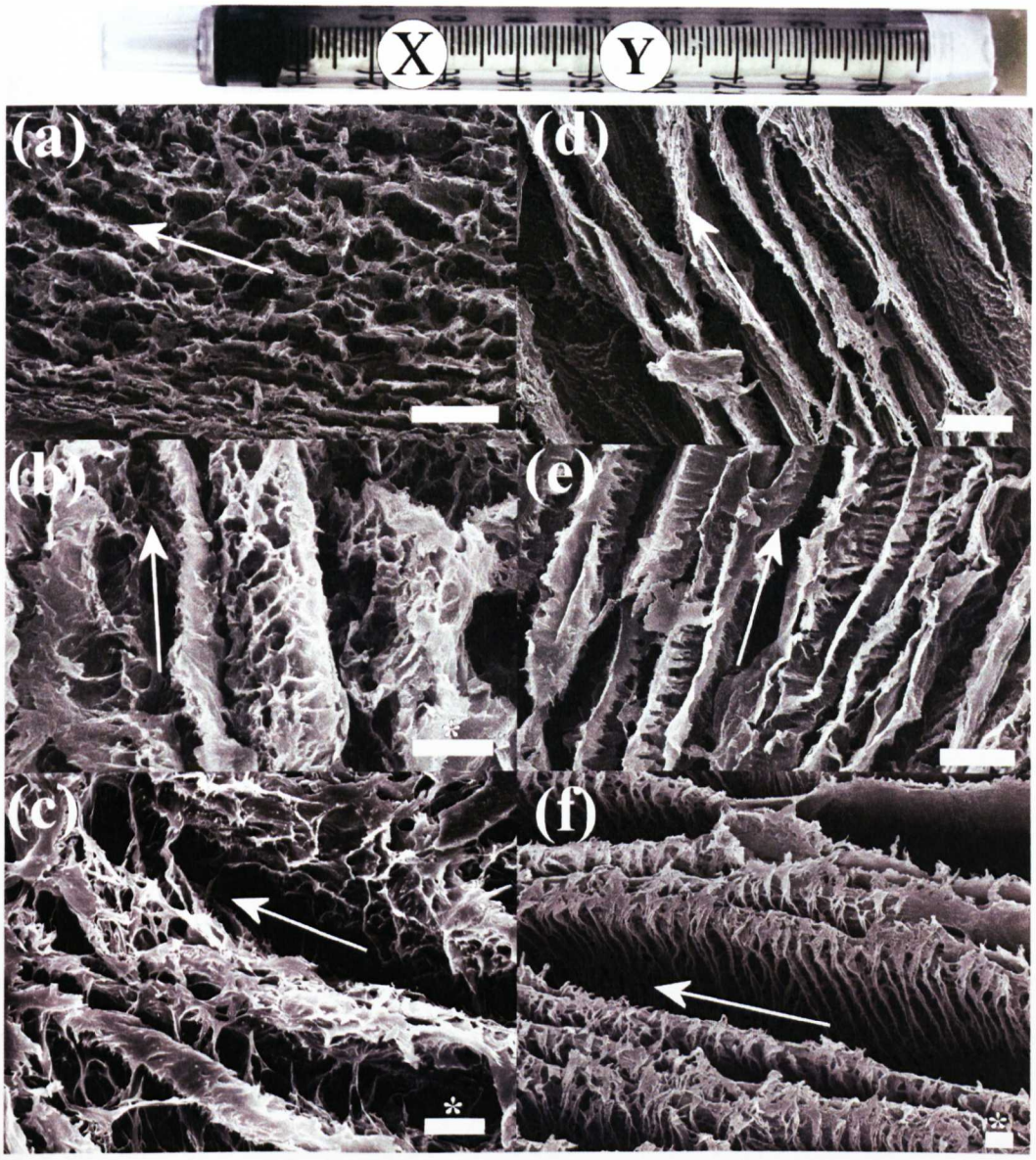

Figure 5.18 Longitudinal-sectional SEM images of PVA monoliths (2.5 wt.%) originating from (a-c) the X and (d-f) Y regions, respectively, prepared at dipping rates of (a, d) 2 mm min^{-1}, (b, e) 5.9 mm min^{-1} and (c, f) 10 mm min^{-1}. Scale bars: (a), (d-e) = 50 μm and (b-c) and (f) = 10 μm (*).

Freezing Rate (mm min^{-1})	Average pore diameters or channel separations (*)/μm (Pore diameter ranges/μm)	
	X region	Y region
2	Interior: 6.9 μm (0.57-18.9 μm) Exterior: 19.5 μm (4.9-43.9 μm)	23.6 μm (3.0-71.4 μm)
5.9	12.1 μm (1.4-42.6 μm)	26.5 μm (*) (23.7-28.7 μm)
10	7.2 μm (0.9-20.9 μm)	33.3 μm (*) (15.7-86.3 μm)

Table 5.5 Average pore diameters and ranges of cross-sectional images of PVA scaffolds (2.5 wt. %).

Cross-sectional SEM images of the X regions of PVA scaffolds, prepared at an increased concentration (5 wt. %) revealed similarly porous morphologies (**Figure 5.19**). In general, the average pore diameters decreased in size with increasing freezing rates, as observed previously with the PVA scaffolds prepared at a lower concentration (2.5 wt. %). Average pore diameters and ranges are summarised in **Table 5.6**. Scaffolds prepared at the lowest freezing rate (2 mm min^{-1}) displayed inter-connected channels, with an average pore diameter of 15.2 μm (**Figure 5.19a**). In comparison, PVA scaffolds prepared at an increased freezing rate (5.9 mm min^{-1}) displayed pores with a reduced average pore diameter of 6.2 μm (**Figure 5.19b**). Furthermore, scaffolds prepared at the fastest freezing rate (10 mm min^{-1}) displayed an irregularly-shaped, closed porous network, containing small pores, with average diameters of 4.5 μm (**Figure 5.19c**)

Comparable cross-sectional, SEM images of PVA scaffolds (5 wt.%) from the Y region displayed lamellar architecture, with the separation and nature of the channels dependent on the freezing rate. Images from scaffolds prepared at a freezing rate of 2 mm min^{-1} revealed well-defined walls, with an average thickness and separation of 33.4 and 16.3 μm, respectively. Interestingly, the walls of these structures were composed of highly sophisticated porous pillars. Increases in the freezing rate to 5.9 and 10 mm min^{-1} produced similar lamellae structures with "fish-bone" morphology, as reported previously by the Cooper

group.[209] The channels were separated by an average distance of 9.2 and 44.4 μm for freezing rates of 5.9 and 10 mm min^{-1}, respectively (**Figure 5.19e-f**).

SEM images of longitudinal sections of PVA scaffolds (5 wt.%) from region X, displayed aligned macroporous channels for freezing rates of 2 and 5.9 mm min^{-1} corresponding to the direction of the growth of the ice crystals, which is consistent with the freezing direction (**Figure 5.20a-c**). In the case of freezing at the fastest rate of 10 mm min^{-1} the channels were extremely poorly defined (**Figure 5.20c**). Analysis of sections originating from region Y, displayed, on the other hand, well-alligned channels (**Figure 5.20d-f**).

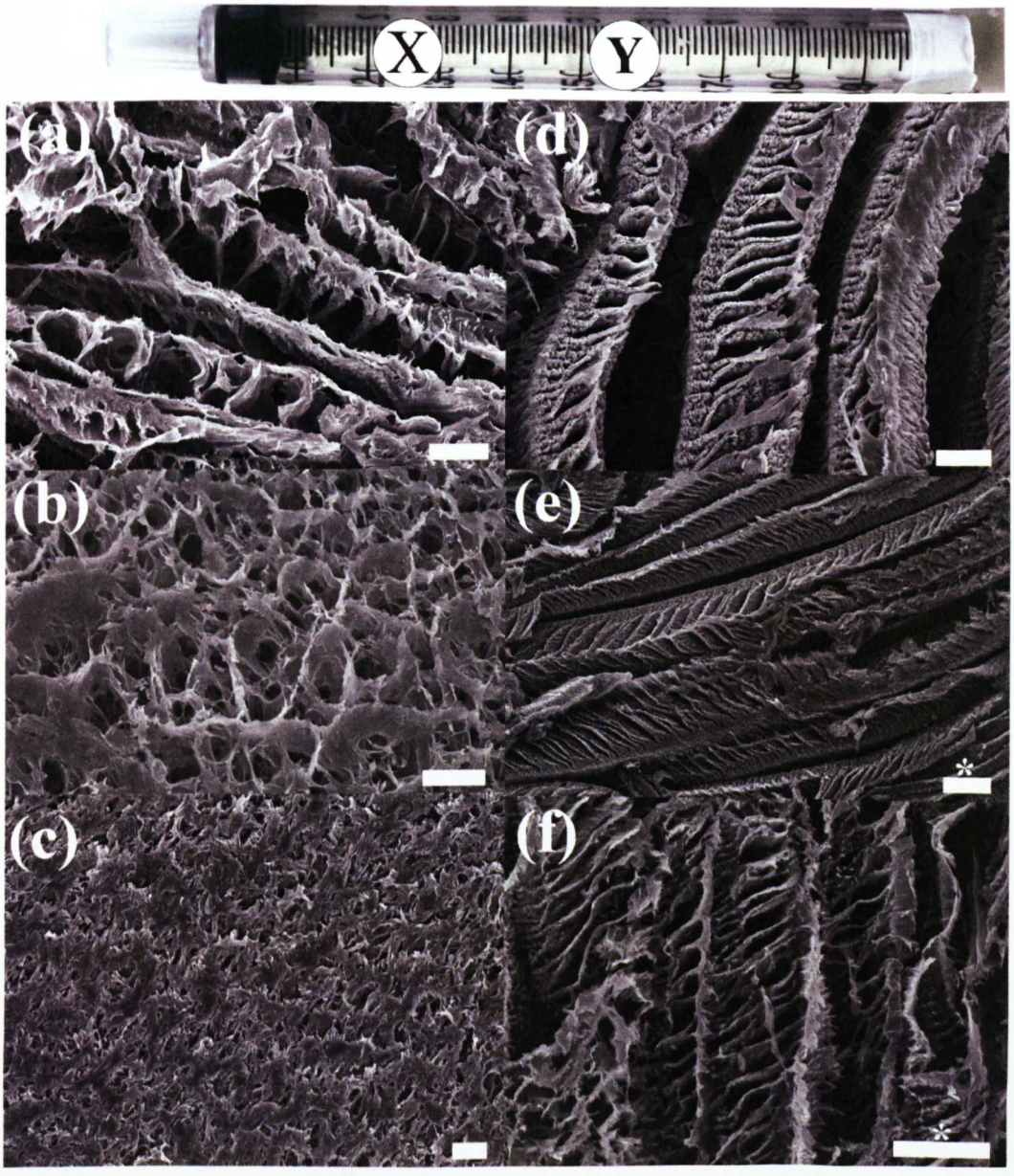

Figure 5.19 Cross-sectional SEM images of PVA monoliths (5 wt.%) originating from (a-c) the X and (d-f) Y regions, respectively, prepared at dipping rates of (a, d) 2 mm min^{-1}, (b, e) 5.9 mm min^{-1} and (c, f) 10 mm min^{-1}. Scale bars: (a-d) = 20 μm and (e-f) = 50 μm (*).

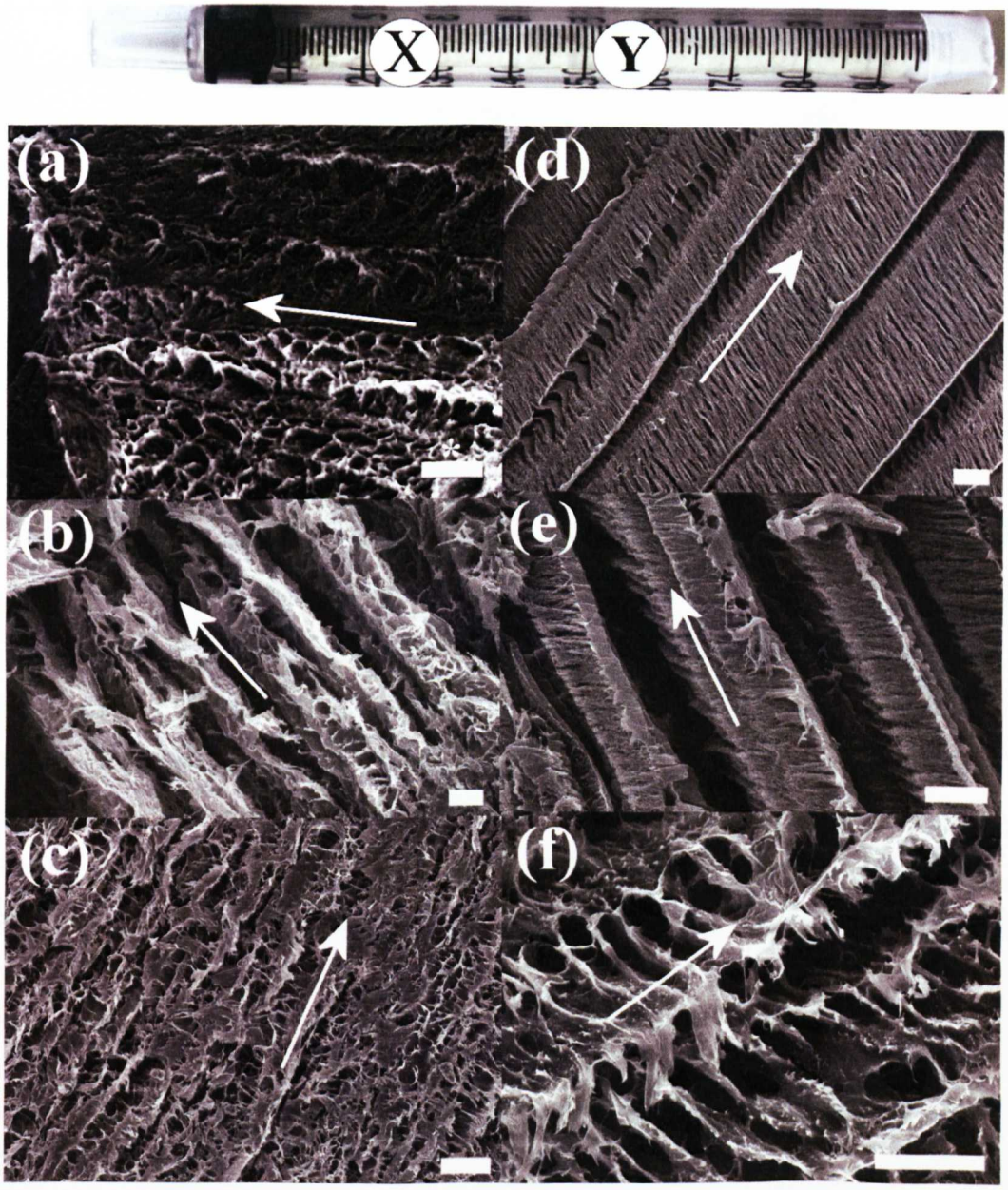

Figure 5.20 Longitudinal-sectional SEM images of PVA monoliths (5 wt.%) originating from (a-c) the X and (d-f) Y regions, respectively, prepared at dipping rates of (a, d) 2 mm min^{-1}, (b, e) 5.9 mm min^{-1} and (c, f) 10 mm min^{-1}. Scale bars: (a) = 100 μm (*) and (b-f) = 20 μm.

Freezing Rate (mm min^{-1})	Average separation of channels/μm (Pore diameter ranges/μm)	
	X region	**Y region**
2	15.2 μm (7.3-25.6 μm)	16.3 μm (5.4-28.7 μm) Thickness of walls: 33.4 μm (20.9-46.8 μm)
5.9	6.2 μm (1.4-14.5 μm)	9.2 μm (3.0-21.1 μm)
10	4.5 μm (1.0-13.0 μm)	44.4 μm (28.7-56.3 μm)

Table 5.6 Average pore diameters and ranges of cross-sectional images of PVA scaffolds (5 wt.%).

Both the X and Y regions of the PVA scaffolds (5 wt. %) displayed a degree of radial heterogeneity in the cross-sectional images, with larger pores observed at the exterior of the scaffold and smaller pores observed in the interior. This observation was similarly reported by Gutierrez et al.[229] The extent of this effect increased with increases in the freezing rates, demonstrating an increase in the area of the non-porous core, as shown in the SEM images in **Figure 5.21**. This observed heterogeneity may be due to inefficient cooling of the monolith due to increasing freezing rates, which impedes the formation of ice crystals at the core but enables effective ice crystal formation to occur at the periphery.

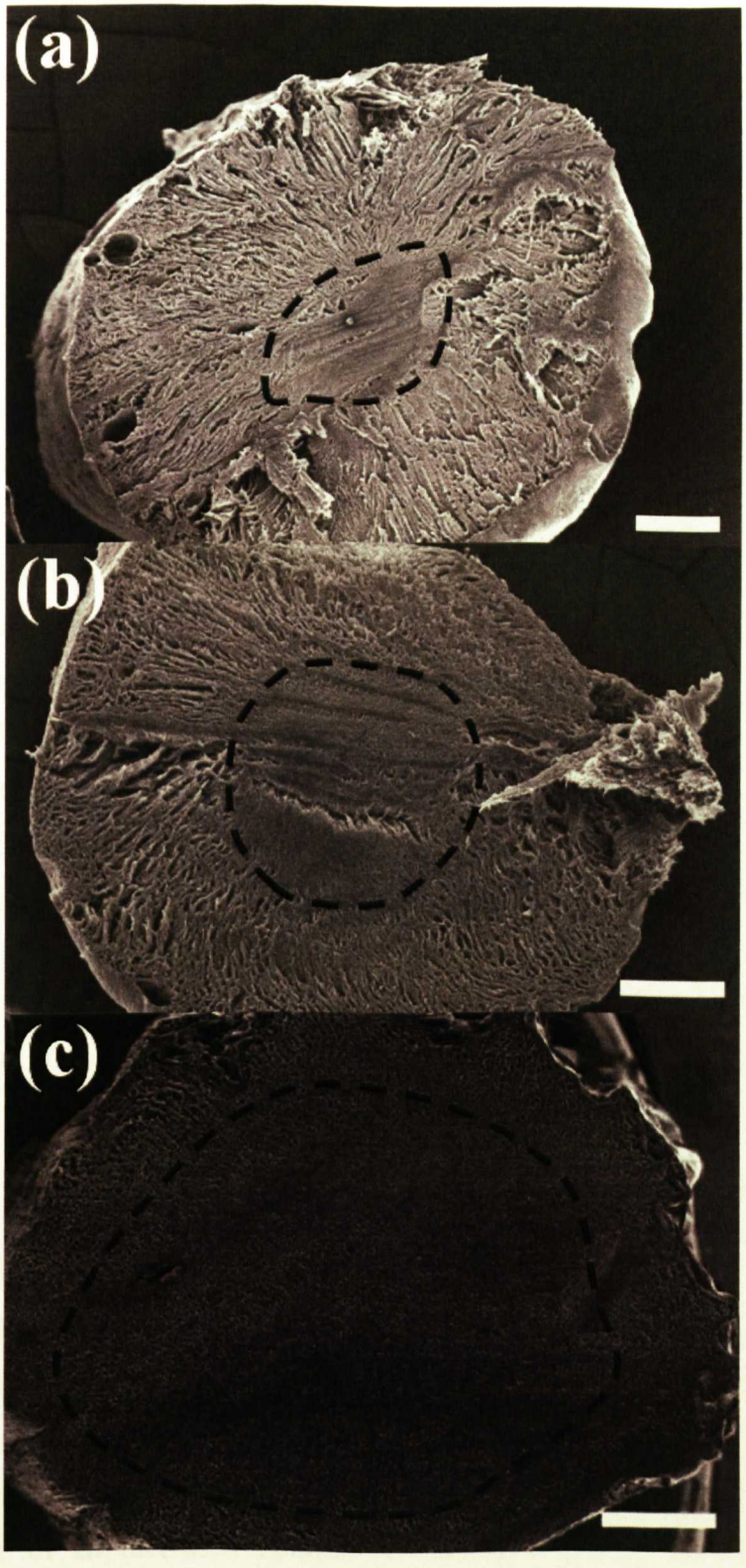

Figure 5.21 Cross-sectional SEM images of PVA scaffolds (5 wt. %) prepared at dipping rates of (a) 2 mm min^{-1}, (b) 5.9 mm min^{-1} and (c) 10 mm min^{-1}, showing an increase in the degree of radial heterogeneously with increasing freezing rate, scale bar = 0.5 mm.

In summary, the application of the ISISA technique to PVA, appears to produce monoliths with different degrees of macroporosity, depending on the section of the monolith being investigated (region X or Y), the concentration of PVA (2.5 or 5 wt. %) and the freezing rates (2, 5.9 or 10 mm/min). Ultimately the morphological features that are produced are directly controlled by the size of ice crystals that form.

Investigation of different areas of the scaffold presented varied morphologies. In general, the middle regions of the scaffold (Y) displayed more regular and well-defined features, forming either interconnected porous or lamellar architectures. In comparison the regions proximal to the immersion end presented less well-defined features and smaller, closed pores. These regional variations may be due to the presence of temperature gradients in the monolith, which will have a retarding effect on the formation of ice crystals in the scaffold. One reason for the temperature gradient is related to the fact that liquid nitrogen is a poor thermal conductor, which means that regions proximal to the immersion end will not be effectively cooled and frozen, contributing to the formation of smaller ice crystals and irregularly shaped pores.[229]

Increasing the concentration of PVA from 2.5 to 5 wt. %, appeared to contribute towards the formation of macroporous structures with increased order after sublimation of the ice crystals. Although previous reports predict that increases in the concentration of PVA impede the ice crystal growth, there are additional factors which influence the crystallisation process.[229, 268] In particular, the shape and size of the polymer, including the molecular weight and degree of hydrolysis will determine the effectiveness of ice crystal formation in PVA solutions. Indeed, these results demonstrate that increases in the PVA concentration provided more structural integrity to the macroporous channel, possibly due to the presence of an increased amount of matter in the walls and therefore contributed to the formation of larger channels and pores.

Variation of the freezing rate for PVA scaffolds (2.5 wt. %) demonstrated a general decrease in the pore diameters for scaffolds obtained from region X, with increasing freezing rates. This similar trend was more evident in scaffolds with a

higher PVA concentration (5 wt. %), with pore diameters decreasing from 15.2 to 4.5 μm, as the freezing rate was increased from 2 to 10 mm min^{-1}, respectively. This is intuitive because lower freezing rates provide more time for ice crystallisation to occur, contributing to the formation of larger ice crystals.

In comparison, SEM analysis conducted on PVA scaffolds (2.5 wt. %) from regions obtained from the middle of the scaffold (Y), demonstrated that the slowest freezing rate in general produced porous macroporous morphologies, with increases in the freezing rate contributing to the formation of lamellae channels. In comparison, PVA scaffolds at a higher concentration (5 wt.%) demonstrated the consistent formation of lamellae features, with the slowest freezing rate producing channelled structures with well-defined thick walls and open porous channels, again possibly as a result of the increased amount of time for ice crystals to form contributing towards the formation of large ice crystals.

5.4.3 Ice-Crystal Templating (ISISA) of PSS-G/PVA Homogeneous Solutions

As discussed previously in this chapter, in order to fabricate graphene-based scaffolds which are self-supporting, an additional polymer is required to provide structural support to the scaffold. As demonstrated in the previous section, ISISA processing of PVA solutions, with concentrations of 2.5 and 5 wt. %, resulted in the formation of white monoliths with macroporous architecture. For this reason, PVA was chosen to fabricate PSS-G/PVA composite scaffolds. Given the previous observations, an optimum PVA stock sol concentration and freezing rate of 5wt. % and 5.9 mm min^{-1}, respectively were chosen to investigate the formation of PSS-G/PVA scaffolds. PVA stock sols with lower concentrations were desirable for a number of reasons. Firstly, the lower solution viscosity made it easier to form homogeneous sols, which could be subsequently transferred to the syringes for freezing. Furthermore, lower polymer concentrations are favourable as they help to promote ice crystal formation on freezing and reduce the degree of heterogeneity observed in the pore diameters.[229]

PSS-G/PVA monoliths were successfully prepared by combining PVA sols (0.5 mL, 5 wt. %) with PSS-G sols (0.5 mL, 0.5 wt.%). The PSS-G/PVA homogeneous sols (1:10 wt. ratio) were subsequently transferred to 1 mL syringes and uni-directionally frozen in liquid nitrogen, as described previously for PVA, resulting in the formation of black, handleable monoliths, which were typically 5 cm in length (**Figure 5.22**). Importantly, the PSS-G/PVA monoliths were fully intact and at first site appeared to be mechanically stronger, compared to frozen monoliths prepared in the absence of PVA. SEM was applied for closer inspection of the morphological features of the PSS-G/PVA freeze-dried monoliths (1:10 wt. ratio), prepared at a freezing rate of 5.9 mm min^{-1} in the regions proximal to the immersion end (X) and the centre of the scaffold (Y).

Figure 5.22 Photographic images of PSS-G/PVA freeze-dried monoliths prepared by the ISISA technique, (a) before removal from the syringe showing the different sections investigates X (immersion end), Y and Z; (b) at 1:5 wt. ratio; (c) 1:10 wt. ratio; (d) 3:20 wt. ratio.

SEM images of cross-sections from region X displayed ordered, lamellar architecture with poorly cross-linked channels separated by an average distance of 5 μm, which ranged from 3.7 to 12.2 μm (**Figure 5.23a-b**). In comparison, SEM images from the Y region displayed cross-linked, channel-like architectures with larger pore diameters ranging from 5 to 25 μm (**Figure 5.23c**). Moreover, higher-magnification SEM images of the lamellar region indicated that the walls were approximately 1 μm thick and particularly textured, comprising a network of loosely packed graphene sheets, embedded in the polymer matrix (**Figure 5.23d**). Furthermore, SEM images of longitudinal sections, displayed well-alligned macroporous channels oriented in the freezing direction, as described previously for PVA monoliths (**Figure 5.24**).

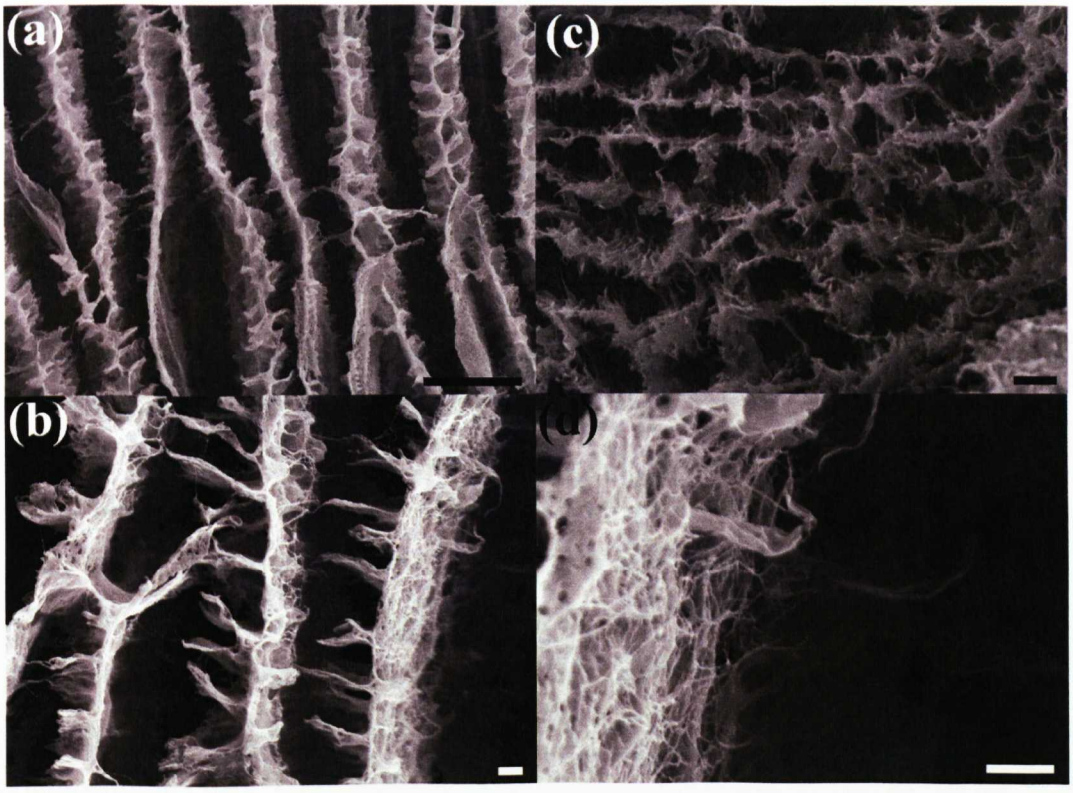

Figure 5.23 Cross-sectional SEM images of PSS-G/PVA monoliths (1:10 wt. ratio), (a, b, d) from region X and (c) from region Y. Scale bars = 10 μm, figure (a) and (c) and 1 μm, figures (b) and (d).

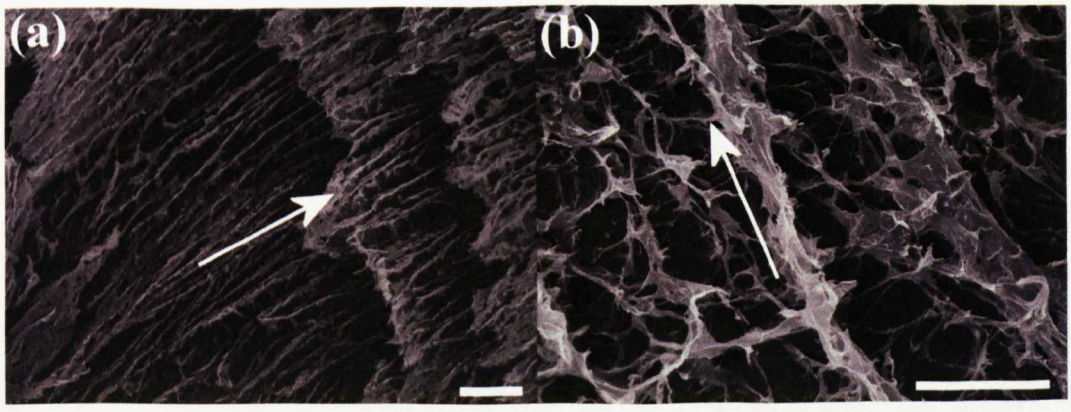

Figure 5.24 Longitudinal SEM images of PSS-G/PVA monoliths (1:10 wt. ratio), (a) from region X and (b) from region Y. Scale bars = 10 μm.

5.4.4 Mechanistic Discussion for the Formation of Macroporous Scaffolds

The formation of macroporous architecture is ultimately controlled by the size and shape of ice crystals that form during the freezing process which act as templates and cause all matter residing in the aqueous solution to be segregated to the external regions of the ice crystals. Therefore, in order to understand the mechanism of formation of well-aligned scaffolds, attention must be placed on the mechanism of formation of the ice crystals.

It is well known that cooling of water, below the freezing point, results in the formation of crystalline ice. Ice crystallisation is highly dependent on the freezing temperature and rate in addition to the presence of any external impurities or components in the water and can be inhibited if the freezing rate exceeds 10^6 °C/s and the freezing temperature drops below the glass transition temperature (-137 °C) in addition to increases in the solute concentration above a certain threshold level.[269] In this study we demonstrated the effective ice-templating of PVA and PSS-G/PVA solutions to produce macroporous architectures, however there were significant variations in the size and shape of the channels, with certain regions exhibiting larger pores compared to others.

The pore size is tightly controlled by the nature and concentration of the solute, the freezing rate and freezing temperature. In general, large solutes and/or high solute concentrations yield small crystals, while small solutes and/or low solute concentration yield large one. Furthermore, variation in the scaffold morphology can be created due to the generation of temperature gradients which form when the sample is lowered into the liquid nitrogen, as follows.[230]

When samples are uni-directionally lowered into liquid nitrogen, a temperature gradient is created, parallel to the freezing direction. Furthermore, an ice front is created, which is located along the non-immersed section, perpendicular to the direction of freezing. Diffusional heat losses cause the temperature at the ice front to be greater than the temperature of liquid nitrogen (-196 °C). As the sample is gradually lowered into liquid nitrogen, the ice front moves further away from the immersion end, with a corresponding further increase in the

temperature, until it is high enough to promote ice crystal growth. In general, larger ice crystals form at higher freezing temps and vice-versa. This means the pore diameter is directly related to the distance from the immersion end. In regions which are closer to the immersion end (region X), the freezing temperature is lower, contributing to the formation of small ice crystals and as a consequence of this smaller pores after sublimation of the ice. The size of ice crystals are additional affected by the freezing rate. Fast freezing rates have the consequence of reducing the gap between the ice front and the immersion end, resulting in lower freezing temperatures and the formation of small ice crystals.[230]

Furthermore, previous reports demonstrated that it is possible to grow ice-crystals in the form of platelets, with a high aspect ratio, if steady-state conditions are applied, contributing to the formation of lamellar microstructures after sublimation of the ice, with the lamellae thickness dependent on the freezing rate.[224]

5.4.5 Compressional Testing of the Ice-Templated Macroscopic Graphene-Polymer Composites

The incorporation of PSS-G sheets into the walls of the PVA scaffold as discussed in the previous section, did not appear to hinder the formation of macroporous architecture. Furthermore, the preparation of sections for SEM analysis demonstrated that the scaffolds were in general, much tougher to cut, this led to further investigation of the mechanical and structural properties of the PSS-G/PVA composite scaffolds. Mechanical testing was performed by applying compressional loads to cylindrical sections (4 mm in diameter, 5 mm in length) taken from regions proximal to the immersion end of the syringe (X) and the middle region (Y) of both PVA control and PSS-G/PVA composite monoliths. Stress-strain graphs acquired from mechanical testing displayed linear elastic properties at low stress, followed by a collapsed plateau, indicative of failure of the polymeric wall structure (**Figure 5.25**). Compressional moduli were subsequently calculated from the linear slope of the elastic region. The small, curved region observed in the initial stages of the graph corresponded to non

conformed contact between the plate and the specimen, which contributed towards an underestimate of the initial range of strains place on the sample.

Mechanical testing of the graphene-containing macroporous monoliths indicated that although the structures had low average compressional moduli, these were threefold higher then ISISA-derived samples of PVA scaffolds alone. Typical values ranged from 1.49 to 5.65 and 0.23-1.87 MPa for PSS-G/PVA monoliths (PSS-G/PVA wt. % = 1:50) and PVA scaffolds, respectively. Interestingly, the mechanical properties of the scaffolds appeared to depend on the region tested. In general, PVA monoliths derived from the region in the middle of the scaffold (region Y) exhibited a tenfold increase in the Young's moduli, when compared with the X region (**Table 5.7**). The opposite trend, however, was observed in the case of PVA scaffolds reinforced with PSS-stabilised graphene sheets (PSS-G), where a higher Young's modulus was observed in sections originating from the region proximal to the immersion end of the syringe (region X).

This is consistent with previous SEM observations which demonstrated that in the case of sections of PVA monolith, derived from the middle of the scaffold (Y), a more ordered structure is displayed, compared with the X region, contributing to a stronger matrix. In the case of PSS-G/PVA scaffolds, on the contrary, where the X region appears to be stronger than the Y region, this may be related to increased structural order in addition to gravitational effects causing PSS-G sheets to sink to the bottom of the syringe, contributing to a greater proportion of PSS-G sheets to be present in the walls of the macroporous matrix, resulting in significant strengthening of the scaffold.

These preliminary results indicated that incorporation of PSS-G sheets into the scaffolds appeared to increase the structural stability of the microstructured walls. Further work in this area could investigate the effects of increase graphene loadings and variation of freezing rate on the compressional properties of the scaffolds.

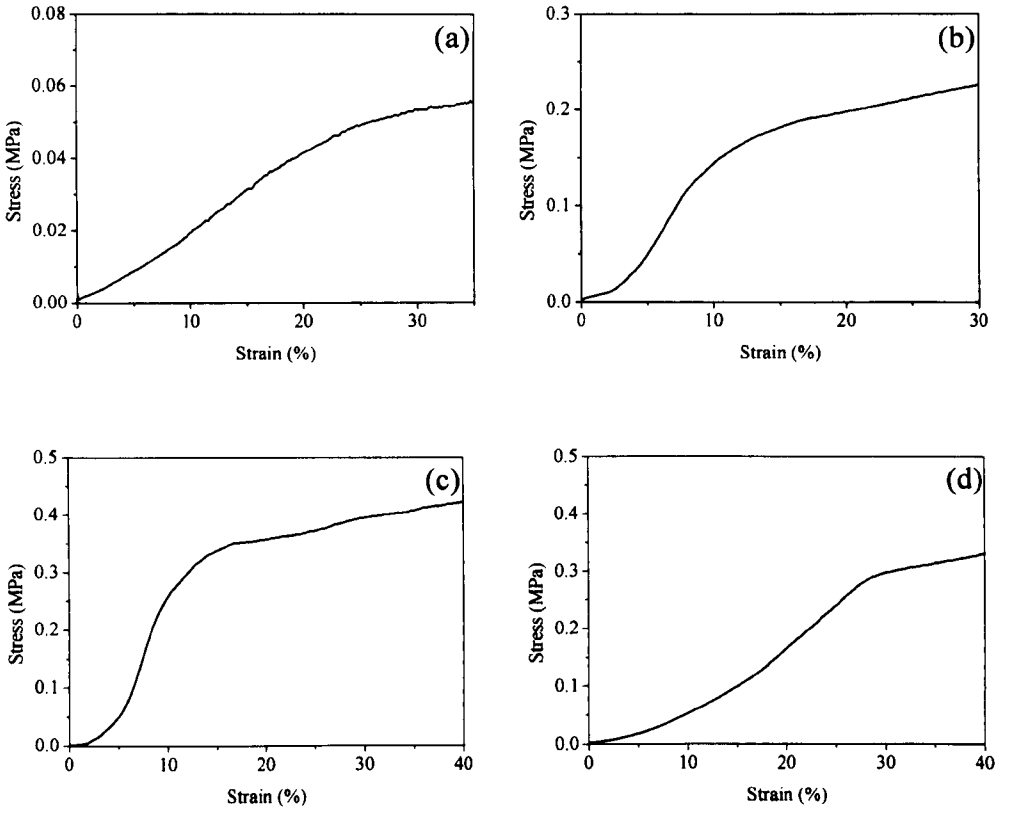

Figure 5.25 Stress-strain graphs of (a-b) PVA monoliths and (c-d) PSS-G/PVA monoliths (1:50 wt. ratio). Samples (a,c) correspond to sections from region X and samples (b,d) correspond to sections from region Y.

Sample	Young's Compressional Moduli (MPa)	
	X Region	Y Region
PVA control scaffold	0.290 (0.23-0.36)	2.002 (1.87-2.13)
PSS-G/PVA scaffold	5.168 (4.88-5.65)	1.636 (1.49-2.07)

Table 5.7 Comparison of the Young's compressional moduli for control PVA and PSS-G/PVA monoliths, from the X and Y regions.

5.4.6 Electrostatically-Induced Assembly of PSS-G Dispersions onto Colloidal Polymer Beads

In the previous section, unilamellar PSS-G sheets were successfully templated into higher-order three-dimensional macroporous architectures, based on the stepwise formation of ice crystal templates during unidirectional freezing processes and their subsequent removal on sublimation. In this section, templating of polymer-stabilised graphene sheets on the micro-scale is investigated using electrostatic-induced assembly of negatively charged PSS-stabilised graphene sheets and positively charged polymer coated colloidal beads or microparticles.

As discussed in section 5.1.4, there are numerous reports demonstrating the application of colloidal beads or particles, as templates for a range of organic (biological), inorganic or polymeric materials, based on electrostatic-induced assembly. In many case, these colloidal microparticles act as sacrificial templates and can be readily removed by dissolution or calcination processes. As the portfolio of particle templates is vast, this section seeks to demonstrate the methodology of graphene templating on the micro-scale, through the application of polystyrene particles (PS). PS beads were chosen for these studies, not only because they are readily available but also because they can be easily dissolved with an organic solvent, for examples dichloromethane or toluene to produce hollow micrometre-sized spheres.

PSS-G dispersions are highly negatively charged (zeta potential = -73 mV) due to the presence of sulfonate groups attached to the backbone of the stabilising polymer, in additional to residual oxygen-containing functional groups on the basal planes of the graphene sheets. Direct addition of PSS-G dispersions to a colloidal suspension of negatively charged PS beads (zeta potential = -48 mV), did not result in precipitation or sedimentation. In order to successfully assemble the polyanionic PSS-G sheets onto the surface of negatively charged micro-metre sized PS bead (diameter ~ 990 nm), the surface of the beads had to be initially primed with a positively charged polymer. Poly(allylamine hydrochloride) (PAH) is a well established polymer for this application and PS beads were

repeatedly incubated in PAH sols for 30 mins (three cycles), followed by three centrifugation/washing cycles to ensure effective removal of unassociated polymer and uniform distribution of the positively charged polymer on the surface of the bead. Zeta potential measurements of PAH-coated PS beads demonstrated successful association of the polymer with the bead surface (PAH-PS beads, zeta potential = +37 mV).

Addition of PAH-PS beads to PSS-G sols and subsequent agitation of the solution, through the use of a vortexer, resulted in immediate sedimentation. The black sediment was isolated via centrifugation and subsequently washed. SEM was applied for closer inspection of the morphological features of the PSS-G/PS bead nanocomposite. SEM images of the black precipitate indicated that the surface of the polystyrene beads was uniformly coated in sheet-like features consistent with PSS-G sheets (**Figure 5.27**). Closer inspection of the topographic features of the graphene-coated PS beads, using higher magnification SEM images, revealed crinkled features and roughened textures, previously observed in TEM images of flexible, ultrathin polymer-coated graphene sheets. Furthermore, edges of overlapping and individual sheets were observed, particularly at the interface between aggregated particles, where they appeared to link neighbouring beads. In contrast SEM images of uncoated beads (PS beads) displayed smooth, untextured surfaces (**Figure 5.26**).

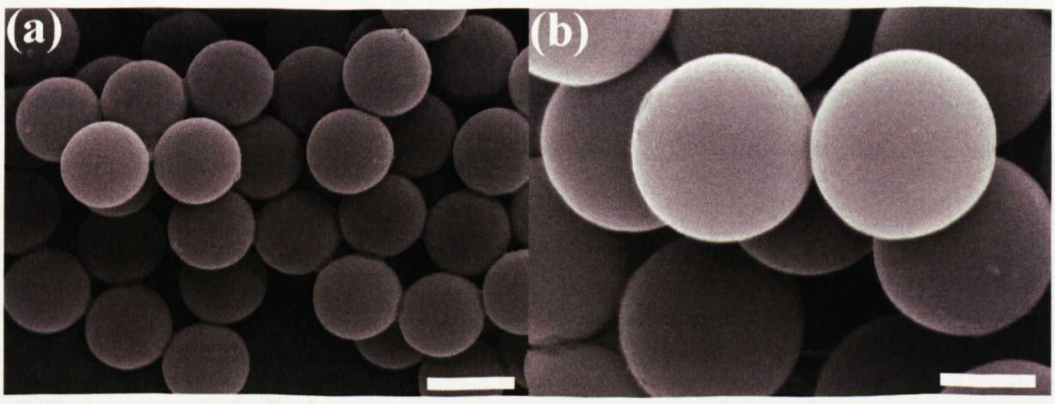

Figure 5.26 SEM images of uncoated polystyrene beads at (a) low and (b) high magnification, showing the smooth bead surface. Scale bars = 1 μm and 500 nm, respectively.

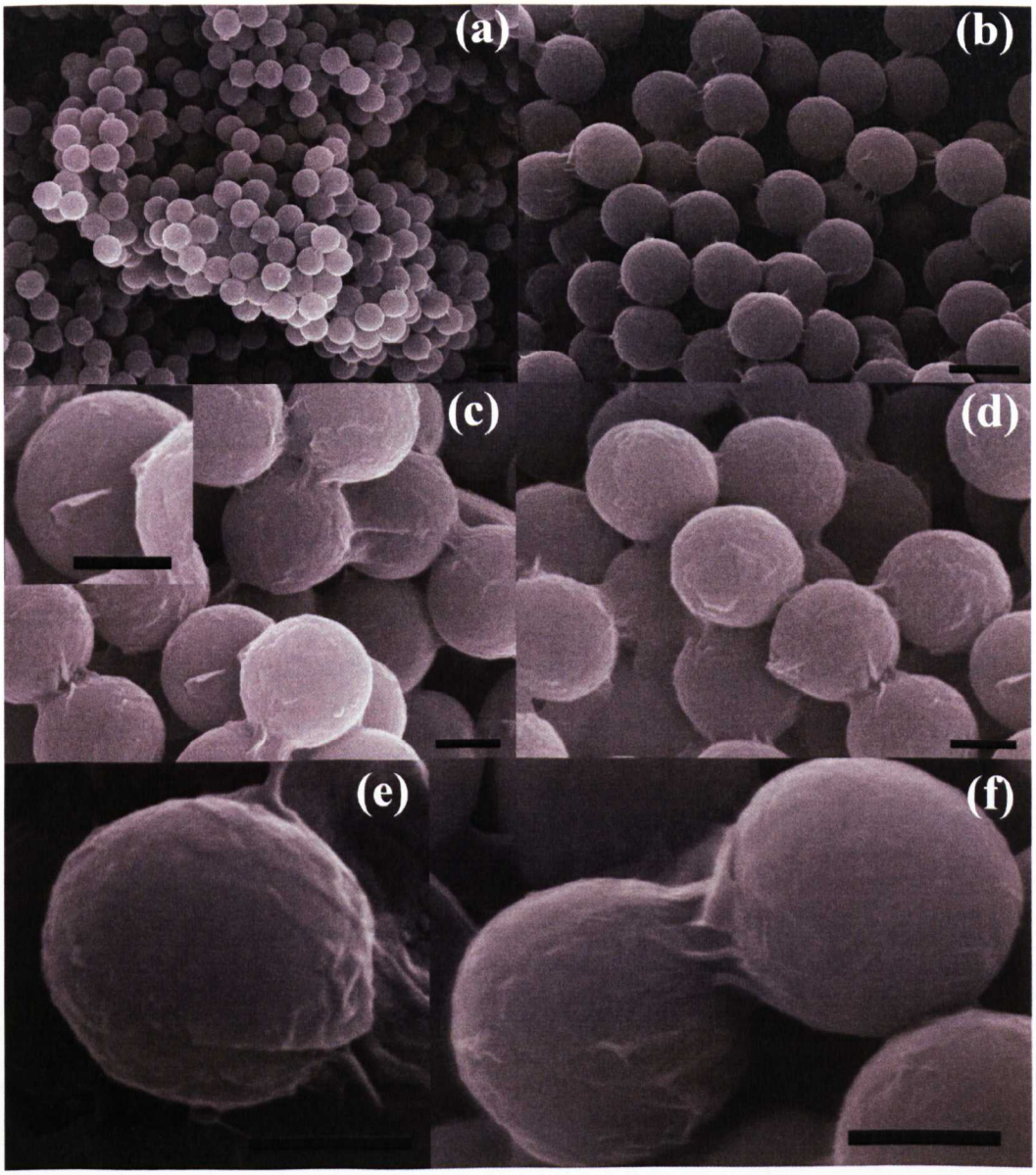

Figure 5.27: SEM images of PSS-G coated PAH-functionalised polystyrene beads. (a) View showing coated beads with surface textures. The inset displays an enlarged image showing the curled edge of an adsorbed PSS-G sheet and (b) high-magnification image showing over-lapping PSS-G sheets on neighbouring beads. Scale bars = 500 nm.

Further investigation of the morphological features of the coated PS beads surface was conducted using TEM, which displayed a coating of PSS-G sheets on the surface of PS beads. The outer shell appeared to be extremely thin, from particle sizing measurements (less than 50 nm), suggesting that the walls of the beads were coated in a nanocomposite PSS-G coating (**Figure 5.29**). In

comparison polystyrene beads with no coating, displayed an extremely clean surface (**Figure 5.28**).

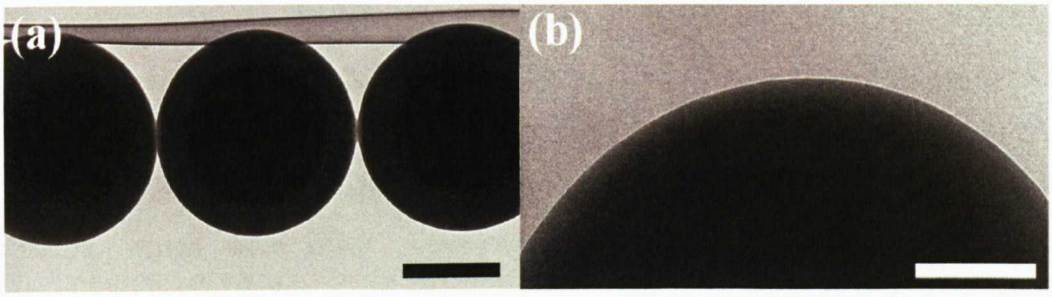

Figure 5.28 TEM images of control polystyrene beads with no PSS-G coating. (a) low magnification image showing several PS beads with no features connecting the beads and (b) high magnification image showing the clear surface of a bead with no surface features observable. Scale bars = 500 and 200 nm, respectively.

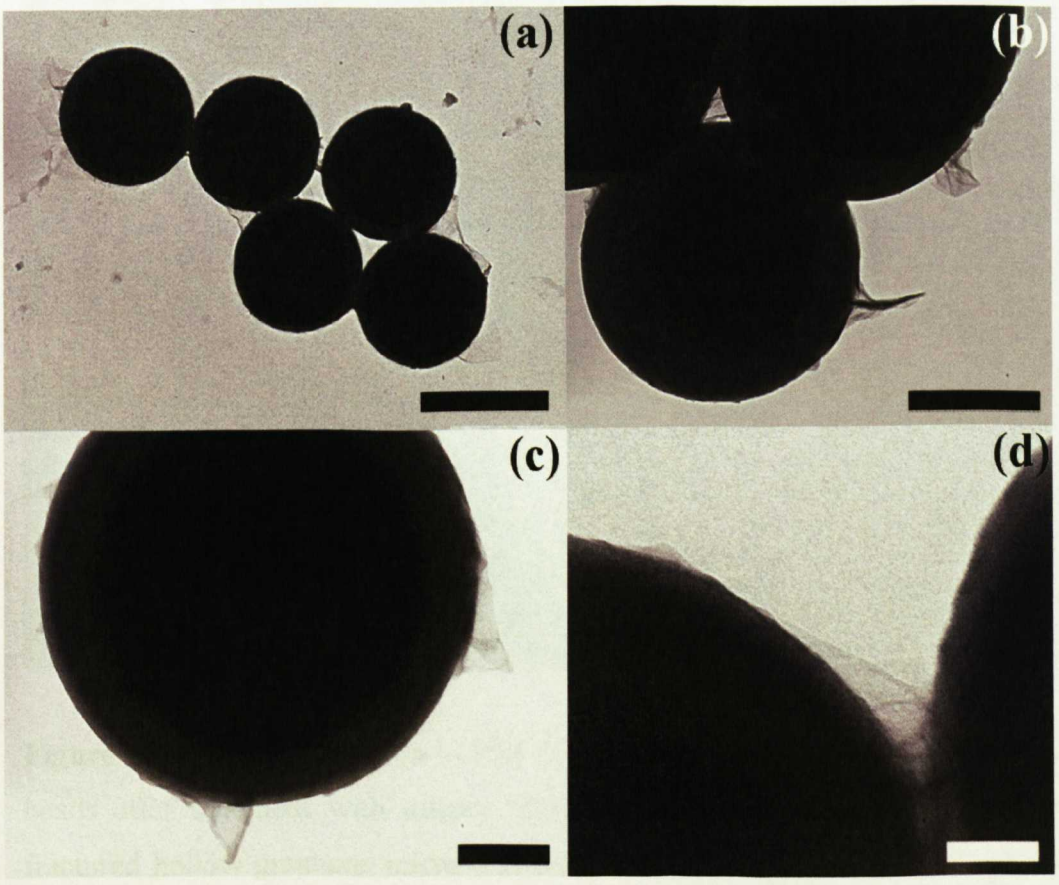

Figure 5.29 TEM images of PSS-G coated PAH-functionalised polystyrene beads. (a,d) Images showing highly transparent PSS-G sheets connecting neighbouring beads; (b-c) Images showing crinkled PSS-G sheet anchored to the

surfaces of the PAH-functionalised beads. Scale bars = 1 μm, 500, 200 and 100 nm, for figures a, b, c and d respectively.

Removal of the sacrificial core was achieved by addition of toluene to dried aggregates of PSS-G coated beads, which resulted in dissolution and removal of the polystyrene template. SEM images (**Figure 5.30**) showed the presence of deflated hollow spheres often with continuous walls. Sizing of the deflated shells, which were often continuously deformed into elliptical structures, produced values in the range of 540-930 nm, and 652-1234 nm for the short and long range axes, respectively. The results indicated that removal of the template beads was possible but the resulting graphene shells were extremely fragile when dried and exposed to the high-vacuum conditions of the SEM.

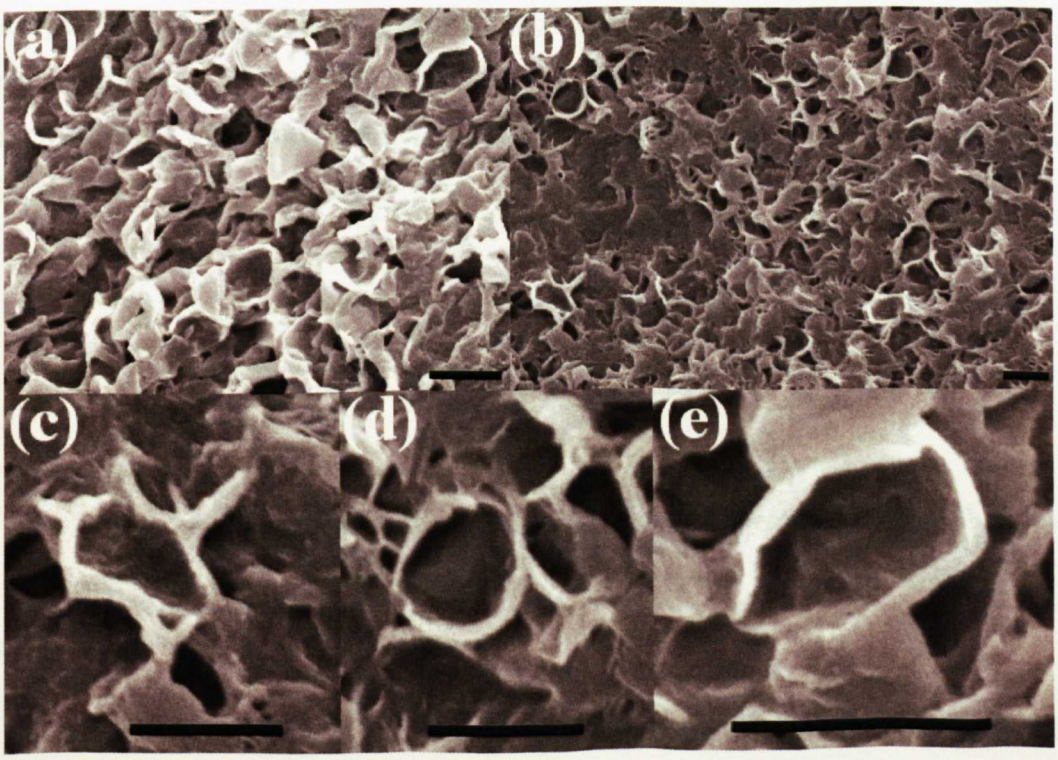

Figure 5.30 SEM images of (a-b) PSS-G coated PAH-functionalised polystyrene beads after treatment with toluene showing aggregated film of deflated and fractured hollow graphene microspheres and (c-e) higher magnification images showing individual, single deflated hollow graphene microsphere. Scale bars = 1 μm.

A generalised schematic for the potential development of hollow PSS-G microspheres, via the electrostatically driven templating of PSS-stabilised graphene sheets on PAH-functionalised PS beads, as demonstrated from SEM and TEM imaging, is shown in **Figure 5.31**.

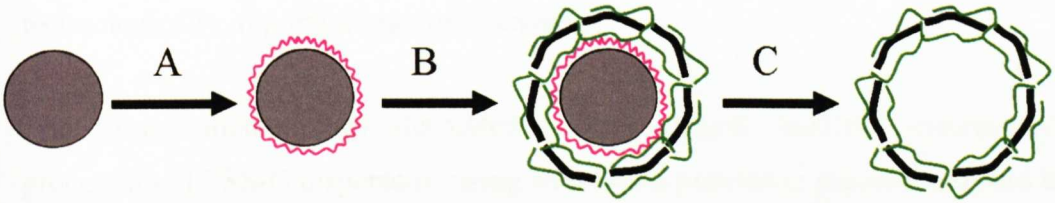

Figure 5.31 Schematic showing the colloidal templating of hollow PSS-G microspheres: (A) functionalisation of polystyrene beads with poly(allyl amine hydrochloride) (PAH); (B) electrostatically-induced templating of negatively charged PSS-G sheets on the positively charged bead surface; (C) removal of the core template by subsequent treatment with toluene to produce hollow PSS-G microspheres, which become deflated under the high-vacuum conditions of the SEM.

5.5 Conclusions and Further Work

In summary, the work discussed in this chapter highlights the potential of applying two well-established template-directed methods on the micro-and macroscale to control the assembly of complex three-dimensional structures of technologically important graphene lamellae.

The formal methodology discussed in this chapter involved macroscopic processing of PSS-G dispersons, using an internal patterning protocol induced by directional freeze-casting. This technique is more commonly known as ISISA, and involves the formation of close-packed ice crystals, which act as effective templating agents, during cryogenic processing. Direct application of ISISA to PSS-G sols resulted in the formation of poorly formed scaffolds due to the low sol viscosity. Further development of this strategy showed that homogenous sols containing PVA and PSS-G sols, could successfully be uni-directionally frozen in liquid nitrogen and subsequently submitted to high vacuum freeze-drying, causing sublimation of the ice crystals to produce monolithic scaffolds with well-ordered macro-channelled structures. This technique is a highly effective templating strategy due to the oriented growth of ice crystals in the freezing direction, which has the resulting effect of compacting or segregating the PSS-G and PVA components to the channel regions between neighbouring ice crystals. Subsequent sublimation of the ice crystals resulted in the formation of vacant pores, where the ice was originally situated, with PSS-G and PVA components location in the walls of the pores.

Unfortunately, experiments undertaken to measure the conductivity of the graphene scaffolds, demonstrated that the scaffolds did not conduct electricity, this is primarily due to the low concentration of graphene sheets in the as-prepared scaffolds and the resistance of the PVA matrix. Previous work investigating the fabrication of carbon nanotube (CNT)/Chitosan composite scaffolds fabricated electrical conductive monoliths but at a much higher content of CNT.[236] Further work in the fabrication of conducting PSS-G/PVA monoliths could investigate increasing the weight percent of graphene dispersion present in the scaffolds, in an attempt to improve the electrical conductivity properties.

As discussed and demonstrated in this chapter there is a vast array of variables which effect the formation of macroporous architecture in cryogenically processed monoliths. This in turn provides a multitude of additional experiments which could be conducted to optimise this procedure. Further to variation of PSS-G content to improve the electrical properties of the monoliths, alternative studies could investigate the effect of varying factors including freezing rates, polymer molecular weight and the shape of the vessel used for freezing. In addition, studies involving the application of other polymers, in place of PVA, could provide interesting further work for improvement of both the mechanical and electrical properties of PSS-G based scaffolds. Polymers of interest include chitosan, due to its previous success in producing well-defined CNT composite scaffolds, conducting polymers, as a means of increasing electrical conductivity and dextran, an effective biopolymer metal nanoparticle stabiliser, creating the opportunity to incorporate metal nanoparticles into the scaffold and add additional functionality to the scaffolds.

The latter methodology discussed in this chapter, demonstrated the possibility of templating polymer-stabilised graphene sheets at the micro-scale. This was achieved through the assembly of highly negatively charged PSS-stabilised graphene sheets onto the surface of positively charged poly(allyl amine hydrochloride)-coated polystyrene beads, indicating that electrostatically induced assembly provides an alternative feasible assembly route for controlling the higher-order assembly of graphene-based architectures from polymer-stabilised graphene sheets dispersed in aqueous solutions. This study was limited to the assembly of graphene dispersions on polystyrene beads with a diameter of approximately 1 μm. Further work could investigate the application of alternative bead templates including silica and melamine beads, in addition to beads with larger diameters.

In conclusion, the two methods described in this chapter have particular advantages and disadvantages. For example, although the fabrication of macroporous scaffolds is inexpensive, relatively facile, highly reproducible and readily tailored by varying the experimental conditions, as discussed above, the process demands considerable amounts of dispersible graphene if conductive

frameworks are to be produced. On the other hand, relatively small quantities of polymer-stabilised graphene dispersions are required for the formation of hollow microspheres, but the process involved judicious control over the wrapping and template-removal processes. Nevertheless, the work discussed in this chapter indicates that given the current diversity of template-directed strategies, and the relative ease of producing PSS-G dispersions in high yield, new advances in the fabrication of graphene-polymer micro- and macroscopic structures should be forthcoming. It is possible that such materials could play a key role in the development of the next generation of electronic components, including batteries and transistors, solar cells and catalytic supports.

CHAPTER 6 SUMMARY

Materials with a layered structure are an extensively studied topic in chemistry, with significant focus on their application as host matrices in intercalation studies to produce hybrid nanocomposites with advanced functions. Intercalation in layered materials is achieved *primarily by swelling, ion-exchange* or exfoliation/re-assembly protocols.

Organoclays in particular, are highly attractive host materials for a broad range of intercalants due to their facile synthesis under ambient conditions. Furthermore the exfoliation of clay is controllable and reproducible in water, due to the presence of organic functional groups anchored to the phyllosilicate clay framework. The work presented in chapter 3 demonstrated the effective polymer-mediated immobilisation of cytochrome *c* in an aminopropyl functionalised phyllosilicate clay matrix to produce a hybrid bio-inorganic composite with the immobilised proteins demonstrating sustained structure and activity. Further work could be directed towards the development of alternative novel organic functionalised clays which exfoliate in water to fabricate anionically charged sheets and could therefore be directly assembled in the presence of cationic biomolecules to produce fully intercalated nanocomposites.

The application of graphite as a host matrix in nanocomposite assembly is potentially highly attractive due to the exceeding electrical, mechanical and thermal properties associated with this layered material. Despite these advantages, intercalation in graphite layered hosts, in comparison with organoclays, requires a more vigorous approach. Graphite intercalation compounds are well established but require synthesis under relatively harsh conditions, including high temperatures and pressures. In addition, intercalation is restricted to specific types of donor and acceptor guests, which must be able to endure the extreme synthetic conditions. Furthermore, the stability of GICs, in general, can be a significant problem, which promotes the requirement for their careful storage and handling.

The recent discovery of 2D atomically thick sheets of graphene has provided an alternative approach for the generation of exfoliated graphene sheets allowing their facile assembly and formation of intercalation compounds under amenable, aqueous conditions. The work reported in chapter 4 investigated the fabrication of reduced graphene sheets using chemical synthetic pathways. In particular, graphite was initially oxidised in the presence of a mixture of sulphuric acid and potassium permanganate, resulting in the modification of the individual graphene sheets and effective dispersion in aqueous solutions. Stepwise reduction of graphene oxide, maintaining the separation of the individual sheets using single-stranded DNA polymer strands, effectively produced aqueous dispersions of exfoliated functionalised reduced graphene sheets.

The relative ease of processing these aqueous graphene dispersions is displayed by the facile preparation of electrically conductive mesolamellar films using direct evaporation or vacuum-induced assembly. Furthermore, the cationic biopolymer functionalisation of the graphene sheets can be exploited for further assembly of the sheets in the presence of oppositely charged anionic guest species. This strategy was successfully demonstrated through the co-intercalation of the cationic proteins cytochrome *c* and lysozyme.

The work reported in chapter 4 is the first example of the integration of two of nature's fundamental biological building blocks, DNA and graphene sheets, which creates a huge scope of opportunities. The functionalisation of graphene sheets with specific and biologically relevant polymer strands could potentially be applied in highly sensitive DNA based sensors. However, further work is required including full electrochemical testing of the ssDNA-graphene hybrid material to assess its suitability for the development of a biosensor device. The co-intercalation behaviour of ssDNA-graphene sheets is a further attractive property of this system as it enables potentially a wide array of guest species to be further incorporated into the graphene matrix, provided they are appropriately charged.

The relative ease of producing graphene-based films is an additional outcome of the work presented in chapter 4, which could be used to fabricate electrically and

thermally conductive thin, flexible films. The specific mechanical and electrical properties of these films could be further tailored through the use of alternative polymers or biopolymers. Preliminary studies involving the stabilisation of graphene sheets with dextran and poly(vinyl pyrrolidone) resulted in the fabrication of stable graphene dispersions. Subsequent vacuum filtration of these polymer-stabilised graphene dispersions enabled thin, handleable, flexible graphene-based films to be generated. Further work in this area with respect to investigation of the mechanical and electrical properties of the graphene-based films would be beneficial in the progress and development of this study.

As shown in chapter 4, aqueous dispersions of graphene sheets could be easily processed into self-supporting films. Chapter 5 extended these studies by investigating the application of templating protocols as alternative processing routes. The work reported in this chapter successfully demonstrated the possibility of developing both micro- and macroporous graphene-based architectures. Macroporous monoliths were fabricated using ice-templating routes, whereas graphene-based assemblies on the micro scale were produced using electrostatically driven assembly techniques. Both templating strategies involved relatively facile approaches conducted at room temperature and normal pressure.

The incorporation of graphene sheets into the walls of a PVA-based monolith demonstrated inprovements in the mechanical compressional testing. Electrical testing of these architectures, however, proved to be unsuccessful, due to their low graphene content. Future work involving the ice-segregation induced self-assembly protocol could investigate increasing the content of graphene in the starting solutions, to try and produce an electrically conductive monolith. In addition, further functionality could be incorporated into the monolith before cryogenic processing, including biomolecules and metal nanoparticles, for example, which might increase their potential application in catalysis and solar cell devices.

Initial studies involving the templating of graphene sheets on a sacrifical colloidal polymer bead demonstrated both the effective wrapping of the bead and

the possibility of its removal using chemical dissolution techniques. Further work could extend this strategy and investigate variation in the diameter and nature of the polymer core, in addition to the number of layers applied to the bead.

CHAPTER 7 REFERENCES

[1] G. Centi, S. Perathoner, in *Workshop on Innovative Applications of Layered Materials: from Catalysis to Nanotechnology*, Elsevier Science Bv, Alessandria, ITALY, **2006**, pp. 3.

[2] B. Sels, D. De Vos, M. Buntinx, F. Pierard, A. Kirsch-De Mesmaeker, P. Jacobs, *Nature* **1999**, *400*, 855.

[3] A. Vaccari, *Catalysis Today* **1998**, *41*, 53.

[4] E. R. Ruiz-Hitzky, M. Darder, P. Aranda, *Journal of Materials Chemistry* **2005**, *15*, 3650.

[5] J. H. Choy, S. Y. Kwak, J. S. Park, Y. J. Jeong, J. Portier, *Journal of the American Chemical Society* **1999**, *121*, 1399.

[6] J. H. Choy, S. Y. Kwak, Y. J. Jeong, J. S. Park, *Angewandte Chemie-International Edition* **2000**, *39*, 4042.

[7] A. I. Khan, L. X. Lei, A. J. Norquist, D. O'Hare, *Chemical Communications* **2001**, 2342.

[8] N. A. Chernova, M. Roppolo, A. C. Dillon, M. S. Whittingham, *Journal of Materials Chemistry* **2009**, *19*, 2526.

[9] M. S. Whittingham, *Chemical Reviews* **2004**, *104*, 4271.

[10] J. M. Tarascon, M. Armand, *Nature* **2001**, *414*, 359.

[11] M. Osada, T. Sasaki, *Journal of Materials Chemistry* **2009**, *19*, 2503.

[12] J. M. Oh, T. T. Biswick, J. H. Choy, *Journal of Materials Chemistry* **2009**, *19*, 2553.

[13] E. Ruiz-Hitzky, M. Darder, P. Aranda, in *Bio-inorganic Hybrid Materials: Strategies, Syntheses, Characterization and Application* (Eds.: Eduardo Ruiz-Hitzky, K. Ariga, Y. Lvov), WILEY-VCH, **2008**.

[14] E. Ruiz-Hitzky, A. Van-Meerbank, in *Handbook of Clay Science* (Eds.: F. Bergaya, B. K. G. Theng, G. Lagaly), Elsevier Ltd., **2006**.

[15] M. A. Bizeto, A. L. Shiguihara, V. R. L. Constantino, *Journal of Materials Chemistry* **2009**, *19*, 2512.

[16] B. K. G. T. G. L. F. Bergaya, *Handbook of Clay Science*, Elsevier, **2006**.

[17] R. E. Grim, *Science* **1962**, *135*, 890.

[18] C. C. Perry, T. Keeling-Tucker, *Journal of Biological Inorganic Chemistry* **2000**, *5*, 537.

[19] P. M. Dove, J. D. Rimstidt, in *Silica: Physical Behavior, Geochemistry and Materials Applications, Vol. 29*, Mineralogical Soc America, Washington, **1994**, pp. 259.

[20] M. E. Essington, *Soil and Water Chemistry: An Integrative Approach*, CRC Press, **2004**.

[21] K. A. Carrado, in *Handbook of Layered Materials* (Eds.: Scott M. Auerbach, Kathleen A. Carrado, P. K. Dutta), Marcel Dekker, Inc, **2004**.

[22] *The X-Ray Identification and Crystal Structures of Clay Minerals*, Jarrold and Sons Ltd., Norwich, **1961**.

[23] K. A. Carrado, *Applied Clay Science* **2000**, *17*, 1.

[24] M. Darder, M. Colilla, E. Ruiz-Hitzky, *Chemistry of Materials* **2003**, *15*, 3774.

[25] M. Darder, M. Colilla, E. Ruiz-Hitzky, in *EUROCLAY 2003 Meeting*, Elsevier Science Bv, Modena, ITALY, **2005**, pp. 199.

[26] M. Darder, E. R. Ruiz-Hitzky, *Journal of Materials Chemistry* **2005**, *15*, 3913.
[27] L. A. White, *Journal of Applied Polymer Science* **2004**, *92*, 2125.
[28] H. M. Park, X. C. Li, C. Z. Jin, C. Y. Park, W. J. Cho, C. S. Ha, *Macromolecular Materials and Engineering* **2002**, *287*, 553.
[29] H. X. Qiu, J. G. Yu, J. L. Zhu, *Polymers & Polymer Composites* **2005**, *13*, 167.
[30] J. H. Wu, J. M. Lin, M. Zhou, C. R. Wei, *Macromolecular Rapid Communications* **2000**, *21*, 1032.
[31] S. B. Kalambur, S. S. Rizvi, *Polymer International* **2004**, *53*, 1413.
[32] S. A. McGlashan, P. J. Halley, *Polymer International* **2003**, *52*, 1767.
[33] J. V. de Melo, S. Cosnier, C. Mousty, C. Martelet, N. Jaffrezic-Renault, *Analytical Chemistry* **2002**, *74*, 4037.
[34] O. Talibudeen, *Nature* **1950**, *166*, 236.
[35] V. Krikorian, M. Kurian, M. E. Galvin, A. P. Nowak, T. J. Deming, D. J. Pochan, *Journal of Polymer Science Part B-Polymer Physics* **2002**, *40*, 2579.
[36] P. Aranda, E. Ruizhitzky, *Chemistry of Materials* **1992**, *4*, 1395.
[37] R. A. Vaia, S. Vasudevan, W. Krawiec, L. G. Scanlon, E. P. Giannelis, *Advanced Materials* **1995**, *7*, 154.
[38] P. Aranda, Y. Mosqueda, E. Perez-Cappe, E. Ruiz-Hitzky, *Journal of Polymer Science Part B-Polymer Physics* **2003**, *41*, 3249.
[39] E. Ruiz-Hitzky, P. Aranda, *Advanced Materials* **1990**, *2*, 545.
[40] J. T. Kloprogge, S. Komarneni, J. E. Amonette, *Clays and Clay Minerals* **1999**, *47*, 529.
[41] D. O'Hare, in *Inorganic Materials*, 2nd ed. (Eds.: D. W. Bruce, D. O'Hare), John Wiley & Sons, **1997**.
[42] K. A. Carrado, *Industrial & Engineering Chemistry Research* **1992**, *31*, 1654.
[43] K. A. Carrado, J. E. Forman, R. E. Botto, R. E. Winans, *Chemistry of Materials* **1993**, *5*, 472.
[44] R. M. Barrer, L. W. R. Dicks, *Journal of the Chemical Society a - Inorganic Physical Theoretical* **1967**, 1523.
[45] K. A. Carrado, P. Thiyagarajan, R. E. Winans, R. E. Botto, *Inorganic Chemistry* **1991**, *30*, 794.
[46] K. A. Carrado, L. Q. Xu, *Chemistry of Materials* **1998**, *10*, 1440.
[47] S. L. Burkett, A. Press, S. Mann, *Chemistry of Materials* **1997**, *9*, 1071.
[48] Y. Fukushima, M. Tani, *Journal of the Chemical Society-Chemical Communications* **1995**, 241.
[49] L. Ukrainczyk, R. A. Bellman, A. B. Anderson, *Journal of Physical Chemistry B* **1997**, *101*, 531.
[50] G. R. Williams, D. O'Hare, *Journal of Materials Chemistry* **2006**, *16*, 3065.
[51] J. H. Choy, S. Y. Kwak, J. S. Park, Y. J. Jeong, *Journal of Materials Chemistry* **2001**, *11*, 1671.
[52] S. Y. Kwak, Y. J. Jeong, J. S. Park, J. H. Choy, in *2nd International Symposium on Soft Solution Processing*, Elsevier Science Bv, Tokyo, Japan, **2000**, pp. 229.
[53] D. Shan, S. Cosnier, C. Mousty, *Analytical Chemistry* **2003**, *75*, 3872.

[54] S. Vial, C. Forano, D. Shan, C. Mousty, H. Barhoumi, C. Martelet, N. Jaffrezic, in *4th Maghreb/Europe Meeting on Material and Their Applications for Devices and Physical, Chemical and Biological Sensors (MADICA 2004)*, Elsevier Science Bv, Tunis, TUNISIA, **2004**, pp. 387.
[55] F. Leroux, J. Gachon, J. P. Besse, *Journal of Solid State Chemistry* **2004**, *177*, 245.
[56] M. Darder, M. Lopez-Blanco, P. Aranda, F. Leroux, E. Ruiz-Hitzky, *Chemistry of Materials* **2005**, *17*, 1969.
[57] C. O. Oriakhi, I. V. Farr, M. M. Lerner, *Journal of Materials Chemistry* **1996**, *6*, 103.
[58] P. B. Messersmith, S. I. Stupp, *Chemistry of Materials* **1995**, *7*, 454.
[59] N. T. Whilton, P. J. Vickers, S. Mann, *Journal of Materials Chemistry* **1997**, *7*, 1623.
[60] R. I. Kaiser, *Chemical Reviews* **2002**, *102*, 1309.
[61] H. O. Pierson, *Handbook of Carbon, Graphite, Diamond and Fullerenes Properties, Processing and Applications*, Noyes Publications, **1993**.
[62] B. T. Kelly, *Physics of Graphite*, Applied Science Publishers, **1981**.
[63] http://minerals.usgs.gov/minerals/pubs/commodity/graphite/mcs-2009-graph.pdf.
[64] H. Lipson, A. R. Stokes, *Proceedings of the Royal Society of London Series a-Mathematical and Physical Sciences* **1942**, *181*, 0101.
[65] F. A. Levy, *Intercalated Layered Materials*, D. Reidel Publishing Company.
[66] M. S. Dresselhaus, G. Dresselhaus, *Advances in Physics* **1981**, *30*, 139.
[67] T. Enoki, *Graphite Intercalation Compounds and Applications*, Oxford University Press, **2003**.
[68] R. Niess, E. Stumpp, *Carbon* **1978**, *16*, 265.
[69] E. P. Giannelis, *Advanced Materials* **1996**, *8*, 29.
[70] S. Pavlidou, C. D. Papaspyrides, *Progress in Polymer Science* **2008**, *33*, 1119.
[71] M. Alexandre, P. Dubois, *Materials Science & Engineering R-Reports* **2000**, *28*, 1.
[72] X. M. Chen, J. W. Shen, W. Y. Huang, *Journal of Materials Science Letters* **2002**, *21*, 213.
[73] X. S. Du, M. Xiao, Y. Z. Meng, *Journal of Polymer Science Part B-Polymer Physics* **2004**, *42*, 1972.
[74] G. H. Chen, C. L. Wu, W. G. Weng, D. J. Wu, W. L. Yan, *Polymer* **2003**, *44*, 1781.
[75] M. Xiao, L. Y. Sun, J. J. Liu, Y. Li, K. C. Gong, *Polymer* **2002**, *43*, 2245.
[76] P. Xiao, M. Xiao, P. G. Liu, K. C. Gong, *Carbon* **2000**, *38*, 626.
[77] R. Bissessur, P. K. Y. Liu, W. White, S. F. Scully, *Langmuir* **2006**, *22*, 1729.
[78] R. Bissessur, P. K. Y. Liu, S. F. Scully, *Synthetic Metals* **2006**, *156*, 1023.
[79] Y. Matsuo, K. Tahara, Y. Sugie, *Carbon* **1996**, *34*, 672.
[80] Y. Matsuo, K. Hatase, Y. Sugie, *Chemistry of Materials* **1998**, *10*, 2266.
[81] N. A. Kotov, I. Dekany, J. H. Fendler, *Advanced Materials* **1996**, *8*, 637.
[82] L. Stryer, *Biochemistry*, 4th ed., W. H. Freeman & Company, New York, **1995**.
[83] E. Ruiz-Hitzky, K. Ariga, Y. Lvov, *Bio-inorganic Hybrid Nanomaterials: Strategies, Syntheses, Characterisation and Application*, Wiley-VCH.

[84] E. Dujardin, S. Mann, *Advanced Materials* **2002**, *14*, 775.
[85] H. E. Schoemaker, D. Mink, M. G. Wubbolts, *Science* **2003**, *299*, 1694.
[86] A. Schmid, J. S. Dordick, B. Hauer, A. Kiener, M. Wubbolts, B. Witholt, *Nature* **2001**, *409*, 258.
[87] U. T. Bornscheuer, *Angewandte Chemie-International Edition* **2003**, *42*, 3336.
[88] I. Gill, A. Ballesteros, *Trends in Biotechnology* **2000**, *18*, 282.
[89] I. Gill, A. Ballesteros, *Trends in Biotechnology* **2000**, *18*, 469.
[90] E. Topoglidis, A. E. G. Cass, G. Gilardi, S. Sadeghi, N. Beaumont, J. R. Durrant, *Analytical Chemistry* **1998**, *70*, 5111.
[91] E. Topoglidis, C. J. Campbell, A. E. G. Cass, J. R. Durrant, *Langmuir* **2001**, *17*, 7899.
[92] J. Deere, E. Magner, J. G. Wall, B. K. Hodnett, *Chemical Communications* **2001**, 465.
[93] J. Fan, J. Lei, L. M. Wang, C. Z. Yu, B. Tu, D. Y. Zhao, *Chemical Communications* **2003**, 2140.
[94] H. H. P. Yiu, P. A. Wright, *Journal of Materials Chemistry* **2005**, *15*, 3690.
[95] Y. J. Han, G. D. Stucky, A. Butler, *Journal of the American Chemical Society* **1999**, *121*, 9897.
[96] C. H. Lei, Y. S. Shin, J. Liu, E. J. Ackerman, *Journal of the American Chemical Society* **2002**, *124*, 11242.
[97] F. Caruso, C. Schuler, *Langmuir* **2000**, *16*, 9595.
[98] Y. Lvov, F. Caruso, *Analytical Chemistry* **2001**, *73*, 4212.
[99] C. Schuler, F. Caruso, *Macromolecular Rapid Communications* **2000**, *21*, 750.
[100] M. Kreiner, B. D. Moore, M. C. Parker, *Chemical Communications* **2001**, 1096.
[101] A. Dyal, K. Loos, M. Noto, S. W. Chang, C. Spagnoli, K. Shafi, A. Ulman, M. Cowman, R. A. Gross, *Journal of the American Chemical Society* **2003**, *125*, 1684.
[102] D. Avnir, S. Braun, O. Lev, M. Ottolenghi, *Chemistry of Materials* **1994**, *6*, 1605.
[103] D. Avnir, T. Coradin, O. Lev, J. Livage, *Journal of Materials Chemistry* **2006**, *16*, 1013.
[104] L. M. Ellerby, C. R. Nishida, F. Nishida, S. A. Yamanaka, B. Dunn, J. S. Valentine, J. I. Zink, *Science* **1992**, *255*, 1113.
[105] F. H. Dickey, *Journal of Physical Chemistry* **1955**, *59*, 695.
[106] D. L. Venton, K. L. Cheesman, R. T. Chatterton, T. L. Anderson, *Biochimica Et Biophysica Acta* **1984**, *797*, 343.
[107] M. Glad, O. Norrlow, B. Sellergren, N. Siegbahn, K. Mosbach, *Journal of Chromatography* **1985**, *347*, 11.
[108] H. Frenkel-Mullerad, D. Avnir, *Journal of the American Chemical Society* **2005**, *127*, 8077.
[109] D. Ma, M. Li, A. J. Patil, S. Mann, *Advanced Materials* **2004**, *16*, 1838.
[110] J. L. Vickery, S. Thachepan, A. J. Patil, S. Mann, *Molecular Biosystems* **2009**, *5*, 744.
[111] M. I. Carretero, *Applied Clay Science* **2002**, *21*, 155.
[112] J. H. Choy, J. S. Jung, J. M. Oh, M. Park, J. Jeong, Y. K. Kang, O. J. Han, *Biomaterials* **2004**, *25*, 3059.

[113] C. V. Kumar, A. Chaudhari, *Journal of the American Chemical Society* **2000**, *122*, 830.
[114] C. V. Kumar, A. Chaudhari, *Chemistry of Materials* **2001**, *13*, 238.
[115] C. V. Kumar, A. Chaudhari, *Chemical Communications* **2002**, 2382.
[116] T. Coradin, A. Coupe, J. Livage, *Journal of Materials Chemistry* **2003**, *13*, 705.
[117] A. J. Patil, S. Mann, *Journal of Materials Chemistry* **2008**, *18*, 4605.
[118] T. Mizutani, Y. Fukushima, O. Kamigaito, *Bulletin of the Chemical Society of Japan* **1990**, *63*, 618.
[119] T. Mizutani, Y. Fukushima, A. Okada, O. Kamigaito, *Bulletin of the Chemical Society of Japan* **1990**, *63*, 2094.
[120] C. J. Brinker, G. W. Scherer, *Sol-Gel Science, The Physics and Chemistry of Sol-Gel Processing*, Academic Press, Inc., **1990**.
[121] A. J. Patil, E. Muthusamy, S. Mann, *Journal of Materials Chemistry* **2005**, *15*, 3838.
[122] S. C. Holmstrom, A. J. Patil, M. Butler, S. Mann, *Journal of Materials Chemistry* **2007**, *17*, 3894.
[123] A. J. Patil, E. Muthusamy, S. Mann, *Angewandte Chemie-International Edition* **2004**, *43*, 4928.
[124] A. J. Patil, M. Li, E. Dujardin, S. Mann, *Nano Letters* **2007**, *7*, 2660.
[125] C. H. Lee, J. Lang, C. W. Yen, P. C. Shih, T. S. Lin, C. Y. Mou, *Journal of Physical Chemistry B* **2005**, *109*, 12277.
[126] J. M. Berg, J. L. Tymoczko, L. Stryer, 5th ed., W. H. Freeman & Company, New York, **2002**.
[127] P. Valette, M. Thomas, P. Dejardin, *Biomaterials* **1999**, *20*, 1621.
[128] I. Ichinose, Y. Hashimoto, T. Kunitake, *Chemistry Letters* **2004**, *33*, 656.
[129] J. M. Miller, B. Dunn, J. S. Valentine, J. I. Zink, *Journal of Non-Crystalline Solids* **1996**, *202*, 279.
[130] R. E. M. Diederix, M. Ubbink, G. W. Canters, *European Journal of Biochemistry* **2001**, *268*, 4207.
[131] E. Busi, B. D. Howes, R. Pogni, R. Basosi, R. Tinoco, R. Vazquez-Duhalt, *Journal of Molecular Catalysis B-Enzymatic* **2000**, *9*, 39.
[132] J. Deere, E. Magner, J. G. Wall, B. K. Hodnett, *Biotechnology Progress* **2003**, *19*, 1238.
[133] N. H. Kim, M. S. Jeong, S. Y. Choi, J. H. Kang, *Bulletin of the Korean Chemical Society* **2004**, *25*, 1889.
[134] R. Vazquez-Duhalt, *Journal of Molecular Catalysis B-Enzymatic* **1999**, *7*, 241.
[135] E. H. Lan, B. C. Dave, J. M. Fukuto, B. Dunn, J. I. Zink, J. S. Valentine, *Journal of Materials Chemistry* **1999**, *9*, 45.
[136] W. Jin, J. D. Brennan, *Analytica Chimica Acta* **2002**, *461*, 1.
[137] J. F. Diaz, K. J. Balkus, *Journal of Molecular Catalysis B-Enzymatic* **1996**, *2*, 115.
[138] Y. Goto, N. Takahashi, A. L. Fink, *Biochemistry* **1990**, *29*, 3480.
[139] Y. Fukushima, M. Tani, *Bulletin of the Chemical Society of Japan* **1996**, *69*, 3667.
[140] J. C. Olchowicz, D. R. Coles, L. E. Kain, G. MacDonald, *Journal of Chemical Education* **2002**, *79*, 369.
[141] J. H. Dawson, *Science* **1988**, *240*, 433.

[142] E. N. Kadnikova, N. M. Kostic, *Journal of Molecular Catalysis B-Enzymatic* **2002**, *18*, 39.
[143] S. Prasad, N. C. Maiti, S. Mazumdar, S. Mitra, *Biochimica Et Biophysica Acta-Protein Structure and Molecular Enzymology* **2002**, *1596*, 63.
[144] R. A. Copeland, *Enzymes A Practical Introduction to Structure, Mechanism, and Data Analysis*, **1996**.
[145] A. M. Klibanov, *Science* **1983**, *219*, 722.
[146] P. Hildebrandt, M. Stockburger, *Journal of Physical Chemistry* **1986**, *90*, 6017.
[147] A. Fujita, H. Senzu, T. Kunitake, I. Hamachi, *Chemistry Letters* **1994**, 1219.
[148] K. S. Novoselov, A. K. Geim, S. V. Morozov, D. Jiang, Y. Zhang, S. V. Dubonos, I. V. Grigorieva, A. A. Firsov, *Science* **2004**, *306*, 666.
[149] S. Stankovich, R. D. Piner, X. Q. Chen, N. Q. Wu, S. T. Nguyen, R. S. Ruoff, *Journal of Materials Chemistry* **2006**, *16*, 155.
[150] C. Berger, Z. M. Song, T. B. Li, X. B. Li, A. Y. Ogbazghi, R. Feng, Z. T. Dai, A. N. Marchenkov, E. H. Conrad, P. N. First, W. A. de Heer, *Journal of Physical Chemistry B* **2004**, *108*, 19912.
[151] C. Berger, Z. M. Song, X. B. Li, X. S. Wu, N. Brown, C. Naud, D. Mayou, T. B. Li, J. Hass, A. N. Marchenkov, E. H. Conrad, P. N. First, W. A. de Heer, *Science* **2006**, *312*, 1191.
[152] D. V. Badami, *Nature* **1962**, *193*, 569.
[153] K. V. Emtsev, A. Bostwick, K. Horn, J. Jobst, G. L. Kellogg, L. Ley, J. L. McChesney, T. Ohta, S. A. Reshanov, J. Rohrl, E. Rotenberg, A. K. Schmid, D. Waldmann, H. B. Weber, T. Seyller, *Nature Materials* **2009**, *8*, 203.
[154] P. W. Sutter, J. I. Flege, E. A. Sutter, *Nature Materials* **2008**, *7*, 406.
[155] A. Reina, X. T. Jia, J. Ho, D. Nezich, H. B. Son, V. Bulovic, M. S. Dresselhaus, J. Kong, *Nano Letters* **2009**, *9*, 30.
[156] X. Wang, L. J. Zhi, N. Tsao, Z. Tomovic, J. L. Li, K. Mullen, *Angewandte Chemie-International Edition* **2008**, *47*, 2990.
[157] B. Brodie, *Ann. Chim. Phys.* **1855**, *43*, 351.
[158] B. Brodie, *Philos. Trans. R. Soc. London* **1859**, *A159*, 249.
[159] L. Staudenmaier, *Ber. Dtsch. Chem. Ges.* **1898**, *31*, 1481.
[160] W. S. Hummers, R. E. Offeman, *Journal of the American Chemical Society* **1958**, *80*, 1339.
[161] H. Y. He, J. Klinowski, M. Forster, A. Lerf, *Chemical Physics Letters* **1998**, *287*, 53.
[162] A. Lerf, H. Y. He, M. Forster, J. Klinowski, *Journal of Physical Chemistry B* **1998**, *102*, 4477.
[163] C. Gomez-Navarro, R. T. Weitz, A. M. Bittner, M. Scolari, A. Mews, M. Burghard, K. Kern, *Nano Letters* **2007**, *7*, 3499.
[164] H. C. Schniepp, J. L. Li, M. J. McAllister, H. Sai, M. Herrera-Alonso, D. H. Adamson, R. K. Prud'homme, R. Car, D. A. Saville, I. A. Aksay, *Journal of Physical Chemistry B* **2006**, *110*, 8535.
[165] M. J. McAllister, J. L. Li, D. H. Adamson, H. C. Schniepp, A. A. Abdala, J. Liu, M. Herrera-Alonso, D. L. Milius, R. CarO, R. K. Prud'homme, I. A. Aksay, *Chemistry of Materials* **2007**, *19*, 4396.
[166] D. Li, M. B. Muller, S. Gilje, R. B. Kaner, G. G. Wallace, *Nature Nanotechnology* **2008**, *3*, 101.

[167] Y. X. Xu, H. Bai, G. W. Lu, C. Li, G. Q. Shi, *Journal of the American Chemical Society* **2008**, *130*, 5856.
[168] S. Stankovich, R. D. Piner, S. T. Nguyen, R. S. Ruoff, *Carbon* **2006**, *44*, 3342.
[169] S. Stankovich, D. A. Dikin, G. H. B. Dommett, K. M. Kohlhaas, E. J. Zimney, E. A. Stach, R. D. Piner, S. T. Nguyen, R. S. Ruoff, *Nature* **2006**, *442*, 282.
[170] S. Niyogi, E. Bekyarova, M. E. Itkis, J. L. McWilliams, M. A. Hamon, R. C. Haddon, *Journal of the American Chemical Society* **2006**, *128*, 7720.
[171] V. C. Tung, M. J. Allen, Y. Yang, R. B. Kaner, *Nature Nanotechnology* **2009**, *4*, 25.
[172] Y. C. Si, E. T. Samulski, *Chemistry of Materials* **2008**, *20*, 6792.
[173] N. Liu, F. Luo, H. X. Wu, Y. H. Liu, C. Zhang, J. Chen, *Advanced Functional Materials* **2008**, *18*, 1518.
[174] R. Hao, W. Qian, L. H. Zhang, Y. L. Hou, *Chemical Communications* **2008**, 6576.
[175] X. L. Li, X. R. Wang, L. Zhang, S. W. Lee, H. J. Dai, *Science* **2008**, *319*, 1229.
[176] C. Valles, C. Drummond, H. Saadaoui, C. A. Furtado, M. He, O. Roubeau, L. Ortolani, M. Monthioux, A. Penicaud, *Journal of the American Chemical Society* **2008**, *130*, 15802.
[177] X. L. Li, G. Y. Zhang, X. D. Bai, X. M. Sun, X. R. Wang, E. Wang, H. J. Dai, *Nature Nanotechnology* **2008**, *3*, 538.
[178] J. D. Watson, F. H. C. Crick, *Cold Spring Harbor Symposia on Quantitative Biology* **1953**, *18*, 123.
[179] D. Voet, 3rd ed. (Ed.: J. Voet), J. Wiley & Sons, **2004**.
[180] M. Zheng, A. Jagota, E. D. Semke, B. A. Diner, R. S. McLean, S. R. Lustig, R. E. Richardson, N. G. Tassi, *Nature Materials* **2003**, *2*, 338.
[181] M. Zheng, A. Jagota, M. S. Strano, A. P. Santos, P. Barone, S. G. Chou, B. A. Diner, M. S. Dresselhaus, R. S. McLean, G. B. Onoa, G. G. Samsonidze, E. D. Semke, M. Usrey, D. J. Walls, *Science* **2003**, *302*, 1545.
[182] Z. Li, Z. Wu, K. Li, *Analytical Biochemistry* **2009**, *387*, 267.
[183] C. Nethravathi, M. Rajamathi, *Carbon* **2006**, *44*, 2635.
[184] X. B. Fan, W. C. Peng, Y. Li, X. Y. Li, S. L. Wang, G. L. Zhang, F. B. Zhang, *Advanced Materials* **2008**, *20*, 4490.
[185] **From JCPDS file # 1-640**.
[186] N. Kovtyukhova, E. Buzaneva, A. Senkevich, *Carbon* **1998**, *36*, 549.
[187] P. G. Liu, K. C. Gong, P. Xiao, M. Xiao, *Journal of Materials Chemistry* **2000**, *10*, 933.
[188] T. Kyotani, H. Moriyama, A. Tomita, *Carbon* **1997**, *35*, 1185.
[189] N. I. Kovtyukhova, P. J. Ollivier, B. R. Martin, T. E. Mallouk, S. A. Chizhik, E. V. Buzaneva, A. D. Gorchinskiy, *Chemistry of Materials* **1999**, *11*, 771.
[190] A. Hamwi, V. Marchand, *Journal of Physics and Chemistry of Solids* **1996**, *57*, 867.
[191] U. Zielke, K. J. Huttinger, W. P. Hoffman, *Carbon* **1996**, *34*, 983.
[192] D. Briggs, G. Beamson, *Analytical Chemistry* **1993**, *65*, 1517.
[193] S. Park, J. H. An, R. D. Piner, I. Jung, D. X. Yang, A. Velamakanni, S. T. Nguyen, R. S. Ruoff, *Chemistry of Materials* **2008**, *20*, 6592.

[194] J. Campos-Delgado, J. M. Romo-Herrera, X. T. Jia, D. A. Cullen, H. Muramatsu, Y. A. Kim, T. Hayashi, Z. F. Ren, D. J. Smith, Y. Okuno, T. Ohba, H. Kanoh, K. Kaneko, M. Endo, H. Terrones, M. S. Dresselhaus, M. Terrones, *Nano Letters* **2008**, *8*, 2773.
[195] J. I. Paredes, S. Villar-Rodil, A. Martinez-Alonso, J. M. D. Tascon, *Langmuir* **2008**, *24*, 10560.
[196] A. B. Bourlinos, D. Gournis, D. Petridis, T. Szabo, A. Szeri, I. Dekany, *Langmuir* **2003**, *19*, 6050.
[197] E. Fuente, J. A. Menendez, M. A. Diez, D. Suarez, M. A. Montes-Moran, *Journal of Physical Chemistry B* **2003**, *107*, 6350.
[198] G. Socrates, *Infrared and Raman Characterisation Group Frequencies: tables and charts*, 3rd ed., **2001**.
[199] C. Hontoria-Lucas, A. J. Lopez-Peinado, J. D. Lopez-Gonzalez, M. L. Rojas-Cervantes, R. M. Martin-Aranda, *Carbon* **1995**, *33*, 1585.
[200] M. Mermoux, Y. Chabre, A. Rousseau, *Carbon* **1991**, *29*, 469.
[201] C. Y. Lee, L. J. Gamble, D. W. Grainger, D. G. Castner, *Biointerphases* **2006**, *1*, 82.
[202] N. Zammatteo, C. Girardeaux, D. Delforge, J. J. Pireaux, J. Remacle, *Analytical Biochemistry* **1996**, *236*, 85.
[203] M. Rosa, R. Dias, M. D. Miguel, B. Lindman, *Biomacromolecules* **2005**, *6*, 2164.
[204] H. A. Becerril, J. Mao, Z. Liu, R. M. Stoltenberg, Z. Bao, Y. Chen, *Acs Nano* **2008**, *2*, 463.
[205] H. Shirahama, J. Lyklema, W. Norde, *Journal of Colloid and Interface Science* **1990**, *139*, 177.
[206] K. H. Rhodes, S. A. Davis, F. Caruso, B. J. Zhang, S. Mann, *Chemistry of Materials* **2000**, *12*, 2832.
[207] D. Y. Wang, R. A. Caruso, F. Caruso, *Chemistry of Materials* **2001**, *13*, 364.
[208] A. M. Yu, Z. J. Liang, F. Caruso, *Chemistry of Materials* **2005**, *17*, 171.
[209] H. F. Zhang, I. Hussain, M. Brust, M. F. Butler, S. P. Rannard, A. I. Cooper, *Nature Materials* **2005**, *4*, 787.
[210] M. G. Worster, J. S. Wettlaufer, *Journal of Physical Chemistry B* **1997**, *101*, 6132.
[211] G. P. Chen, T. Ushida, T. Tateishi, *Biomaterials* **2001**, *22*, 2563.
[212] S. V. Madihally, H. W. T. Matthew, *Biomaterials* **1999**, *20*, 1133.
[213] M. H. Ho, P. Y. Kuo, H. J. Hsieh, T. Y. Hsien, L. T. Hou, J. Y. Lai, D. M. Wang, *Biomaterials* **2004**, *25*, 129.
[214] Z. S. Li, H. R. Ramay, K. D. Hauch, D. M. Xiao, M. Q. Zhang, *Biomaterials* **2005**, *26*, 3919.
[215] H. W. Kang, Y. Tabata, Y. Ikada, *Biomaterials* **1999**, *20*, 1339.
[216] L. Ren, K. Tsuru, S. Hayakawa, A. Osaka, *Biomaterials* **2002**, *23*, 4765.
[217] J. S. Mao, L. G. Zhao, Y. J. Yin, K. D. Yao, *Biomaterials* **2003**, *24*, 1067.
[218] C. Y. Hsieh, S. P. Tsai, D. M. Wang, Y. N. Chang, H. J. Hsieh, *Biomaterials* **2005**, *26*, 5617.
[219] N. Dagalakis, J. Flink, P. Stasikelis, J. F. Burke, I. V. Yannas, *Journal of Biomedical Materials Research* **1980**, *14*, 511.
[220] H. Schoof, L. Bruns, A. Fischer, I. Heschel, G. Rau, *Journal of Crystal Growth* **2000**, *209*, 122.

[221] W. F. Daamen, H. T. B. van Moerkerk, T. Hafmans, L. Buttafoco, A. A. Poot, J. H. Veerkamp, T. H. van Kuppevelt, *Biomaterials* **2003**, *24*, 4001.
[222] W. Tao, M. Z. Li, R. J. Xie, *Macromolecular Materials and Engineering* **2005**, *290*, 188.
[223] S. Stokols, M. H. Tuszynski, *Biomaterials* **2006**, *27*, 443.
[224] S. Deville, E. Saiz, A. P. Tomsia, *Biomaterials* **2006**, *27*, 5480.
[225] W. Mahler, M. F. Bechtold, *Nature* **1980**, *285*, 27.
[226] S. R. Mukai, H. Nishihara, S. Shichi, H. Tamon, *Chemistry of Materials* **2004**, *16*, 4987.
[227] T. Fukasawa, M. Ando, T. Ohji, S. Kanzaki, *Journal of the American Ceramic Society* **2001**, *84*, 230.
[228] S. W. Sofie, F. Dogan, *Journal of the American Ceramic Society* **2001**, *84*, 1459.
[229] M. C. Gutierrez, Z. Y. Garcia-Carvajal, M. Jobbagy, T. Rubio, L. Yuste, F. Rojo, M. L. Ferrer, F. del Monte, *Advanced Functional Materials* **2007**, *17*, 3505.
[230] M. C. Gutierrez, M. L. Ferrer, F. del Monte, *Chemistry of Materials* **2008**, *20*, 634.
[231] M. C. Gutierrez, Z. Y. Garcia-Carvajal, M. Jobbagy, L. Yuste, F. Rojo, C. Abrusci, F. Catalina, F. del Monte, M. L. Ferrer, *Chemistry of Materials* **2007**, *19*, 1968.
[232] S. R. Mukai, H. Nishihara, H. Tamon, *Chemical Communications* **2004**, 874.
[233] H. Nishihara, S. R. Mukai, D. Yamashita, H. Tamon, *Chemistry of Materials* **2005**, *17*, 683.
[234] H. Nishihara, S. R. Mukai, Y. Fujii, T. Tago, T. Masuda, H. Tamon, *Journal of Materials Chemistry* **2006**, *16*, 3231.
[235] M. Nieto-Suarez, G. Palmisano, M. L. Ferrer, M. C. Gutierrez, S. Yurdakal, V. Augugliaro, M. Pagliaro, F. del Monte, *Journal of Materials Chemistry* **2009**, *19*, 2070.
[236] M. C. Gutierrez, M. J. Hortiguela, J. M. Amarilla, R. Jimenez, M. L. Ferrer, F. del Monte, *Journal of Physical Chemistry C* **2007**, *111*, 5557.
[237] M. C. Gutierrez, M. Jobbagy, N. Rapun, M. L. Ferrer, F. del Monte, *Advanced Materials* **2006**, *18*, 1137.
[238] M. L. Ferrer, R. Esquembre, I. Ortega, C. R. Mateo, F. del Monte, *Chemistry of Materials* **2006**, *18*, 554.
[239] A. J. P. C. Suwanchawalit, R. K. Kumar, S. Wongnawa, S. Mann, *Journal of Materials Chemistry* **2009**, *in press*.
[240] S. Deville, E. Saiz, A. P. Tomsia, *Acta Materialia* **2007**, *55*, 1965.
[241] M. C. Gutierrez, Z. Y. Garcia-Carvajal, M. J. Hortiguela, L. Yuste, F. Rojo, M. L. Ferrer, F. del Monte, *Journal of Materials Chemistry* **2007**, *17*, 2992.
[242] V. F. Petrenko, R. W. Whitworth, *Physics of Ice*, **1999**.
[243] P. Atkins, J. d. Paula, *Atkins' Physical Chemistry*, 7th ed., **2002**.
[244] R. K. Iler, *Journal of Colloid and Interface Science* **1966**, *21*, 569.
[245] G. Decher, *Science* **1997**, *277*, 1232.
[246] C. Tedeschi, F. Caruso, H. Mohwald, S. Kirstein, *Journal of the American Chemical Society* **2000**, *122*, 5841.
[247] J. Schmitt, G. Decher, W. J. Dressick, S. L. Brandow, R. E. Geer, R. Shashidhar, J. M. Calvert, *Advanced Materials* **1997**, *9*, 61.

[248] Y. G. Guo, J. S. Hu, H. P. Liang, L. J. Wan, C. L. Bai, *Advanced Functional Materials* **2005**, *15*, 196.
[249] S. F. Ai, G. Lu, Q. He, J. B. Li, *Journal of the American Chemical Society* **2003**, *125*, 11140.
[250] F. Caruso, R. A. Caruso, H. Mohwald, *Science* **1998**, *282*, 1111.
[251] F. Caruso, *Chemistry-a European Journal* **2000**, *6*, 413.
[252] F. Caruso, X. Y. Shi, R. A. Caruso, A. Susha, *Advanced Materials* **2001**, *13*, 740.
[253] J. H. Shi, Z. Y. Chen, Y. J. Qin, Z. X. Guo, *Journal of Physical Chemistry C* **2008**, *112*, 11617.
[254] A. Rogach, A. Susha, F. Caruso, G. Sukhorukov, A. Kornowski, S. Kershaw, H. Mohwald, A. Eychmuller, H. Weller, *Advanced Materials* **2000**, *12*, 333.
[255] F. Caruso, *Advanced Materials* **2001**, *13*, 11.
[256] F. Caruso, R. A. Caruso, H. Mohwald, *Chemistry of Materials* **1999**, *11*, 3309.
[257] R. A. Caruso, A. Susha, F. Caruso, *Chemistry of Materials* **2001**, *13*, 400.
[258] F. Caruso, M. Spasova, A. Susha, M. Giersig, R. A. Caruso, *Chemistry of Materials* **2001**, *13*, 109.
[259] A. A. Mamedov, N. A. Kotov, M. Prato, D. M. Guldi, J. P. Wicksted, A. Hirsch, *Nature Materials* **2002**, *1*, 190.
[260] M. Olek, J. Ostrander, S. Jurga, H. Mohwald, N. Kotov, K. Kempa, M. Giersig, *Nano Letters* **2004**, *4*, 1889.
[261] M. Sano, A. Kamino, J. Okamura, S. Shinkai, *Nano Letters* **2002**, *2*, 531.
[262] X. J. Huang, Y. Li, H. S. Im, O. Yarimaga, J. H. Kim, D. Y. Jang, S. O. Cho, W. P. Cai, Y. K. Choi, *Nanotechnology* **2006**, *17*, 2988.
[263] M. A. Correa-Duarte, A. Kosiorek, W. Kandulski, M. Giersig, V. Salgueirino-Maceira, *Small* **2006**, *2*, 220.
[264] R. Verdejo, F. Barroso-Bujans, M. A. Rodriguez-Perez, J. A. de Saja, M. A. Lopez-Manchado, *Journal of Materials Chemistry* **2008**, *18*, 2221.
[265] J. J. Liang, Y. Huang, L. Zhang, Y. Wang, Y. F. Ma, T. Y. Guo, Y. S. Chen, *Advanced Functional Materials* **2009**, *19*, 2297.
[266] T. P. Nguyen, S. A. de Vos, *Applied Surface Science* **2004**, *221*, 330.
[267] B. Schoeler, G. Kumaraswamy, F. Caruso, *Macromolecules* **2002**, *35*, 889.
[268] T. Inada, S. S. Lu, *Crystal Growth & Design* **2003**, *3*, 747.
[269] V. Velikov, S. Borick, C. A. Angell, *Science* **2001**, *294*, 2335.

CHAPTER 8 Appendix

8.1 Analysis of Enzyme Kinetics[a]

This section provides a brief introduction to the kinetic analysis of enzyme-catalysed reactions, which was presented in chapter 3. In particular steady state kinetics conditions can be applied which involve experimental conditions where the enzyme-substrate (ES) complex builds up to a "steady state" level.

When an enzyme is initially mixed with a substrate in solution, the concentration of the substrate [S] decreases whilst the concentration of product [P] simultaneously increases and this can be modelled by first order kinetic behaviour.

In the early stages of the reaction, the rate of formation of [P] or rate of loss of [S] has a liner relationship, which allows the initial velocity of the enzyme-substrate reaction to be approximated from the initial slope of the linear plot of [S] or [P] as a function of time. One would expect, based on first order kinetic behaviour, that the velocity should increase linearly with increases in [S]. However, further analysis of the velocities of enzyme-catalysed reactions at different starting [S] displayed a saturation point at high [S]. Brown (1902) proposed a qualitative explanation for this observation, suggesting that is it related to the formation of an enzyme-substrate complex, as shown in **Equation 8.1**.

$$E + S \underset{k_{-1}}{\overset{k_1}{\rightleftharpoons}} ES \xrightarrow{k_2} E + P$$

Equation 8.1

---

[a] R. A. Copeland, *Enzymes A Practical Introduction to Structure, Mechanism, and Data Analysis*, **1996**.

The substrate is bound to the active site of the enzyme, which is the region that directly binds with the substrate and contains the catalytic residues that are involved in the bond making and breaking process, enabling the formation of the product. From **Equation 8.1** it can be deduced that there are two possible routes for the ES complex to proceed in, it can either dissociate to from free enzyme and substrate, with a rate constant k_{-1} or the reaction can proceed in a forward direction to form enzyme and product, with a rate constant k_2. It is assumed that the latter option is the primary route for enzyme-catalysed reactions, which contributes to a catalytic rate of reaction as shown in **Equation 8.2**.

$$v = k_2[\mathrm{ES}]$$

Equation 8.2

Henri and Michaelis and Menten, in the early 1900s, subsequently provided a quantitative description of the enzyme kinetics, based on Brown's model. This approach involved applying a steady state approach with a few assumpions as follows. Firstly in the early stages of the reaction all the enzyme molecules can be accounted for in the form of free enzyme or the enzyme-substrate complex, as shown in **Equation 8.3**.

$$[\mathrm{E_T}] = [\mathrm{E}] + [\mathrm{ES}]$$

Equation 8.3

The enzyme-substrate complex is an intermediate in the catalytic reaction and its rate of change of concentration can be approximated to be zero, through the application of steady state kinetics. This allows an expression for the rate of formation and rate of loss of the enzyme-substrate complex to be derived, using **Equation 8.1** as shown in **Equation 8.4** and **Equation 8.5**, respectively.

$$\text{Rate of formation of ES complex} = k_1[\mathrm{E}][\mathrm{S}]$$

Equation 8.4

$$\text{Rate of loss of ES complex} = (k_{-1} + k_2)[\mathrm{ES}]$$

Equation 8.5

Under steady state conditions the concentration of the intermediate complex, ES essentially remains the same, this means the expressions in **Equation 8.4** and **Equation 8.5** can be equated, as shown in **Equation 8.6** and subsequently re-arranged to give an expression for [ES], as shown in **Equation 8.7**.

$$k_1[E][S] = (k_{-1} + k_2)[ES]$$

Equation 8.6

$$[ES] = \frac{[E][S]}{(k_{-1} + k_2)/k_1}$$

Equation 8.7

Equation 8.7 can be simplified by combining the rate constants in a single term know as the Michaelis constant, K_m, as shown in **Equation 8.8**, resulting in an expression for [ES] as shown in **Equation 8.9**.

$$K_m = \frac{k_{-1} + k_2}{k_1}$$

Equation 8.8

$$[ES] = \frac{[E][S]}{K_m}$$

Equation 8.9

Equation 8.9 can be subsequently arranged by substituting **Equation 8.3** in terms of [E], resulting in a simplified expression for the concentration of enzyme-substrate, as shown in **Equation 8.10**.

$$[ES] = [E_T] \frac{[S]}{[S] + K_m}$$

Equation 8.10

We can subsequently substitute **Equation 8.10** into **Equation 8.2** to obtain an expression for the overall rate of the reaction shown in **Equation 8.11**.

$$v = k_2[E_T] \frac{[S]}{[S] + K_m}$$

Equation 8.11

At high concentrations of substrate, all the catalytic sites are saturated and the reaction velocity reaches a maximum value, V_{max}, resulting in the expression shown in **Equation 8.12**.

$$V_{max} = k_2 [E_T]$$

Equation 8.12

Combining **Equation 8.11** with **Equation 8.12** results in the Michaelis-Menten **Equation 8.13**.

$$v = \frac{V_{max}[S]}{[S] + K_m}$$

Equation 8.13

Experimentally the maximum rate of reaction, V_{max} and the Michaelis constant, K_m can be determined by calculating the rate of catalysis at a range of substrate concentrations. The kinetic parameters associated with a particular enzyme can be deduced by linearising the Michaelis-Menten equation (**Equation 8.13**) by calculating the reciprocal of both sides of the expression, as shown in **Equation 8.14**. This results in a standard equation for a straight line graph, in the form of $y = mx + c$. Plotting 1/V against 1/[S] results in a linear plot, commonly known as a Lineweaver-Burk plot, with the gradient equal to K_m/V_{max}, the y-intercept equal to $1/V_{max}$ and the x-intercept equal to $-1/K_m$. This allows K_m and V_{max} to be calculated from the slope and y-intecepts of the Lineweaver-Burk plot, respectively, as shown in **Figure 8.1**. V_{max} can be calculated from the reciprocal of the y-intercept. K_m can be calculated either from the slope of the linear plot

multiplied by the calculated V_{max} value or from the negative, reciprocal of the extrapolated x-intercept value.

$$\frac{1}{v} = \frac{1}{V_{max}} + \frac{K_m}{V_{max}[S]}$$

Equation 8.14

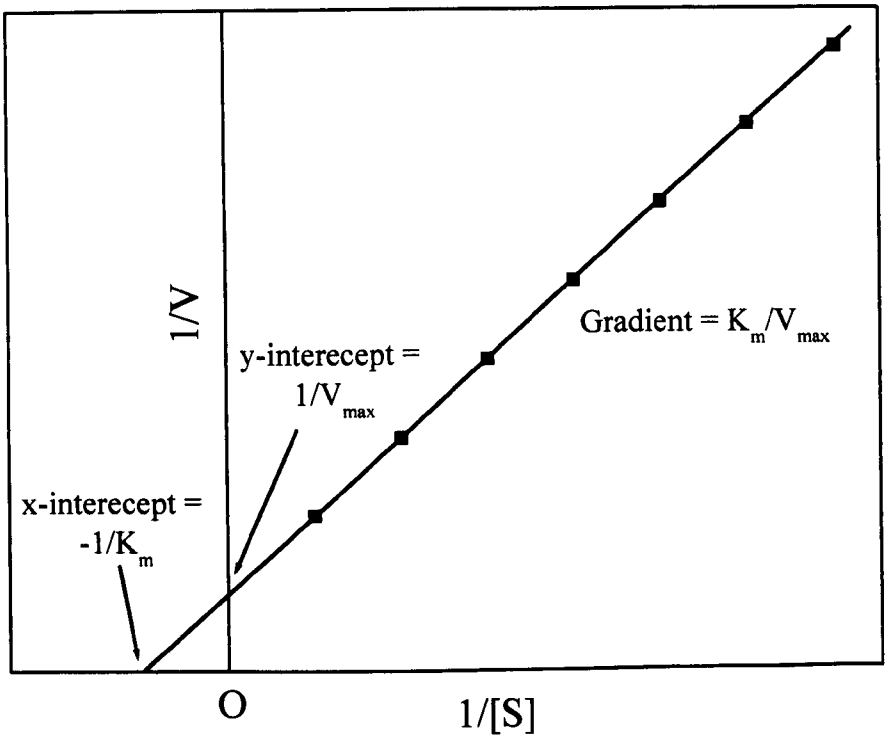

Figure 8.1: Lineweaver-Burk Plot of enzyme kinetics

8.2 Measurement of Specific Enzyme Activity

In chapter 3, the enzyme activity was measured using a peroxidase-type assay, involving an electron donor, ABTS, which is oxidised to form the cationic radical, $ABTS^{\bullet+}$ and can be conveniently followed spectrophotometrically, by measuring the change in absorbance at 414 nm. The increase in concentration of the product, $[ABTS^{+\bullet}]$ is directly proportional to the increase in absorbance and

can be calculated by re-arranging the Beer-Lambert Law in terms of the concentration, (units: M or $molL^{-1}$), as shown in **Equation 8.15**.

$$\Delta A = \varepsilon.c.l \qquad c = \frac{\Delta A}{\varepsilon.l}$$

Equation 8.15

Where ΔA is the increase in absorbance of $ABTS^{+\cdot}$, ε is the extinction coefficient of $ABTS^{+\cdot}$, 3.6×10^4 M^{-1} cm^{-1} at 415nm, c is the concentration of $ABTS^{+\cdot}$ and l is the thickness of the sample, this is controlled by the path length of the cuvette which is usually 1cm.

The rate of reaction can subsequently be calculated from **Equation 8.16**. The rate of reaction is the decrease in the concentration of substrate per unit time or the increase in the concentration of product produced per unit time,

(units: $molL^{-1}min^{-1}$ or $Mmin^{-1}$).

$$\text{Rate} = \frac{[\text{product}]}{\text{time}}$$

Equation 8.16

The enzyme activity (E.A.) is a measure of the number of moles of enzyme converted per unit time and can be calculated from **Equation 8.17**,

(units: $\mu mol\ min^{-1}$).

E.A. = Rate × Reaction Volume

Equation 8.17

Finally, the specific activity (S.A.), which quantifies the enzyme efficiency and is equivalent to the number of moles of enzyme converted per unit time per unit mass of enzyme, can be calculated from **Equation 8.18**, (units: $\mu molmg^{-1}min^{-1}$).

$$\text{S.A.} = \frac{\text{E.A.}}{\text{Mass of Enzyme Present}}$$

Equation 8.18